



Mechanical Behaviour of Lined Pipelines under Welding and Impact

A Thesis Submitted for the Degree of Doctor of
Philosophy

By

Obeid Obeid

Brunel University London

College of Engineering, Design and Physical Sciences

Department of Mechanical, Aerospace and Civil
Engineering

October 2016

Declaration

This thesis titled “Mechanical Behaviour of Pipelines under Welding and Impact” is submitted for the Degree of Doctor of Philosophy in the Department of Mechanical, Aerospace and Civil Engineering, College of Engineering, Design and Physical Sciences at Brunel University London.

I, O. Obeid, the undersigned, hereby declare that the research work in this thesis was carried out in accordance with the Regulations of Brunel University London. The work presented in this thesis is original, except where indicated in the text by special reference. The research has not formed the basis for any submission of any other degree. The views expressed in this thesis are those of the author.

The above-titled thesis has not been presented to any other University for award either in the United Kingdom or overseas.

Publications Based on this Research

Obeid. O. and Alfano, G., Bahai, H. (2014) 'Analysis of the Temperature Evolution during Lined Pipe Welding', *In Advanced Materials Research*. Vol. 1016. Trans Tech Publications, pp. 753-757

Obeid. O. and Alfano, G., Bahai, H. (2016) 'Thermo-mechanical analysis of a single-pass weld overlay and girth welding in lined pipe', *Journal of Materials Engineering and Performance*. Submitted (under review).

Signed:

Date: 31st October 2016



Obeid Obeid

Dedication

This research is dedicated to all innocent Syrian civilians who have lost their lives in the current war where my younger sister, *Noha*, is within these victims.

May their souls rest in peace.

Also, it is dedicated to

my parents,

brothers,

sisters

whose love, support, guidance and sacrifices are boundless.

Abstract

The research presented in this thesis covers two critical problems regarding lined pipes: dynamic impact and welding. A lined pipe consists of an inner layer (the liner) made of corrosion resistant alloy (CRA), e.g. AISI304 stainless steel, and an outer layer made of low carbon steel, e.g. carbon-manganese steel, C-Mn. To manufacture the lined pipe, a special heat treatment, known as tight fit pipe (TFP), based on cooling the liner to -200°C , heating the backing pipe to $+500^{\circ}\text{C}$ and inserting the liner inside the outer pipe, was used in this work. Both welding and impact with external objects are responsible for accumulating high levels of plastic strains and residual stresses which could lead to failure in the pipe sometime after the impact or the welding.

The special welding process used in lined pipes typically consists of the overlay welding (inner welding) of the liner with the C-Mn steel pipe for each segment and the girth welding (outer welding) of the two segments. To simulate this welding process using the ABAQUS code, nonlinear heat-transfer and mechanical finite-element (FE) analyses have been conducted. A distributed power density of the moving welding torch and a non-linear heat transfer coefficient accounting for both radiation and convection have been used in the analysis and implemented in ABAQUS user-subroutines.

The modelling procedure has been validated first against previously published experimental results for stainless steel and carbon steel pipe welding separately. The model has been then used to determine the isotherms induced by the one-pass weld overlay and the one-pass girth welding and to clarify their influence on the transient temperature field and residual stress in the lined pipe. Furthermore, the influence of the cooling time between weld overlay and girth welding and of the welding speed have been examined thermally and mechanically as they are key factors that can affect the quality of lined pipe welding.

The same FE numerical procedure to analyse line pipe welding is then applied to simulate six cases experimentally tested in the lab within this project. Furthermore,

two cases have been analysed first, namely a reference case, in which the effect of the TFP pre-heat treatment is neglected, and a second one where the pre-heat treatment has been taken into consideration. During welding, the FE thermal history and mechanical strain results for both cases correlate well with the experimental ones in the region with the highest residual stresses, because the effect of initial residual stresses is cancelled in the regions subject to very high temperatures. After welding, the numerical and experimental results have proved that the initial residual stresses due to the TFP pre-heat treatment are reasonably important in the liner whereas they are practically negligible in the C-Mn pipe.

The same reference case is then compared numerically and experimentally with further five parametric cases to study the effect of welding properties (weld overlay and girth welding materials), geometric parameters (using weld overlay and liner) and welding process parameters (heat input). The numerical temperature fields and residual stresses are in good agreement with their experimental counterparts for all cases.

The dynamic impact problem is a crucial one for lined pipes because of the reduction in the thickness of the outer pipe ensured by the internal protection from corrosion given by a thinner liner. In this case, the lined pipe is more affected by potential impact with external objects (so-called ‘third party interference’ in the Oil and Gas industry). In general, a dent produced by a freely dropped weight is responsible to a large extent of catastrophic failure in pipelines. Therefore, in this work, 3D FE models have been developed to simulate the mechanism of vertical free drop of a weight from different heights resulting in damage in the pipe. Models have been executed using a three-dimensional non-linear explicit-dynamics FE code, ABAQUS/EXPLICIT. In order to precisely simulate the response of the pipe to subsequent impacts and spring back, an elastic-plastic constitutive law is adopted using the isotropic Hooke’s law and a Von Mises yield criterion, with work hardening based on an isotropic hardening rule associated with the equivalent plastic strain rate. Strain-rate dependent properties are specified for both materials, C-Mn and AISI304, to take into account the change in velocities during impact. The numerical strain results are reasonably consistent with the experimental ones recorded by four strain gauge rosettes positioned symmetrically around the dent

centre. Numerical and experimental results are comprehensively analysed and discussed also in terms of practical implications in the industry.

Acknowledgements

All praises and humble thanks are to Almighty ALLAH (GOD), who gave me the valour and strength for successful completion of my PhD thesis done under a critical period in my life. Five years have passed since I started the work for this study which coincided with the bloody war in my beloved country, Syria. Honestly, I lost the bet to finish my studying after completely finishing the fierce war in Syria. The war is still going over there and innocent civilians are still falling victims to such barbarian war. I promise them to have a successful research to be a part of Syria future.

I specially owe my deep gratitude to my Principal Supervisor, Dr GIULIO ALFANO, for all his continuous unlimited support and supreme guidance. I am certainly sure that the only thing which brings this thesis to light is the vibrant and skilful leadership of Dr ALFANO. He managed my education and development in FEA and a number of things to enhance my research skills from the first day in PhD studying with a respectful manner. I have reached this point in my life because of his encouragement and support to stand up and continue my way in PhD in spite of the critical circumstances. I was certainly given the best humble human, intelligent, vibrant and skilful supervisor I could ever have had.

I also have a lot of appreciations for Prof HAMID BAHAI for sharing his knowledge, fruitful comments and discussions. I greatly appreciate his efforts and guidance during the current research.

Special words of appreciation have to be extended to my Home Supervisors, Dr MOWAFFAK ALMONAJJED, for his valuable knowledge, suggestions and encouragement throughout the years of MSc and PhD studying.

My special thanks have to be extended to energetic and skilful technicians in Brunel University. Some of them had a direct impact on my research. A special word of acknowledgment goes to Mr Paul Yates who found feasible methods to conduct experiments successfully. A very deep expression of gratitude goes as well to Mr Keith Withers who spent his last moment before retiring from Brunel University

preparing the impact apparatus with fruitful suggestions to do the impact tests. Many thanks go also to Mr Ali Ahmadnia whose brilliant ideas and suggestions had a strong impact on my project. My deep gratitude goes also to Mr Guy Fitch who welded all pipes with perfect and professional method. I am so grateful for help and assistance achieved by all staff in Mechanical Workshop (in particular, Philip and John) and in BCAST workshop (in particular, Peter and Samantha).

Acknowledgements are due with equal strength to my Home University in Syria, ALBAATH UNIVERSITY, and BRITISH COUNCIL (in particular, Mr TIMOTHY STOBBS) for unlimited support during my studying.

Finally, but most importantly, I must thank my family in Syria for continuous encouragement, moral support and interest in my project. It is difficult to put in words how the prayers of my father and mother keep me strong enough despite a big loss I have in my home city, Palmyra. I lost my younger sister, NOHA, in this war. She was a successful pharmacist and mother. She spent her 30 years studying and working harder to build a great future for herself. She strongly insisted to reach the peak of success but a one bullet from DAESH (ISIS) was enough to be shot dead and to finish her future. All my family and her son are very proud of her and great achievements she did.

Obeid Obeid

London, October 2016

Table of Contents

Declaration	i
Publications Based on this Research.....	i
Dedication	ii
Abstract	iii
Acknowledgements	vi
Table of Contents	viii
Symbols.....	xii
Glossary	xv
List of Figures	xvii
List of Tables.....	xxiv
Chapter 1 Introduction	1
1-1. Background and Motivation	1
1-2. Aims and Objectives	3
1-3. Summary of Research Approach.....	4
1-3-1. Lined Pipe Welding.....	4
1-3-2. Lined Pipe Denting	5
1-4. Thesis Outline.....	6
Chapter 2 Literature Review	9
2-1. Introduction	9
2-2. Previous Contributions to the Numerical and Experimental Work Pertaining to Pipe Welding Approach	9
2-2-1. Analytical, 2-D and 3-D Approaches.....	9
2-2-2. Developed FE Approaches.....	13
2-3. Previous Contributions to the Numerical and Experimental Analysis of Pipes Subject to Denting	22
2-4. Lined pipe geometries and material specifications	29
2-5. Conclusions	32
Chapter 3 Experimental Setup for the Welding Process.....	34
3-1. Introduction	34
3-2. Manufacturing Procedure	35
3-3. Preparation for Welding Process	38

3-3-1. Thermal Fields Measurement.....	39
3-3-2. Strain Measurement	40
3-4. Welding Operation	43
3-5. Post-Welding Requirement	46
3-5-1. Measurement of Residual Stresses by Hole-Drilling.....	47
3-5-2. Measurement of Residual Stresses by X-Ray Diffraction (XRD)	48
3-6. Conclusions	49
Chapter 4 Experimental Setup for the Impact Process	50
4-1. Introduction	50
4-2. Dents.....	51
4-3. Experimental Specimens and Materials	53
4-4. Experimental Apparatus	53
4-4-1. Measuring the Impact Velocity.....	56
4-4-2. Measuring the Dented Pipe Geometries.....	56
4-5. NDT Tests	57
4-6. Conclusions	58
Chapter 5 FE Analysis of a Single-Pass Weld Overlay and Girth Welding.....	59
5-1. Introduction	59
5-2. Description of Welding Conditions.....	59
5-3. Thermal Analysis	60
5-3-1. Modelling of the Heat Source	60
5-3-2. Thermal Properties	63
5-4. Validation	66
5-5. Finite Element Modelling of the Lined Pipe	69
5-5-1. Description of the Lined Pipe Joint and Welding Conditions.....	69
5-5-2. Finite Element Mesh	73
5-5-3. Thermal Analysis	74
5-5-4. Mechanical Analysis	76
5-6. Results of the Thermal Analysis	77
5-6-1. Thermal History during the Weld Overlay	78
5-6-2. Thermal History during Girth Welding.....	81
5-7. Effect of Welding Factors	82
5-7-1. Effect of Welding Factors on Thermal History.....	82
5-7-2. Effect of Welding Factors on Residual Stresses	85
5-8. Conclusions	89
Chapter 6 Results of Experimental Testing and of FEA of Lined Pipe Welding. 91	

6-1. Introduction	91
6-2. Manufacturing Process	92
6-2-1. Description of the Lined Pipe and Welding Parameters	92
6-3. Finite Element Modelling.....	96
6-3-1. Thermal Analysis	97
6-3-2. Structural Analysis	100
6-4. Results and Discussions	102
6-4-1. Temperature Fields.....	102
6-4-2. Structural Response.....	107
6-5. Residual Stress and Plastic Deformation.....	118
6-5-1. Residual Stresses on the Inner Surface	118
6-5-2. Residual Stresses on the Outer Surface.....	120
6-6. Verification of the Experimental Results	122
6-7. Conclusions	124
Chapter 7 Parametric Study of Lined Pipe Welding.....	127
7-1. Introduction	127
7-2. Results and Discussion	128
7-2-1. Thermal Results	128
7-2-2. Structural Response.....	132
7-3. Mesh Convergence Analysis	146
7-4. Radial Shrinkage	150
7-5. Conclusions	151
Chapter 8 Experimental and FE Models of Lined Pipe Impact.....	153
8-1. Introduction	153
8-2. Numerical Model.....	154
8-2-1. FE Mesh of Impact Components.....	156
8-2-2. Contact Regions, Velocity and Loads	157
8-3. Parametric Study	158
8-3-1. Finite Element Analysis	158
8-3-2. Dented Pipe Geometries.....	160
8-3-3. Strain Behaviour in the Dented Region	161
8-3-4. Residual Stresses	169
8-3-5. Energy Consumed in the Whole Model.....	174
8-3-6. Collision Velocity	177
8-4. Mesh Convergence Analysis	180
8-5. Verification of the Experimental Results	182

8-6. Conclusions	184
Chapter 9 Summary, Conclusions and Future Work Recommendations	186
9-1. Major conclusions	186
9-2. Limitations.....	192
9-3. Recommendations for Future Work	192
References	195
Appendix A.....	202
A-1. Tools utilized in Welding tests	202
A-2. Tools utilized in impact tests	203

Symbols

d	Dent depth
D	Pipe outer diameter
t	Pipe thickness
$\Delta\sigma$	Maximum stress
Δp	Cyclic pressure
S-N	Stress-Number of cycles
L_{carbon}	C-Mn pipe length (m)
D_{carbon}	C-Mn pipe outer diameter (mm)
t_{carbon}	C-Mn pipe thickness (mm)
$L_{\text{stainless}}$	AISI 304 pipe length (m)
$D_{\text{stainless}}$	AISI 304 pipe outer diameter (mm)
$t_{\text{stainless}}$	AISI 304 pipe thickness (mm)
ρ	Density (kgm^{-3})
E	Young's modulus (GPa)
σ_{stress}	Yield stress (MPa)
σ_{strength}	Ultimate strength (MPa)
ν	Poisson's ratio
a	Half-length of heat source (mm)
b	Depth of heat source (mm)
c	Half-width of heat source (mm)
q	Power density (Wm^{-3})
Q	Total heat input (W)
V	Voltage (volts)
I	Current (amperes)
μ	Welding efficiency (%)
R	Radial distance of the heat torch centre from the pipe axis (mm)
θ	Angle of moving torch around the pipe (Rad)
ω	Angular velocity (Rad/s)

t	Current time (s)
t_0	Initial time (s)
H	Enthalpy of material
κ	Conductivity
l	Latent heat
c	Heat capacity
f_1	Volumetric liquid fraction
T_{solid}	Solidus temperature
T_{liquid}	Liquidus temperature
\vec{q}	Heat flux vector
T_{amb}	Ambien temperature
T	Current temperature
h_{con}	Convective heat transfer coefficient
ε_{em}	Effective radiation emissivity
σ_{bol}	Boltzman constant
ε_{kl}	Total strain
ε_{kl}^{el}	Elastic strain
ε_{kl}^{pl}	Plastic strain
ε_{kl}^{th}	Thermal strain
Z	Axial distance starting from the WCL
q_c	Heat loss upon C-Mn surface
A_c	Surface area of C-Mn exposed to atmosphere
T_c	Surface temperature of C-Mn pipe
T_a	Ambient temperature
h_c	Heat transfer coefficient between the surface of C-Mn pipe and the atmosphere of room
q_s	Heat gain upon AISI304 surface
A_s	Surface area of AISI304 exposed to atmosphere
T_s	Surface temperature of AISI304 pipe
h_s	Heat transfer coefficient between the surface of AISI304 pipe and the atmosphere of room
q_{total}	Total heat loss
$q_{radiation}$	Radiation heat loss

$q_{conviction}$	Convection heat loss
$h_{convection}$	Convective heat transfer coefficient
A	Pipe surface area
T_{pipe}	Current temperature at the pipe surface
$d\varepsilon_{ij}$	Increment of the total strain
$d\varepsilon_{ij}^e$	Elastic strain increment
$d\varepsilon_{ij}^p$	Plastic strain increment
$d\varepsilon_{ij}^{th}$	Thermal strain increment
v	Velocity of free drop (m/s)
g	Acceleration of gravity
h	Height
I	Height of punched pipe (mm)
W	Width of punched pipe (mm)
H_{carbon}	Dent depth of C-Mn pipe (mm)
$H_{stainless}$	Dent depth of AISI304 pipe (mm)
D_{carbon}	Outer diameter of undeformed C-Mn pipe (mm)
$D_{stainless}$	Outer diameter of undeformed AISI304 pipe (mm)
$S, \text{ Mises}$	Von Mises Stress (N)
$NT11$	Temperature ($^{\circ}\text{C}$)
$S, S33$	Axial residual stress (N)
$S, S22$	Hoop residual stress (N)
E_{TOT}	Total energy (W)
E_I	Internal energy (W)
E_{VD}	Viscous dissipation energy (W)
E_{KE}	Kinetic energy (W)
E_{FD}	Frictional dissipation energy (W)
E_W	Work energy (W)
E_{SE}	Recoverable (elastic) strain energy (W)
E_{PD}	Plastic dissipation energy (W)
E_{IW}	Internal work energy (W)
E_{EW}	External work energy (W)

Glossary

2D	Two Dimensional
3D	Three Dimensional
AISI	American Iron and Steel Institute
API	American Petroleum Institute
ASME	American Society of Mechanical Engineers
ASTM	American Society for Testing and Materials
AWS	American Welding Society
BCAST	Brunel Centre for Advanced Solidification Technology
BM	Base Material
CL	Weld Centreline
C-Mn	Carbon Manganese
CO ₂	Carbon Dioxide
CRA	Corrosion Resistant Alloy
DPI	Dye Penetrant Inspection
EPRG	European Pipeline Research Group
Exp.	Experimental
FE	Finite Element
FEM	Finite Element Method
FZ	Fusion Zone
GMAW	Gas Metal Arc Welding
GTA	Gas Tungsten Arc
GTAW	Gas Tungsten Arc Welding
H ₂ S	Hydrogen Sulfide
HAZ	Heat Affected Zone
LPI	Liquid Penetrant Inspection
MIG	Metal Inert Gas
NDT	Non-Destructive Testing

Num.	Numerical
PDMA	Pipeline Defect Assessment Manual
PHMSA	Pipeline and Hazard Materials Safety Administration
SAW	Submerged Arc Welding
SCF	Stress Concentration Factor
SMAW	Shielded Metal Arc Welding
SMYS	Specified Minimum Yield Stress
SS	Stainless Steel
TC	Thermocouple
Temp.	Temperature
TFP	Tight Fit Pipe
TIG	Tungsten Inert Gas
TSOFT	Softening Temperature
WCL	Weld Centreline
WM	Welding Material
XRD	X-Ray Diffraction

List of Figures


Figure 2-1 Pipe and weld dimensions with welding directions towards positive ϕ -direction (Jonsson and Josefson, 1988), dimensions in mm	10
Figure 2-2. Comparison between analytical and experimental results on the outer surface for residual (a) axial stresses and (b) hoop stresses (Jonsson and Josefson, 1988)	11
Figure 2-3. Experimental and FE models used in study (Karlsson, 1989; Josefson, et al., 1989; Karlsson and Josefson, 1990), dimensions in mm	12
Figure 2-4. 2D FE model used in thermal and mechanical analysis, shaded elements are the filler material (Karlsson, 1989)	12
Figure 2-5. Pipe and groove dimensions in mm (Deng and Murakawa, 2006).	15
Figure 2-6 The axial residual stress distributions on (a) the inner surface and (b) the outer surface (Deng and Murakawa, 2006).....	16
Figure 2-7. Dissimilar pipe, sketched in mm (Deng and Kiyoshima ,2010).	18
Figure 2-8. Detailed dimensions of (a) pipe and (b) test points (Akbari and Sattari, 2009)	19
Figure 2-9. (a) Hoop and (b) axial residual stresses on outer surface along axial direction (Akbari and Sattari, 2009)	19
Figure 2-10. Dissimilar pipe, sketched in mm (Deng et al. ,2011).....	21
Figure 2-11. Experiment set up (Flower, 1993).....	23
Figure 2-12. Fatigue life of unconstrained and constrained plain dents. open symbols (O) denote tests without failure and closed symbols () denote tests with failure during the test (Cosham and Hopkins, 2004).....	26
Figure 2-13. Failure (maximum) stress of smooth dents on welds and plain dents (Cosham and Hopkins, 2004).....	27
Figure 2-14. Experimental hoop strain of specimen 23H under internal pressure (Pinheiro and Pasqualino, 2009)	27
Figure 2-15. Pipe dimensions in mm (Allouti et al. ,2012).....	29
Figure 2-16 (a) Sketch of a saw test; (b) A lined pipe specimen subjected to a ring-split test (Vedeld et al., 2012)	31

Figure 2-17 Schematic representation of lined pipe manufacturing (Yuan and Kyriakides, 2014).....	32
Figure 3-1 The steps of manufacturing set up (a) heating up the outer pipe to 500°C (b) cooling down the liner to -200°C (c) putting the outer pipe in Jacket with 500°C (d) topping the liner inside the C-Mn pipe (e) cooling down the lined pipe to room temperature.....	38
Figure 3-2 Cutting 3 mm from the liner and chamfering the edge of C-Mn by 30° ..	38
Figure 3-3 Thermocouples located on the inner and outer surfaces.	39
Figure 3-4 Protecting the tips of thermocouples on the outer surface by adhesive ...	40
Figure 3-5 Mounting the strain gauges, ZFCAL-17 and ZFLA-11 on the inner and outer surfaces accordingly.....	41
Figure 3-6 The electrical components required to get the results of temperature measurements.	42
Figure 3-7 Measuring the temperatures and strains during welding.....	43
Figure 3-8 Rod types, E70S-2 (brass colour) and ER308L (grey colour)	45
Figure 3-9 Lined pipe welding process using TIG welding.....	46
Figure 3-10 Residual stress gauge rosette with three elements, FRS-2.....	47
Figure 3-11 X-ray diffractometer instrument, Bruker D8 Advance	48
Figure 3-12 Microscopic examination to measure the FZ and HAZ dimensions	49
Figure 4-1 The definition of dent depth (ASME B31.4, 2012).....	52
Figure 4-2 Apparatus of the collision experiments	54
Figure 4-3 Positions of the strain gauges	55
Figure 4-4 The stages of collision after the first contact between the indenter and pipe at (a) 7.5 ms (b) at 250 ms.....	56
Figure 4-5 Experimental set up for measuring pipe geometries	57
Figure 4-6 Using DPI penetrants to detect the surface-breaking cracks.....	58
Figure 5-1 Weld preparation to seal the pipe at ends.....	60
Figure 5-2 Ellipsoidal weld bead with semi-axes a , b and c	61
Figure 5-3 Effect of radiation and convection in Lined pipe	65
Figure 5-4 Karlsson and Josefson FE model, dimensions in mm (Karlsson and Josefson, 1990).....	66

Figure 5-5 Distributions of (a) temperatures ($^{\circ}\text{C}$) (b) Inner hoop residual stress at $\theta=150^{\circ}$ numerically computed in this work and experimentally validated in (Karlsson and Josefson, 1990)	67
Figure 5-6 Deng and Murakawa experiment, dimensions in mm (Deng and Murakawa, 2006)	68
Figure 5-7 Comparison of (a) thermal histories ($^{\circ}\text{C}$) and (b) Inner hoop residual stresses at $\theta=180^{\circ}$ numerically computed in this work and experimentally validated in (Deng and Murakawa, 2006)	69
Figure 5-8 Dimensions of analysis model.....	70
Figure 5-9 Power density distributions of Goldak ellipsoidal heat source models, liner and carbon steel	72
Figure 5-10 Three-Dimensional FEM.....	73
Figure 5-11 Yield strength of C-Mn steel and SUS304 corresponding to 1% hardening (Deng et al., 2008; Malik et al., 2008)	77
Figure 5-12 Maximum temperatures in (a) weld overlay and (b) girth welding ($^{\circ}\text{C}$)	78
Figure 5-13 Schematic illustration showing temperature measurement positions on axial direction (mm).....	79
Figure 5-14 Temperature histories during weld overlay at (a) 90° , (b) 180° and (c) 270°	80
Figure 5-15 Temperature histories during girth welding at (a) 90° , (b) 180° and (c) 270°	81
Figure 5-16 Thermal history at 270° with 270 seconds interval time (248-518 s) in case A.....	83
Figure 5-17 Thermal history at 270° with 1 second interval time (248-249 s) in case B.....	83
Figure 5-18 Thermal history for a doubled welding speed, case C	84
Figure 5-19 Thermal history with respect to reduce the speed to half , case D.....	85
Figure 5-20 Comparison of residual stresses at 270° central angle in case A and case B: (a) axial stress distributions on the inner surface, (b) hoop stress distributions on the inner surface, (c) axial stress distributions on the outer surface and (d) hoop stress distributions on the outer surface	87
Figure 5-21 Comparison of residual stresses at 270° central angle in case A, C and D: (a) axial stress distributions on the inner surface, (b) hoop stress distributions on the	

inner surface, (c) axial stress distributions on the outer surface and (d) hoop stress distributions on the outer surface	89
Figure 6-1 Schematic semi-sketch of welded lined pipe, dimensions in mm	92
Figure 6-2 Locations of thermocouples and the welding direction for three passes, dimensions in mm	95
Figure 6-3 3-D FE model	97
Figure 6-4 Yield strength of C-Mn steel and AISI304 corresponding to 1% hardening (Deng and Murakawa, 2008; Malik et al., 2008)	102
Figure 6-5 The thermal history of weld overlay centre at 90°, 180° and 270° central angle	103
Figure 6-6 The thermal history of second pass centre of girth welding at 90°, 180° and 270° central angle	103
Figure 6-7 Temperature distributions for two points located at 180° central angle on the inner and outer surfaces (a) through the whole pre-heat treatment and welding (b) through the first seconds of pre-heat treatment	104
Figure 6-8 Thermal field distributions for thermocouples (a) TC1 (b) TC2 (c) TC3 (d) TC4 (e) TC5 and (f) TC6	106
Figure 6-9 Mechanical strain history during welding associated with thermal history on the outer surface for (a) gauge A (b) gauge B (c) gauge C (d) gauge D (e) gauge E (f) gauge F	112
Figure 6-10 Mechanical strain history during welding associated with thermal history on the inner surface for (a) gauge G (b) gauge H (c) gauge I (d) gauge J (e) gauge K (f) gauge L	115
Figure 6-11 Axial residual strain at 180° central angle on the inner surface along the axial direction	116
Figure 6-12 Hoop residual strain at 180° central angle on the inner surface along the axial direction	116
Figure 6-13 Axial residual strain at 180° central angle on the outer surface along the axial direction	117
Figure 6-14 Hoop residual strain at 180° central angle on the outer surface along the axial direction	117
Figure 6-15 Axial residual stress at 180° central angle on the inner surface along the axial direction	119

Figure 6-16 Hoop residual stress at 180° central angle on the inner surface along the axial direction.....	120
Figure 6-17 Axial residual stress at 180° central angle on the outer surface along the axial direction.....	121
Figure 6-18 Hoop residual stress at 180° central angle on the outer surface along the axial direction.....	121
Figure 6-19 Radial shrinkage at 180° central angle on the inner surface along the axial direction.....	122
Figure 6-20 Temperature results of repeated tests for case A at (a) TC1 and (b) TC4 at 180° central angle.....	123
Figure 6-21 Axial residual stress results of repeated tests for case A on (a) the inner surface and (b) the outer surface at 180° central angle	124
Figure 7-1 Experimental and numerical macrograph at 270° central angle	129
Figure 7-2 Locations of thermocouples and the welding direction for three passes, dimensions in mm	130
Figure 7-3 (a) Axial and (b) hoop residual stress distributions of case A at 270° central angle	134
Figure 7-4 Initiation and growth of crack at the area of C-Mn pipe above weld overlay.....	134
Figure 7-5 Comparison of residual stresses at 270° central angle between case A and case B: (a) axial stress distributions on the inner surface, (b) hoop stress distributions on the inner surface, (c) axial stress distributions on the outer surface, and (d) hoop stress distributions on the outer surface	137
Figure 7-6 Comparison of residual stresses at 270° central angle between case A and case C: (a) axial stress distributions on the inner surface, (b) hoop stress distributions on the inner surface, (c) axial stress distributions on the outer surface, and (d) hoop stress distributions on the outer surface	140
Figure 7-7 Comparison of residual stresses at 270° central angle among case A, case D and case E: (a) axial stress distributions on the inner surface, (b) hoop stress distributions on the inner surface, (c) axial stress distributions on the outer surface, and (d) hoop stress distributions on the outer surface.....	143
Figure 7-8 Comparison of residual stresses at 270° central angle between case A and case F: (a) axial stress distributions on the inner surface, (b) hoop stress distributions	

on the inner surface, (c) axial stress distributions on the outer surface, and (d) hoop stress distributions on the outer surface	146
Figure 7-9 Coarse 3-D FE model	147
Figure 7-10 The thermal history of weld overlay centre at 90°, 180° and 270° central angle for coarse and normal mesh.....	147
Figure 7-11 The thermal history of second pass centre of girth welding at 90°, 180° and 270° central angle for coarse and normal mesh	148
Figure 7-12 Residual stress distributions for coarse and normal mesh models at 270° central angle: (a) axial stress distributions on the inner surface, (b) hoop stress distributions on the inner surface, (c) axial stress distributions on the outer surface, and (d) hoop stress distributions on the outer surface.....	149
Figure 7-13 Radial shrinkage for six cases on the inner surface at 270° from the WCL.....	150
Figure 8-1 Plastic strain rate for (a) C-Mn pipe (Wiesner, 1999) and (b) AISI304 pipe (Handbook, 1973)	155
Figure 8-2 Schematic of dented lined pipe dimensions in mm.....	156
Figure 8-3 FE mesh of the quarter lined pipe model, case B.....	158
Figure 8-4 The stages of collision at (a) original position of indenter and lined pipe (un-deformed mesh), (b) deformed shape at 7.5 ms, (c) deformed shape at 75 ms and (d) deformed shape at 250 ms	160
Figure 8-5 Deformed geometries of dented pipe	160
Figure 8-6 positions of the strain gauges, dimensions in mm.....	162
Figure 8-7 Strain histories in Rosette (a) GR1 (H1A), (b) GR4 (H1A), (c) GR1 (H2A), (d) GR4 (H2A), (e) GR1 (H3A), (f) GR4 (H3A), (g) GR1 (H1B), (h) GR4 (H1B), (i) GR1 (H2B), (j) GR4 (H2B), (k) GR1 (H3B) and (l) GR4 (H3B).....	169
Figure 8-8 Residual Von Mises stresses in the dented region of H1B specimen on the (a) top surface of C-Mn pipe (b) bottom surface of C-Mn pipe (c) top surface of AISI304 pipe (d) bottom surface of AISI304 pipe	170
Figure 8-9 Hoop residual stress distribution starting from the dent centre on the outer surface (C-Mn pipe) at (a) the longitudinal planes in case A (b) the longitudinal planes in case B (c) the transverse planes in case A (d) the transverse planes in case B	173

Figure 8-10 Consuming energy in the whole model in test (a) H1A, (b) H2A, (c) H3A, (d) H1B, (e) H2B, (f) H3B	177
Figure 8-11 Velocity of dent centre and indenter-tip during the first minute of impact in test (a) H1A, (b) H2A, (c) H3A, (d) H1B, (e) H2B, (f) H3B	180
Figure 8-12 Coarse mesh of the quarter lined pipe model of case H1A with (a) 1.5h size and (b) 2h size.....	181
Figure 8-13 Axial and hoop strain histories of case H1A at Rosette GR1 location for three mesh sizes.....	182
Figure 8-14 Strain results of repeated test for case H1A at rosette GR1	183
Figure 8-15 Strain results of repeated test for case H1B at rosette GR1	183
Figure A-1 Thermal module used to covert analogue signal to digital signal (ADC)	202
Figure A-2 Strain module used to covert analogue signal to digital signal (ADC) .	203
Figure A-3 Welding power source, GENESIS 150	203
Figure A-4 Laser distance measuring tool to specify the heights.	204
Figure A-5 High digital speed camera	204

List of Tables

Table 2-1 Mechanical properties of specimen (Flower, 1993)	22
Table 3-1 Chemical composition of AISI 10305 (C-Mn) and AISI304	35
Table 3-2 Mechanical properties of materials used in collision experiments	35
Table 3-3 Chemical compositions of ER308L and E70S-2	44
Table 3-4 Mechanical properties of ER308L and E70S-2	44
Table 5-1 Thermo-mechanical properties of C-Mn (Karlsson and Josefson, 1990)..	71
Table 5-2 Thermo-mechanical properties of SUS304 (Deng and Murakawa, 2006)	71
Table 5-3 Heat source parameters and welding parameters.....	72
Table 5-4 Simulation procedure	74
Table 6-1 Thermo-mechanical properties of C-Mn (Karlsson and Josefson, 1990)..	94
Table 6-2 Thermo-mechanical properties of AISI304 (Deng and Murakawa, 2006; International Nickel Limited, 1974).....	94
Table 6-3 locations of strain gauges on the inner and outer surfaces at the axial and hoop directions	96
Table 6-4 Heat transfer parameters	99
Table 6-5 Heat source and welding parameters	100
Table 7-1 Comparison between numerical and experimental results at six location during welding	130
Table 8-1 Numerical and experimental results of pipe geometries including dent depth.....	160

Chapter 1

Introduction

1-1. Background and Motivation

The expected continuous growth of harsh operating conditions and corrosive production fluids, such as CO₂ and H₂S, make the use of C-Mn steel pipe for offshore and flow line impossible in Oil & Gas pipelines, and hence, the need for corrosion mitigation is required. One alternative is the use of a lined pipe, consisting of a thinner inner layer (the liner) and outer layer (backing steel) (Hilberink, 2011). The liner is made of corrosion resistant alloy (CRA) such as Alloy625, 304 and 316L stainless steel (SS) whilst the backing steel is made of low-cost carbon steel in which Magnesium Mn percentage is over 1%. A lined pipe particularly has a wide range of applications in onshore pipelines and offshore submarine-pipeline. Consequently, it is used in highly corrosive environments containing CO₂, Cl and H₂S associated with severe levels of temperature and pressure. The lined pipe can be installed in Oil & Gas industry to optimize the resistance to chloride and sulphide stress corrosion cracking (SCC) in aggressive environments. Furthermore, it is utilised to resist erosion corrosion and corrosion fatigue. In consequence, the lined pipe is sufficiently a good option for reasonable cost and high corrosion resistance for long time.

Before installation, lined pipes require to be assembled together by welding. This is a complex process requiring two sequential types of welding. The liner is typically fixed using a weld overlay to seal its end with the outer pipe. A girth welding is then executed to join two adjacent specimens of the formed pipe. The sealing weld, that is the weld overlay, is necessary in welding lined pipes to prevent moisture and dirt to go through the gap according to Nederlandse Aardolie Maatschappij BV (NAM) recommendations. In 1981, NAM had experienced failures in a lined pipe because cracks induced by dirt and moisture propagated within the fusion zone (FZ) of girth welding (De Koning et al., 2004). After the liner ends were cut off and sealed by a

weld overlay, no further failure had been experienced and the lined pipes were in service over a long lifetime.

There is no work reported in the literature on the mechanical integrity assessment of lined pipes accounting for the effects of the welding process. Such types of assessment require consideration of thermal fields and residual stresses induced during welding. There are a lot of obstacles which make full-scale experiments and modelling of lined pipe welding difficult and expensive. Therefore, one aim of this project is to develop and experimentally validate a nonlinear finite element (FE) modelling procedure for welding of lined pipes, associated with a number of parametric studies. By achieving this aim, large-scale lined pipes can be sufficiently modelled following the procedure deployed in this work.

In parallel to the lined pipe welding problem, the higher cost of the liner and of the manufacturing of lined pipes lead to reduce the thickness of C-Mn pipe. Consequently, the entire wall of a lined pipe may not be strong enough to resist the external interference during excavation or instalment in case of impacts with external objects, which may cause dents.

According to CONCAWE report about pipelines failure, fatigue failure of an oil pipeline occurred because it had been dented during the construction in 1973 (Davis et al., 2011). Successive fatigue cycles had contributed to initiate and propagate cracks which eventually caused the failure with €810,000 for clean-up costs because the pipeline was laid under a rural road.

In general, the damage occurring on the upper half of the pipe horizontally laid has historically led to the highest number of pipeline failures. Dents belonging to such type are significantly vulnerable to failure as they could contain cracks or gouges. In this case, immediate inspection and possible repair are required. In addition, an unconstrained dent without restriction underneath the dent could be to re-round with changes in internal pressure which in turns delays failure. Nevertheless, it is also possible that theses defects could initiate and grow in service and the failure could be at some time after the first impact. Therefore, this issue is pivotal in terms of the complexity of maintenance when an inshore or offshore lined pipe is in service.

There is also no investigation reported in the literature about the effect of dynamic collisions on lined pipes. Therefore, a second aim of this PhD work is to develop and experimentally validate a nonlinear FE model for simulating the dynamic impact of an external object on a lined pipe.

It is against this background that the following main research questions have been formulated and addressed in the thesis:

- What procedures should be applied to develop, execute and validate a FE model capable of simulating the welding process of a lined pipe with high accuracy?
- Is it possible to develop an effective procedure to manufacture small-scale lined pipe specimens in a lab environment at a reasonable cost, maintaining the levels of initial residual stresses acceptable?
- What are the main factors which can affect the quality and results of the welding process of a lined pipe?
- What procedures should be applied to develop, execute and validate a FE model capable of simulating a lined pipe subject to a dynamic impact comparable with the ones which might occur during installation?
- To what extent the response of a lined pipe subject to dynamic impact differs from the response of a similar pipe without liner in terms of the residual stresses and strains?
- What is the effect of the energy and the velocity of the impact on the damage within a lined pipe?

1-2. Aims and Objectives

The aims of this work is to experimentally and numerically study both the welding of lined pipes and the impact of lined pipes with external objects resulting in dents, in both cases evaluating the resulting residual stresses.

Specific objectives of the work are as follows:

1. To manufacture lined pipe specimens using a special pre-heat treatment, called tight fit pipe (TFP) procedure, and evaluate the residual stresses induced by such method.

2. To experimentally measure the temperature field and residual stresses in lined pipes during and after welding, analysing the effect of factors including the welding material, the heat input and the omission of the weld overlay.
3. To develop a numerical nonlinear FE model simulating the welding process of lined pipes, and validate the model against experimental measurements.
4. To experimentally measure the deformation, strains and residual stresses induced in a lined pipe and in a normal (non-lined) pipe as a result of impacts with an indenter dropped from different heights.
5. To develop a numerical nonlinear FE model simulating the impact of an indenter on lined pipes, and validate the model against experimental measurements.

1-3. Summary of Research Approach

In this work, experimental testing has been conducted for both the welding process and the dent inducing impact. Furthermore, two nonlinear FE procedures have been developed to simulate the two problems.

1-3-1. Lined Pipe Welding

To study lined pipe welding, in the experimental part of the project, the TFP procedure has been applied to insert the liner inside the outer pipe. Furthermore, special high temperature strain gauges were used to record the strains during lined pipe welding.

Six cases have been studied in this research with different factors affecting the quality and results of the welding process. The first case is considered the reference case where the weld overlay and girth welding have been executed with different materials of their base metals, accordingly. For this case the TFP pre-heat treatment was also taken into consideration. In the second case, the material of girth welding is the same of the weld overlay material. In the third case, the effect of neglecting the weld overlay has been discussed. In this case, the two parts of the lined pipe have been solely joined using girth welding. The material of girth welding in this case is the same used in first case. In the fourth case, the heat input is lowered to 75% of the

heat input in first case for all welds. In a similar way, the heat input in the fifth case is dropped to 50% of that in first case. The liner with weld overlay is not considered in the last case.

In the numerical part of the work, 3-D thermo-mechanical FE models have been developed and executed using ABAQUS. Only one-half of the lined pipe specimen, one joint, is modelled due to the symmetry around the weld centreline (WCL). The problems are described by uncoupled quasi-static thermo-mechanical equations. In other words, the deformation depends on the temperature in the welding model whereas temperatures are assumed to be independent of deformation. As a result, the thermal analysis is carried out first to get the thermal history as a function of time throughout the lined pipe joint. This analysis required developing subroutines by FORTRAN codes to simulate the heat source movement and the deposit of the welding beads sequentially. The element birth technique is adopted in the FE models to simulate depositing the filler materials in the weld overlay and girth welding with the moving heat source. This technique involves deactivating all beads first and then depositing the weld beads sequentially once the heat source reaches the targeted bead.

This thermal history is then considered as an input for the mechanical analysis in which the mechanical properties are temperature dependant. The numerically predicted thermal history and residual stresses have been studied for particular locations on the inner and outer surfaces in comparison with their experimental counterparts.

1-3-2. Lined Pipe Denting

To study the denting of a lined pipe resulting from the impact with external objects, the experimental part involved freely dropping the indenter down from a specific height of 1, 1.5 and 2 m to punch the external surface of C-Mn pipe with a specified velocity. Fundamentally, the kinematic energy has been consumed completely to produce indentation in the lined pipe before the indenter and pipe retreat vertically as a reaction of collision. The hitting tool and pipe fall down after that because of their weights. The weight is a block of 200 kg, in addition to a spherical indenter. The

collision leaves permanent deformation in the lined pipe which in turn produces residual stress in the base materials, AISI304 and C-Mn.

In the numerical part of the work, 3D FE models are developed to simulate the mechanism of vertical free drop of weight from different heights resulting in damage in the pipe. Models are executed using a three-dimensional non-linear FE code, ABAQUS/EXPLICIT 6.13 (Dassault Systèmes, 2014). In order to precisely simulate the response of a collided pipe to subsequent impacts and spring back, an elastic-plastic constitutive behaviour is adopted using the isotropic Hooke's law whereas the plastic behaviour is based on the Von Mises criterion. Work hardening is considered in this work using the isotropic hardening rule associated with the equivalent plastic strain rate. The weights include those of a block, the spherical indenter, the liner and C-Mn pipe. Different plastic strain rates are specified for both materials of lined pipe, C-Mn and AISI304, in conjunction with the change in impact velocity.

Impact is a dynamic test where the equivalent plastic strain rate plays a key role in determining the mechanical properties of punched material. Typically, the maximum velocity of impact is coincident with the initial contact between the indenter and external surface of pipe to gradually slow down later through indentation process. The pipes, liner and C-Mn, are idealized with solid continuum element, 8-node full integration, liner brick elements (C3D8). The mesh is refined more in the dented region in both cases to get more precise results.

1-4. Thesis Outline

The thesis is divided into nine chapters and the contributions in each chapter is summarised as follows.

Chapter 1 presents an introduction to the two basic problems studied regarding lined pipes: welding and impact. It provides the background and motivation, the aims and objectives, a summary of the research approach applied in this work and finally the thesis outline.

Chapter 2 covers the efforts of previous work to tackle the impact and welding process in pipes chronologically. A comprehensive literature review on circumferential welding and impact on pipes is discussed in detail. Lack of literature

reporting studies on lined pipes in regards to impact and welding led to address this gap as a significant contribution in this thesis.

Chapter 3 provides details of the experimental setup to insert the CRA liner inside the outer pipe C-Mn using the TFP procedure. Moreover, the experimental strategy to obtain the thermal and mechanical results during and after welding, including the use of thermocouples, high temperatures strain gauges, residual strain gauges and X-ray diffraction, is explained in detail.

Chapter 4 describes the experimental setup and procedure applied in conducting impact tests. Furthermore, a detailed explanation for some basic dent types is given to facilitate understanding the impact process.

In Chapter 5 the simulation of lined pipe welding is presented in detail. The numerical procedure is validated against previously published experimental results for stainless steel and carbon steel welding separately. The model is then used to predict the transient temperature field and residual stress distributions during the weld overlay (inner welding) and the girth welding (outer welding) of a lined pipe. Furthermore, a sensitivity analysis to determine the influence of the cooling time between weld overlay and girth welding and of the welding speed is conducted in terms of thermal and mechanical aspects.

Chapter 6 investigates the effect of initial residual stresses obtained from the pre-heat treatment utilized to insert the liner inside the C-Mn pipe. At first, the numerical analysis of heat treatment is discussed. The thermal and structural numerical results are compared against the experimental results recorded by thermocouples, high temperature strain gauges, residual stress gauges and X-ray diffraction.

In chapter 7 the six cases of lined pipe welding discussed in Section 1.3.1 have been studied experimentally and numerically. For all cases, the numerical thermal and residual stress results are compared against the experimental measurements and the effect of different factors to the quality of the welding process and residual stress results has been discussed.

In Chapter 8 the results of the experimental testing and numerical simulation of lined pipe impact are presented, compared and discussed.

Finally, in Chapter 9 conclusions are drawn from the presented thesis and proposals for future work are made.

Chapter 2

Literature Review

2-1. Introduction

Measurement of thermal fields and strain history during welding or impact can be very expensive and time consuming. It is often not feasible to obtain detailed measurements for all points located at critical positions. In this chapter, the efforts of previous contributions to evaluate experimental findings and to use them to develop and validate analytical and numerical work are presented.

2-2. Previous Contributions to the Numerical and Experimental Work Pertaining to Pipe Welding Approach

2-2-1. Analytical, 2-D and 3-D Approaches

The first two-dimensional analytical models derived from experimental results for butt-welded pipes were proposed by Vaidyanathan et al. (1973) and Leggatt (1982). In (Vaidyanathan et al., 1973), the theory is applied at first on a butt-welded flat plate to get an approximate solution for the residual stress parallel to the welding. The plate is then ‘deformed’ into a pipe, so that this residual stress becomes as an initial hoop stress. After that, this new circular cylinder is allowed to deform. The minimum elastic strain energy is used as a condition to determine the radial displacement and therefore compute the final residual stress. In (Leggatt, 1982), the residual stress is considered as a function of the ultimate temperature attained at any point. In turns, the hoop force is computed by integrating the resulting hoop stress.

Jonsson and Josefson (1988) found a good agreement between experiments and the above mentioned analytical methods, although the analytical solutions did not consider the yield stress variations and the phase transformation effects. The single

pass butt-welded pipe tested by Jonsson and Josefson (1988) has an outer diameter of 203 mm with 8.8 mm thickness, with a 5.5 mm deep V-groove. The pipe material was carbon-manganese C-Mn (Swedish standard steel SIS2172) and the welding method used was MIG (Metal Inert Gas) as shown in Figure 2-1. For both analytical methods, the net heat input used was 560 KJ/m, assuming 77% for arc efficiency. The yield stress of weld metal was about 380 MPa while it was 310 MPa for the base material at room temperature.

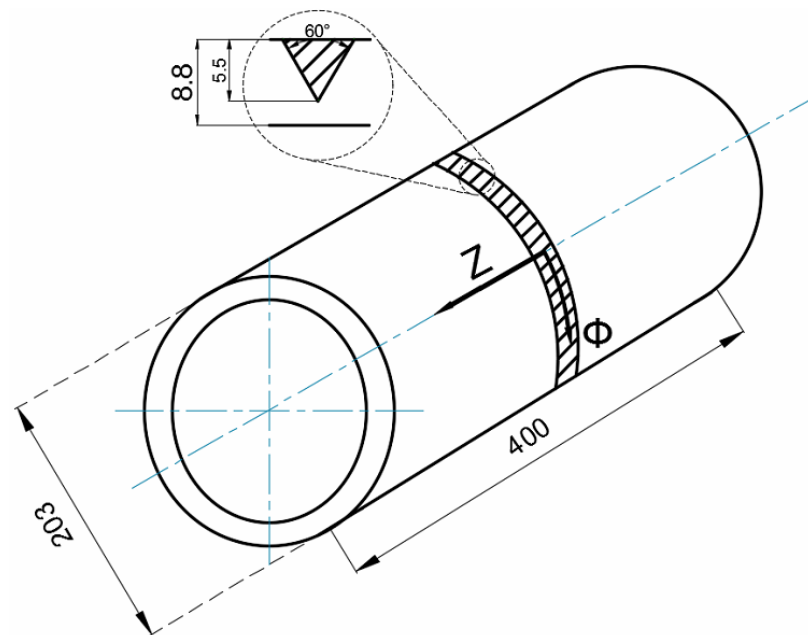


Figure 2-1 Pipe and weld dimensions with welding directions towards positive ϕ -direction (Jonsson and Josefson, 1988), dimensions in mm

Figure 2-2(a) and (b) compare the experimentally determined axial and hoop residual stresses on the outer surface with the two analytical solutions by Vaidyanathan et al. (1973) and Leggatt (1982), respectively. From Figure 2-2(a), it is clear that the experimental axial residual stress distribution on the outer surface is in good agreement with both analytical solutions. Indicating by z the distance from the welding centre line (WCL), or just the 'centre', for $Z < 20$ mm, the method by Vaidyanathan et al. (1973) seems to give a good prediction but the axial stresses beyond this range seem to be quite overestimated. Similarly, the analytical hoop residual stresses resulting from the method by Vaidyanathan et al. (1973) seem to be in good agreement with the experimental results on the outer surface, although the

analytical result in the welding centreline is somewhat lower as shown in Figure 2-2(b).

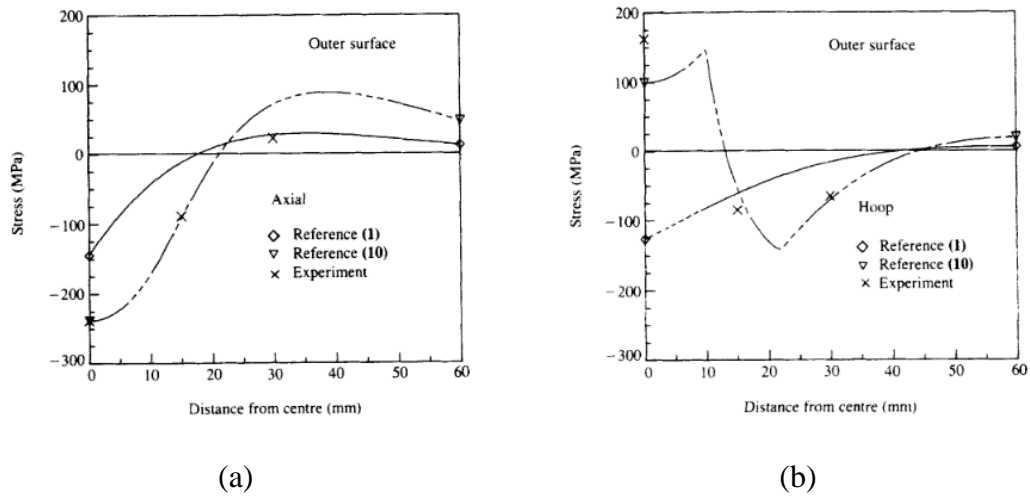


Figure 2-2. Comparison between analytical and experimental results on the outer surface for residual (a) axial stresses and (b) hoop stresses (Jonsson and Josefson, 1988)

Despite the good agreement between analytical and the experimental results found by Jonsson and Josefson (1988), the analytical methods are still not capable to take non-linear effects into account. The non-linearity in welding process is a result of many aspects, such as temperature dependent material properties, temperature dependent heat coefficients (convection and radiation), plasticity, latent heat and the phase transformation. Because of that, it is essential to use numerical methods, such as the FEM, to obtain more realistic models. Therefore, Karlsson (1989) and Karlsson and Josefson (1990) developed an FE model using the code ADINAT/ADINA to simulate the thermal and mechanical analysis for a circumferential pipe with an outer diameter of 114.3 mm and a wall thickness of 8.8 mm, 5.5 mm deep V-groove (Figure 2-3). They studied the case of a single-pass girth welding using metal inert gas type MIG deposited in the groove with filling material made of C-Mn (Swedish standard steel SIS2172). Due to the symmetry around the weld centreline, only one-half of the pipe was analysed, which is 200 mm long.

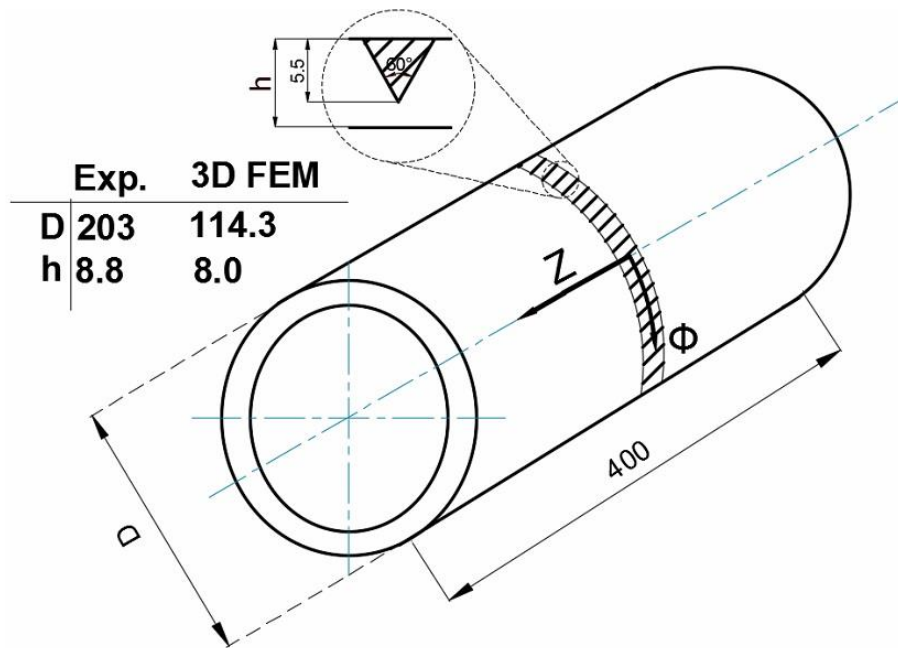


Figure 2-3. Experimental and FE models used in study (Karlsson, 1989; Josefson, et al., 1989; Karlsson and Josefson, 1990), dimensions in mm

Karlsson (1989) studied the influence of mesh density by developing two different FE meshes with two different diameters. The coarse mesh contains 13 elements associated with 3 elements in the thickness direction whereas the finer mesh has 127 elements associated with 9 elements along the thickness direction. The two outer diameters were 114.3 mm and 203 mm as used in the experiment (Jonsson and Josefson, 1988) as shown in Figure 2-4.

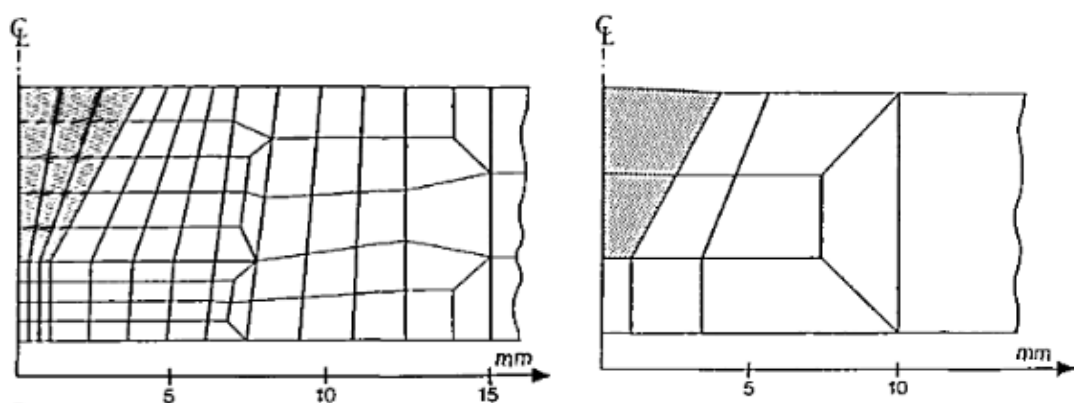


Figure 2-4. 2D FE model used in thermal and mechanical analysis, shaded elements are the filler material (Karlsson, 1989)

The findings demonstrate that the coarse mesh is sufficiently good for computing the hoop and axial residual stresses on the inner and outer surface with sufficient accuracy.

Karlsson and Josefson (1990) presented a model which was the first fully 3-D thermal and mechanical study of a butt-welded pipe reported in the literature. The FE codes ADINAT and ADINA were used to develop thermal and mechanical analyses, respectively. The element birth technique is adopted in this model to simulate the deposition of welding material into the groove. Although a coarse mesh, namely 3 elements in the thickness direction, is used in the 3D FE-model, the numerical axial and hoop residual stresses are again consistent with the experimental results from (Jonsson and Josefson, 1988) at central angle of 150° away from the start/stop position. Furthermore, the predicted residual stresses are in reasonable agreement with the analytical solution in (Vaidyanathan et al., 1973).

Joseson et al. (1989) developed three different FE-models corresponding to the pipe geometries used in the experimental investigation by Karlsson (1989), Karlsson and Josefson (1990) and Jonsson and Josefson (1988). A fully 3-D model, a rotationally symmetric model and a shell type model have been numerically studied. The numerical results prove that the residual stress distributions of FE model corresponding to the experimental pipe geometries are in good agreement with the experimental results (Jonsson and Josefson, 1988) and the analytical method in (Vaidyanathan et al., 1973).

2-2-2. Developed FE Approaches

Brickstad and Josefson (1998) developed a FE non-linear analysis using ABAQUS code to examine the effect of some parameters (pipe thickness, heat input, inner diameter, weld metal yield stress, inter-pass time and number of weld passes) on the residual stresses in axisymmetric multi-pass girth-butt-welded stainless steel joints. In particular, they studied the sensitivity of the axial and hoop stresses to the variation of these parameters at the fusion zone (FZ) and heat affected zone (HAZ). Different pipe diameters in the range of 76.2 mm to 680 mm with thickness in the range of 7.1mm to 40 mm were simulated. The number of weld passes considered

varies according to the wall thickness from 4 to 36. The maximum allowed inter-pass temperature in the study was between 100°C-150°C.

The element birth technique is associated with a high softening temperature (TSOFT) approach to deposit the un-deformed filler material to the deformed pipe geometry resulted from the previous pass. The TSOFT procedure keeps elements not yet activated at a high softening temperature (1200°C) with a low stiffness and a very low yield stress. In the thermal analysis, the heat input is modelled by applying a distributed heat flux on every element to keep the maximum temperature at 2 mm far away from the FZ boundaries within 800-900°C. Furthermore, a combined heat transfer coefficient is applied for all free boundaries of the pipe taking both convection and radiation loss into consideration. In the mechanical analysis, the Von-Mises yield criterion associated with flow rule and bilinear kinematic hardening law are considered. The numerical residual stress results have a good agreement with ASME XI results under the influence of various heat input for the 7.1 mm thick pipe. In recent years, a significant improvement of FE codes gives a high flexibility in modelling 3-D and 2-D axi-symmetric models.

Abid et al. (2005) presented a comparative study of 3-D and 2-D FE analyses for distortions and residual stress fields produced by MIG welding in a tacked pipe-flange joint. The heat source movement is based on Goldak heat input distribution. Moreover, element birth technique is performed to deposit the filler material. Both types of FE models are validated against thermal and structural experimental results. The length of specimen is 200 mm whereas the outer diameter is 115 mm associated with a 6 mm deep V-groove and 1.2 mm root gap. Both the pipe and flange have the same material, carbon-manganese (C-Mn), and their thermo-mechanical properties taken from Karlsson and Josefson (1990) are subjected to Swedish standard steel SIS 2172. The same material properties are also used for the filler material, a ER70S-6 carbon steel wire. Although the 2-D FE models are much less computational time and data storage, around 5% of the 3-D FE models, residual stresses predicted by the 2-D simulation are absolutely higher than their counterparts measured and predicted by the 3-D simulation. As a consequence, the 3-D FE model is recommended for girth welding of the pipe-flange specimen.

Deng and Murakawa (2006) developed a 3-D and a 2-D FE model to analyse temperature history and residual stresses in multi-pass girth weld. The pipe is made of stainless steel SUS304 with outer diameter of 114.3 mm, thickness of 6 mm and length of 800 mm, as shown in Figure 2-5.

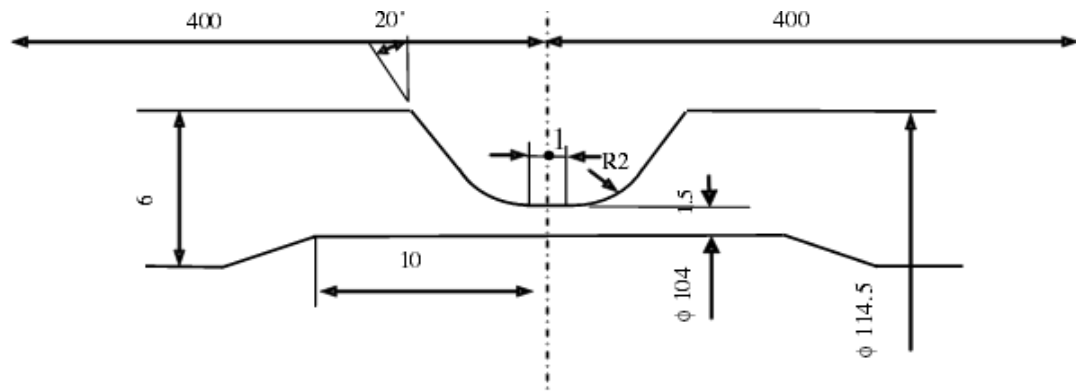


Figure 2-5. Pipe and groove dimensions in mm (Deng and Murakawa, 2006).

The pipe is welded by two passes of gas tungsten arc (GTA). In the 3-D model, the heat source is applied as a volumetric heat source with a double ellipsoidal distribution developed by Goldak et al. (1984). The results of the thermal analysis confirm a steady-state of thermal distribution around the heat source, which in turn lead to homogenous distribution of residual stresses. The thermal and structural results of both 3-D FE model and 2-D model are reasonably in good agreement with the experimental results. Furthermore, the axial residual stresses on the outer and inner surfaces exhibit 'contrary' distributions, as shown in Figure 2-6.

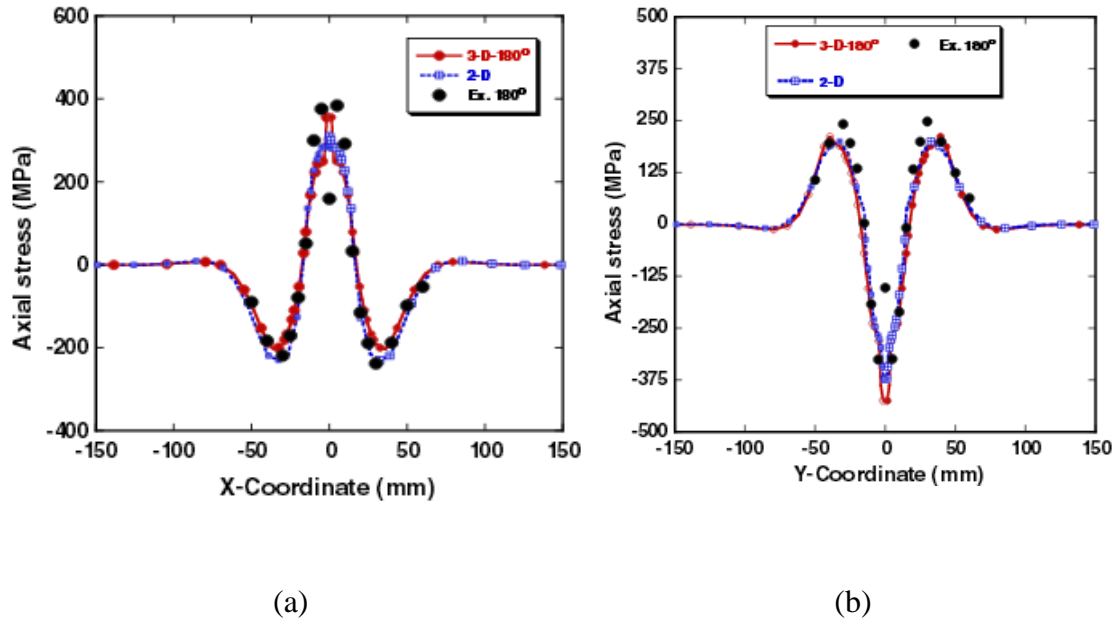


Figure 2-6 The axial residual stress distributions on (a) the inner surface and (b) the outer surface (Deng and Murakawa, 2006)

The distributions are said to be ‘contrary’ because tensile axial residual stresses are produced on the inner surface whereas compressive axial stresses are generated on the outer surface at the FZ and HAZ. Beyond these zones, both stress profiles change sign, so that compressive axial stresses and tensile axial stresses are produced on the inner and outer surfaces, respectively. Also, the shape of axial stress distributions is to a large extent similar to that of the hoop stress distribution on the inner surface.

Another important and recent contribution regarding the analysis of the GTA welding of thin-walled cylinders of low carbon steel was presented by Malik et al. (2008) to confirm the reliability of previous findings (Deng and Murakawa, 2006). Malik et al. (2008) presented a computational approach for thermal and mechanical analyses of circumferential welding. A full 3-D model developed using the code ANSYS was employed for two cylinders with a V-groove and two tack welds at start and middle welding section. The properties of low carbon steel AH36, which is basically C-Mn steel, are taken from (Michaleris and DeBiccari, 1997). Combined convection and radiation heat transfer coefficient are applied on all surfaces exposed to environment. Malik et al. (2008) reached the same findings of Deng and Murakawa (2006) that high tensile axial residual stresses occurred on the inner surface while compressive axial stresses are produced on the outer surface along and

near the weld centreline. Away from weld centreline, there is also a reversal in the axial residual stress distributions, which turn from tensile into compressive. There is a significant effect of two tacks at 0° central and 180° on the axial stresses on the inner surface, whereas no influence is found on the hoop stresses. Ignoring the weld start/stop effects keeps hoop stress distributions to a large extent uniform.

The effect of initial stresses produced by post-heat treatment on residual stresses induced by laser welding has been numerically and experimentally investigated by Deng and Kiyoshima (2010). After the manufacturing process, the laser beam was utilized to join two cylinders made of SUS3016 stainless steel. The whole length of pipe is 800 mm. The inner diameter is 200 mm with wall thickness of 10 mm as shown in Figure 2-7. In the FE model, due to the symmetry, only half of the pipe is simulated to study the thermo-mechanical behaviour. Furthermore, two cases has been numerically discussed, where one is modelled with only laser beam welding process whilst the other one includes both the post heat treatment and welding. At the FZ and its vicinity, the residual stresses are not affected by the initial residual stresses and just subjected to stresses induced by welding. Beyond this region, the initial residual stresses induced by post special heat treatment have significant influence on the final residual stresses after welding.

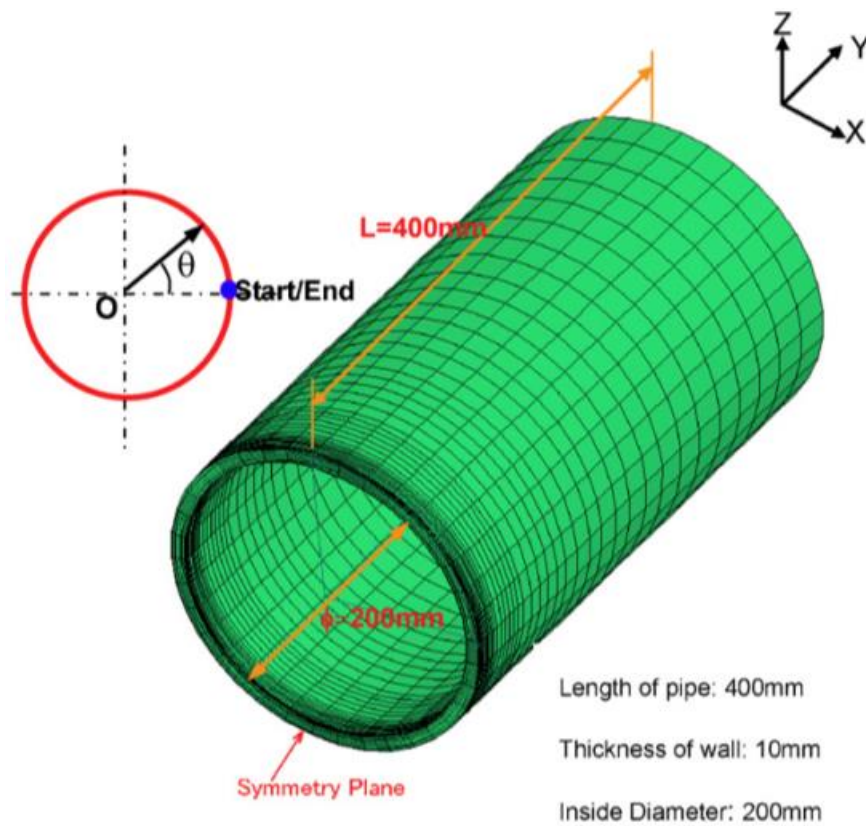


Figure 2-7. Dissimilar pipe, sketched in mm (Deng and Kiyoshima ,2010).

The numerical analysis of welding of dissimilar pipes is still a new field, with few articles in the literature addressing such problem. Akbari and Sattari (2009) developed a FE model of dissimilar cylinders to study the thermo-mechanical behaviour and the effect of heat input on the residual stress distribution. Both dissimilar joints have a nominal diameter of 200 mm with V-groove edges. One joint was made of A106-B carbon steel and the other one was A240-TP304 stainless steel, as shown in Figure 2-8.

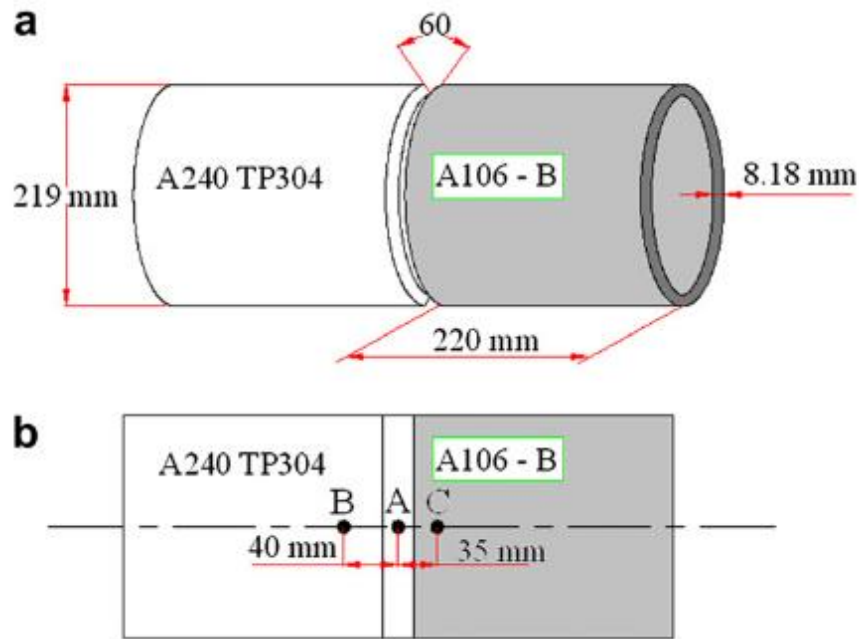


Figure 2-8. Detailed dimensions of (a) pipe and (b) test points (Akbari and Sattari, 2009)

Comparing the numerical with the experimental results, there is a reasonably good agreement between them, where the hole-drilling strain gauges were used to experimentally measure the residual stresses as shown in Figure 2-9.

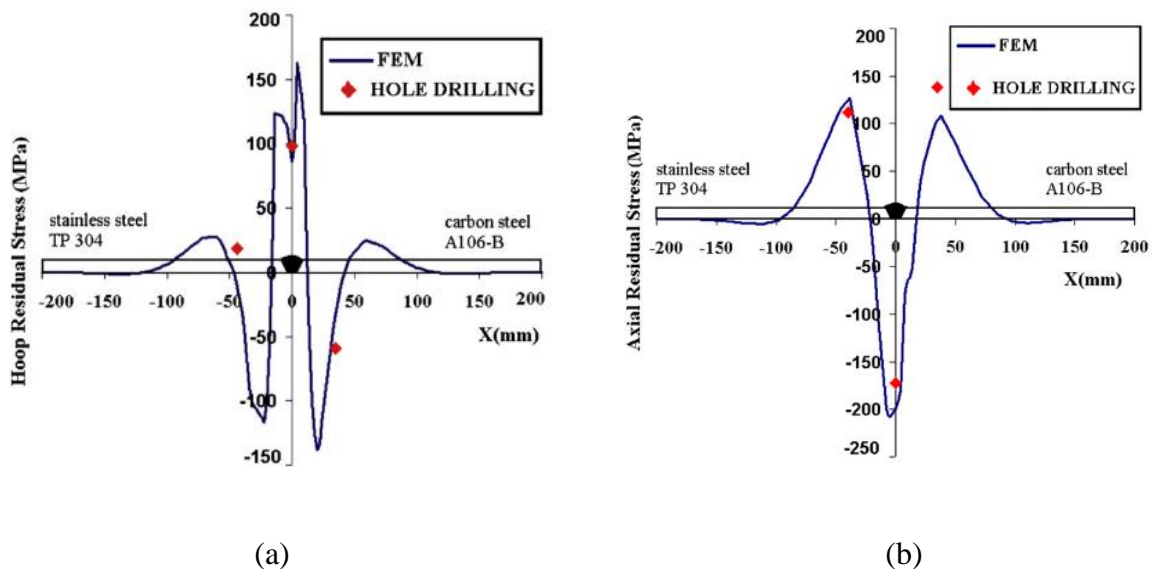


Figure 2-9. (a) Hoop and (b) axial residual stresses on outer surface along axial direction (Akbari and Sattari, 2009)

Reducing the heat input leads to lower the compressive and tensile stress distributions on the stainless steel side more than their counterparts on the carbon steel joint. The reason is attributed to the decrease in the temperature fields in the stainless steel more than carbon steel because the heat coefficient of stainless steel is less than that of carbon steel.

Woghiren and Brennan (2009) presented a parametric stress analysis for welded KK joint used in the leg structure of inshore Oil & Gas platform. Over 120 models have been developed to extract the stress concentration factor SCF values. The models using a combination of shell and solid elements have been developed using ABAQUS. The extracted SCF values were used to derive six equations using MINITAB to quickly identify the location of the maximum stress location and the possibility of fatigue cracks. Consequently, it is a key to also identify the location of applying non-destructive test NDT procedures and schedules. These equations also allow the rapid optimization of multi-planar joints.

Residual stress distributions induced by dissimilar pipe welding have been numerically and experimentally investigated by Deng et al. (2011). One joint is made of low alloy steel (SFVQ1A) whilst the other one is made of austenitic stainless steel (SUSF316). Tungsten inert gas welding (TIG) was employed to deposit 36 passes with Alloy 82 as a filler material. During welding, the heat source was fixed whilst the two joints were rotated on roller. The whole length of the dissimilar pipe is 800 mm and the outer diameter is 184.5 mm. The low alloy joint was clad with one layer on the inner surface and one buttering layer on the right end as shown in Figure 2-10. Both layers were deposited by TIG process where Y308 electrode was used to deposit the cladding layer whilst Alloy 82 electrode was used to perform the buttering layer. To reduce residual stresses and improve the toughness in the HAZ, post weld heat treatment (PWHT) was achieved by keeping the dissimilar pipe for 10 hours at 625°C. 3-D FE model has been developed to simulate the welding process based on the moving heat source. Comparing the predicted results with the experimental ones, there are large initial residual stresses in both joints due to the manufacturing process. Consequently, significant discrepancies are obtained between the final numerical and experimental residual stress at the regions away from the FZ

and HAZ. The initial stresses are cancelled in the FZ and HAZ because higher thermal cycles experienced in those regions.

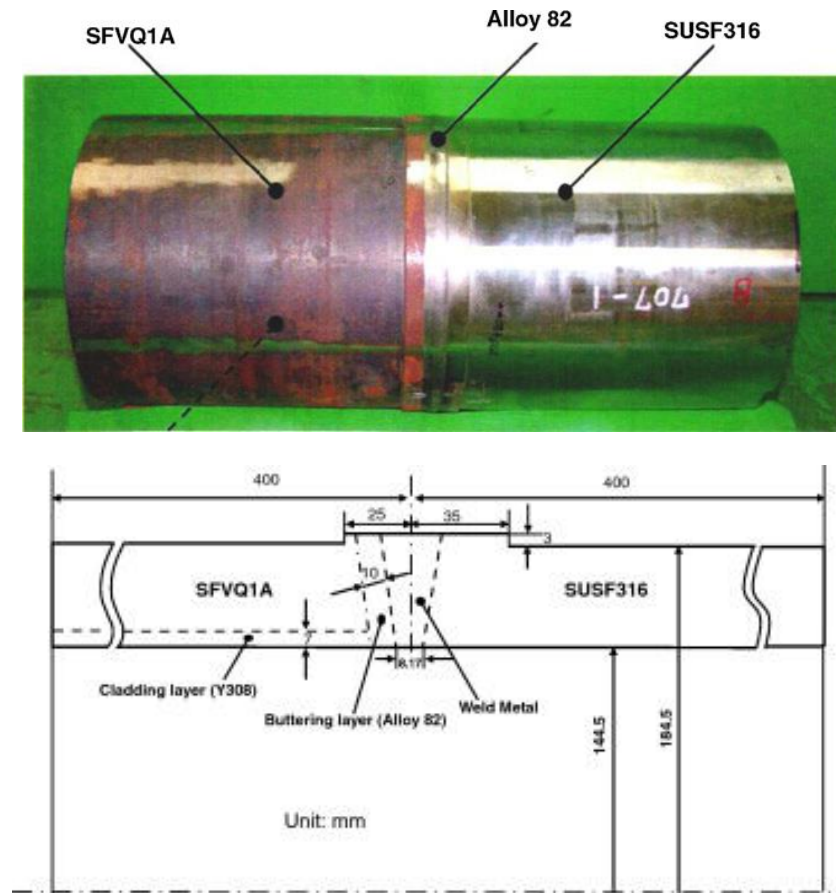


Figure 2-10. Dissimilar pipe, sketched in mm (Deng et al. ,2011).

Lee et al. (2013) developed also a 3-D model of welding of dissimilar pipes with thermal and elastic-plastic stress analysis using a FE approach, validating the procedure through published experimental work. The parent materials of the pipe are SP42 and SUS304 for carbon steel and stainless steel, respectively. Furthermore, the residual stress distributions in the corresponding similar steel pipe welds are examined for a comparison. Two different heat transfer coefficients are also applied corresponding to their base materials, carbon steel (Abid and Siddique, 2005) and stainless steel (Brickstad and Josefson, 1998), where the radiation and convection losses are considered in each coefficient. From the thermal results, the findings illustrate that the temperature history is steady as the heat source moved around the pipe. Structurally, the stress distributions in the SUS304 side are similar to the

corresponding similar stainless steel joint whereas stress distributions in the SPPS42 side are considerably different from those in similar carbon steel.

2-3. Previous Contributions to the Numerical and Experimental Analysis of Pipes Subject to Denting

One of the problems which undermine the mechanical integrity of pipes is indentation by external interference. Third party damage or external interference is historically considered the main cause of pipeline failures in service. Thus, pipes subjected to impact by external interference require examining the stress behaviour to determine the maintenance type. The following pages report relevant literature addressing the behaviour of dented pipes.

Flower (1993) studied the effect of pipeline dents (without gouges) under cyclic internal pressure numerically and experimentally. The experiment was conducted on 8 pipes with outer diameter of 323.85 mm and 6 m long, with different thicknesses and materials as shown in Table 2-1.

Table 2-1 Mechanical properties of specimen (Flower, 1993)

Specimen No.	D/t	Hoop ultimate strength ksi	Hoop yield stress ksi	% elongation	Impact strength Ft.lb	comment	Max. grade
A-1	18.6	72.4	55.1	39	23.3	Seamless	X52
A-2	19.0	88.9	65.8	32	15.3	Seamless	X60
B-1	40.9	82.0	53.1	32	20.5	Seamless	X52
C-2	51.0	74.4	57.3	33	27.0	ERW	X52
H	24.78	74.0	52.1	37	55.0	Seamless	X52
E	31.96	74.7	51.2	32	32.0	Seamless	X46
F	31.93	74.7	51.2	32	31.2	Seamless	X46
G	50.35	92.2	84.0	20	44.0	Seamless	X80

The test was composed of three stages starting with producing the dent, applying test pressure and then applying fatigue loading. The dent sizes, in terms of d/D dent depth-to-pipe outer diameter, were 5, 10, 20% where the maximum size of dent,

20%, was placed on the centre and the smaller dents on either end, as shown in Figure 2-11.

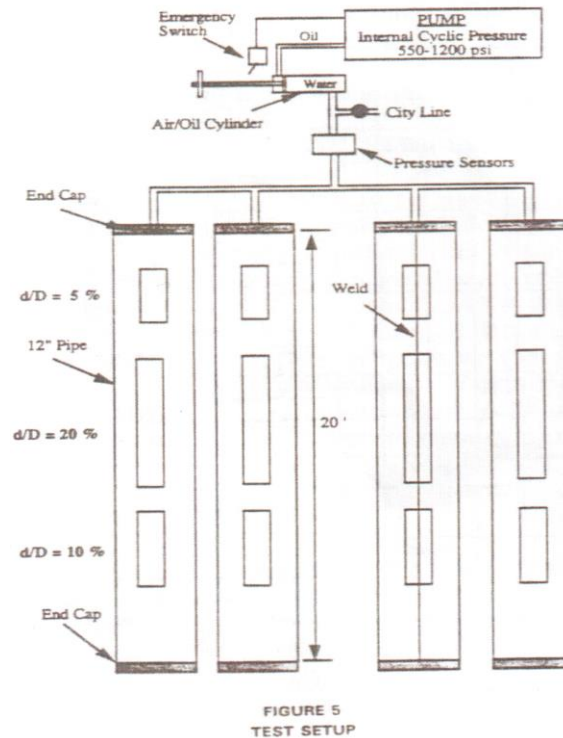


Figure 2-11. Experiment set up (Flower, 1993)

As a result, fatigue test was applied on 8 pipes with various outer diameter-to-thickness ratios (D/t). 13 out of 24 dents with various depths produced on the 8 pipes got failure. The failed dents had visible deformation as $D/t > 30$ and $d/D > 5\%$, whilst no visible deformations were on the thick wall samples. All cracks were longitudinal with an approximate length 2-3 inches. The samples without visible leakage sustained from 50,000 to 70,000 internal cycles with varied pressure from 0 to 82.7 bar. On the other side, the fatigue life was infinite for most cases of smaller D/t and d/D . Moreover, ANSYS code was used to evaluate the elastic state of the dented pipes through 3-D models with elastic quadrilateral shell elements. The pipes were pressurized to two pressure loads, 38 bar and 82.7 bar. It was observed that the stresses produced in the pipes were beyond the yield stress for the majority of cases having $d/D = 20\%$ and $D/t = 50$. The numerical results show there is no variation in stresses according to change in dent length whilst the dent depth plays a vital role. ABAQUS code was also applied in the plastic state to determine more accurate

predictions of the maximum stress range for the corresponding cyclic pressure, $\Delta\sigma/\Delta p$. An elastic-plastic model was used with a half symmetric 3-D shell element, whereas the indenter was considered a rigid body. There are two locations of maximum $\Delta\sigma/\Delta p$ ratio on the plastic model. The first one is close to the dent center whilst the second one is on the side of the model at an angle of 70° from the vertical with respect to the inner surface. Those two locations are the onset of cracks in the experiment. Also, pipe with longitudinal seam welds survived without failure.

Further work conducted by Flower et al. (1995) studied the effect of dents, gouges welding seams subjected to internal cyclic pressure loading. The research included two groups corresponding to different D/t ratios. The experimental work considered a range of such ratio from 18 to 94 whilst the FEA was done for a range from 18 to 100. According to the numerical and experimental results, plain smooth dents with $d/D < 5\%$ should not be a problem if the internal pressure is less than 69 bar.

The experimental results prove that the depth of gouge plays a key role in the fatigue life of a pipe and that grinding the gouges is considered a feasible solution to repair this defect. In fact, the fatigue life of ground gouges can be three times more than for the unground ones.

The gouges are classified according to the d/t ratio, depth to wall thickness. An analytical approach was proposed to estimate the fatigue life of pipe and to be compared with the experimental results. The experimental results from Phase I (without gouges) and Phase II (with gouges and welds) indicate that neither the dent type nor dent length play a key role in the fatigue life whereas D/t ratio, dent depth and welding type have a significant influence on the pipe life. Also, gouge depth of 5% (without grinding) can have its fatigue life three times and half more than the gouge depth of 15%. The cyclic pressure variations Δp play a crucial role in fatigue life where pipes with $\Delta p = 27.6$ bar live ten folds greater than those with $\Delta p = 62$ bar. The results prove also that the gouges without dent have the longest lives because no micro-cracks are produced at the gouge root. These micro-cracks have a big impact on the crack growth which in turn reduces the fatigue life. Gouges with 15% depth or more of the wall thickness could fail directly whilst gouges with 5-10% could fail after thousands of cycles which represent 1% of what the life of gouge without dent.

A series of tests were done to study girth and longitudinal welds. The findings point out that a dent with $d/D=5\%$ does not fail if these dents are located on the longitudinal weld or 71° off the seam weld. All the other tests failed but it was noticeable that the dent located directly on the seam weld did not have significant difference in fatigue life with those located 71° of this weld. Dents located on the girth welding have shorter fatigue life than those on the seam welding. The results emphasised that stress concentration factor (SCF) varies from 5 to 3 and it is associated with the dent depth, where the maximum SCF occurred in the deepest dents.

Alexander and Kiefner (1997) examined the effect of smooth and rock dents caused by rock not removed under the pipelines during installation, also called 'constrained dents'. The findings demonstrate that the constrained dents do not re-round whilst the unconstrained dents re-round elastically at first to 24-67% of the maximum indentation after pressurization to 65% of specified minimum yield strength (SMYS) which is 105.7 bar. After that, dents re-round inelastically due to increasing the internal pressure. As the pressure attains its burst pressure of the pipe (130-151% of SMYS), dents virtually disappear. The threat of unconstrained dent is around 2% or less to fail within the useful service life of pipeline especially if there is no stress concentration. A constrained rock dent is a bigger threat for pipeline especially if sharp and hard enough because leak has been developed at 78% of SMYS.

Rinehart (2004) presented a general study for pressurized cylindrical shells, focusing on the effect of localized geometric imperfections on the stress behaviour. He derived the analytical approach and a computational method by using 2-D and 3-D FEA for a dented cylindrical shell. The circumferential stress concentration has two peaks on the 2-D dent. One is located at the centre of dent whilst the other at dent periphery. Furthermore, stress concentration is in linear relationship with the ratio d/D and D/t . Furthermore, dent width has a big impact on the dent stress concentration whereby a wider dent has a lower stress concentration. The stress concentration on the periphery of dent is relatively not influenced by the dent width. Dent depth and dent length have a big effect on the SCF and this influence is based on their magnitudes relative to cylinder diameter. A simple elastic FE model was

developed to determine the peak stress at the dent centre and dent periphery by given depth and length.

The Pipeline Defect Assessment Manual (PDMA) project was run by Cosham and Hopkins (2004) to specify the best methods to assess defects of a pipe. A variety of dent types such as plain dent, dents on welds and dents containing defects were studied. Also, theoretical analysis and assessment methods were conducted for small and full scale tests.

Experimental results demonstrate that the plain dent has a fatigue life less than that of an equivalent circular section of pipe (Alexander and Kiefner, 1997; Eiber et al., 1981). 45 of 99 full scale fatigue tests resulted in a failure in the dented region. Also, the larger dent depth, the larger the stress and strain concentration in the dent, as shown in Figure 2-12. The mean stress plays a crucial role in re-rounding the dent which in turn reduces the stress concentration. The higher the mean stress, the longer the fatigue life is.

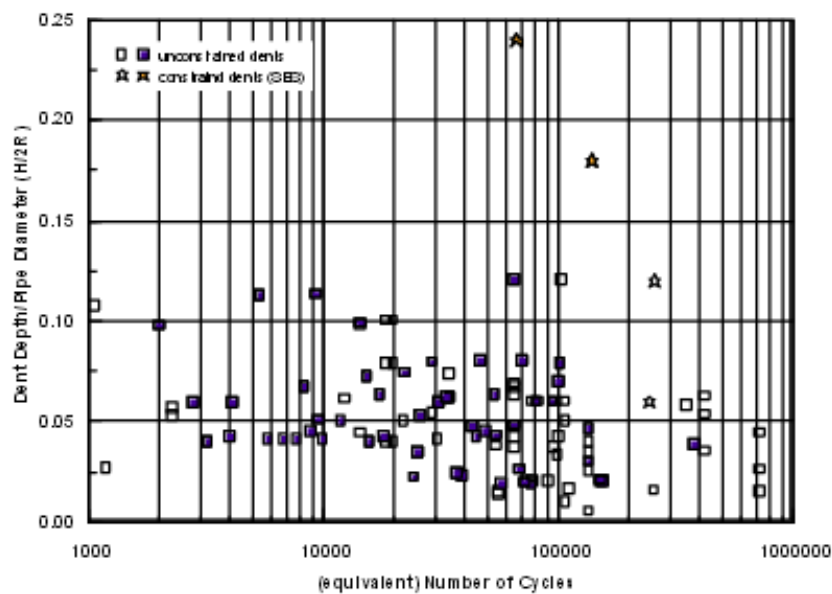


Figure 2-12. Fatigue life of unconstrained and constrained plain dents. open symbols (O) denote tests without failure and closed symbols (●) denote tests with failure during the test (Cosham and Hopkins, 2004)

The fatigue life of dented seam and girth weldings might be lower than those of an equivalent plain dent or undented welded pipe, as shown in Figure 2-13.

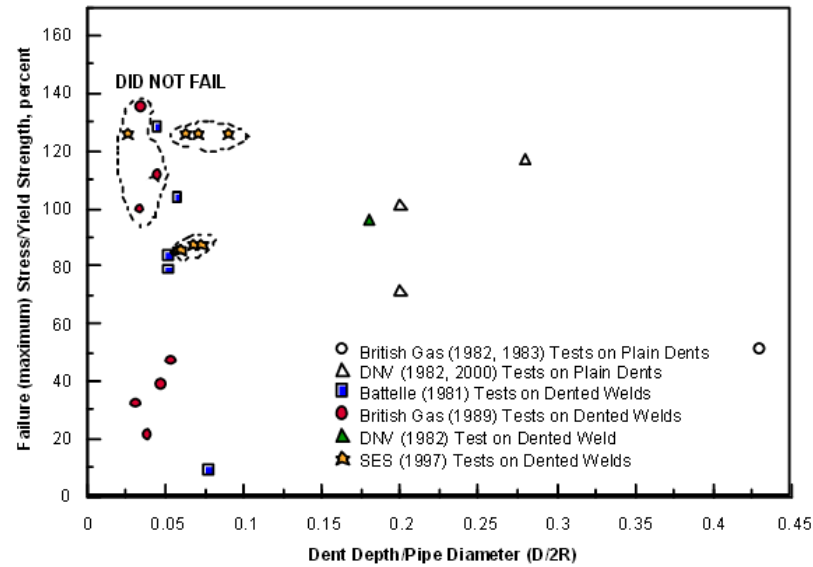


Figure 2-13. Failure (maximum) stress of smooth dents on welds and plain dents (Cosham and Hopkins, 2004)

Pinheiro and Pasqualino (2009) developed an approach for fatigue analysis of damaged steel pipelines under cyclic pressure. Experiments were conducted on small-scale specimens to evaluate the strain behaviour of a dented pipe under cyclic internal pressure. The experimental findings illustrate that the first cycle of internal pressure forced the dented region to deform plastically while the subsequent cycles deformed elastically if the maximum pressure, 72% of the specified minimum yield strength, 264 MPa, is not increased, as shown in Figure 2-14.

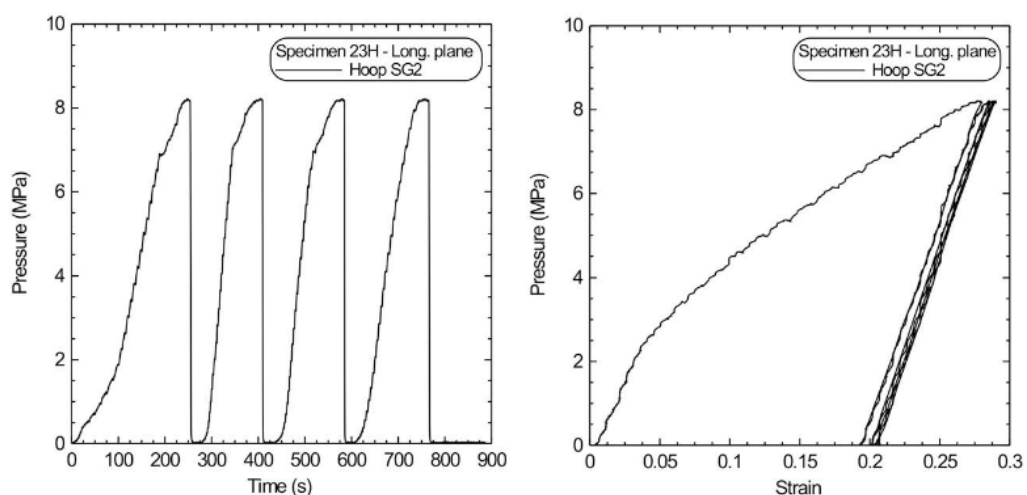


Figure 2-14. Experimental hoop strain of specimen 23H under internal pressure (Pinheiro and Pasqualino, 2009)

A non-linear 3-D shell type elastic-plastic models were developed in ABAQUS to produce stress concentration factors SCFs for different spherical dent dimensions. Higher SCFs are located at the dent periphery. There is a good agreement between the numerical and experimental results of d/D and residual strains. Small-scale tests had also been executed to estimate the life expectancy of a dented pipe under cyclic internal pressure. The experimental results are also in consistence with S-N curves proposed by Cunha et al. (2007).

The effect of dent depth on the burst pressure of pipelines has been presented by Allouti et al. (2012). A series of tests, including denting tests first and then burst tests, were conducted. FE models have been developed to compare the experimental results against the numerical ones. The tests were achieved on five pressure vessels made of A37 steel. The outer diameter is 88.9 mm associated with wall thickness of 3.2 mm. The whole length of all specimens are 600 mm as shown in Figure 2-15. Dents have been punched by a spherical indenter with diameter of 40 mm at low strain rate. The critical pressure for all samples is around 31 MPa. The findings points out that the pipe will not fail with dent depth up to 10% of the pipe outer diameter subjected to critical pressure. Above 10% of the dent depth-outer diameter ratio, all specimens got failure under the same critical pressure. For all tests, the numerical results of load versus displacement are in good agreement with the experimental results. The study found out that maximum Vickers microhardness values occur at dented region which in turn lead to increase the ultimate strength due to strain hardening to about 30%. As a result, the fracture occur far away from the dented region.

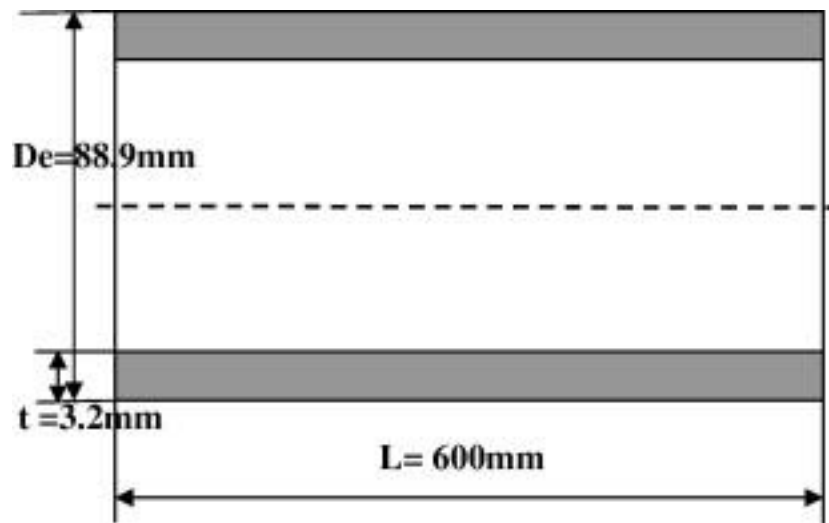


Figure 2-15. Pipe dimensions in mm (Allouti et al. ,2012).

2-4. Lined pipe geometries and material specifications

As already discussed in Chapter 1, lined pipes are composed of external Carbon Manganese steel (CMn) pipes, normally called baking steel, in contact internally with a thin liner made of corrosion resistant alloy (CRA), typically 1-3 mm thick. The CRA is used to protect the outer pipe from the transported corrosive products while the baking steel provides the structural capacity.

Despite their significant use in the industry, only in the last decade lined pipes have the subject of research studies regarding their structural response. Hilberink (2011), in his PhD thesis identified the main factors which have influence on the mechanical behaviour of lined pipe during bending. He developed 3-D FE models to simulate the case of pure bending and validated it against experimental results for a four point bending test. . In this test, the outer pipe is made of X65 steel with a wall thickness of 14.3 mm and an outer diameter of 324.7 mm. The liner is made of 316L stainless steel with 3 mm thickness and 293.1 mm outer diameter. The length of the lined pipe specimen is 6 m in total. The liner was inserted inside the outer pipe by the Tight Fit Pipe (TFP) where a thermo-hydraulic manufacturing process was used. As a result, contact stresses are produced between the liner and the outer pipe. These stresses were experimentally measured by mounting strain gauges on the inner surface. Hilberink observed that the tensile initial axial stress leads to increase the global

bending strain at which the liner starts wrinkling, whilst the compressive initial axial stress leads to decrease that. Furthermore, the hoop initial stress has larger influence on the bending strain than the initial axial stress when the liner starts wrinkling.

Vedeld et al. (2012) investigated the surface interaction properties between the backing steel and liner in lined pipe. The interaction bond between the outer pipe and the liner includes residual compressive stresses in the liner and residual tensile stresses in the backing steel. The contact pressure between the backing steel and liner results from the compressive residual hoop stresses. In this study, several factors which involve the influence of hoop and axial stress interaction, boundary conditions and friction behaviour have been discussed in two different test regimes. The first test regime is called the saw test which is performed by mounting strain gauges on the inner surface of the liner surface. Then, a cut through the whole cross section of lined pipe is performed as shown in Figure 2-16(a). After that, changes in the axial and hoop stresses along the length of the pipe have been recorded by the strain gauges. In this test, the outer pipe is made of X65 steel with a wall thickness of 19.1 mm and an outer diameter of 323.9 mm. The liner is made of 316L stainless steel with 3 mm thickness. The second test regime is called the ring-split test. A ring is cut through the whole cross section of uniform lined pipe segment. The strain gauges were mounted around the mid-section on the inner surface of liner. After that, the outer pipe is cut into two halves along the axial direction without cutting the liner as shown in Figure 2-16(b). In this test, the liner is free to expand axially and radially where the release of axial and radial strains is recorded by strain gauges. In this test, the outer pipe is made of X65 steel with a wall thickness of 8.9 mm and an outer diameter of 1 mm. The liner has the same material properties and wall thickness of the first test regime.

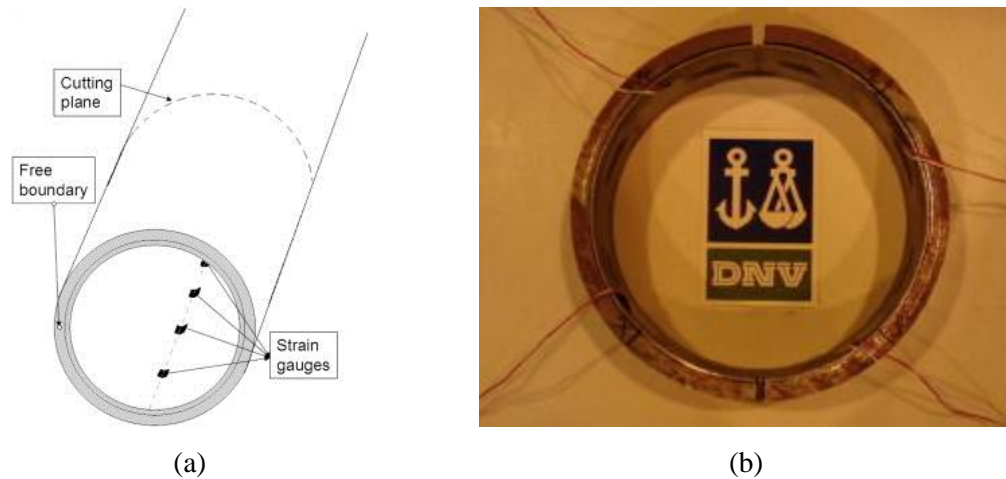


Figure 2-16 (a) Sketch of a saw test; (b) A lined pipe specimen subjected to a ring-split test (Vedeld et al., 2012)

In industrial applications, the liner can detach from the backing steel because of severe plastic bending, which can result in large levels of buckling that obstructs the flow. Yuan and Kyriakides (2014) have developed a numerical modelling approach to determine to what extent the lined pipe can be bent before the failure of the liner. The 3-D FE model using ABAQUS code starts with the manufacturing simulation where the outer pipe and liner inflate together to develop interference contact pressure between them. In detail, the carrier pipe, outer pipe, is made of X65 steel whilst the liner is made of alloy 825 stainless steel. The liner is cut to approximately 12 m length and then placed inside the carrier pipe. For ease insertion, a small gap (g_0) is allowed between the outer pipe and liner. After that, both pipes are enclosed inside two semi-circular stiff dies. Then, hydraulic pressure is applied to expand the liner and come in contact with the outer pipe. The pressure keeps increasing until the outer pipe comes in contact with the stiff dies as sketched in Figure 2-17. The pressure is then released to allow two pipes to contract where the outer pipe tends to spring back more the liner because the X65 steel has higher yield strength, 448 MPa, than that of alloy 825 stainless steel, 276 MPa. Consequently, an interference contact pressure is produced between them. The finish outer diameter and wall thickness of the X65 steel pipe is 323.9 mm 17.9 mm, respectively. The finish outer diameter of the liner extends to 288 mm with a wall thickness of 3 mm. After simulating the manufacturing process, the lined pipe is bent under pure bending which leads to differential ovalization. Eventually, part of the liner may separate from the outer

pipe. It is observed that bending the pipe under adequate amounts of internal pressure can delay liner failure.

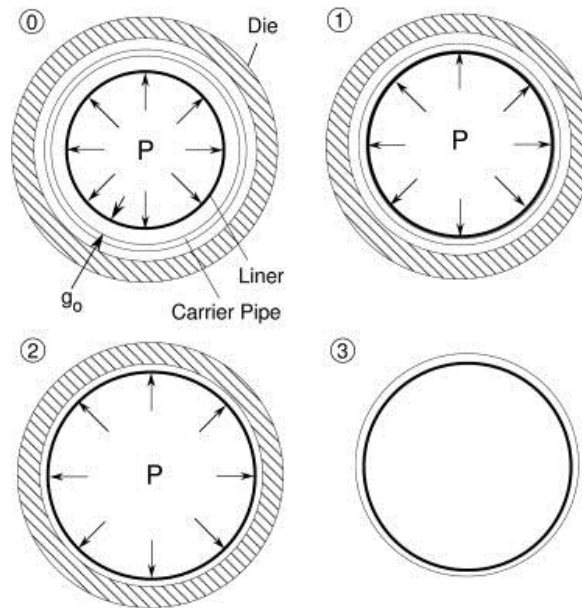


Figure 2-17 Schematic representation of lined pipe manufacturing (Yuan and Kyriakides, 2014)

2-5. Conclusions

From the foregoing discussion, previous contributions have been made to study the circumferential welding of pipes and cases of pipe impact. It is evident that the translation from experimental to analytical, axisymmetric and full 3-D FE analyses can be mainly attributed to improved computational power available. Nevertheless, all these studies deserve credit because they are still being reference work for a lot of recent research. In this research, for example, a mesh convergence analysis in welding takes advantage of the findings of Karlsson (1989). Furthermore, the validation of the numerical lined pipe welding procedure applied in this study is first made against the thermal and mechanical results in (Karlsson and Josefson, 1990). The effects of some welding parameters, such as heat input and inter-pass temperature, on residual stresses are based on (Brickstad and Josefson, 1998).

Welding and impact results, in this study, strongly depend on the results of recent contributions as well. In welding models, the validation of stainless steel pipe welding is based on the thermal and residual stresses in (Deng and Murakawa, 2006).

Moreover, much attention has been paid to the influence of heat coefficients on residual stresses, following Akbari and Sattari (2009). In pipe impact, the effect of dent size in this research goes along with the findings in (Flower, 1993) where the ratio of $d/D > 10\%$ is also considered detrimental damage in lined pipe. The location of stress concentration in a dented lined pipe is also consistent with the finding in (Pinheiro and Pasqualino, 2009).

Up to now, studies on lined pipe welding and impact are still lacking. In the welding case, the major drawback is to simulate two different welds associated with two different parent materials. In the impact case, most of the previous studies consider the dent formed in pipe as a static dent without taking the impact velocity into account. Furthermore, the effect of sequential strikes on the residual stresses in the dented pipe is ignored in the majority of previous contributions. Above all, manufacturing a lined pipe is a complicated process requiring special heat treatment to insert the liner inside the outer pipe.

With the rapid development of FE techniques in dynamic impact and circumferential welding modelling, more realistic 3-D FE models become a recognised need in research and industry. This need requires further improvement in commercial FE codes to adopt special techniques which cope with complicated cases such as sequential thermal and mechanical analyses, adaptive mesh management and sequential dynamic and static analyses.

ABAQUS code is considered a flexible FE code capable of creating complicated structure models. The flexibility arises from the capability to use subroutine files based on FORTRAN code. In this research, thermal and mechanical lined pipe welding analyses using ABAQUS code are developed using FORTRAN user-subroutines to simulate the heat torch movement and heat coefficient factors. Dynamic explicit analysis is adopted in the impact model to simulate the indenter and lined pipe movements.

Chapter 3

Experimental Setup for the Welding Process

3-1. Introduction

During the welding process, a large number of variables and interactions govern the high non-uniform and rapid change in temperature distributions underneath the welding torch (Hilberink, 2011). Moreover, the thermal fields produced in the lined pipe during welding are affected by various factors, such as the heat input, the filler material flow in the welding pool depending on the latent heat, thermo-mechanical material properties and the heat transfer to the environment and contacting materials (Spina et al., 2007). These numerous factors with governing equations based on assumptions and approximate mathematical formulations make lined pipe welding simulation a complex task. Therefore, the validation of numerical results obtained from FE models against the experimental results is an essential step to make such models acceptable in practice.

Regardless of the credibility of our numerical models, concrete evidence is still required to support the reliability of numerical results and procedures because there is no reliable experimental data published in the literature about lined pipe welding yet. The only way we have is to supplement the FE models with shop floor applications by executing full-scale experiments with the required machines and instruments to set up. At first, it is necessary to discuss the manufacturing process of lined pipe which is a big challenge in this research and it is more difficult than conducting welding process itself. One of the achievements of this research is that lined pipes have been manufactured in Brunel workshops without assistance from any third party, especially when 1 m of lined pipe could cost about £18,000. Because of that, this chapter discusses in detail the procedures of manufacturing and welding lined pipe associated with the required instruments to record the temperature and stress/strain during and after welding.

3-2. Manufacturing Procedure

The procedure begins with two pipes, a C-Mn steel (AISI 10305) pipe and a stainless steel (AISI304) pipe. The chemical compositions of each material are shown in Table 3-1.

Table 3-1 Chemical composition of AISI 10305 (C-Mn) and AISI304

Steel grade	C %	Si %	Mn %	P %	S %	Al %	Cr %	Ni %
AISI 10305	≤ 0.17	≤ 0.35	≤ 1.2	≤ 0.045	≤ 0.045	≥ 0.02	-	-
AISI304	≤ 0.08	≤ 1	≤ 2	≤ 0.045	≤ 0.03	-	18-20	8-10.5

The mechanical properties of both materials including the density (ρ), Young's modulus E , yield stress (σ_{stress}), ultimate tensile strength (σ_{UTS}), Poisson's ratio (ν) and Hardness are given for two pipes in Table 3-2.

Table 3-2 Mechanical properties of materials used in collision experiments

Steel grade	ρ (kgm^{-3})	E (GPa)	σ_{stress} (MPa)	σ_{UTS} (MPa)	ν	Hardness (Vickers)
AISI 10305	7860	210	349	390	0.26	100
AISI304	7900	198.5	265	505	0.294	129

Each pipe is cut into 200 mm long pieces. The outer diameter of the C-Mn is 114.3 mm with thickness of 6.35 mm. The stainless steel pipe has an outer diameter of 101.6 mm with 1.5 mm thickness as shown in Figure 6-1. The tolerance of the pipe thickness is ± 0.35 mm and ± 0.15 mm for C-Mn and AISI304, respectively. It is clear that it might be difficult to insert the AISI304 stainless steel piece inside the C-Mn steel as the thickness clearance is positive for C-Mn and AISI304. In a matter of fact, this drawback has occurred in our experiments.

Typically in industry, lined pipes are manufactured using a combination of thermal expansion and cold shrinking in order to guarantee a high and reliable fit-in stress between the liner and backing steel pipe (Focke, 2007; Focke et al., 2006; Focke et al., 2005). The first step in our manufacturing procedure is to heat up the outer pipe in a furnace to about 500°C where the metal microstructure keeps without phase

transformation. Thereafter, the pipe is moved away from the furnace to a portable ceramic knuckle heater, known as jacket heater. The purpose of putting the C-Mn pipe inside the jacket is to keep the pipe temperature 500°C as the liner inserts inside. In the same time, the AISI304 stainless steel pipe is immersed in liquid Nitrogen where the temperature is around -200°C (De Koning and Nakasugi, 2004). After that, the liner is moved away from the liquid Nitrogen with -200°C to be inserted vertically inside the C-Mn steel joint which is still heated inside the jacket. Then, the compound pipe (lined pipe) is taken away from the jacket to cool naturally down to room temperature; Figure 3-1 illustrates the manufacturing process.



(a)



(b)



(c)



(d)



(e)

Figure 3-1 The steps of manufacturing set up (a) heating up the outer pipe to 500°C (b) cooling down the liner to -200°C (c) putting the outer pipe in Jacket with 500°C (d) topping the liner inside the C-Mn pipe (e) cooling down the lined pipe to room temperature

Once the lined pipe reaches room temperature, the hardness is examined for both materials. Measuring the hardness is a simple way to check there is no change in the metal structure. In particular, martensitic structure (brittle structure with higher hardness) is not formed in the pipe structure which in turn means the mechanical properties have not changed. The hardness magnitudes under a normal diamond indenter load of 20 Kg_f are 99.7 Hv and 127 Hv for C-Mn and AISI304 pipes, respectively.

Finally, the lined pipe joint used in welding is ready to be machined using CNC milling machine, Bridgeport VMC 500, by cutting 3 mm of liner and chamfering the backing steel by 30° from one end, as shown in Figure 3-2.



Figure 3-2 Cutting 3 mm from the liner and chamfering the edge of C-Mn by 30°

3-3. Preparation for Welding Process

Full-scale lined pipe welding experiments are carried out to record the transient thermal and strain fields. With this purpose, thermocouples and strain gauges were

mounted on the inner and outer surfaces according to the international standards ASTM E1237 and ASTM E1561. The locations of thermocouples and strain gauges are specified numerically first to avoid any mistakes in recoding results.

3-3-1. Thermal Fields Measurement

Measurement of the thermal fields in the lined pipe is necessary in our project because there are no articles in the literature reporting similar work. Measuring the transient temperature history is obtained through thermocouples mounted directly on the liner and backing steel surfaces. Consequently, the measured thermal fields are taken from 6 specified points located at the HAZ on the inner and outer surfaces of the lined pipe. The first thermocouple on both the inner surface and outer surface is located 4 mm away from the edge of the weld overlay and girth welding, as shown in Figure 3-3.

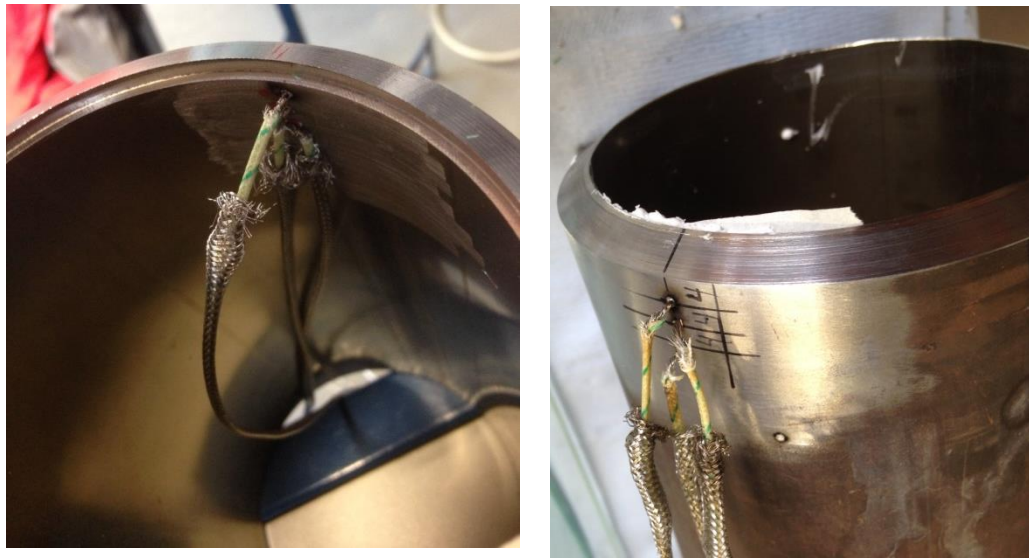


Figure 3-3 Thermocouples located on the inner and outer surfaces.

Thermocouples type K, applicable within a range of temperatures from -200 to 1250°C , are used. The thermocouples are directly mounted on the inner and outer surface of lined pipe by sparking welding. After that, high temperature adhesive is used over the thermocouples to protect them from the heat of the welding torch and also to keep them bonded to the lined pipe surfaces. The maximum continuous working temperature of the adhesive is $\leq +1000^{\circ}\text{C}$ which is quite enough to keep the

tips of thermocouples fixed with the lined pipe surfaces and without significant effect of extra heat from the welding torch, as shown in Figure 3-4.



Figure 3-4 Protecting the tips of thermocouples on the outer surface by adhesive

The second end of the thermocouple is connected directly to 16-channel Module NI 9213, as shown in Figure A-1 in Appendix A-1.

The thermal history results are recorded every 0.001 second by LabVIEW software. In this way, the transient thermal history for all thermocouple locations at any particular time can be easily saved on an MS Excel file.

The thermal history in the FZ is difficult to be measured precisely by thermocouples because of the difficulty in fixing them on specified points due to the excessive temperature in this area. Consequently, infrared optical camera, FLIR T, is used to validate the temperature in the welding pool of the weld overlay and the girth welding and also to add extra level of accuracy to thermocouple readings. The temperature range calibration is up to 2000°C, which is sufficient to measure the temperature on the FZ of weld overlay and girth welding.

3-3-2. Strain Measurement

High temperature strain gauges are used to record the transient strain history during the weld overlay and girth welding passes. This type of strain gauges is also suitable to measure the residual strain after cooling down of the lined pipe to room temperature. They are not used widely because of their relatively high cost.

Two types of high temperature strain gauges are used to record the strain history axially and circumferentially, taking into account the lined pipe surface materials, as shown in Figure 3-5. In particular, uniaxial strain gauges are mounted on the outer surface (C-Mn pipe), ZFLA-11. On the inner surface (AISI304 pipe), biaxial strain gauges, ZFCAL-17, are used because the material of liner is different, and therefore it has a different coefficient of thermal expansion. More precisely, the coefficients of thermal expansion of ZFLA-11 and ZFCAL-17 are 11.8×10^{-6} and $17 \times 10^{-6} \text{ } ^\circ\text{C}^{-1}$, respectively.

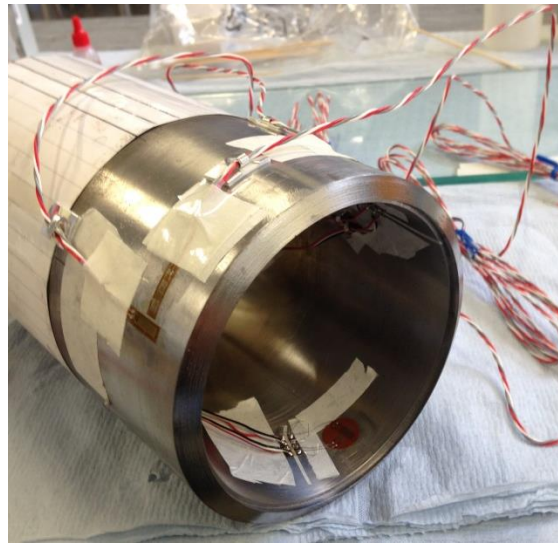


Figure 3-5 Mounting the strain gauges, ZFCAL-17 and ZFLA-11 on the inner and outer surfaces accordingly

The thermal and mechanical measured strain results are recorded every 0.001 second through 8-channel Module NI 9235 as shown in Figure A-2 in Appendix A-1. They are connected to LabVIEW software fitted with a data logger in a similar way as for the thermocouples.

Figure 3-6 shows the data acquisition with connections where the thermocouples, strain gauges, NI 9213, NI 9235, chassis (NI CompactDAQ) and LabVIEW software are components integrated together to form the configuration of data acquisition system.

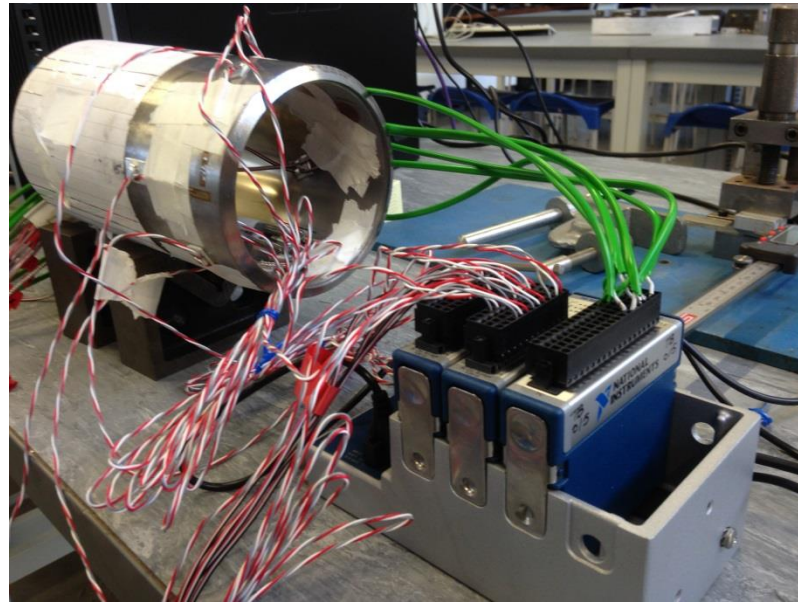


Figure 3-6 The electrical components required to get the results of temperature measurements.

In our work, the procedure of installing bonded strain gauges is implemented according to ASTM E1237. Furthermore, special adhesive NP-50 is used to keep the high temperature strain gauges bonded with pipe surfaces in higher temperature. NP-50 is a compound adhesive composed of two-component room-temperature-curing polyester adhesive for bonding QF, ZF and BF series strain gauges. Also, a high temperature adhesive is used over the high temperature strain gauges to protect them from the heat of welding torch (no extra heat) and also to keep them bonded to lined pipe surfaces. By mounting the strain gauges and thermocouples on the lined pipe, two joints of lined pipe are ready to be welded with weld overlay first and then with girth welding passes to join them together as shown in Figure 3-7.



Figure 3-7 Measuring the temperatures and strains during welding

Basically, the analysis procedure which is used to determine the directions and magnitudes of the principal surface strains and then to determine stress transformations goes along with ASTM E1561.

3-4. Welding Operation

Arc welding is the most common type of welding process used widely in steel construction such as pipelines, ships and pressure vessels (Lindgren, 2014). Arc welding has countless advantages in terms of ability to provide high quality welds for various types of steels and thickness and also using suitable equipment to move easily on site. The main equipment is the power supply machine used to create an electric arc between an electrode and the base material which is protected by gas atmosphere. Based on the electrode type, arc welding is classified into three kinds as follows:

- Shielded Metal Arc Welding (SMAW), known generally as stick or arc welding, uses a consumable stick electrode. Arc welding could be used for construction, manufacturing and repairs for thick metal (over 4 mm).
- Gas Metal Arc Welding (GMAW) commonly so called Metal Inert Gas (MIG) depends on a continuous-fed consumable electrode. Therefore, it could

be an automated welding process by using robotic MIG welders. It has the ability to weld different types of metals with a wide variety of thickness.

- Gas Tungsten Arc Welding (GTAW) widely known as Tungsten Inert Gas (TIG) uses a non-consumable tungsten electrode. In this type, an inert gas protection from atmosphere contamination is required. TIG welding is more able to produce robust, clean, neat and tidy welds. In this work, all welds have been executed by TIG welding.

Two types of consumable rods are used in TIG welding. The first one is made of stainless steel ER308L which is suitable with 300 stainless steel series where 304 is the most common. Due to the higher weldability of ER308L, it could be also used in carbon steel pipe welding, MIG (GMAW) and Submerged Arc (SAW). ER308L conforms to AWS A5.9 ER308L. The second rod is made of mild steel alloy E70S-2 which could also be used with cast steel welding. E70S-2 is a triple deoxidized wire (Aluminium, Titanium, Zirconium) which provides defect free weld deposits when properly used on most carbon steels. It is used especially for pipe welding. ER70S-2 conforms to AWS A5.18 ER70S-2. The chemical compositions and the mechanical properties of ER308L and E70S-2 corresponding to AWS A5.9 and AWS A5.18 ER70S-2 specifications, respectively, are reported in Table 3-3 and Table 3-4. Figure 3-8 shows the types of welding rods used in experiments.

Table 3-3 Chemical compositions of ER308L and E70S-2

Rod type	C %	Si %	Mn %	P %	S %	Mo%	Cr %	Ni %	Cu %	Zr%	Al%	Ti%
ER308L	≤ 0.03	0.3-0.65	≤ 1-2.5	≤ 0.03	≤ 0.03	≤ 0.75	19.5-22	9-11	≤ 0.75	-	-	-
ER70S-2	≤ 0.07	0.4-0.7	0.9-1.4	≤ 0.025	≤ 0.035	0.15	0.15	0.15	≤ 0.50	0.02-0.12	0.05-0.15	0.05-0.15

Table 3-4 Mechanical properties of ER308L and E70S-2

Material	Yield Strength (MPa)	Ultimate Tensile Strength (MPa)		Elongation (%)
ER308L	400		587	36
ER70S-2	440		520	28



Figure 3-8 Rod types, E70S-2 (brass colour) and ER308L (grey colour)

In the numerical simulation of FE models, the welding torch moves with constant speed, which in turn it is mandatory to be constant experimentally. The complexity of lined pipe welding in terms of the internal welding, i.e. weld overlay, drives us to weld the pipe manually. The pipe is rotated with a constant speed over two lubricated V-blocks where the friction is negligible as shown in Figure 3-9.



Figure 3-9 Lined pipe welding process using TIG welding

In our work, the practical procedure of lined pipe welding is consistent with international standards such as the American Welding Society AWS D1.1 and American Petroleum Institute API 1104. The welding power source utilized is GENESIS 150 AC-DC to provide the required amperage and voltage to deposit the filler materials in the grooves with high quality as depicted in **Error! Reference source not found.** Appendix A-1. Also, GENESIS 150 has the flexibility to change the amperage to increase and reduce the magnitude of welding heat input.

3-5. Post-Welding Requirement

The welding process is responsible for generating residual stresses. The effects of residual stresses on the lined pipe could be either good or detrimental based on their sign, magnitude and distribution along the entire pipe (Measurements, 2007). In the majority of welding cases, the residual stresses are considered to be a potential cause

of nucleation of cracks which leads to detrimental damage to the pipe in service. In the lined pipe, the danger of initiation cracks is doubled because of the sealing weld, i.e. the weld overlay. Besides recording the stresses during welding, two techniques have been used to measure the residual stresses in the welded lined pipe, hole-drilling and X-ray diffraction.

3-5-1. Measurement of Residual Stresses by Hole-Drilling

The hole-drilling method is often considered as semi-destructive because of the small localized damage that it causes by drilling through the pipe thickness. Nevertheless, this damage does not significantly affect the usefulness of the specimen (ASTM-E837, 2008). The reference hole with diameter of 2 mm and depth of 2 mm is drilled vertically through the pipe thickness using a high speed milling machine. Due to the removal of the material, the diameter of the reference hole changes because of strain relaxation. The procedure applied in this method is based on ASTM-E837. The residual stress gauges with three elements, FRS-2, are mounted on the inner surface (liner) and outer surface (C-Mn pipe) as shown in Figure 3-10.

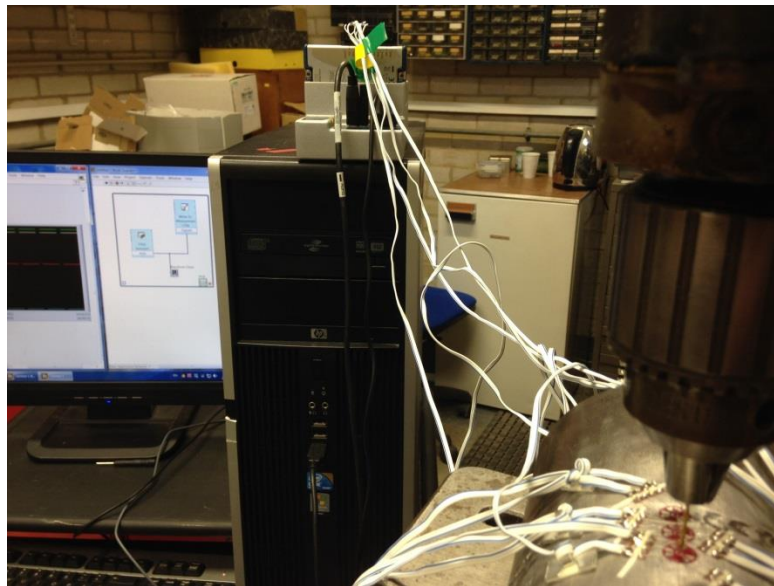


Figure 3-10 Residual stress gauge rosette with three elements, FRS-2

3-5-2. Measurement of Residual Stresses by X-Ray Diffraction (XRD)

To check the reliability of experimental results done by hole-drilling, X-Ray diffraction technique has been used to measure the axial and hoop residual stresses in the welded lined pipe. This method is based on the interaction of the incident rays (monochromatic X-ray) with the welded sample to produce constructive interference and a diffracted ray when Bragg's Law is satisfied with conditions. This law ($n\lambda=2d \sin \theta$) expresses the relation between the wavelength of electromagnetic radiation ($n\lambda$), the diffraction angle (θ) and the lattice spacing in a sample (d). The X-rays are generated by a cathode ray tube (Cr-Ka1 tube), filtered to produce monochromatic radiation, collimated to concentrate (1mm), and directed toward the sample ($2\theta=156^\circ$). As a result, the residual stresses can be mapped across the FZ, HAZ and base materials on the outer surface (C-Mn pipe) and the inner surface (AISI304 pipe). A Bruker D8 Advance X-ray diffractometer instrument has been used to do that as shown in Figure 3-11.

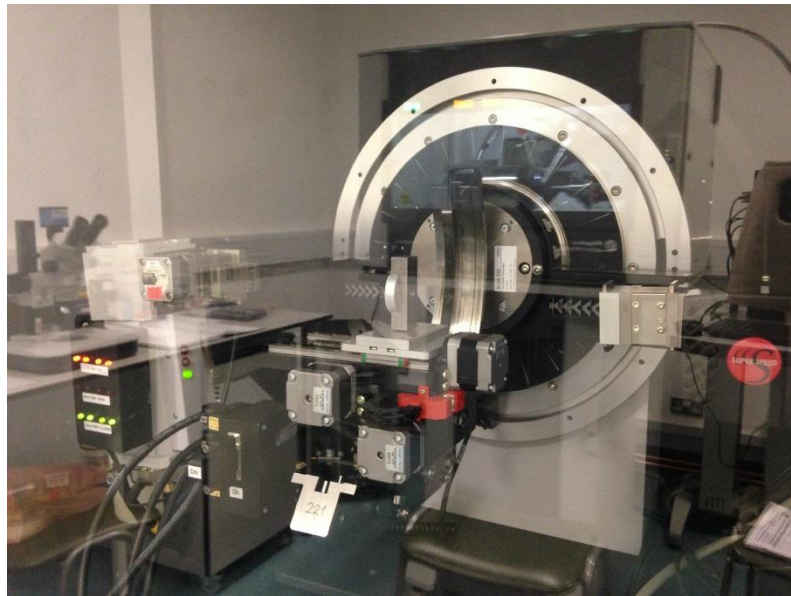


Figure 3-11 X-ray diffractometer instrument, Bruker D8 Advance

Moreover, a small sample of welding cross section is cut to reveal the FZ and HAZ boundaries under microscopic examination. To do that, rough and fine polishing are achieved using silicon carbide abrasive paper with different grit sizes mounted on a rotating disc with water coolant. Afterwards, final polishing is executed by

Aluminium oxide. Next step is to etch the sample with 10% natal (10ml Nitric Acid and 90ml Methanol) for 10 seconds. After that, the sample is ready for microscopic examination, as shown in Figure 3-12.

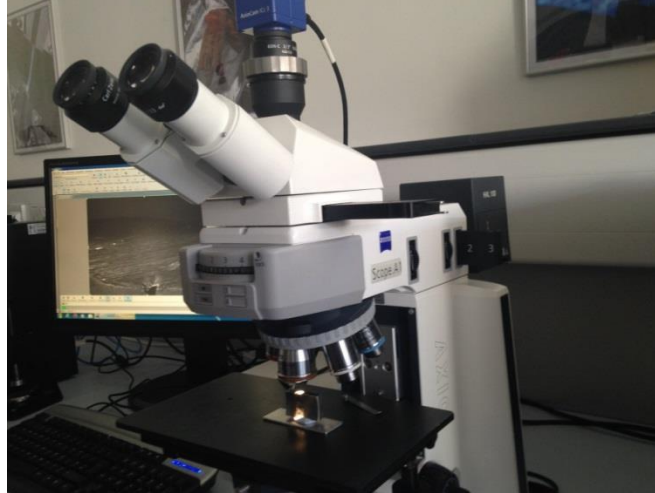


Figure 3-12 Microscopic examination to measure the FZ and HAZ dimensions

3-6. Conclusions

Details about the applied procedure of special thermal manufacturing process known as tight fit pipe (TFP) to insert the CRA liner inside the C-Mn pipe have been provided in this chapter. The chapter also presents an overview of experimental methods used to validate the numerical results for the lined pipe welding models, which will be presented later in this research. To do that, strategies based on international standards, ASTM E1237, ASTM E1561, AWS D1.1 and API 1104, have effectively been used. To examine the reliability of experimental residual stresses results, two techniques have been executed for this purpose, hole-drilling and X-ray diffraction.

Chapter 4

Experimental Setup for the Impact Process

4-1. Introduction

Mechanical damage resulting from an outside object hitting a pipe is a big threat for its integrity. Dents can be generated in an offshore or onshore pipe and commonly happen when excavation equipment or heavy objects being operated within the pipeline area come in contact with the pipe wall. This contact could produce dents with different types and geometries accumulating high levels of plastic strain and residual stresses.

Lined pipelines are used to reduce the cost by decreasing the thickness of the carbon steel backing, up to a half. Unfortunately, Lined pipelines are more vulnerable to be dented by external interference or third part because of this minimization of the backing steel thickness. After hitting, the cylindrical pipe may rebound or re-round little bit but there may remain considerable amount of residual stresses in the dent, depending on the conditions of collision such as velocity, shape and density of the hitter body. Consequently, dents can be the main cause of crack initiation.

The Marathon Pipelines had been damaged after three years of the in-line inspection causing in the loss of 489,000 gallons of crude oil and the cost of this damage was approximately \$12.6M. According to pipe line accident report (Race, 2008), the main reason for this damage was fatigue cracking because of fluctuating internal pressure. Another report (Johnston, 2002) stated that the cracks were initiated in the dent because of increasing stress concentration at the site of damage.

A lot of studies (Alexander and Kiefner, 1997; Fowler, 1993; Fowler et al., 1994) attributed the possibility of fatigue behaviour of dented steel pipelines to the stress concentration factors (SCFs). Consequently, it is important to have more

understanding of stress behaviour for the sake of predicting the fatigue life of dents found in the pipe. SCFs are mainly function of the dent and pipe dimensions.

4-2. Dents

It is fundamental to define the terminology used here and the types of dents in pipelines. In this work, the term “dent” is defined as a permanent plastic deformation of the cross section of the pipe caused by external forces (ASME B31.4, 2012). Smooth dent, plain dent, kinked dent, unconstrained dent and constrained dent are the major defect classifications that typically arise when the damage is estimated. A smooth dent is characterised as a dent which varies smoothly in the curvature of the pipe wall. A plain dent is a smooth dent without reduction in wall thickness because of gouges, cracks or other imperfections such as girth or seam welds. A kinked dent is a dent with a sudden change in curvature of pipe wall because of defects such as gouges or cracks. Furthermore, the dent could be classified into unconstrained or constrained dent, according to its ability to move under internal pressures. Thus, an unconstrained dent is able to re-round elastically (spring back) as the internal pressure is changed or the indenter is removed (Race, 2008). On contrary, a constrained dent is not free to move, as in the case of a rock dent caused by laying the pipe onto a rock in the trench during construction.

A large number of studies have reported that unconstrained smooth plain dents do not significantly reduce the burst strength of pipelines. As a result, pipe repair is not required unless dents are very deep. Therefore, dent depth plays an important role in determining the dent severity. Recently, some authors have reported that the dent depth is not sufficient to determine the severity without considering the strain in the dent (pipe material), which is a stronger indicator for the dent severity. The dent depth is defined in standard ASME B31.4 (2012) and ASME B31.8 (2012) as “the gap between the lowest point in the dent and the trajectory of this point on the original contour of the pipe”. There is another definition of dent depth as “the maximum reduction in the diameter of the pipe compared to the original diameter” (Cosham and Hopkins, 2004). The definition of dent depth includes both the local indentation and the ovality (out-of-roundness) of the pipe diameter. Therefore, the criteria to specify the dent severity is expressed by the percentage dent depth-to-pipe

diameter, H/D , as shown in Figure 4-1. Increasing the percentage leads to increase the possibility of failure.

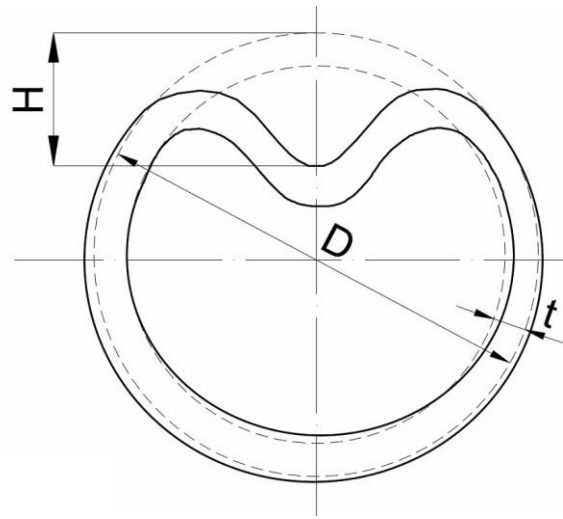


Figure 4-1 The definition of dent depth (ASME B31.4, 2012)

Another issue which is associated with dent depth measurement is spring back. The impact process produces both elastic and plastic strains in the material. The elastic strain is recovered when the indenter is removed, so that the dent moves outwards. If the dent is unconstrained, the dent is pushed out by the internal pressure changes. Re-rounding is comprised of initial plastic recovery of the dent depth based on the internal pressure and the pipe properties.

In the literature, most of dents which have been reported with full scale tests have been initially loaded with zero pressure. After that, the pipe is pressurised and therefore the dent is re-rounded by internal pressure. In such cases, the effect of spring back and re-rounding should be considered by using a spring back correction factor. However, the Pipeline Defect Assessment Manual (PDAM) has considered the spring back correction factor in conjunction with the revised European Pipeline Research Group (EPRG) factor, where the dent depth at zero is equal to 1.43 of the re-rounded dent depth (Corder and Chatain, 1995). The location of the point at which the stress concentration is the largest is based on the length of dent in the static impact. The location of the maximum stress and strain is at the rim of a short dent, which is defined as a dent whose axial length is less than twice the dent width.

Increasing the length of the dent with respect to the width makes the maximum stress concentration move to the root of dent (Rinehart and Keating, 2002).

In our work, the types of dent in all tests are unconstrained dynamic short plain dent where the indenter drops freely from a specific height and hits the lined pipe sequentially until consuming the kinetic energy. Therefore, the pipe material and equivalent plastic strain rate play an important role in the shape of dent and stress/strain behaviour (Nicholas, 1980).

4-3. Experimental Specimens and Materials

Specimens of lined pipe used for impact testing were manufactured at Brunel University (BCAST lab) using exactly the same procedure used for the specimens used for welding tests. The backing pipes and the liner are also the same as for the welding test, so the reader is referred to Chapter 3 for the manufacturing procedure, dimensions of the line pipe and the composition of materials.

Experiments were conducted for two groups of pipes. The first one, case A, consists of C-Mn pipes without liner (AISI304). The second group, case B, consists of lined pipes composed of C-Mn pipe cladding with AISI304 pipe internally as shown in Figure 8-2. Each specimen in both cases has a total length of 200 mm. The chemical compositions and the mechanical properties for each material are reported in Table 3-1 and Table 3-2.

4-4. Experimental Apparatus

The apparatus which is customised to apply free drop test is depicted in Figure 4-2. The apparatus is composed of a steel square block with total net weight of 200 kg. The apparatus is equipped with a semi-spherical indenter (denting tool) with diameter of 51.75 mm at the bottom surface. At the top surface of the block, a metal chain connects the block with a mechanism of pulley to draw the blocks up and down. The block slides up and down freely inside a greasy square chamber. The external wall of chamber is scaled in the range of 0 to 3 m along the height of chamber which is 3 m. Furthermore, a laser distance measuring tool is used to specify the particular height of free drop precisely from the tip of indenter to the

outside surface of pipe (dent centre), as shown in Figure A-4 in Appendix A-2. After reaching a prescribed height, the chain is released from block. Consequently, the block freely slides down through the chamber because of the gravity of its weight to hit the pipe in the centre of the expected dent region located at the middle section of pipe.

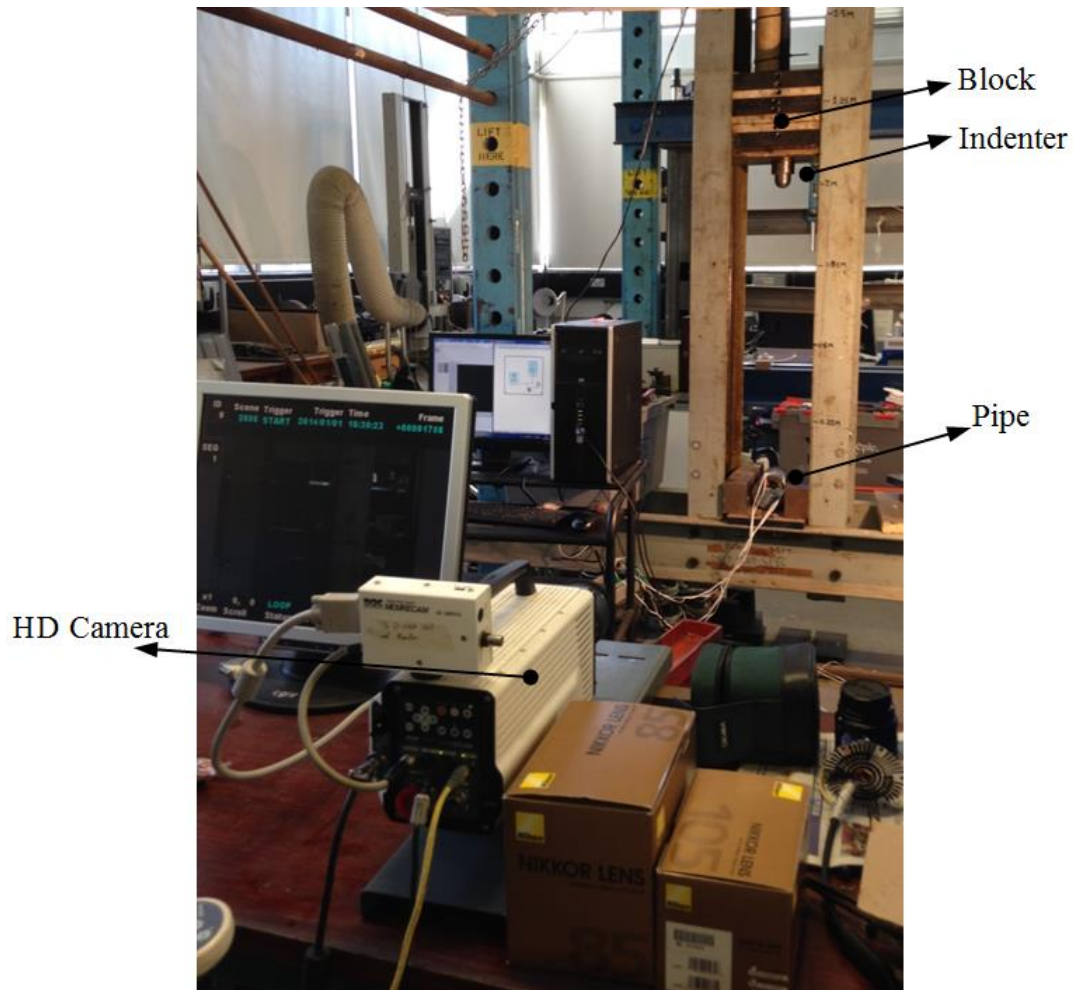


Figure 4-2 Apparatus of the collision experiments

Also, Figure 4-2 clarifies that the specimen is laid down horizontally on a rigid bottom plate and also trapped between two thick rigid plates on its sides with 3 mm clearance on each side. The main goal of our experiments is to examine the high levels of strain in the dented region. With this aim, different types of strain gauges were used to record the strain history during impact process, including strain gauges FRA-5-11 and YEFCA-5-11 for short and large strain, respectively. Furthermore, bi-axial and tri-axial strain gauges were used but just the results of normal strains (axial

and hoop strain) are plotted in this study because of the small value of 45° strain (diagonal strain). The procedure applied to install the strain gauges on the pipe is corresponding to Standard ASTM E1237. The strain gauges is connected to a data acquisition system (LabVIEW) to record the strain history during the impact process as explained earlier in the previous chapter. Afterwards, the stresses are computed from the strain according to Standard ASTM E1561.

The positions of the four strain gauges around the dent are determined first using the FE model to specify locations precisely without damaging the gauges and to acquire high levels of strain closer to dent centre. Strain gauges are firmly fixed on the outside surface using a special adhesive glue, polyurethane coating (lacquer), to avoid removing gauges during instant impact test because of successive collisions in the indentation process. Figure 4-3 shows the locations of four strain rosettes (GR1, GR2, GR3 and GR4) symmetrically surrounding the dent centre located at the pipe middle section. The strain histories are transferred from strain gauges to the data acquisition via LabVIEW.



Figure 4-3 Positions of the strain gauges

4-4-1. Measuring the Impact Velocity

Due to the friction between the weight and apparatus walls, it is necessary to measure the actual impact velocity. In our case, a digital high speed camera, MEMRECAM HX-7, is a good choice to measure the impact velocity and also to capture the sequential strikes after the first collision between the indenter and pipe. The MEMRECAM HX-7 offers full HD resolution at up to 2000 frames per second (fps). Error! Reference source not found. in Appendix A-2 depicts the MEMRECAM HX-7 digital camera used in experiments. Figure 4-4 illustrates the sequential strikes with respect to impact time.

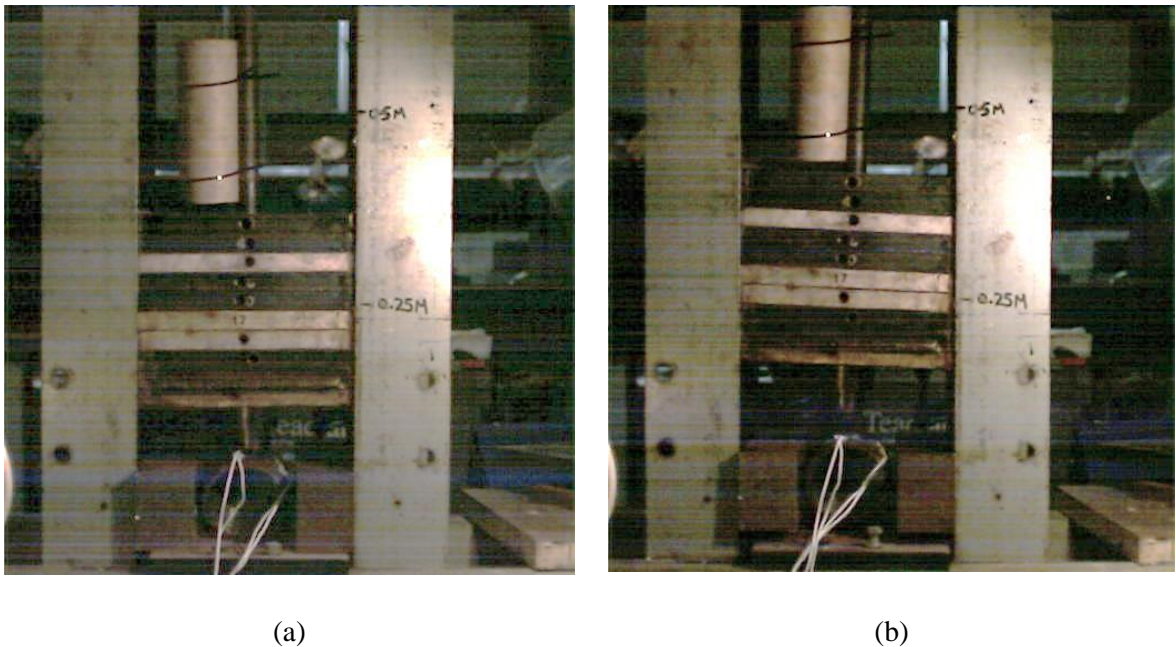


Figure 4-4 The stages of collision after the first contact between the indenter and pipe at (a) 7.5 ms (b) at 250 ms

4-4-2. Measuring the Dented Pipe Geometries

After completing the impact process, the deformed geometry of the pipe is measured with aid of a conventional callipers and a displacement transducer sliding on a greased flat plate perfectly, while the pipe is mounted on V-groove blocks as shown

in Figure 4-5. In this way, the deformation obtained from the FE model can be compared with the experimental measurements.

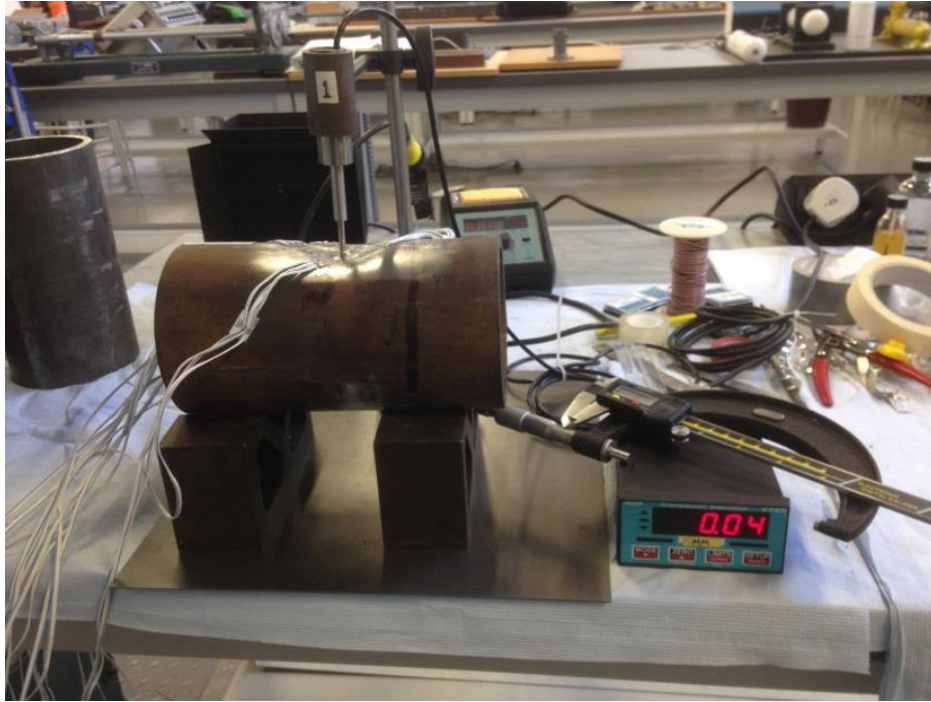


Figure 4-5 Experimental set up for measuring pipe geometries

4-5. NDT Tests

Dye penetrant inspection (DPI), also called liquid penetrant inspection (LPI) or penetrant testing is considered a visual inspection in non-destructive testing NDT to detect flaws such as cracks on the pipe surface. DPI is used in this work to check the possibility to get surface cracks after impact and welding as shown in Figure 4-6.



Figure 4-6 Using DPI penetrants to detect the surface-breaking cracks

The principle of DPI is that the liquid dye penetrant is sprayed on the pipe surface, red spray, and accesses the flaws by capillary action. The penetrant is then wiped by cleaner spray or alcohol liquid. A developer spray, white powder, is used afterwards to draw out the red penetrant from the surface-breaking cracks. Cracks with opening of 150 nanometres could be detected by DPI test.

4-6. Conclusions

This chapter has presented a description of the experimental setup and procedures used to validate the numerical results of FE impact models which will be presented later in this research. In particular, procedures based on international standards, ASTM E1237 and ASTM E1561, to effectively provide precise experimental results have been applied

Chapter 5

FE Analysis of a Single-Pass Weld Overlay and Girth Welding

5-1. Introduction

In this chapter, using the ABAQUS software, a three-dimensional FE model is developed to simulate the evolution of the temperature field and residual stresses in a lined pipe made of a SUS304 stainless-steel liner and a C-Mn steel pipe. The proposed method uses non-linear modelling of the heat flux through exposed metal surfaces and accounts for the moving heat source during welding. These two features are implemented by coding two separate user subroutines in ABAQUS.

The presented numerical procedure is validated against previously published experimental results for stainless steel and carbon steel welding separately. The model has been then used to predict the transient temperature field and residual stress distributions during the weld overlay (inner welding) and the girth welding (outer welding) of a lined pipe. Furthermore, a sensitivity analysis to determine the influence of the cooling time between weld overlay and girth welding and of the welding speed has been conducted thermally and mechanically, as these are key parameters that can be fine-tuned to improve the welding quality.

5-2. Description of Welding Conditions

As discussed in the previous chapters, an overlay welding between the pipes is normally used also as a way to seal the gap between them, and therefore avoid that moisture, grease and dirt penetrate the gap, as shown in Figure 5-1.

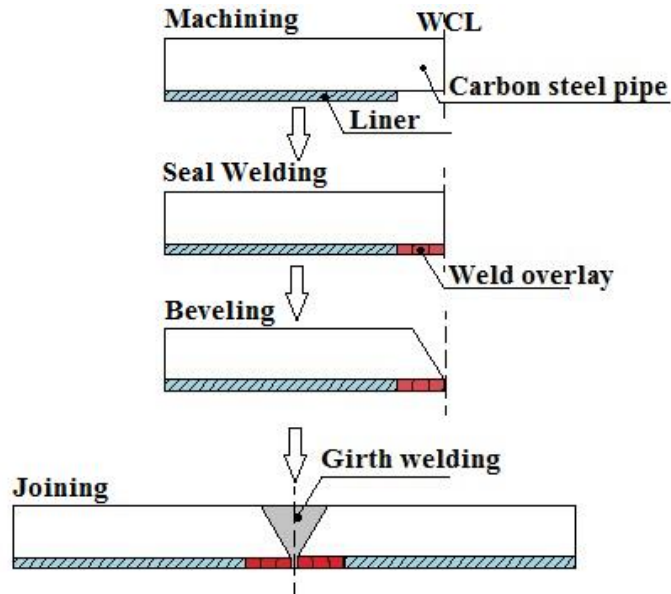


Figure 5-1 Weld preparation to seal the pipe at ends

The weld overlay filler material is chosen to have corrosion resistance which preferably exceeds that of the liner material. The arrangement could be swapped between seal welding (weld overlay) and bevelling (chamfer) because the main purpose is to seal the pipe ends. After that, a girth welding is deployed to join two segments of the lined pipe together. The filler material of the girth welding could be either carbon steel the same as the material of backing pipe or stainless steel, discussed later in detail in Chapter 7. In this chapter, the materials of the weld overlay and girth welding have the same thermal and mechanical properties of the liner and backing pipe, except the yield stress, respectively.

5-3. Thermal Analysis

5-3-1. Modelling of the Heat Source

The physical phenomena associated with the interaction between the welding torch and the weld pool are complex. The two-dimensional circular disc model proposed by Pavelic et al. (1969) assumes for the thermal flux the following Gaussian distribution in the plane.

$$q(x, y) = q_{max} e^{-wr^2} \quad (5.1)$$

where $q(x, y)$ is the surface flux at a distance $r = \sqrt{x^2 + y^2}$ from the centre of the heat source, q_{max} is the maximum flux at the centre and w is a distribution-width coefficient.

Goldak et al. (1984) extended this approach to a three-dimensional model in which the heat source q is represented with a Gaussian distribution of the power density in an ellipsoid with centre that, for simplicity, is first taken as $(x_0, y_0, z_0) = (0,0,0)$:

$$q(x, y, z) = q_{max} e^{-Ax^2} e^{-By^2} e^{-Cz^2} \quad (5.2)$$

The actual ellipsoid is defined as the volume within which the point-wise heat source is greater than 5% of the maximum one (Goldak et al., 1986), i.e. where $q(x, y, z) > 0.05q_{max}$. This allows one to define constants A , B and C as follows, with good approximation:

$$A = \frac{3}{a^2} \quad B = \frac{3}{b^2} \quad C = \frac{3}{c^2} \quad (5.3)$$

where a , b and c are the semi-axes of the ellipsoid in directions x , y and z , respectively, as illustrated in Figure 5-2.

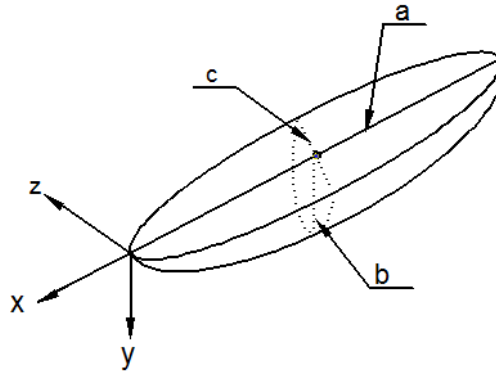


Figure 5-2 Ellipsoidal weld bead with semi-axes a , b and c

For example, along the z direction, it results:

$$q(0,0,c) = q_{max} e^{-Cc^2} = 0.05q_{max} \quad (5.4)$$

which leads to:

$$C = -\frac{\ln(0.05)}{c^2} = \frac{2.996}{c^2} \quad (5.5)$$

The total heat input, Q , is obtained as follows:

$$\begin{aligned}
Q &= \frac{1}{2} \int_{-\infty}^{+\infty} \int_{-\infty}^{+\infty} \int_{-\infty}^{+\infty} q_{max} e^{-Ax^2} e^{-By^2} e^{-Cz^2} dx dy dz = \frac{q_{max} \pi \sqrt{\pi}}{2\sqrt{ABC}} \\
&= \frac{q_{max} abc \pi \sqrt{\pi}}{6\sqrt{3}}
\end{aligned} \tag{5.6}$$

As a result, the power density as a function of position x, y, z is given as:

$$q(x, y, z) = \frac{6\sqrt{3}Q}{abc\pi\sqrt{\pi}} e^{-3x^2/a^2} e^{-3y/b^2} e^{-3z^2/c^2} \tag{5.7}$$

If we now consider the general case where the centre coordinates x_0, y_0 and z_0 of the welding pool are not zero, the general formula is obtained:

$$q(x, y, z) = \frac{6\sqrt{3}Q}{abc\pi\sqrt{\pi}} e^{-3(x-x_0)^2/a^2} e^{-3(y-y_0)^2/b^2} e^{-3(z-z_0)^2/c^2} \tag{5.8}$$

Notice that total heat input can be related to the applied voltage V and current I in the heat torch as follows:

$$Q = VI\mu \tag{5.9}$$

where μ is the welding efficiency.

In some studies (Goldak et al., 1984), a modified double ellipsoidal heat source model is utilised with a slight readjustment of the heat distribution equation according to the circumferential moving whereby the fractions f_f and f_r of the heat deposited in the front and rear quadrants are needed, where $f_f + f_r = 2$. However, this modification is not used in this work because other authors (Fachinotti et al., 2011; Goldak and Akhlaghi, 2006) found a good correlation with experiments taking f_f and f_r equal to 1.

To account for the rotational movement of the welding front along the circumference, the power density can be given as a function of position and time as follows:

$$q(x, y, z, t) = \frac{6Q\sqrt{3}}{abc\pi\sqrt{\pi}} e^{-3(x-(R\sin\theta+x_0))^2/a^2} e^{-3(y-(R\cos\theta+y_0))^2/b^2} e^{-3(z-z_0)^2/c^2} \tag{5.10}$$

where R is the radial distance of the heat torch centre from the pipe axis, θ is the angle that the torch has travelled around the pipe, starting from a starting point where

$\theta = 0$. Denoting by ω the angular velocity used in welding, it results $\theta = \omega(t - t_0)$, where t is the current time and t_0 is the initial time of the analysis.

Equation (5.10) has been implemented in ABAQUS by coding the FORTRAN DFLUX user-subroutine (Dassault Systèmes, 2014). The position of the weld torch is calculated first in DFLUX according to the welding time t . The power density q is then computed at each integration point.

5-3-2. Thermal Properties

A transient heat-transfer analysis is conducted to evaluate the temperature field history during welding. In this case, the energy balance for each domain is governed by the classical energy balance equation given as (Goldak et al., 1984):

$$\rho \frac{\partial H}{\partial t} - \text{div}(\kappa \nabla T) = -q(x, y, z, t) \quad (5.11)$$

where ρ denotes the density of the materials, H is the enthalpy (per unit volume), t is the time, T is the temperature, $\kappa = \kappa(T)$ is the material thermal conductivity, assumed to be isotropic, and $q = q(x, y, z, t)$ is the welding volume heat input (defined earlier in Section 5.3.1).

The specific enthalpy in Eq. (5.11) is defined as:

$$H(T) = \int_{T_{ref}}^T c \, dT + l f_1(T) \quad (5.12)$$

where l and c are the latent heat and heat capacity, respectively, T_{ref} is an arbitrary reference temperature, and $f_1(T)$ is the volumetric liquid fraction known as a characteristic function of temperature, defined as:

$$f_1(T) = \begin{cases} 0 & T < T_{solid} \\ \frac{T - T_{solid}}{T_{liquid} - T_{solid}} & T_{solid} \leq T \leq T_{liquid} \\ 1 & T > T_{liquid} \end{cases} \quad (5.13)$$

where T_{solid} and T_{liquid} are the solidus and liquidus temperatures, respectively.

The second term in Eq. (5.11) represents the flow of heat out of or into the neighbourhood of a particular point according to the isotropic Fourier heat flux constitutive equation:

$$\vec{q} = -\kappa \nabla T \quad (5.14)$$

where \vec{q} is the heat flux vector. In components:

$$q_x = -\kappa \frac{\partial T}{\partial x} \quad q_y = -\kappa \frac{\partial T}{\partial y} \quad q_z = -\kappa \frac{\partial T}{\partial z} \quad (5.15)$$

where q_x , q_y , and q_z are the heat fluxes in the x , y and z directions, respectively. The thermal material parameters, κ , ρ and c , are all temperatures dependant. The initial condition to Eq. (5.11) is in our case given by:

$$T(x, y, z, 0) = T_0 \quad (5.16)$$

where T_0 is the initial temperature of the pipe, that with a good approximation can be taken as constant in space and equal to the ambient temperature.

The boundary conditions on the outer and inner surfaces are given by:

$$k \frac{\partial T}{\partial x} n_x + k \frac{\partial T}{\partial y} n_y + k \frac{\partial T}{\partial z} n_z + h(T)(T - T_{amb}) = 0 \quad (5.17)$$

where n_x , n_y and n_z are the direction cosines of the normal to the boundary, $h(T)$ is the heat-transfer coefficient, that is defined as a function of temperature as discussed below, T is the current temperature at the pipe surface, whereas T_{amb} is the ambient temperature.

Since we exploit the symmetry of the problem, we need to enforce on the plane of symmetry that the heat flux is zero, which leads to this other boundary condition on this plane:

$$k \frac{\partial T}{\partial x} n_x + k \frac{\partial T}{\partial y} n_y + k \frac{\partial T}{\partial z} n_z = 0 \quad (5.18)$$

In this work, both radiation and convection are taken into account for the boundary conditions during the thermal analysis. During a thermal cycle, radiation and convection take place from all the surfaces exposed to the environment. In particular, radiation heat losses are dominant in and nearby the weld pool whereas convection heat losses are dominant at lower temperatures away from the weld pool (Akbari and Sattari-Far, 2009). As there are two different base materials, two heat transfer coefficients are considered. Each heat coefficient includes a combination of

convection and radiation effects. For the carbon steel surfaces, the total heat transfer coefficient can be written as (Lee et al., 2013):

$$h_{carbon} = h_{con} + \varepsilon_{em}\sigma_{bol}(T + T_{amb})(T^2 + T_{amb}^2) \quad (5.19)$$

where h_{con} is the convective heat transfer coefficient, ε_{em} is the effective radiation emissivity, T is the current temperature at the pipe whereas T_{amb} is the ambient temperature, and σ_{bol} is the Boltzman constant. Following (Malik et al., 2008), in the present study, the convective heat transfer coefficient h_{con} is assumed to be 8 W/m²°C whereas the emissivity ε_{em} is set to be 0.51.

For the stainless steel surfaces, we used the following widely used bilinear law [5]:

$$h_{stainless} = \begin{cases} 0.0668T & \left(\frac{W}{m^2}\right) & 0 < T < 500^\circ C \\ 0.231T - 82.1 & \left(\frac{W}{m^2}\right) & T > 500^\circ C \end{cases} \quad (5.20)$$

because for this material it is a good approximation of the actual cubic expression that would be obtained using Equation (5.20) for typical values of the emissivity of stainless steel of 0.5-0.75 and a range of temperature between ambient and 2400°C.

A FILM user subroutine (Dassault Systèmes, 2014) was used to implement the above expressions of the heat-transfer coefficient in ABAQUS. It is worth noting that ABAQUS allows one single user-subroutine to be written for both materials by simply specifying which surface each condition applies to.

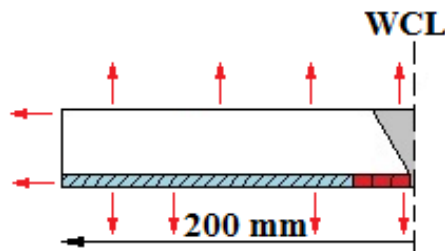


Figure 5-3 Effect of radiation and convection in Lined pipe

As can be seen from Figure 5-3, the radiation and convection take place from all sides of the welded lined pipe exposed to the environment except the area at which the heat flux is applied (Akbari and Sattari-Far, 2009).

To account for material melting and for the heat transfer due to the fluid flow in the weld pool, two methodologies are used (Deng and Murakawa, 2006). A significant increase in the thermal conductivity is assumed above the melting point relatively to that at room temperature. The latent heat is taken into consideration in the thermal effects due to solidification of the weld pool. The latent heat is typically the heat energy that the system stores and releases during the phase transformation.

5-4. Validation

In order to validate the FE procedure for the girth welding, the approach outlined above is used to simulate the problem studied by Karlsson and Josefson (1990), and our numerical results are compared with the experimental ones reported in (Karlsson and Josefson, 1990). The pipe studied has an outer diameter of 114.3 mm and a wall thickness of 8.8 mm, with a 5.5mm-deep V-groove for welding, and the pipe material is C-Mn steel (Swedish standard steel SIS2172). The welding material is MIG (Metal Inert Gas) deposited from the outside into the groove in a single pass with a speed equal to 6 mm/s as shown in Figure 5-4.

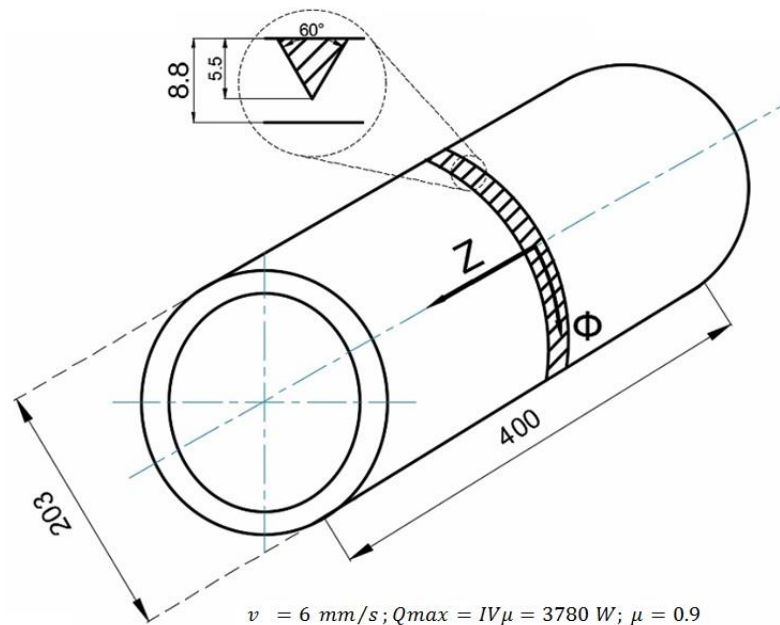


Figure 5-4 Karlsson and Josefson FE model, dimensions in mm (Karlsson and Josefson, 1990)

Our numerical results of the thermal and mechanical analyses have been compared with the experimental measurements at various axial locations, where the

circumferential angle θ from the welding start/stop position is 150° . In the thermal analysis, those points are located on the outer and inner surfaces with respect to the weld centreline CL. It can be seen from the plot shown in Figure 5-5(a) that the thermal simulation results correlate well with the experimental red contour lines. In the mechanical analysis, the residual stress distributions at 150° from start/stop welding location on the inner surface along the axial direction correlate also well with those obtained by the validated experiment performed by Karlsson and Josefson (1990) as shown in Figure 5-5(b).

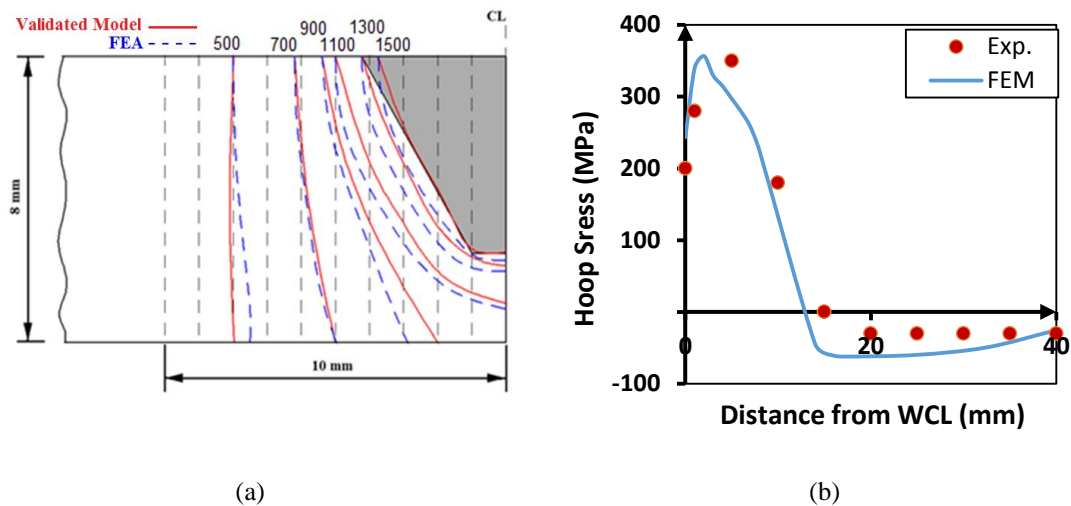


Figure 5-5 Distributions of (a) temperatures ($^\circ\text{C}$) (b) Inner hoop residual stress at $\theta=150^\circ$ numerically computed in this work and experimentally validated in (Karlsson and Josefson, 1990)

In a similar way, to validate the weld overlay FEA approach, the experiment conducted by Deng and Murakawa (2006) has been simulated. The material used in this work was stainless steel (SUS304) and the pipe model has a 114.3 mm outer diameter and 6 mm thickness. Gas Tungsten Arc (GTA) welding was used in the experiments to fill a U-groove by two welding passes with 80 mm/min as welding speed as shown in Figure 5-6.

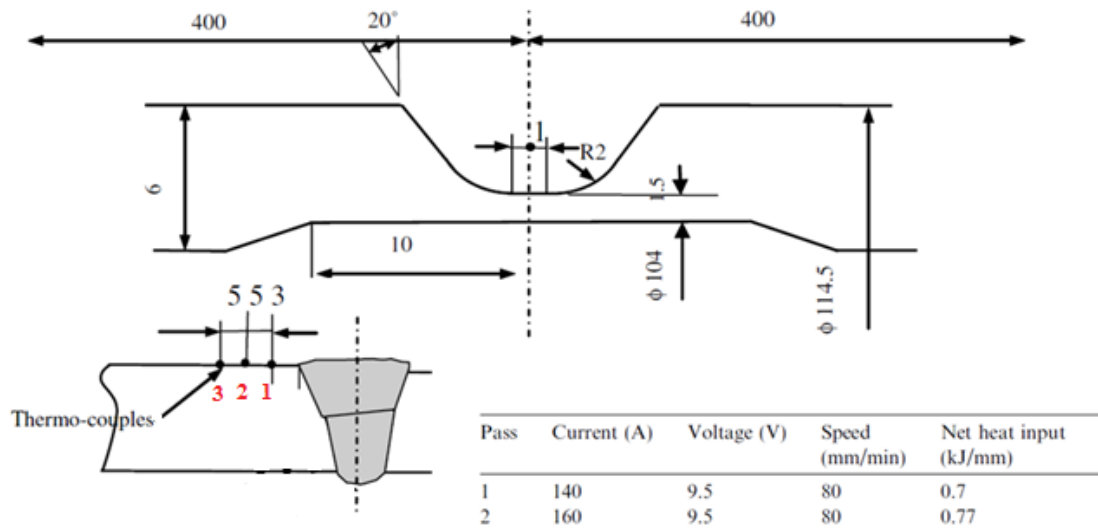


Figure 5-6 Deng and Murakawa experiment, dimensions in mm (Deng and Murakawa, 2006)

The thermal history findings have been numerically compared with their experimental counterparts at three axial locations, points 1, 2 and 3 as shown in Figure 5-6. These points are placed on the outer surface with respect to the axial distance from the weld centre line where the circumferential angle ϕ from the start/stop position is 180° . Figure 5-7(a) shows there is a good match between our thermal FEA results and the experimental ones obtained from (Deng and Murakawa, 2006). Moreover, Figure 5-7(b) shows a good correlation between the results of the hoop residual stresses along the axial distance on the inner surface which are taken from our FE mechanical model and the experimental results in (Deng and Murakawa, 2006) where the angular location θ from the welding start/stop point is 180° .

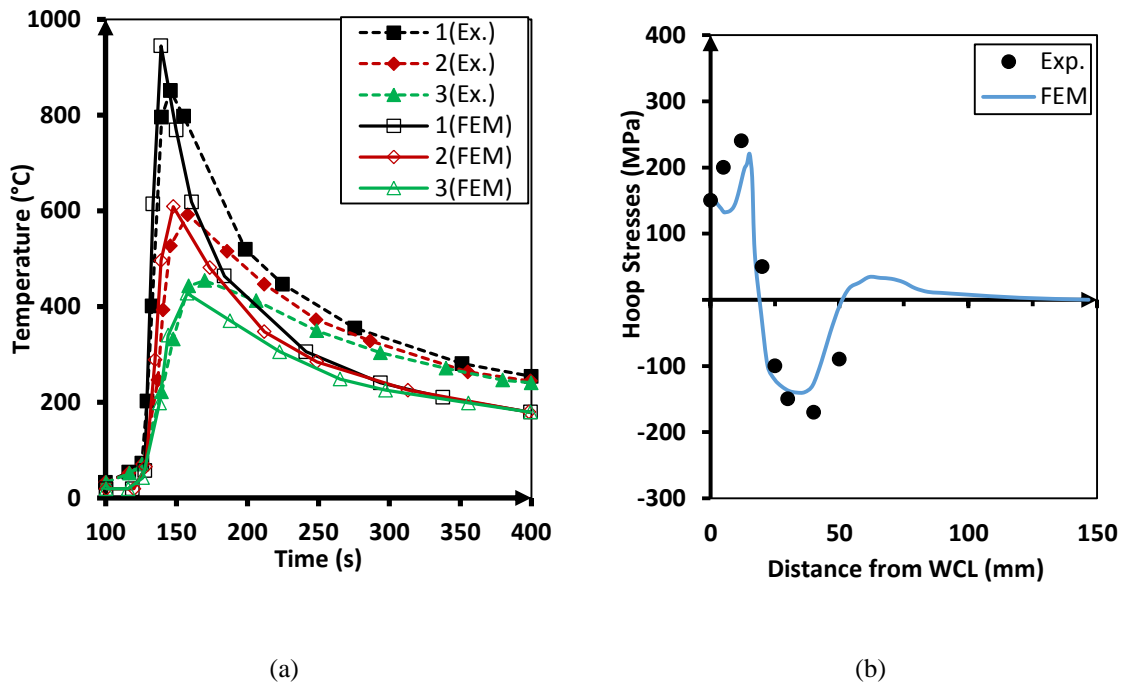


Figure 5-7 Comparison of (a) thermal histories (°C) and (b) Inner hoop residual stresses at $\theta=180^\circ$ numerically computed in this work and experimentally validated in (Deng and Murakawa, 2006)

5-5. Finite Element Modelling of the Lined Pipe

5-5-1. Description of the Lined Pipe Joint and Welding Conditions

Using ABAQUS (Dassault Systèmes, 2014), the FE computational procedure described in Section 5.3, and validated in Section 5.4 for the separate cases of a carbon-steel pipe and a stainless-steel pipe, has been implemented to calculate the transient temperature field and residual stresses during welding of two segments of a lined pipe, in which a one-pass weld overlay and a one-pass butt-welded joints are used. The configuration of the lined-pipe joint has an outer diameter of 114.3 mm and a wall thickness of 6 mm, of which 4.5 mm is the thickness of the C-Mn outer pipe and 1.5 mm is the liner thickness, as schematically shown in Figure 5-8. Only one-half of the pipe, which is 200 mm long, is analyzed due to symmetry around the weld line.

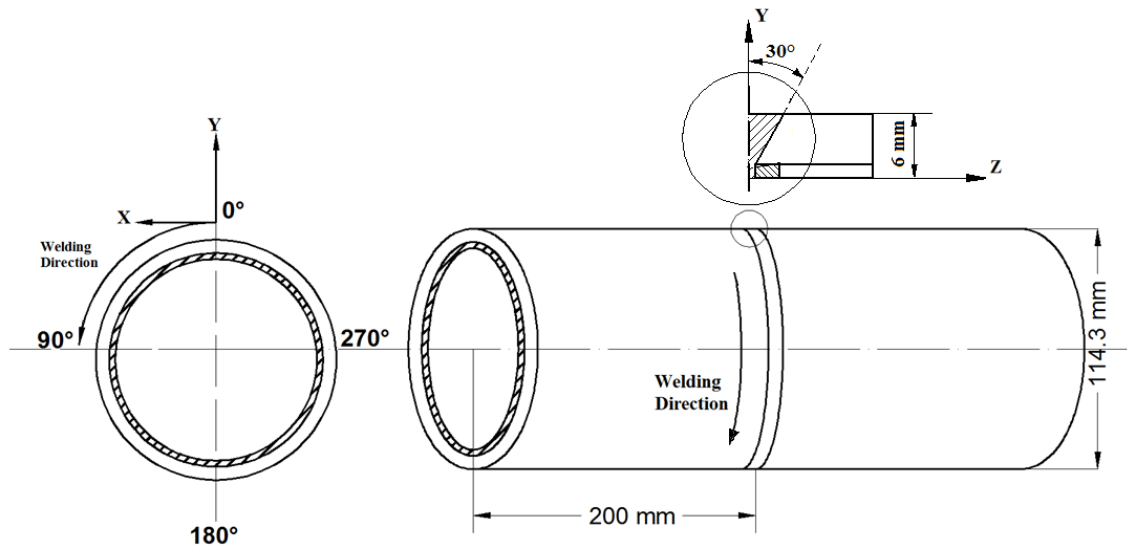


Figure 5-8 Dimensions of analysis model

The outer pipe material is C-Mn steel with a composition of 0.18% C, 1.3% Mn, 0.3% Si, 0.3% Cr, 0.4% Cu (Swedish standard steel SIS2172) and the temperature-dependent thermo-mechanical material properties, namely density, specific heat, latent temperature, thermal expansion, yield stress, Young's modulus and conductivity used for the outer pipe are taken from the work of Karlsson and Josefson (1990) as reported in Table 5-1. The thermo-mechanical properties for the SUS304 SS liner are obtained from the study of Deng and Murakawa (2006) as shown in Table 5-2. Moreover, the MIG-welding is implemented for girth weld whilst the GTA-welding process is used in filling the weld overlay groove. In absence of specific data, we follow (Deng and Murakawa, 2006; Karlsson and Josefson, 1990) so that base metals and weld metals are defined as different materials in ABAQUS-code but having the same thermo-mechanical properties corresponding to their base materials except the yield stress, as illustrated in Table 5-1 and Table 5-2. This is an approximation of reality that in some cases may be inaccurate, but in this work we are using the cases studied in (Deng and Murakawa, 2006; Karlsson and Josefson, 1990) for the two different materials as a way of validating the separate models, and therefore we follow these articles in this simplified assumption and also when analysing the lined pipe.

Table 5-1 Thermo-mechanical properties of C-Mn (Karlsson and Josefson, 1990)

Temperature (°C)	Density (Kg/m ³)	Specific heat (J/Kg°C)	Conductivity (W/m°C)	Thermal expansion (x10 ⁻⁵ °C ⁻¹)	Yield stress (MPa)		Young's modulus (GPa)	Poisson's ratio
					Base	Weld		
0	7860	444	50	1.28	349.45	445.42	210	0.26
100		480	48.5	1.28	331.14	441.29	200	0.28
200		503	47.5	1.30	308.00	416.49	200	0.29
300		518	45	1.36	275.00	376.18	200	0.31
400		555	40	1.40	233.00	325.54	170	0.32
600		592	35	1.52	119.00	172.59	56	0.36
800		695	27.5	1.56	60.00	43.41	30	0.41
1000		700	27	1.56	13.00	14.47	10	0.42
1200		700	27.5	1.56	8.00	9.30	10	0.42
1400		700	35	1.56	8.00	9.30	10	0.42
1600		700	122.5	1.56	8.00	9.30	10	0.42

Table 5-2 Thermo-mechanical properties of SUS304 (Deng and Murakawa, 2006)

Temperature (°C)	Density (kg/m ³)	Specific heat (J/kg°C)	Conductivity (W/m°C)	Thermal expansion (x10 ⁻⁵ °C ⁻¹)	Yield stress (MPa)		Young's modulus (GPa)	Poisson's ratio
					Base	Weld		
0	7900	462	14.6	1.70	265	438.37	198.50	0.294
100	7880	496	15.1	1.74	218	401.96	193	0.295
200	7830	512	16.1	1.80	186	381.5	185	0.301
300	7790	525	17.9	1.86	170	361.25	176	0.310
400	7750	540	18.0	1.91	155	345.94	167	0.318
600	7660	577	20.8	1.96	149	255.71	159	0.326
800	7560	604	23.9	2.02	91	97.41	151	0.333
1200	7370	676	32.2	2.07	25	28.41	60	0.339
1300	7320	692	33.7	2.11	21	16.23	20.00	0.342
1500	7320	700	120	2.16	10	12.17	10	0.388

The numerical values for the variables in the power density distribution Eqs. (5.9) and (5.10) are illustrated in Table 5-3 for each welding materials.

Table 5-3 Heat source parameters and welding parameters.

		SUS304	C-Mn (SIS2172)
Half-length of arc (mm)	a	2.765	3.26
Depth of arc (mm)	b	2.575	3.2
Half-width of arc (mm)	c	1.5	3
Welding current (A)	I	120	170
Voltage (V)	V	8	20
Welding speed (mm/s)	v	1.33	6.25
Welding efficiency	μ	70%; Gas Tungsten Arc (GTA)	85%; MIG (Metal Inert Gas)

Based on the heat torch parameters presented in Table 5-3, the power density distributions of Goldak double ellipsoidal heat source along the welding directions for SUS304 and C-Mn (SIS2172) are depicted in Figure 5-9.

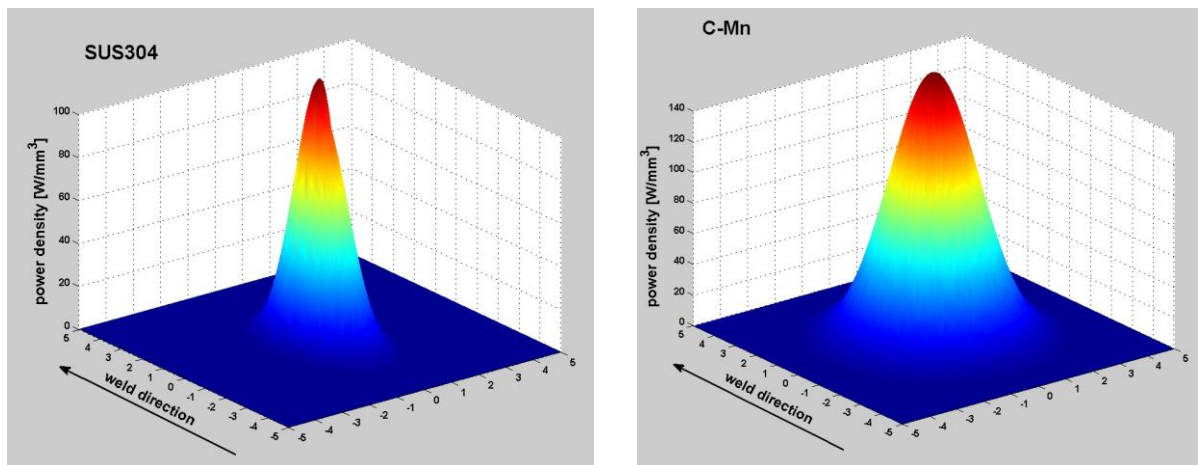


Figure 5-9 Power density distributions of Goldak ellipsoidal heat source models, liner and carbon steel

The latent heat for C-Mn steel (SIS2172) is set to be 247kJ/kg between the solidus temperature 1440 °C and the liquidus temperature 1560 °C. For stainless steel (SUS304), the latent heat is assumed to be 260kJ/kg between 1340 °C and 1390 °C, solidus and liquidus temperature, respectively. Consequently, the melting point for carbon steel is 1500 °C while it is 1365 °C for SUS304. The initial temperature of the lined pipe and the weld bead is set at room temperature, namely 20 °C.

5-5-2. Finite Element Mesh

Only one half of the lined joint is modelled due to symmetry. The three-dimensional FE model contains a total of 51840 nodes associated with 10560 elements. Among these, 17400 nodes and 2400 elements represent the liner geometry whereas the remaining of 51840 nodes and 10560 elements represent the backing pipe geometry.

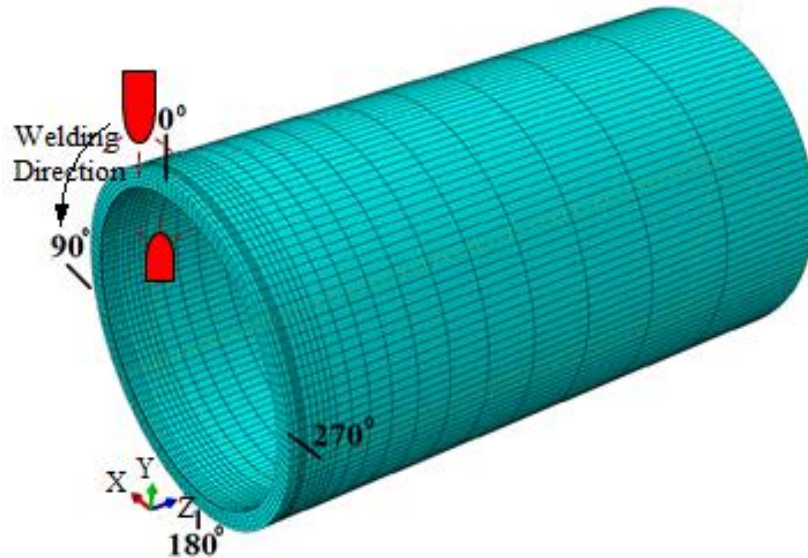


Figure 5-10 Three-Dimensional FEM

A fine mesh has been used in the fusion zone (FZ), the zone where the temperature reaches values beyond the melting point, and its vicinity, i.e. in the heat affected zone (HAZ), because of the higher temperature and flux gradients. The element size increases with the distance from the welding centreline (WCL) for both the C-Mn pipe and the liner. The number of divisions in the circumferential direction is 120. Furthermore, there are 4 layers of elements through the thickness direction, three of them for the C-Mn pipe and one for the liner as shown in Figure 5-10.

Uncoupled thermo-mechanical analyses have been developed to simulate the welding. Therefore, the thermal analysis is simulated first to acquire the thermal history at each node through the lined pipe. This thermal history is then transferred to the mechanical analysis as an input to determine the temperature-dependent mechanical properties. In this case, the FE mesh of the mechanical analysis should have the same mesh associated with the same arrangement of nodes and elements

used in the thermal analysis. In the thermal analysis, 20-node quadratic hexahedral heat-transfer elements, named DC3D20 in ABAQUS, have been employed. In the mechanical analysis, 20-node reduced integration elements, named C3D20R in ABAQUS, are employed to minimise the simulation time.

5-5-3. Thermal Analysis

5-5-3-1. Moving of Filler Metal

A moving heat source combined with the element-birth technique is used to simulate the deposition of the elements of weld bead incrementally. In other words, to represent the transient nature of weld metal deposition (Yaghi et al., 2011), a number of element sets is created, so that the elements forming each weld bead belong to a specific set. In this way each bead in a weld pass can be deposited independently during simulation. At the beginning of the thermal simulation, the element sets of both weld passes are made ‘inactive’ by assigning very low conductivity to them. The deposition of each bead is then modelled using a sequence of ‘steps’. In each step, the element set that is in the current position just reached by the weld torch is re-activated in the FE mesh. The sequential steps of the developed procedure to simulate the welding are described in Table 5-4.

Table 5-4 Simulation procedure

Step(s)	Initial step time (s)	Final step time (s)	Description
1	0	1×10^{-10}	All of the weld passes' elements, SUS304 and C-Mn, are deactivated.
2	1×10^{-10}	2×10^{-10}	The first section of the weld overly pass is added.
3	2×10^{-10}	2.067	The heat source begins to move, applying the heat flux corresponding to liner heat flux equation.
4	2.067	$2.067 + 10^{-10}$	The second bead of the liner weld pass is added.
5	2.067	4.133	The heat source continues its motion.

6-241	4.133	248	Steps 4-5 are repeated adding new sections of the weld overlay pass and applying the liner heat flux.
242	248	518	The torch is removed and the two pipes cool down until the maximum temperature is below 100°C.
243	518	518+10 ⁻¹⁰	The first section of the girth welding pass is added.
244	518	518.479	The heat source moves, applying heat flux corresponding to carbon-steel heat flux equation.
245- 482	518.479	575.5	Steps 243-244 are repeated adding new sections of the C-Mn welding pass and then applying girth welding heat flux.
483	575.5	3575.5	The torch is removed and the two pipes cool down almost to room temperature

5-5-3-2. Conditions of the Thermal Analysis

For an optimally designed welding process, the results provided by the thermal FE analysis should satisfy the following three conditions:

- 1- All integration points in target FZ should reach at least the melting temperature. This guarantees that the FZ melts entirely before cooling down.
- 2- Because welding parameters such as current, voltage, speed and welding pool geometries have constant magnitudes during welding, the temperature history for every node located on the same circumferential line should be close to identical after a relatively short initial transient part of the analysis, except for a time shift.
- 3- The boundary of the HAZ should remain about 2-3 mm from the FZ boundary whereby the net heat input plays a crucial role. The problem is that, even for the cases where weld specifications exist in codes of practices such as API 1104, EN ISO 15609, ASME IX, the data in terms of current, voltage and welding speed are generally given with such wide limits that the net heat input can easily vary by a factor of 4 and still be inside the allowed limits for welding process (Brickstad and Josefson, 1998).

Brickstad and Josefson (1998), who studied a case where the material is stainless steel, and Karlsson and Josefson (1990), who considered carbon steel, found out the typical boundary of the HAZ is located approximately 2-3 mm from the FZ boundary where the temperature is between 800-900°C.

5-5-4. Mechanical Analysis

In the mechanical analysis, body forces and surface tractions are assumed to be neglected according to the definition of residual stresses which are the self-equilibrating internal stresses (Deus and Vilar, 1996; Noyan et al., 1995).

The only load considered in the structural model is the load generated by the transient thermal field at each node during the thermal analysis. This induces non-uniform thermal strain through the entire lined pipe because: a) two base materials with their welding materials have accordingly different coefficients of thermal expansion, b) the initial temperatures of welding and its base material are different and c) high temperature gradients.

Furthermore, the symmetry plane is constrained, which has an effect on the mechanical strain. In general, the total strain is composed of three components given as:

$$\varepsilon_{kl} = \varepsilon_{kl}^{el} + \varepsilon_{kl}^{pl} + \varepsilon_{kl}^{th} \quad (5.21)$$

where the three components on the right hand side of Eq. (21) refers to elastic, plastic and thermal strains, respectively. The mechanical strain is the sum of the elastic and plastic strains.

Isotropic linear elasticity has been assumed with temperature-dependent Young's modulus and Poisson's ratio. To obtain the thermal strain field, isotropic thermal expansion is assumed with a temperature-dependent expansion coefficient. To get the plastic strain, the Von Mises yield criterion with an associate flow rule and linear kinematic hardening rule have been used. Kinematic hardening is assumed to consider the thermal loading and unloading during welding. Yield stress and Young's modulus decrease exponentially with increasing temperature to be near zero as temperature approaches melting point. Therefore, the filler material flows through welding groove with almost free stress and strain. Figure 5-11 illustrates the

temperature-dependant yield stress as the plastic strain of C-Mn and SUS304 is equal to 1% (Deng et al., 2008; Malik et al., 2008).

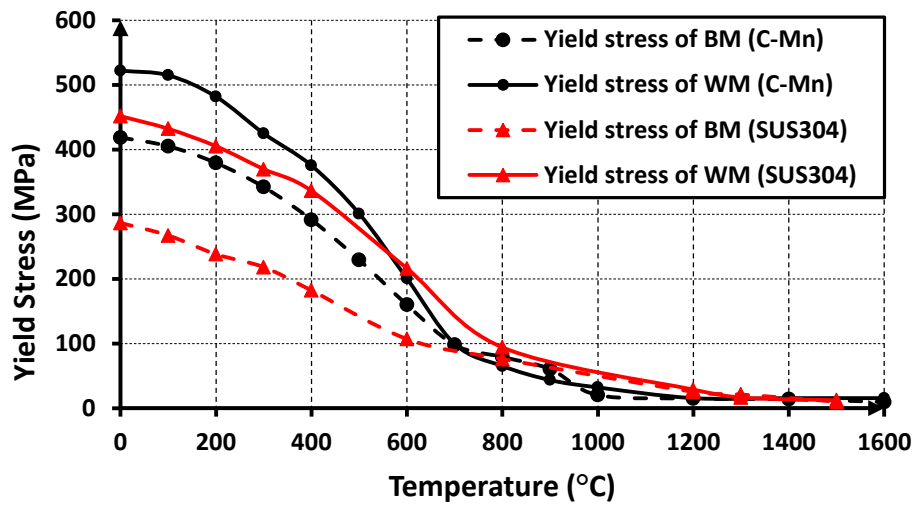


Figure 5-11 Yield strength of C-Mn steel and SUS304 corresponding to 1% hardening (Deng et al., 2008; Malik et al., 2008)

5-6. Results of the Thermal Analysis

The thermal cycles due to welding induce metallurgical changes in the FZ and HAZ. These changes influence the final microstructure of the welded pipe and, therefore, the resistance of the pipe to creep and fracture during service (Yaghi et al., 2011). Furthermore, the HAZ is the most vulnerable part of the pipe because of the accumulation of creep damage at the inter-critical zone near the boundary of the HAZ where the peak temperature is 800-900°C, at which the austenitic transformation happens. As a rule, the HAZ extends up to approximately 2-3 mm from the FZ edge. Consequently, the peak temperatures on the integration points throughout the FE model can be related to the final mechanical and material features, such as residual stresses or phase transformations in the FZ or HAZ. For that reason, the peak temperatures predicted by the FE model are the key output of this analysis and are indicated in Figure 5-12 to show the transient temperature distributions during the welding process for the liner and the carbon steel backing. The maximum temperature, which definitely exceeds the melting point, is attained in the middle of the welding pool coloured in light grey in Figure 5-12. The region located in the

middle of welding pool is the last one eligible to cool down from the melting temperature because there is no direct contact with the air or other external surfaces.

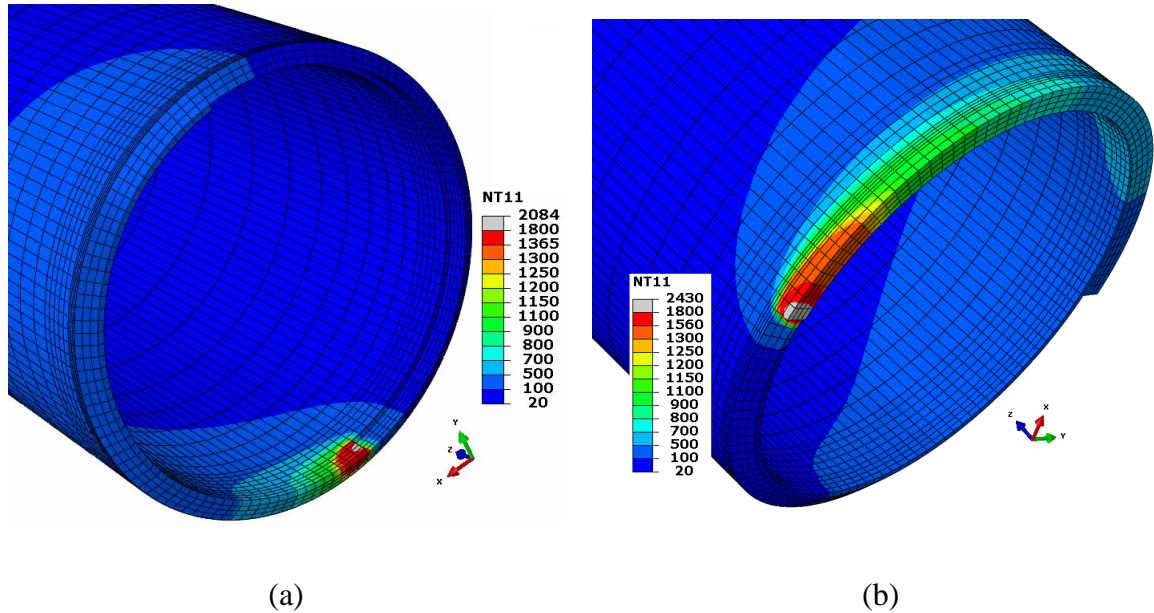


Figure 5-12 Maximum temperatures in (a) weld overlay and (b) girth welding (°C)

5-6-1. Thermal History during the Weld Overlay

The thermal history profiles were predicted at 6 locations along the axial direction. Points T1, T2 and T3 are located on the CRA liner and T4, T5 and T6 are located on backing steel, as sketched in Figure 5-13. For each of these locations, a number of points at different circumferential angles were considered.

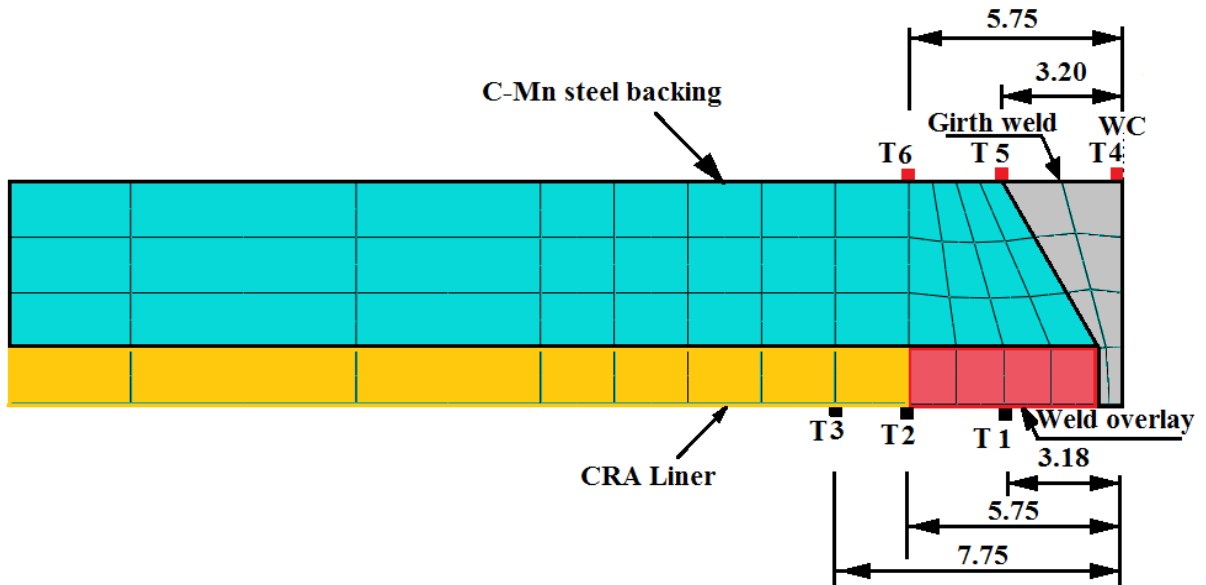


Figure 5-13 Schematic illustration showing temperature measurement positions on axial direction (mm)

Figure 5-14 shows the temperature history for points T1, T2 and T3, at three different circumferential angles 90° , 180° and 270° from the start/stop position. The plots represent the change in temperature as a function of time. As expected, the temperatures start out at the ambient temperature of 20°C . Once the heat source reaches the particular point, the temperature rises very rapidly, especially at point 1 because it is located upon the WCL of weld overlay welding where the torch is moving. The temperature at point T1 reaches a maximum peak temperature of 2084°C as a balance between the flux and the heat losses. It can be seen that the peak temperature stays on the point at a single time instant, due to the constant velocity of the heat source. Once the heat source has passed point T1, a rapid drop in the temperature occurs.

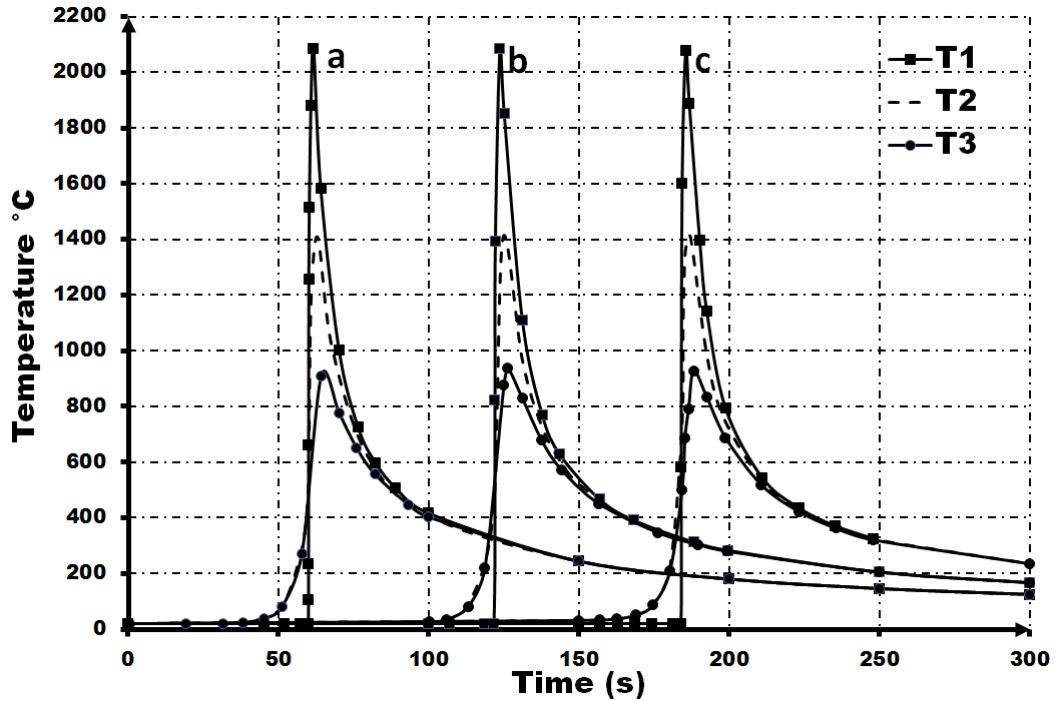


Figure 5-14 Temperature histories during weld overlay at (a) 90°, (b) 180° and (c) 270°

The peak temperature at point 2, located on the FZ boundary of the SUS304 welding, reaches 1405°C which is higher than the melting point of SUS304, 1365°C. As pointed out earlier, Brickstad and Josefson (1998) proved that an optimal power should lead to an extension for the HAZ of up to approximately 2-3 mm from the FZ boundary, where the temperature reaches 800-900°C. In our work, point 3 is located after 2 mm from the FZ boundary where the maximum temperature at this point is around 910°C. In other words, the thermal history predicted by our FE model has met this optimal condition.

The combination effect of incorporating radiation and convection into the heat transfer on the inner and outer surfaces justifies the rapid drop in the temperature in the FZ during cooling where the radiation is the dominant mechanism of heat loss. Away from the weld, heat transfer is dominated by convection into remote regions of the base pipe.

The temperature history and peak temperature obtained at three different circumferential angles of 90°, 180° and 270° from the start/stop position during weld overlay for the previous axial points are practically identical. This shows that steady state, defined here as the condition of self-similar moving of the temperature field, is well established before a circumferential angle of 90° is reached.

5-6-2. Thermal History during Girth Welding

Once the overlay weld is terminated, the whole lined pipe cools down for 270 seconds to reduce the maximum pipe temperature to just below 100°C , which is called inter-pass temperature (Brickstad and Josefson, 1998). The thermal history of three different axial points located at the top surface of the C-Mn backing steel is illustrated in Figure 5-15. Point T4 is placed on the WCL of the girth welding where the heat source is applied. Consequently, the maximum temperature, 2430°C , on the outer pipe is attained at point T4. To check the fluidity is complete in the V-groove, all the integration points there should reach the melting point of SIS2172 which is 1500°C . Point T5, on the FZ boundary is the outmost point from the WCL, 3.2 mm, where the maximum temperature is 1550°C . About 2.55 mm away from the FZ boundary, the temperature has reached 953°C at point T6.

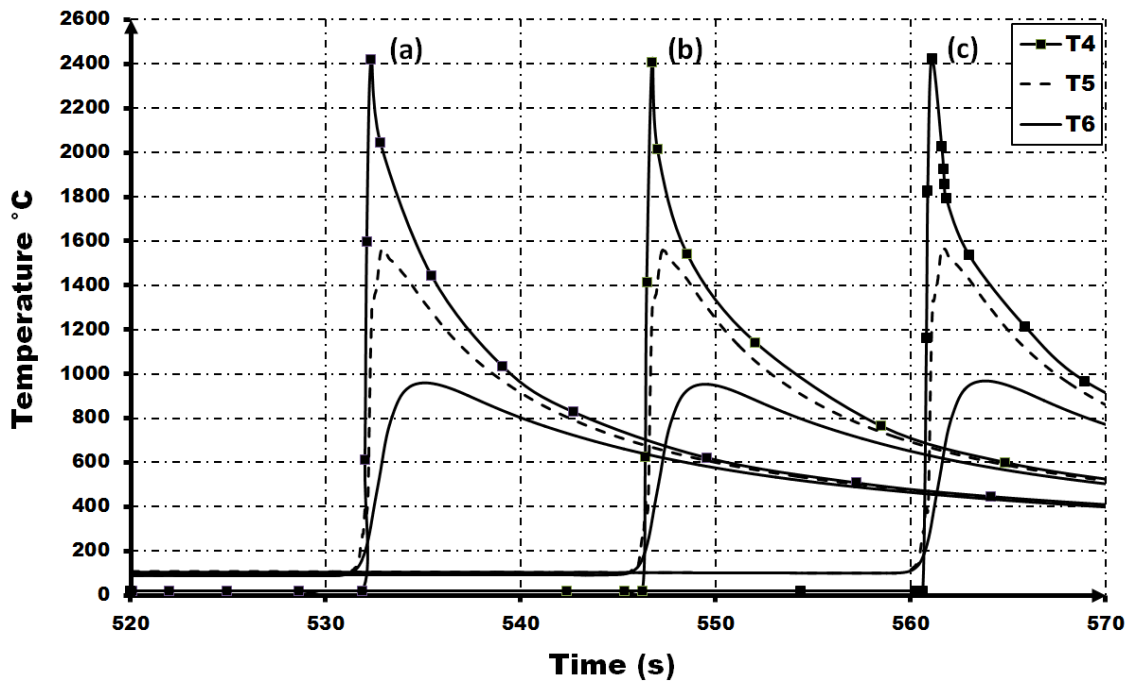


Figure 5-15 Temperature histories during girth welding at (a) 90° , (b) 180° and (c) 270°

Again the curves in Figure 5-15 relative to points at the same axial distance and different circumferential angles are almost identical, showing that steady state is well established during moving the heat source around the pipe. The thermal results reported above for points T1-T6 belong to a typical case, which will be referred to as case A (basic case) in the next section.

5-7. Effect of Welding Factors

In general, the welding parameters play a decisive role in the weld pass quality and affect the total shrinkage. In turn, this affects residual stresses and, ultimately, the probability of crack occurrence (Aloraier et al., 2012). Therefore, it is important to investigate the influence of two important different welding parameters, interval time and welding speed, thermally and mechanically.

5-7-1. Effect of Welding Factors on Thermal History

5-7-1-1. Effect of Interval Time on Thermal History

As discussed in Section 5.6.2., an interval time is needed between the welding passes to reduce the maximum temperature to an appropriate value, which is called inter-pass temperature. Depending on the type of steel, the weld specifications normally specify the allowable range for the inter-pass temperature between 100-180°C. A lower inter-pass than this range does not have a considerable effect on residual stresses (Brickstad and Josefson, 1998). An inter-pass temperature over 250-300°C can lead to excessive increase in residual stresses.

In case A, the lined pipe was allowed to cool down to around 100°C after the weld overlay and before starting the girth weld as shown in Figure 5-16. As can be seen from Figure 5-16, the thermal history distributions for all points except point T4, because not deposited yet, drop down sharply from their peak temperatures accordingly because of cooling down to reach the final inter-pass temperature of 100°C in before all curves rapidly rise up once the girth welding torch reaches the prescribed bead. For example, the temperature at point T5 drops from 1118°C to 100°C before rising up very rapidly to 1550°C again.

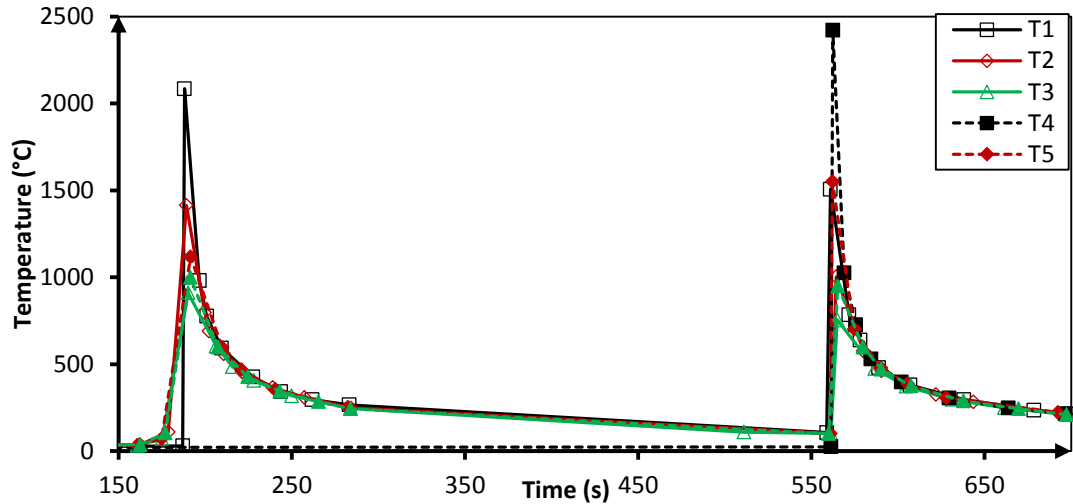


Figure 5-16 Thermal history at 270° with 270 seconds interval time (248-518 s) in case A.

The result of changing the interval time is that, the less interval time is applied, the higher temperature is obtained, as expected. In particular, reducing the interval time to 1 second (case B) increases the minimum interval temperature to 244°C. At point T1, the maximum temperature during the girth welding increases somewhat from 1500°C in case A to 1545°C in case B as shown in Figure 5-17. In the same way, the thermal history at point T5 during interval cooling also drops to 244°C before rapidly heading up to 1615°C.

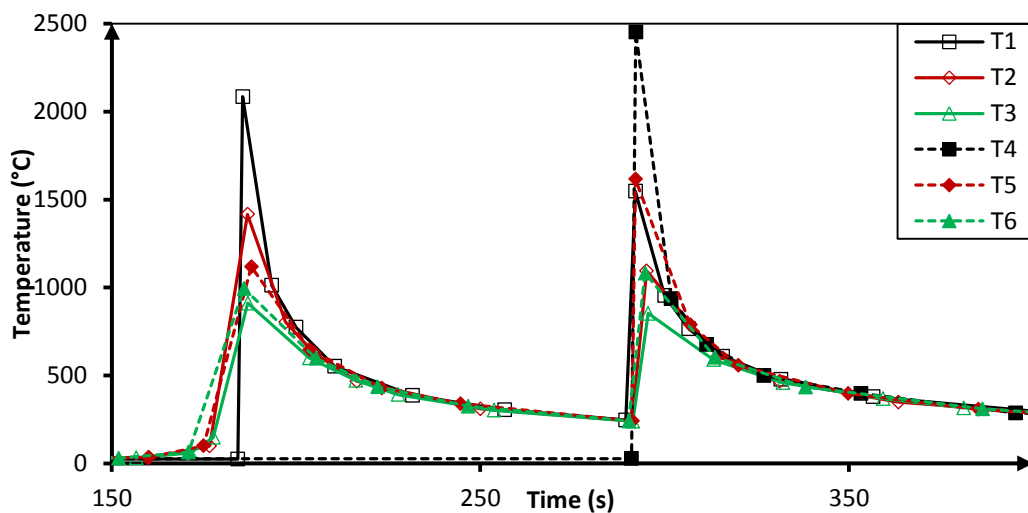


Figure 5-17 Thermal history at 270° with 1 second interval time (248-249 s) in case B.

5-7-1-2. Effect of Welding Speed on Thermal History

Welding speed plays a decisive role in determining the quality of weld but there is also a wide range of possible speeds that can be used (Brickstad and Josefson, 1998; Holloway et al., 2008). Hence, two extra cases have been discussed by doubling (case C) and halving (case D) the welding speed, whereas the other parameters are kept equal to those in Table 5-3 associated with the same interval time, 270 s, in both cases.

In the first case, case C, the overlay and girth welding speeds are doubled to 2.66 and 12.5 mm/s, respectively. At point T2 at 270° from start/stop position, the maximum temperature during overlay welding drops to a value lower than the melting point of C-Mn to reach 1046°C before heading down to 77°C during interval cooling. Likewise, the peak temperature reaches 902°C at point T5 during girth welding which is lower than the melting point for C-Mn as shown in Figure 5-18.

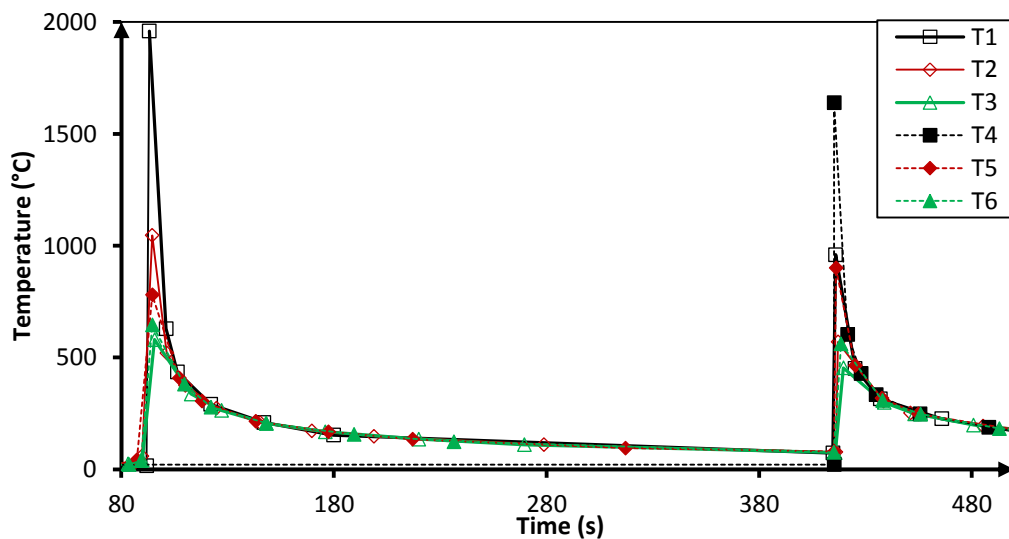


Figure 5-18 Thermal history for a doubled welding speed, case C

In the second case, case D, the welding speeds are halved to 0.665 and 3.125 mm/s during overlay and girth welding, respectively. As expected, the temperature is beyond the melting point of SUS304 and C-Mn in point T2 and T5 to be 1540°C and 1961°C as shown in Figure 5-19, respectively.

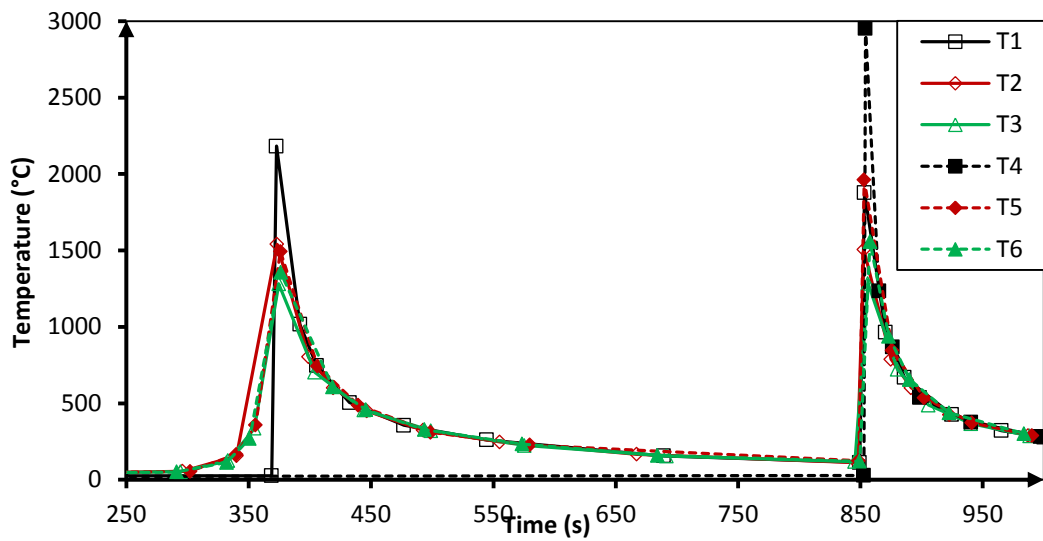


Figure 5-19 Thermal history with respect to reduce the speed to half , case D

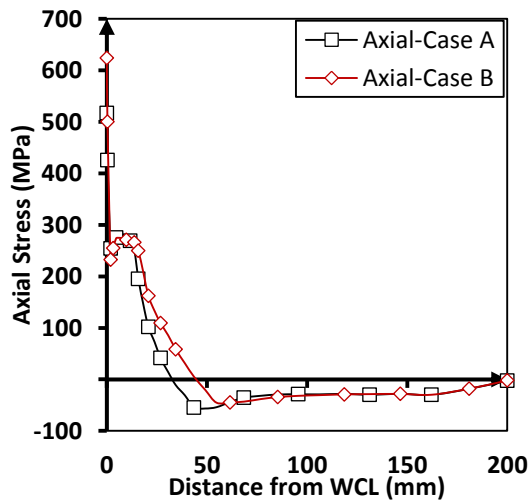
5-7-2. Effect of Welding Factors on Residual Stresses

5-7-2-1. Effect of Interval Time on Residual Stresses

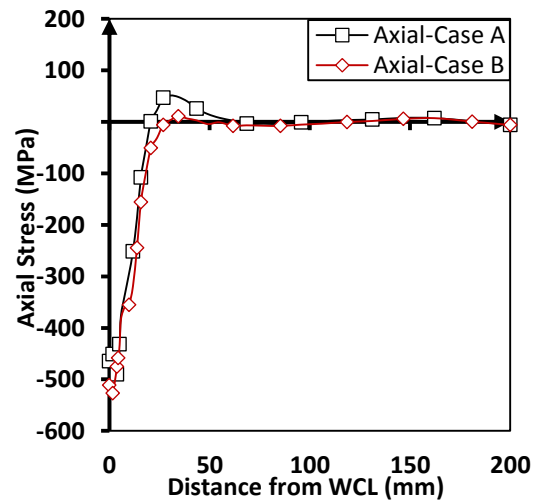
The influence of reducing the interval time to 1 second on the residual stresses has been discussed herein. Figure 5-20(a)-(d) compares the simulated axial and hoop residual stress results on the inner and outer surface at 270° central angle in case A (basic case) and case B (1 second interval time).

On the inner surface, Figure 5-20(a) shows the axial residual stresses along the longitudinal distance starting from the WCL. It is observed that case B is characterised by a larger value of the axial stress on the WCL than its counterpart in case A, namely 624 and 517 MPa, respectively. Furthermore, the extent of the tensile-stress zone in case A is narrower than that in case B, namely 34.6 and 43.5 mm, respectively. Likewise, the maximum hoop residual stress is located at the centreline of the weld overlay, $Z=1.89$ mm, whereas case B is characterised by a somewhat larger tensile stress relatively to case A, namely 277 and 275 MPa, respectively. Starting from the WCL, the extent of the tensile-stress in case B is larger than in case A, namely 49.16 and 39 mm, respectively, as shown in Figure 5-20(b).

On the outer surface, the axial residual stresses are compressive in the FZ and HAZ, whereas the maximum magnitude of compressive stress is located at the WCL for both cases as depicted in Figure 5-20(c). The maximum compressive stress in case B is larger than its counterpart in case A, namely -511 and -464 MPa, respectively. Moreover, case B is characterised by a slightly larger extent of the compressive-stress zone than case A, namely 26.9 and 20.75 mm, respectively. Returning to the hoop stress on the outer surface, in both cases the stress distributions have a waved shape, whereas case A is characterised to some extent by larger absolute residual stress values than in case B along the longitudinal distance, as portrayed in Figure 5-20(d).



(a)



(c)

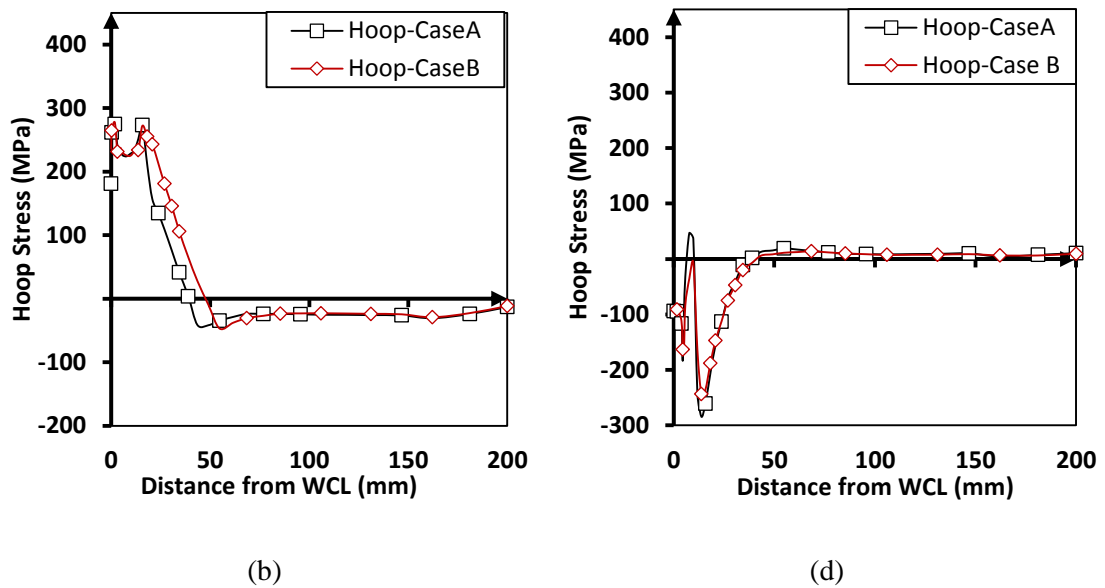


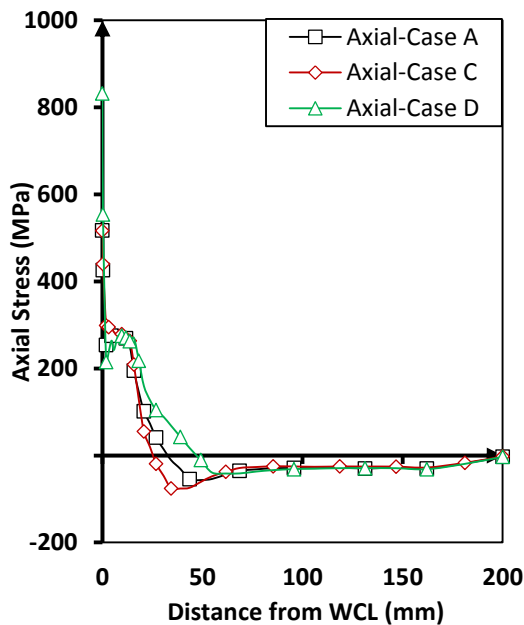
Figure 5-20 Comparison of residual stresses at 270° central angle in case A and case B: (a) axial stress distributions on the inner surface, (b) hoop stress distributions on the inner surface, (c) axial stress distributions on the outer surface and (d) hoop stress distributions on the outer surface

5-7-2-2. Effect of Welding Speed on Residual Stresses

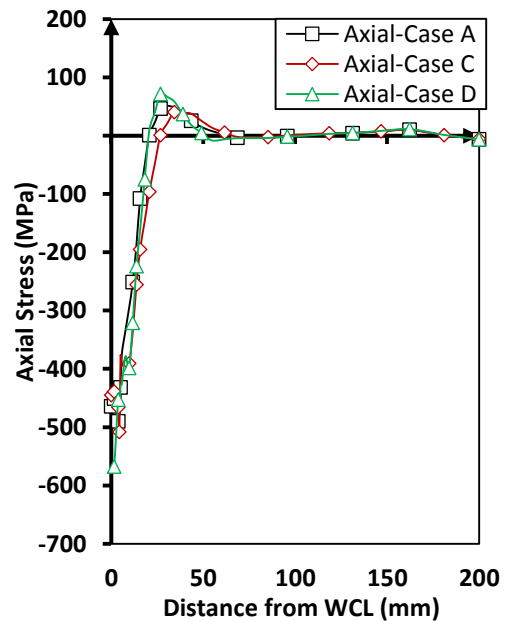
The effects on residual stresses of the doubled and halved welding speed with respect to the typical welding speed in case A have been investigated in this section. Figure 5-21(a)-(d) portrays the comparison between the numerically computed axial and hoop residual stresses on the inner and outer surface at 270° central angle in case A (basic case), case C (doubled welding speed) and case D (halved welding speed). On the inner surface, the axial residual stress distributions for the three cases along the longitudinal direction starting from the WCL are plotted in Figure 5-21(a). It could be seen that reducing the welding speed to half (case D) of a typical one (case A) leads to significantly increase in the axial residual stress in the WCL, 832 MPa. The axial residual stress magnitudes in the FZ and its vicinity, $Z \leq 20.7$ mm, in cases A and C are close to some extent. The extent of the tensile-stress zone in case D is the longest one comparing to other cases whereas case C has the narrowest extent of the tensile-stress zone. Similarly, as for the hoop residual stresses, Figure 5-21(b) shows that case D has the largest magnitude of hoop stress at the WCL, 400 MPa. Up to a distance of about 18mm from the WCL, a good correlation between the results

of cases A and C is found. Also, the extent of the tensile-stress zone of case A is between the longest one (case D) and the narrowest one (case C).

On the outer surface, the axial residual stresses are compressive in the FZ and HAZ as shown in Figure 5-21(c). However, the largest compressive stress at the WCL, equal to 578 MPa, is found in case D. Up to a distance of 13.75 mm from the WCL, the compressive stresses of case A are slightly lower than their counterparts in case C. Furthermore, the compressive-stress zone in case C is slightly longer than in cases A and D. Returning to the hoop stress on the outer surface, in all cases the stress distributions have a waved shape, whereas case D has the largest absolute residual hoop stress value at the WCL in comparison with its counterparts in cases A and C, as clarified in Figure 5-21(d).



(a)



(c)

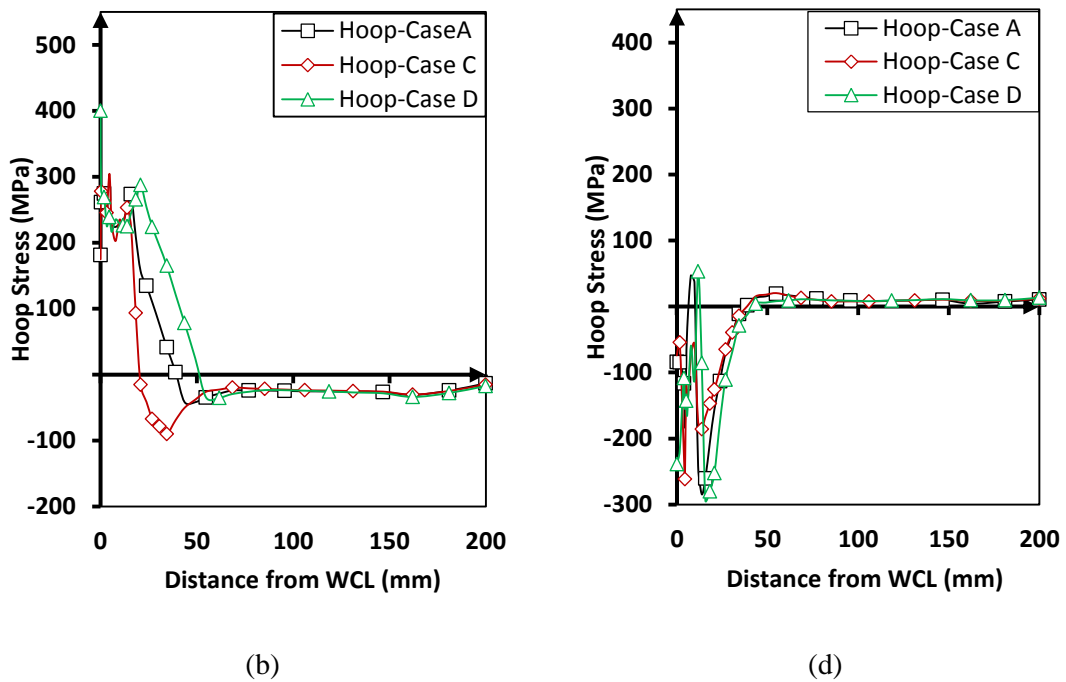


Figure 5-21 Comparison of residual stresses at 270° central angle in case A, C and D: (a) axial stress distributions on the inner surface, (b) hoop stress distributions on the inner surface, (c) axial stress distributions on the outer surface and (d) hoop stress distributions on the outer surface

5-8. Conclusions

In this chapter, a 3-D FE model has been developed to predict temperature fields and residual stress distributions induced by two circumferential welds for a lined-pipe, namely the overlay welding of the stainless steel liner with the C-Mn steel pipe and the girth welding of two segments of pipe. Two user-subroutines have been coded to model a distributed power density of the moving welding torch and to use a non-linear heat transfer coefficient accounting for both radiation and convection. The temperature and stress variations in space and time have been reported in both the axial and the circumferential directions. The model procedure has been validated against experimental results in the literature related to two different cases involving the welding of a C-Mn pipe and a stainless steel pipe. Furthermore, a sensitivity analysis to determine the influence of the cooling time between weld overlay and girth welding and of the welding speed has been conducted thermally and mechanically.

This chapter has shown that the welding parameters, namely interval time and welding speed, play a vital role in the weld pass quality. According to the results in this work, we can draw the following specific conclusions.

- (1) Based on the thermal results, it is clear that the temperature distribution around the heat source reaches steady state when the welding torch moves to fill the weld overlay and girth welding. From the outcome of our investigation it is possible to conclude that the temperature history is not sensitive to the variations of the circumferential angles, except for a small angle close to the starting point, associated with a short initial transient.
- (2) Increasing the inter-pass temperature leads to a significant increase in the temperature at the boundary of FZ. As expected, the less interval time is applied, the higher temperature is obtained during the girth welding.
- (3) Doubling or halving the weld overlay and girth welding speeds leads to significantly decrease or increase the width of the FZ, respectively.
- (4) The largest tensile and compressive axial residual stresses occur at the FZ and its vicinity on the inner and outer surfaces, respectively. Beyond the FZ and its vicinity, compressive and tensile residual stresses are produced on the inner and outer surfaces of lined pipe, respectively. The hoop residual stress results are affected to some extent by the axial residual stress results.
- (5) Minimizing the inter-pass time to 1 second leads to a reasonable increase in the absolute magnitudes of axial residual stresses at the WCL about 21% on the inner surface and 10% on the outer surface.
- (6) Halving the weld overlay and girth welding speeds has more influence in increasing the absolute values of hoop and axial residual stresses at the WCL whereas doubling speed does not have that effect on the results at the FZ according to the basic case, case A.

Chapter 6

Results of Experimental Testing and of FEA of Lined Pipe Welding

6-1. Introduction

The thermal and mechanical response of a lined pipe during welding depends on several main factors such as material properties, heat input, welding pool geometry, boundary conditions and welding sequence. There is a limited number of articles in the literature which have reported lined pipe welding simulation due to the complex sequence of weld overlay and girth welding, as already discussed in Chapter 2. However, the effect of pre-heat treatment to insert the liner inside the C-Mn pipe, known as tight fit pipe (TFP), on the residual stresses during and after lined pipe welding has not been investigated yet. Furthermore, it is worth noting the modelling technique used to move the heat source around the weld overlay to fix and seal the liner at the pipe ends and then around the girth welding to join two specimens of lined pipe has also not been reported.

In this chapter, a three-dimensional FE model is developed using ABAQUS to study the thermal and mechanical behaviour induced by the weld overlay and two passes of girth welding process, described here as case A, reference case. Also, another case, case AH, has been modelled to examine the influence of pre-heat treatment on the stress/strain during and after lined pipe welding. The presented 3-D model is validated thermally and mechanically by comparing the numerical results with the temperature values measured by thermocouples, and with the strains and stresses measured by using high temperature strain gauges, residual stress gauges and X-ray diffraction.

6-2. Manufacturing Process

6-2-1. Description of the Lined Pipe and Welding Parameters

In the present work, the specimen of lined pipe shown in Figure 6-1 is manufactured from two adjacent pipes. The geometry and materials used are described in Chapter 3 and are briefly summarised here for convenience of the reader. The outer pipe is seamless and made of carbon-manganese C-Mn steel equivalent to E235 AISI 10305-1. The inner pipe is made of austenitic stainless steel Cr-Ni, AISI 304, which is well suited to be used in cryogenic service without affecting the ductility (International Nickel Limited, 1974). The nominal chemical compositions of both materials are clarified in Table 3-1 in Chapter 3. The configuration of line pipe specimen has an outer diameter of 114.3 mm and a wall thickness of 7.85 mm, of which 6.35 mm is the outer pipe thickness and 1.5 mm is the thickness of inner pipe. The welded lined pipe is composed of two joints where the length of one specimen is 200 mm. Wet cutting has been used to get the required length of each specimen.

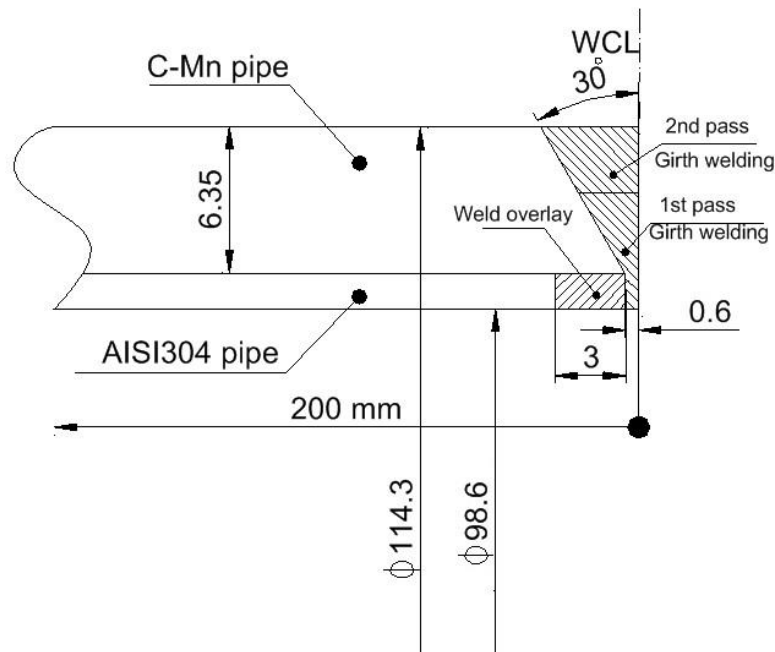


Figure 6-1 Schematic semi-sketch of welded lined pipe, dimensions in mm

The TFP thermal manufacturing process was executed to insert the CRA liner inside the C-Mn pipe (Focke, 2007; Focke et al., 2005). The process is explained earlier in detail in Chapter 3. After heat treatment, each lined pipe specimen is left to reach the ambient temperature naturally. The inner pipe (CRA liner) is cut to 3 mm from one end. Then, the outer pipe is chamfered with 30° from the same end using CNC machine. Afterward, two pieces of lined pipe are faced to be joined together. To perform that, the one-pass weld overlay is deposited at the cut end of the liner with ER308L stainless steel rod by Tungsten Inert Gas (TIG) welding. After that, two joints of lined pipe are assembled and fixed together by filling a two-pass girth welding in the V-groove formed outwardly between them. The girth welding is deposited with E70S2 mild steel rod using TIG welding. The inter-pass temperature between weld overlay and girth welding is normally around 100 °C.

During welding, the heat source is fixed and the two joints of lined pipe are rotated with a uniform speed for each pass (one-pass weld overlay and two-pass girth welding). The weld overlay pass took 240 seconds to complete one revolution and then 270 seconds were used as inter-pass time between weld overlay and girth welding to cool down naturally to room temperature. The first and second pass of girth welding requires 270 seconds each. Also, there is an inter-pass time, again 270 seconds, between them. The entire lined pipe took 3000 seconds to cool down naturally to ambient temperature after completing the welding operation. The welding begins at the central angle $\theta = 0^\circ$ and then progresses through the anti-clockwise circumferential direction of θ to complete one rotation and stop at the same starting point $\theta = 360^\circ$.

In this work, the same thermal-mechanical material properties are used for both base and weld metals except the yield stress, because the weld material has higher yield stress in both C-Mn and AISI304 as shown in Table 6-1 and Table 6-2, respectively.

Table 6-1 Thermo-mechanical properties of C-Mn (Karlsson and Josefson, 1990)

Temperature (°C)	Density (Kg/m ³)	Specific heat (J/Kg°C)	Conductivity (W/m°C)	Thermal expansion (x10 ⁻⁵ °C ⁻¹)	Yield stress (MPa)		Young's modulus (GPa)	Poisson's ratio
					Base	Weld		
0	7860	444	50	1.28	349.45	445.42	210	0.26
100		480	48.5	1.28	331.14	441.29	200	0.28
200		503	47.5	1.30	308.00	416.49	200	0.29
300		518	45	1.36	275.00	376.18	200	0.31
400		555	40	1.40	233.00	325.54	170	0.32
600		592	35	1.52	119.00	172.59	56	0.36
800		695	27.5	1.56	60.00	43.41	30	0.41
1000		700	27	1.56	13.00	14.47	10	0.42
1200		700	27.5	1.56	8.00	9.30	10	0.42
1400		700	35	1.56	8.00	9.30	10	0.42
1600		700	122.5	1.56	8.00	9.30	10	0.42

Table 6-2 Thermo-mechanical properties of AISI304 (Deng and Murakawa, 2006; International Nickel Limited, 1974)

Temperature (°C)	Density (kg/m ³)	Specific heat (J/kg°C)	Conductivity (W/m°C)	Thermal expansion (x10 ⁻⁵ °C ⁻¹)	Yield stress (MPa)		Young's modulus (GPa)	Poisson's ratio
					Base	Weld		
-200	7900	157	8.4	1.22	412	-	181.3	0.294
-100	7900	380	12.6	1.43	319.2	-	181.3	0.294
0	7900	462	14.6	1.70	265	438.37	198.50	0.294
100	7880	496	15.1	1.74	218	401.96	193	0.295
200	7830	512	16.1	1.80	186	381.5	185	0.301
300	7790	525	17.9	1.86	170	361.25	176	0.310
400	7750	540	18.0	1.91	155	345.94	167	0.318
600	7660	577	20.8	1.96	149	255.71	159	0.326
800	7560	604	23.9	2.02	91	97.41	151	0.333
1200	7370	676	32.2	2.07	25	28.41	60	0.339
1300	7320	692	33.7	2.11	21	16.23	20.00	0.342
1500	7320	700	120	2.16	10	12.17	10	0.388

The latent heat for C-Mn steel is set to be 247kJ/kg between the solidus temperature of 1440 °C and the liquidus temperature of 1560 °C. For stainless steel (AISI304), the latent heat is assumed to be 260kJ/kg between 1340 °C and 1390 °C, solidus and liquidus temperatures respectively. Consequently, the melting point for C-Mn is

1500 °C while it is 1365 °C for AISI304. The initial temperature of the lined pipe and the weld bead is set at room temperature.

To record the thermal history, type K thermocouples were placed at 6 axial locations with 180° central angle. Three thermocouples were mounted on the outer surface (C-Mn pipe) and the others on the inner surface (AISI304) to record the thermal history upon those locations during welding and cooling as shown in Figure 6-2.

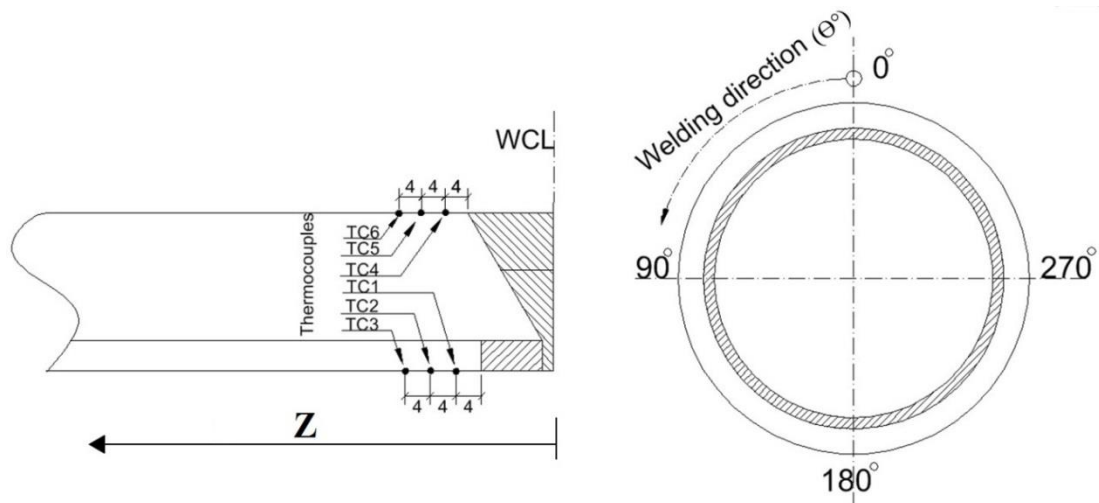


Figure 6-2 Locations of thermocouples and the welding direction for three passes, dimensions in mm

To record the strain history during welding, the lined pipe was also equipped with 12 high temperature strain gauges to measure the axial and hoop strain upon the outer and inner surfaces through welding process and cooling naturally to ambient temperature. In particular, 6 uniaxial ZFLA-11 strain gauges were mounted on the outer surface (C-Mn pipe). Three of them were mounted axially and the others were placed circumferentially. On the inner surface (liner), three biaxial strain gauge rosettes, ZFCAL-17, were also fixed to record the strain history axially and circumferentially. The precise locations of the inner and outer strain gauges are identified in Table 6-3.

Table 6-3 locations of strain gauges on the inner and outer surfaces at the axial and hoop directions

Gauge (outer surface)	A	B	C	D	E	F
Location (Θ° , Z(mm))	(45°, 14)	(36°, 14)	(270°, 14)	(261°, 14)	(135°, 18)	(126°, 18)
Measured strain	Axial	Hoop	Axial	Hoop	Axial	Hoop
Gauge (inner surface)	G	H	I	J	K	L
Location (Θ° , Z(mm))	(45°, 14)	(45°, 14)	(270°, 14)	(270°, 14)	(135°, 18)	(135°, 18)
Measured strain	Axial	Hoop	Axial	Hoop	Axial	Hoop

The thermal and mechanical experimental results were recorded every 0.001 second through LabVIEW software fitted with the data logger.

To record the residual stresses after welding and cooling down to ambient temperature, residual stress gauges with three elements, FRS-2, were mounted on the inner surface (liner) and outer surface (C-Mn pipe). A reference hole with diameter and depth of 2 mm each was drilled vertically through the pipe thickness using a high speed milling machine. Also, the X-Ray diffraction technique has been used to double check the reliability of residual stress measurement.

6-3. Finite Element Modelling

In this section, the 3-D FE analysis of the welding process, executed using ABAQUS, is described. Only one-half of the lined pipe specimen, one joint, was modelled due to the symmetry around the weld centreline WCL. The problem is modelled by uncoupled quasi-static thermo-elasticity equations. In other words, the deformations depend on the temperature in welding model whereas temperatures are independent of deformation. As a result, the thermal analysis is carried out first to get the thermal history as a function of time throughout the lined pipe joint. This thermal history is then considered as an input for the mechanical analysis in which the mechanical properties are temperature dependant. The element type in the thermal analysis is DC3D20 (continuum, three-dimensional 20-node quadratic brick diffusive heat transfer elements with one degree of freedom, which is temperature, at each node). The element type in the mechanical analysis is C3D20 (continuum three-

dimensional 20-noded element, with three translation degrees of freedom at each node). Figure 6-13 shows the mesh of 3-D FE model where the thermal and mechanical analyses employ the same mesh in which the nodes and elements have the same numbers and arrangements. The model is composed of 35220 nodes associated with 7380 elements. It could be seen there is a finer mesh at the FZ and HAZ of weld overlay, inner pipe, and of the two-pass girth welding, outer pipe, due to the high temperatures and their rapid changes in these regions. The weld overlay, liner, girth welding and C-Mn pipe are coloured with red, light blue, yellow and green, respectively, as depicted in Figure 6-3.

The element birth technique is adopted in the FE models to simulate depositing the filler materials in the weld overlay and girth welding during moving the heat source, which was already described in Chapter 5.

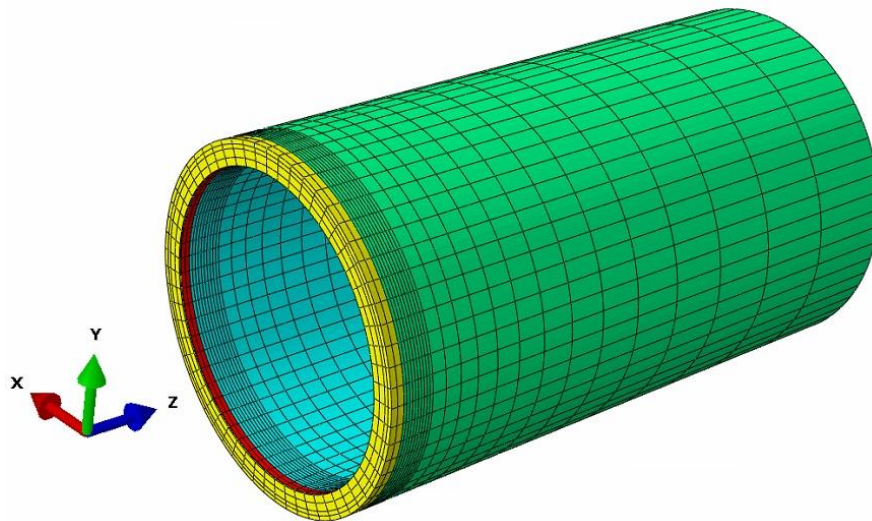


Figure 6-3 3-D FE model

6-3-1. Thermal Analysis

6-3-1-1. Pre-Heat Treatment

The TFP heat treatment described in Chapter 3 has been simulated in the FE model by giving the initial state of temperature for the liner and C-Mn pipe as $-200\text{ }^{\circ}\text{C}$ and $500\text{ }^{\circ}\text{C}$, respectively.

After inserting the liner inside the C-Mn pipe, the lined pipe is naturally exposed to ambient air temperature for 7200 seconds after which the temperature of the whole lined pipe reached room temperature. Through this time, the external surfaces of C-Mn pipe, outer pipe in Lined pipe configuration, are subjected to natural convective exchange with atmosphere corresponding to Newton's law given as:

$$q_c = -h_c(T_c - T_a) \quad (6.1)$$

where q_c is the heat loss upon C-Mn surface, T_c is the surface temperature of C-Mn pipe, T_a is the ambient temperature and h_c is the heat transfer coefficient between the surface of C-Mn pipe and the atmosphere of room which is assumed to be constant and equal to $8 \text{ W/m}^2\text{°K}$.

In a similar way, the AISI304 pipe is forcedly cooled down in liquid nitrogen (-200 °C). After being slid inside the C-Mn pipe, it has been heated up naturally to room temperature. During that, the convective heat exchange between external surfaces of AISI304, inner pipe, and room atmosphere are subjected also to the Newton's law as below:

$$q_s = h_s(T_s - T_a) \quad (6.2)$$

where q_s is the heat gain upon AISI304 surface, T_s is the surface temperature of AISI304 pipe, T_a is the ambient temperature and h_s is the heat transfer coefficient between the surface of AISI304 pipe and the atmosphere of room which is assumed to be constant, $5.7 \text{ W/m}^2\text{°K}$.

6-3-1-2. During Lined Pipe Welding

Basically, the welding process starts after TFP treatment and machining the lined pipe where the whole pipe is at room temperature. During welding, the heat transfer is a combination of heat loss due to radiation and convection. Radiation loss is dominated in the weld zone and its vicinity whereby the temperature magnitudes are near the melting temperature. Convection loss is dominating away from the weld zone. The Stefan-Boltzman law and Newton's law are applied to model the radiation and convection heat loss, respectively. In this work, the thermal boundary conditions are applied on all external exposed surfaces of lined pipe to the environment

including convection and radiation. The total heat loss, q_{total} , is a combination of radiation, $q_{radiation}$, and convection, $q_{convection}$, losses given as follows:

$$q_{total} = q_{radiation} + q_{convection} \quad (6.3)$$

$$q_{convection} = -h_{convection}A(T_{pipe} - T_a) \quad (6.4)$$

$$q_{radiation} = -\sigma_{em}\epsilon_{bol}A(T_{pipe}^4 - T_a^4) \quad (6.5)$$

where $h_{convection}$ is the convective heat transfer coefficient, A is the pipe surface area, T_{pipe} is the current temperature at the pipe surface, T_a is the ambient temperature, ϵ_{em} is the effective radiation emissivity and σ_{bol} is the Stefan-Boltzmann constant.

As the lined pipe is composed of two different materials, each material is characterised by different coefficients governing heat transfer with the room atmosphere, as shown in Table 6-4.

Table 6-4 Heat transfer parameters

Parameters	C-Mn	AISI304
$h_{convection}$ (W/m ² K)	8	5.7
σ_{em}	0.51	0.75
ϵ_{bol} (W/m ² K ⁴)	5.67×10^{-8}	5.67×10^{-8}

A FILM user subroutine (Dassault Systèmes, 2014) has been coded in FORTRAN to implement in ABAQUS the above expressions of the heat-transfer coefficients. It is worth noting that ABAQUS allows one single user-subroutine to be written for both materials by simply specifying which surface each condition applies to.

The heat input transmitted from the heat torch to the lined pipe and weld regions is given by a Gaussian distribution as a function of position and time in the following equation:

$$q(x, y, z, t) = \frac{6Q\sqrt{3}}{abc\pi\sqrt{\pi}} e^{-3(x-(R\sin\theta+x_0))^2/a^2} e^{-3(y-(R\cos\theta+y_0))^2/b^2} e^{-3(z-z_0)^2/c^2} \quad (6.6)$$

where $Q = IV\mu$ is the energy input rate which is given by the product of the current I , voltage V and the weld efficiency μ , R is the radial distance of the heat torch

centre from the pipe axis, θ is the angle from the start/stop point (where $\theta = 0^\circ$) at which the torch has travelled around the pipe. Parameters a , b and c are the semi-axes of the ellipsoidal welding pool in directions, x , y and z , respectively. Equation (6.6) has been implemented in ABAQUS by coding the DFLUX user-subroutine. The position of the weld torch is calculated first in DFLUX according to the welding time t . Thereafter, the power density q is computed at each integration point. The numerical values for the variables used in the power density distribution in Eq. (6.6) are illustrated in Table 6-5 for each welding material.

Table 6-5 Heat source and welding parameters

Parameter	Symbol	Weld overlay	1 st pass girth welding	2 nd pass girth welding
Half-length of arc (mm)	a	4.9	6.2	6.2
Depth of arc (mm)	b	4.9	5.57	5.66
Half-width of arc (mm)	c	1.5 mm	2.62	2.85
Welding current (A)	I	110	220	234
Voltage (V)	V	22	22	22
Welding speed (mm/s)	v	1.3	1.26	1.33
Welding efficiency	μ	70%	70%	70%

To take into consideration the effect of moving heat source with element birth, the one-pass weld overlay and two-pass girth welding are meshed circumferentially into 60 identical elements each. The length of each bead is assumed to be equal to one element block in the circumferential direction. Consequently, the appropriate time step for each pass in the FE model is recognised as given in Eq. (6.7):

$$\text{Step time} = \frac{\text{Total pass time (s)}}{\text{Number of circumferential elements along the WCL}} \quad (6.7)$$

where the total time of weld overlay pass, first girth welding pass and the second welding pass are 240, 270 and 270 seconds associated with 60 elements around WCL, respectively.

6-3-2. Structural Analysis

The same FE mesh used in the thermal analysis is employed in the mechanical analysis apart from the boundary conditions and element type. Herein, the nodal

temperature histories read from the thermal output file are considered thermal loads for each increment in the mechanical simulation. At each structural step, an automatic time increment is executed and geometrical nonlinear effects (large deformation) have been incorporated in the FE model.

During the lined pipe welding process, the effects of volumetric change and the change in the yield stress because of metallurgical martensitic transformation (phase transformation) have been neglected in this work. Therefore, the increment of the total strain, $d\varepsilon_{ij}$, has been broken down into three components as follows:

$$d\varepsilon_{ij} = d\varepsilon_{ij}^e + d\varepsilon_{ij}^p + d\varepsilon_{ij}^{th} \quad (6.8)$$

where $d\varepsilon_{ij}^e$, $d\varepsilon_{ij}^p$ and $d\varepsilon_{ij}^{th}$ are the elastic, plastic and thermal strain increment, respectively. The elastic behaviour relies on the isotropic Hook's law associated with Young's modulus and Poisson's ratio depending on temperature. For the plastic strain, the Von Mises yield criterion has been used. All material nodes are under the influence of multiple thermal loading and unloading, so that the Bauschinger effect should be considered. As a result, a linear kinematic hardening rule has been assumed for both materials C-Mn and AISI304. The expansion and contraction of the line pipe materials rely on the temperature-dependant thermal expansion coefficient to obtain the thermal strain. Figure 6-4 illustrates the temperature-dependant yield stress as the plastic strain of C-Mn and AISI304 is equal to 1% (Deng and Murakawa, 2008; Malik et al., 2008).

The boundary conditions are applied to restrict the axial movement on the circumferential symmetry-plane. Lateral and transversal restrictions are employed at the line pipe end to prevent rigid body motion while allowing the free expansion and contraction upon the whole lined pipe.

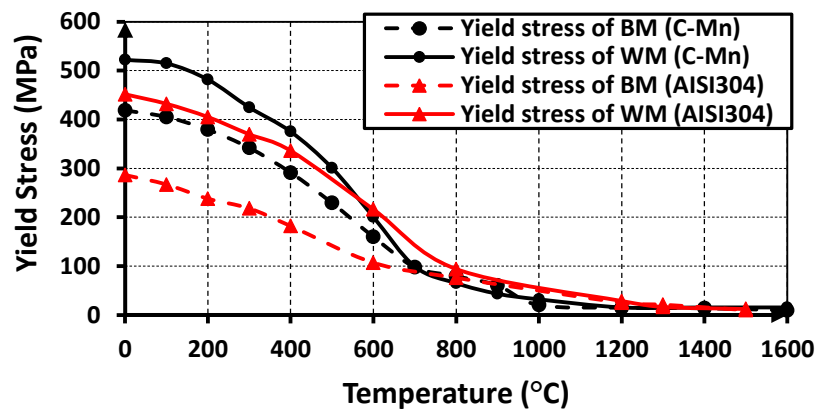


Figure 6-4 Yield strength of C-Mn steel and AISI304 corresponding to 1% hardening (Deng and Murakawa, 2008; Malik et al., 2008)

6-4. Results and Discussions

6-4-1. Temperature Fields

Both cases, A and AH, have the same thermal history results during welding because, after the heat treatment, the temperature reaches room temperature before heading up throughout welding process. It is noted that temperatures in the fusion zones of weld overlay and two-pass girth welding are higher than melting points, 1500 and 1365 °C for C-Mn and AISI304, respectively, as it should be.

Figure 6-5 shows the numerically computed temperature distributions at 90°, 180° and 270° central angle during weld overlay where the girth welding has not been deposited yet. As anticipated, the maximum temperature is achieved at the welding pool centre of weld overlay, 1634°C. From this figure, it can be seen that thermal history of weld overlay pool centres at three circumferential locations, 90°, 180° and 270, reasonably has the same shape and magnitudes of the transient thermal cycle.

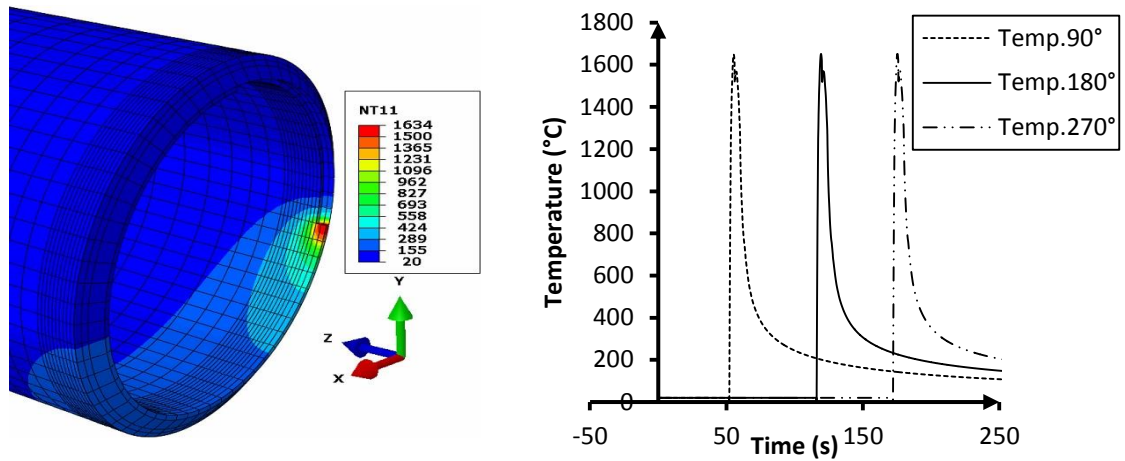


Figure 6-5 The thermal history of weld overlay centre at 90°, 180° and 270° central angle

Likewise, the numerically computed temperature history at the second pass of girth welding has also identical distributions circumferentially around the mid-plane (symmetric line) at three locations, 90°, 180° and 270°. The three curves reach the same peak temperature, 2076°C, and it could be seen that weld overlay and first-pass girth welding and three quarter of the second-pass girth welding has been laid down in their grooves as shown in Figure 6-6.

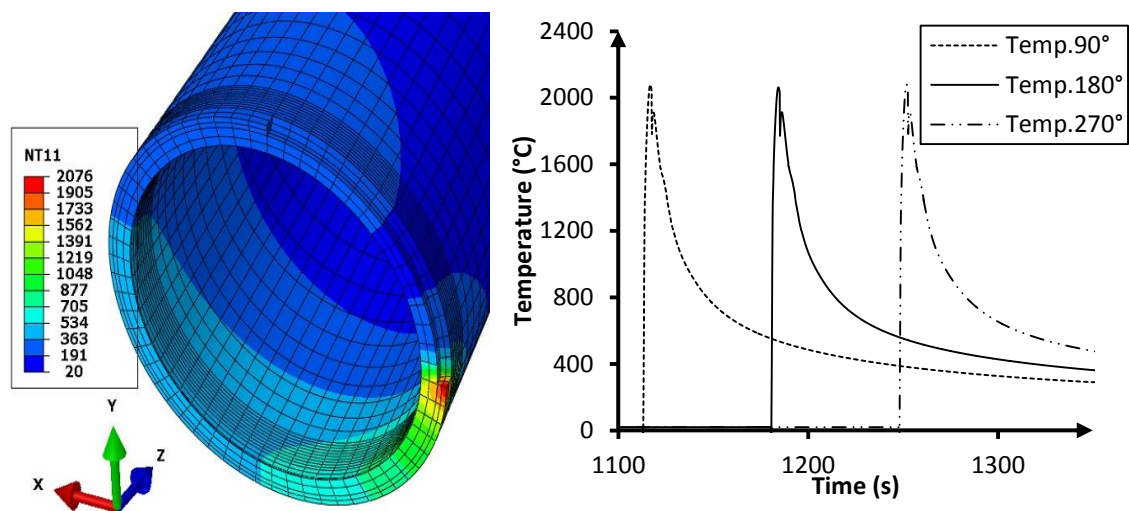
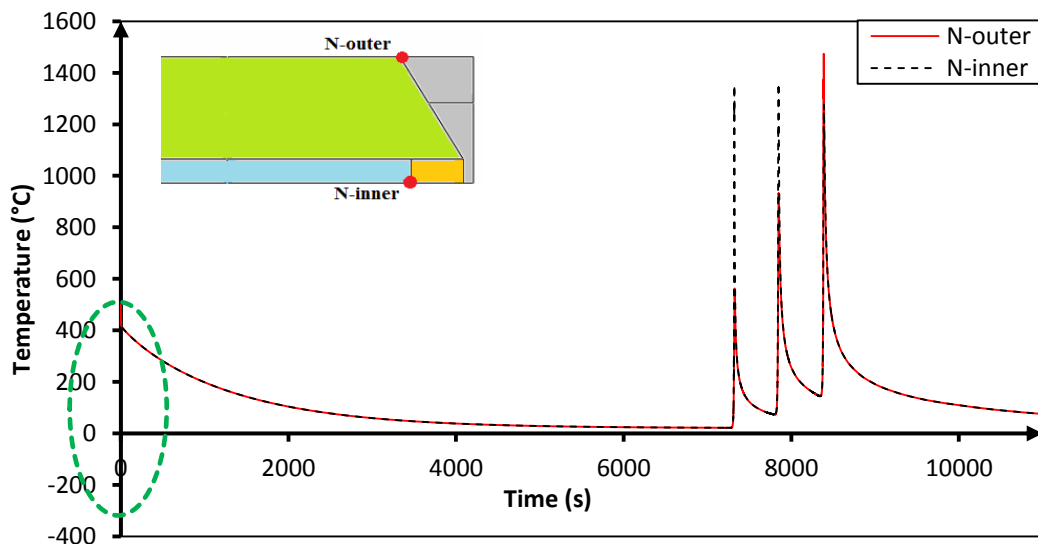
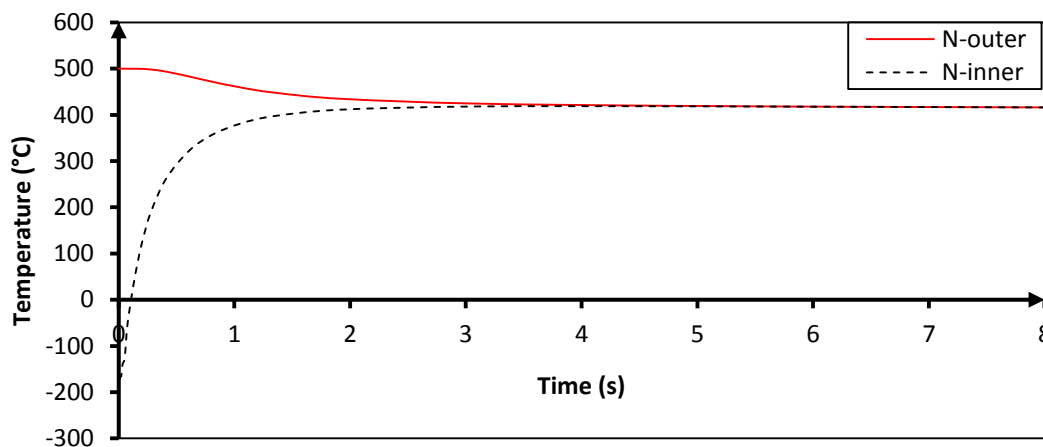


Figure 6-6 The thermal history of second pass centre of girth welding at 90°, 180° and 270° central angle

Figure 6-7 shows the thermal history of two points at 180° circumferential angle on the inner and outer surfaces, including the pre-heat treatment. The inner point is located at the border between the weld overlay FZ and the HAZ of base material, AISI304. The outer point is located between the FZ of the second pass girth welding and the HAZ of backing steel.



(a)



(b)

Figure 6-7 Temperature distributions for two points located at 180° central angle on the inner and outer surfaces (a) through the whole pre-heat treatment and welding (b) through the first seconds of pre-heat treatment

It is observed that the temperature of inner point, N-inner, goes up from -200 °C to meet the thermal distribution of the outer point, N-outer, at 419 °C after 4.30 seconds

of inserting the liner inside the outer pipe where the initial temperature of outer point is 500 °C. It is remarkable that the temperature returns back to room temperature in 7200 seconds, after which the thermal effect of pre-heat treatment has been completely elapsed.

It is clear the cooling/heating rate is different between the backing steel and liner materials which in turn results in different heat treatment residual stresses on the outer and inner pipe. In other words, there is a large rise in liner temperature in comparison with a small drop in outer pipe temperature through the same time. Consequently, initial residual stresses generated in the liner are higher than that in C-Mn pipe.

The temperatures computed by the FE model during lined pipe welding and cooling at six points, TC1-TC6, located at the inner and outer surfaces are compared with the measured ones by thermocouples at 180° central angle along the axial direction as depicted in Figure 6-8(a)-(f).

In general, the experimental thermal results are lower than those predicted by FE model for many reasons. The most important reasons are related to the extrapolated materials properties at high temperatures. Also, the measured results are affected by some specific factors, often called 5M1E (Man, Machines, Materials, Methods, Measurements and Environment), which have a significant influence on the quality of welding measures (Hui, 2011). Overall, the maximum variation between the predicted and measured temperature results is less than 6% which is reasonably acceptable.

It is noticeable that the temperature magnitude is heading up rapidly as the welding torch passes through the bead where the point is located. The cooling phase starts when the specified point reaches its peak temperature and the heat source moves beyond the point. The cooling rate is relatively higher for higher peak temperatures. It is also observed that the point located closer to the welding centreline WCL experiences temperature higher than that located far away from the WCL.

It can be concluded the thermal quantitative comparisons have proved that the numerical results are in good agreement with the experimental ones. Consequently,

the thermal analysis of the developed FE model can be considered validated experimentally.

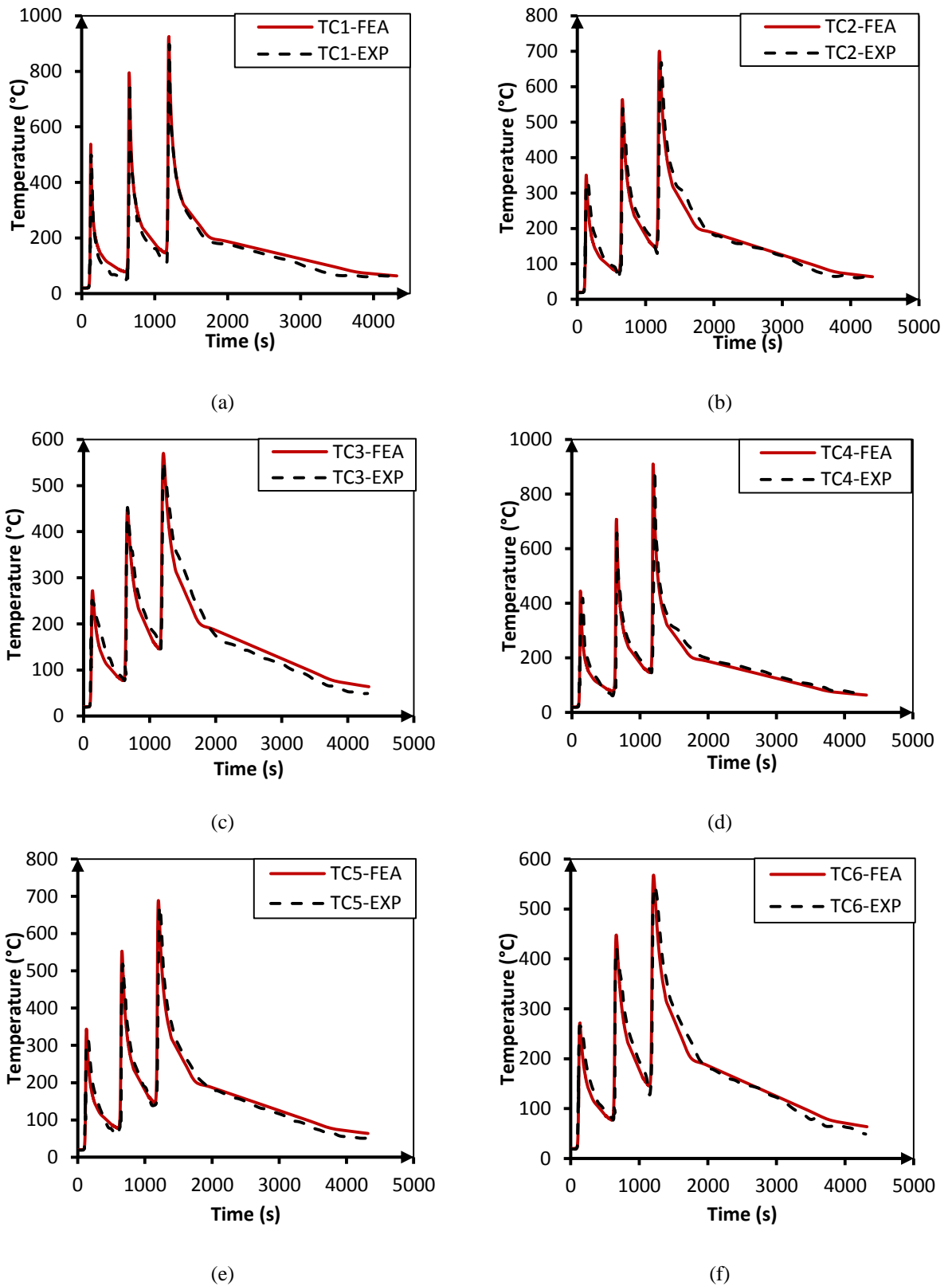


Figure 6-8 Thermal field distributions for thermocouples (a) TC1 (b) TC2 (c) TC3 (d) TC4 (e) TC5 and (f) TC6

6-4-2. Structural Response

6-4-2-1. Strain during Welding

To record the strain history during welding, 12 strain gauges were mounted on the inner (liner) and outer (C-Mn) surfaces. On the outer surface, 6 strain gauges were placed in two different axial locations, $Z = 14$ mm and $Z = 18$ mm far away from the WLC. At the axial location, $Z = 14$ mm, two strain gauges measured the axial strain (gauges A and C) and two strain gauges recorded the hoop strain (gauges B and D) with respect to circumferential angles of 45° , 270° , 36° and 261° , respectively. The last two gauges, E and F, measured the axial and hoop strains during welding at the axial location $Z = 18$ mm and circumferential angle of 135° and 126° , respectively. On the inner surface, two rosette of strain gauges were placed in the axial location, $Z = 14$ mm where two gauges (G and I) measured the axial strain and also two gauges (H and J) measured the hoop strain at circumferential angles of 45° and 270° , respectively. At $Z = 18$ mm with respect to 135° central angle, one biaxial rosette was placed on the inner surface to record the axial and hoop strains at gauges K and L, respectively. The moving heat source produces large temperature gradients which in turns lead to a large thermal expansion in the HAZ of both base materials, C-Mn and AISI304. Table 6-3 clarifies the precise axial and circumferential locations of all strain gauges mounted on the inner and outer surfaces.

During welding, the lined pipe is affected by the thermal and mechanical strains. In order to obtain the mechanical strains from the entire measured strain, the apparent thermal strain is subtracted from the total measured strain results recorded by data acquisition. The apparent thermal strain could be calculated according to the instructions in data sheet of strain gauges. As a matter of fact, the thermal strain has not been subtracted from the total measured strain as the pipe temperature is close to room temperature.

The pure transient experimental and numerical mechanical strain distributions without thermal strain effect during welding process on the outer and inner surfaces are depicted in Figure 6-9 and Figure 6-10, respectively. In the FE models, two models have been developed. The first one, case A, simulates the lined pipe welding process without considering the pre-heat treatment whilst the second one, case AH,

takes into account the effect of pre-heat treatment. It is observed from Figure 6-9 and Figure 6-10, that strain distributions start from zero at beginning of the weld overlay (welding process) in experiment and case A whereas there are somewhat residual strains in case AH.

During the weld overlay pass, strain gauges record a sudden drop in strains to be compression just before the welding torch is being close enough to the location of the particular gauge. The drop happens in both directions axially and circumferentially on the inner and outer surface with different severity (see for example, Figure 6-9(a), gauge A, at 16-35 seconds and Figure 6-10(c), gauge I, at 155-184 seconds). The strains sharply drop down more significantly at the axial direction on the inner surface in gauges G, I and K than their counterparts on the outer surface in gauges A, C and E, respectively. The gauges at the circumferential direction on the outer surface, gauges B, D and F also record a drop in strains lower than those on the inner surface, gauges H, J and L. The reason can be attributed to the increase in pipe radius because of heating nearby the welding torch.

Once the heat source passes the particular gauge, there is a remarkable large drop again in strain in the axial gauges, A, C and E after a short increase in strain whilst significant tensile strains are recorded on the inner surface in gauges G, I and L. Consequently, bending is produced in the pipe because of the shrinkage in the FZ and HAZ due to cooling. Furthermore, strains located at the hoop direction on the inner surface go gradually up before starting the first girth welding pass, gauges H, J and L.

On the outer surface, a remarkable kink is observed in gauges A and B attributed to the heat coming from the welding area close to start/stop point. Thus, a small drop in strain happens before the inter-pass time starting at 240 sec (cooling after weld overlay).

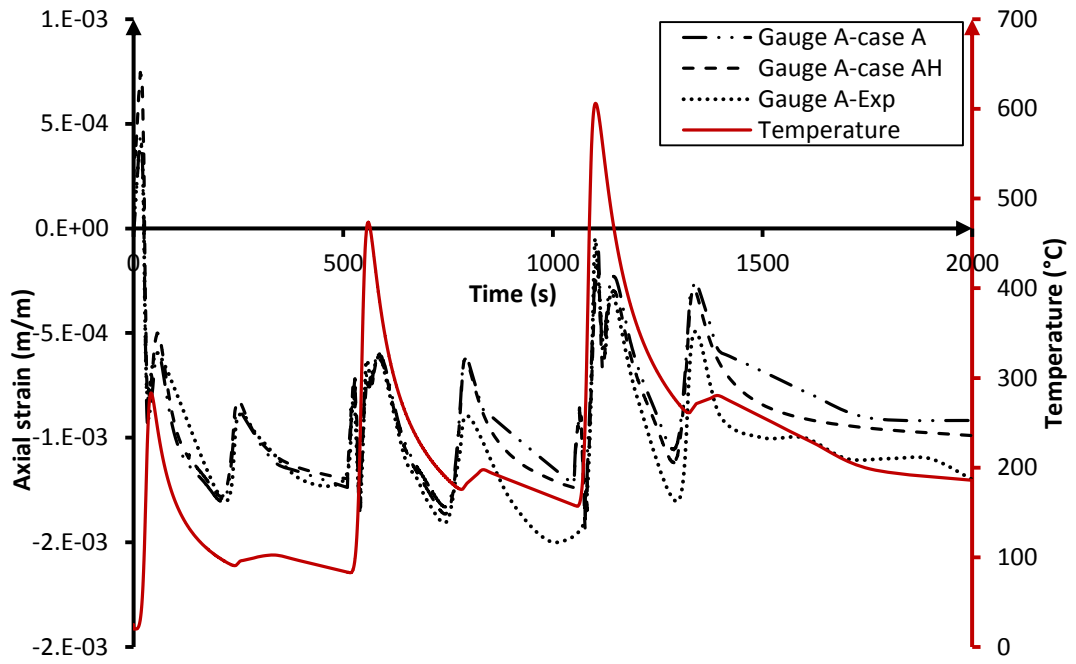
During the first girth welding pass, there is, in a similar way, a sudden drop recorded in all gauges on the inner and outer surfaces because of approaching heat source. In this process, a small drop in strains have been recorded at the axial locations on the outer surface, gauges A, C and E, compared to their counterparts drop on the inner gauges, G, I and K. At the circumferential direction, likewise, a larger strain drop is observed on the inner surface comparing to that on the outer surface accordingly.

Also, the bending effect is apparent after heat source passes the particular gauge where the strain goes further down in the axial direction on the outer surface, e.g. gauge C, and goes sharply up on the inner surface, e.g. gauge I, during the inter-pass cooling. At the hoop direction, strains recorded in the gauges on the inner and outer surface go along with the foregoing discussion of the weld overlay welding.

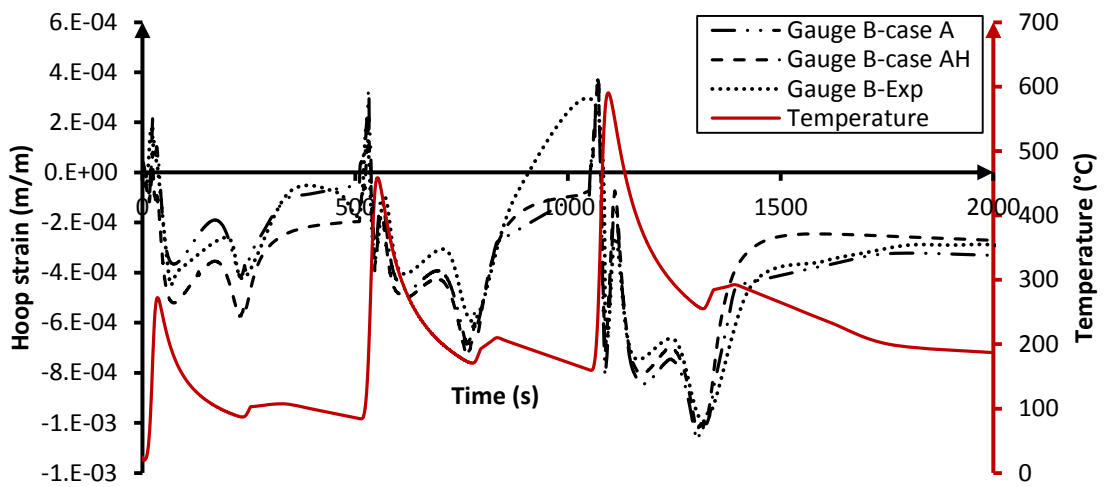
During the second girth welding, the same scenes, which have been experienced in weld overlay and the first girth welding process, happen. It is observed that the range of drop because of approaching the heat source is somewhat larger (absolute value) than the previous drops excluding the gauges which record the axial strains on the outer surface, gauges A, C and E.

During cooling, strain transient distributions go gradually down on the outer surface (compressive strains), whilst gradually going up on the inner surface (tensile strains) especially at the axial strains. As a result, bending occurs in the lined pipe due to the shrinkage of weld zones.

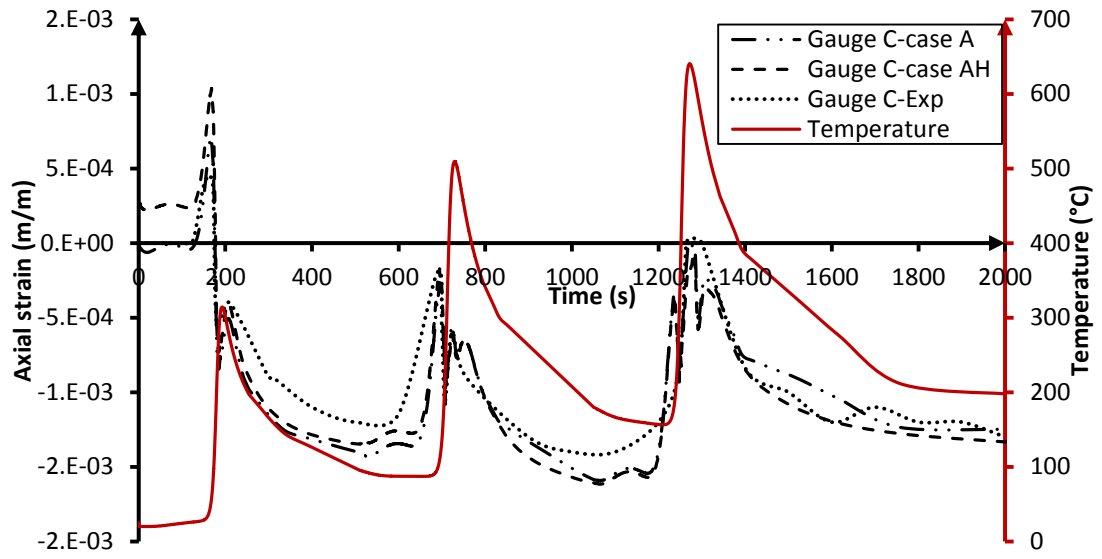
In general, the numerically computed transient strain curves accounting for pre-heat treatment, case AH, correlate well with those of case A during welding at all axial and circumferential gauges on the inner and outer surfaces. Consequently, the deviations in strain between case A and AH are very small and can be ignored during welding in all gauges because of high temperatures which lead to remove the effect of pre-heat treatment residual stresses at the FZ and its vicinity. Furthermore, it is observed that there is a very good agreement between numerical results in case A and case AH and the experimental results.



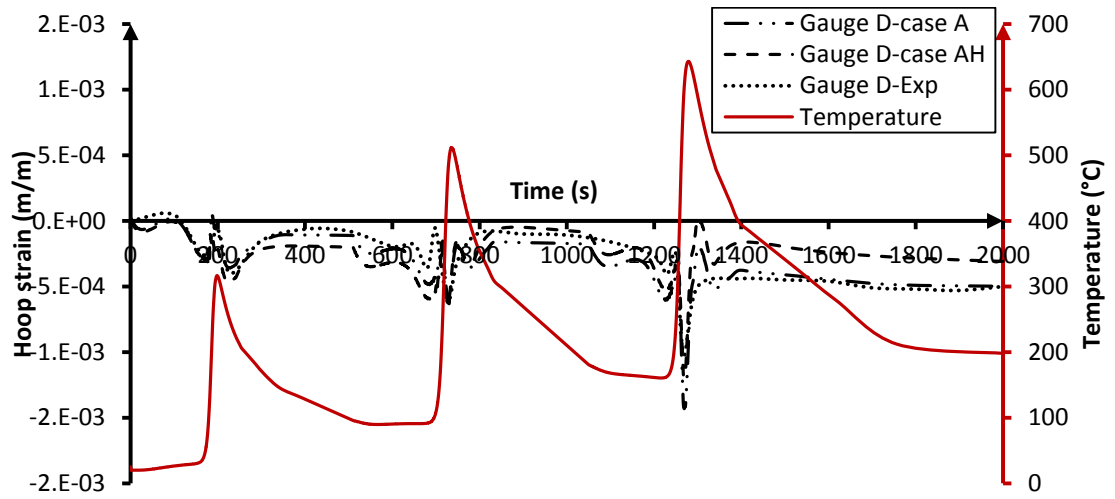
(a)



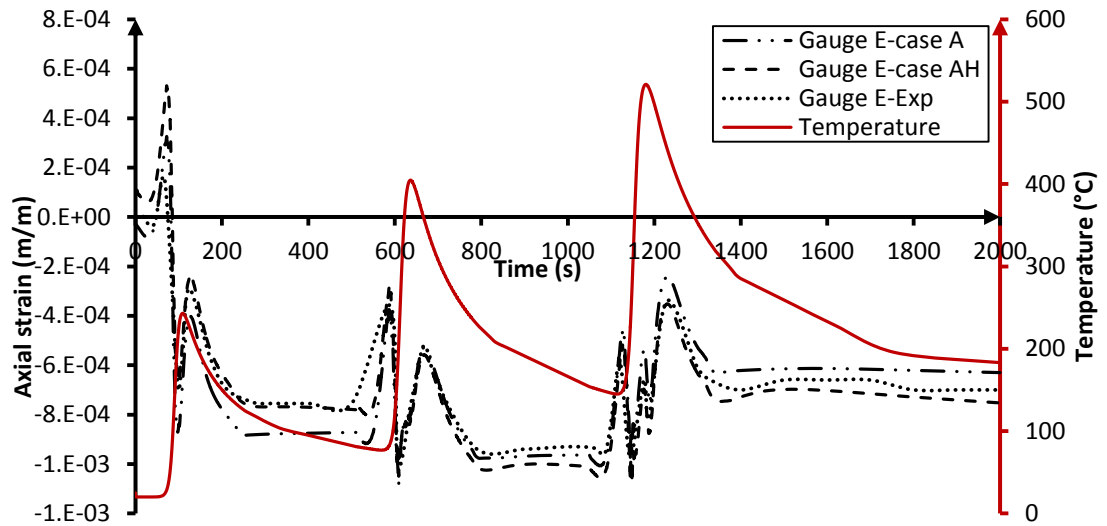
(b)



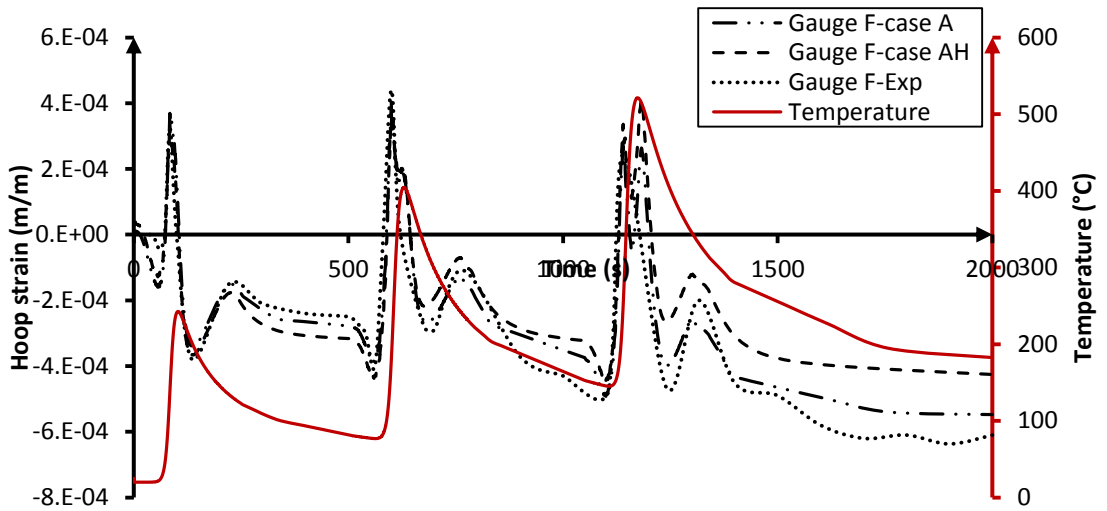
(c)



(d)

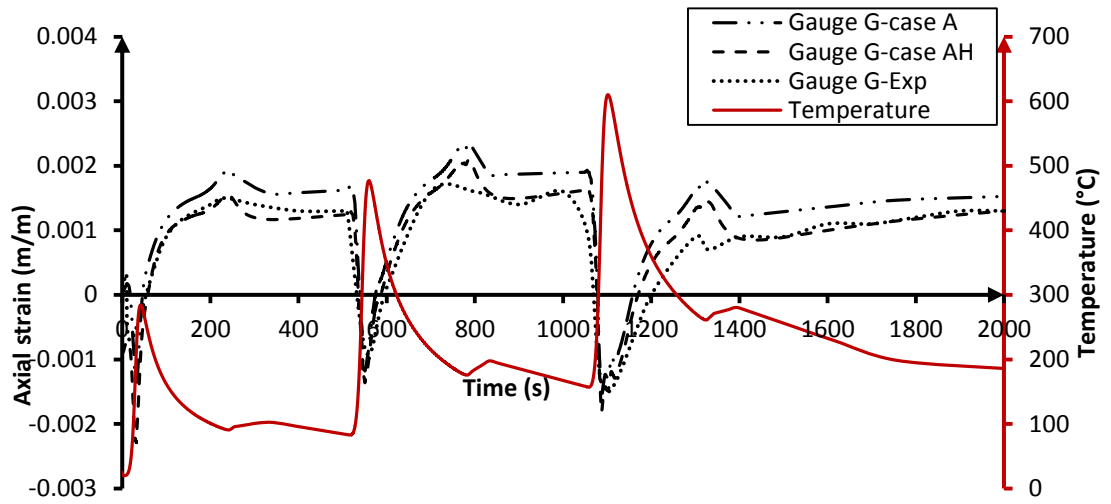


(e)

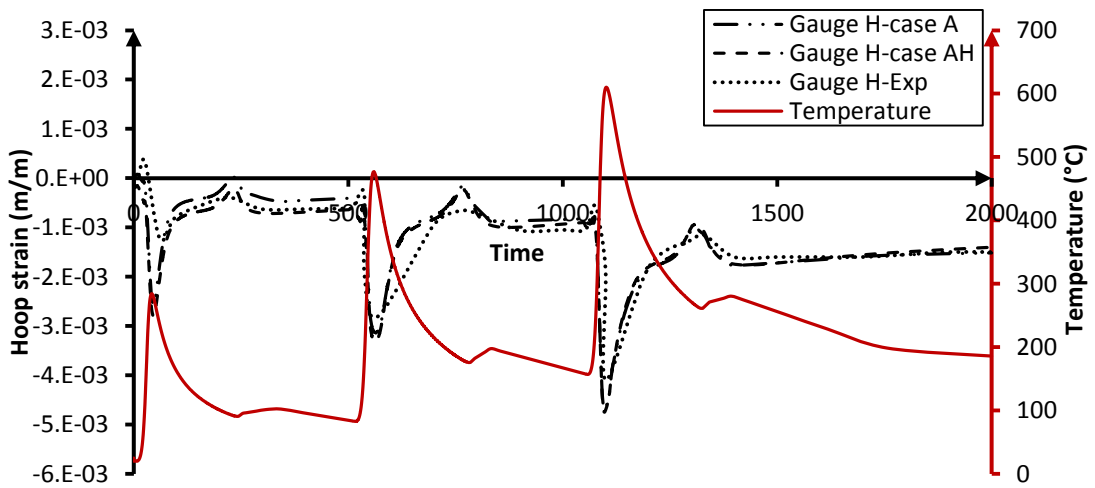


(f)

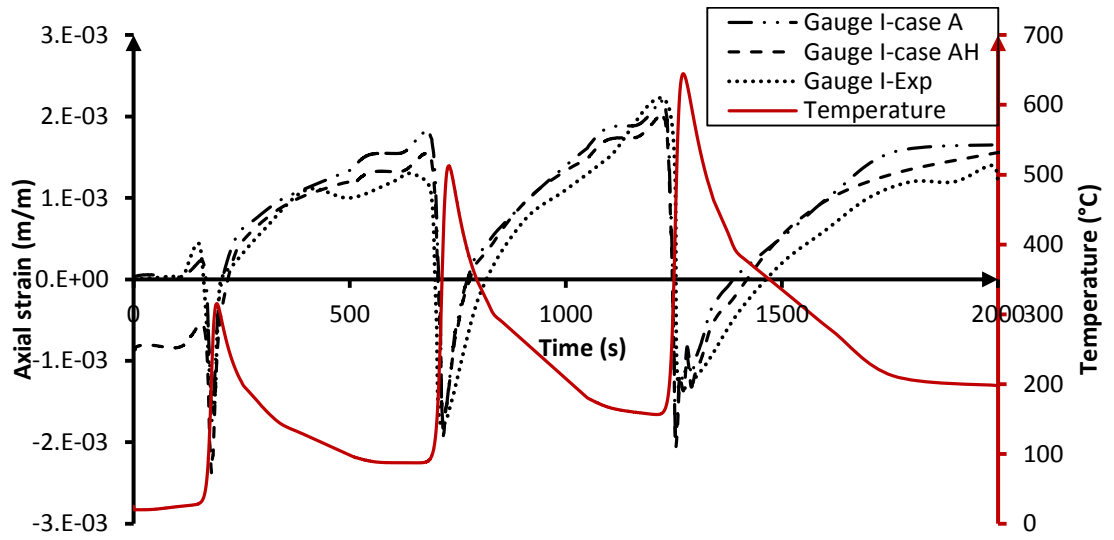
Figure 6-9 Mechanical strain history during welding associated with thermal history on the outer surface for (a) gauge A (b) gauge B (c) gauge C (d) gauge D (e) gauge E (f) gauge F



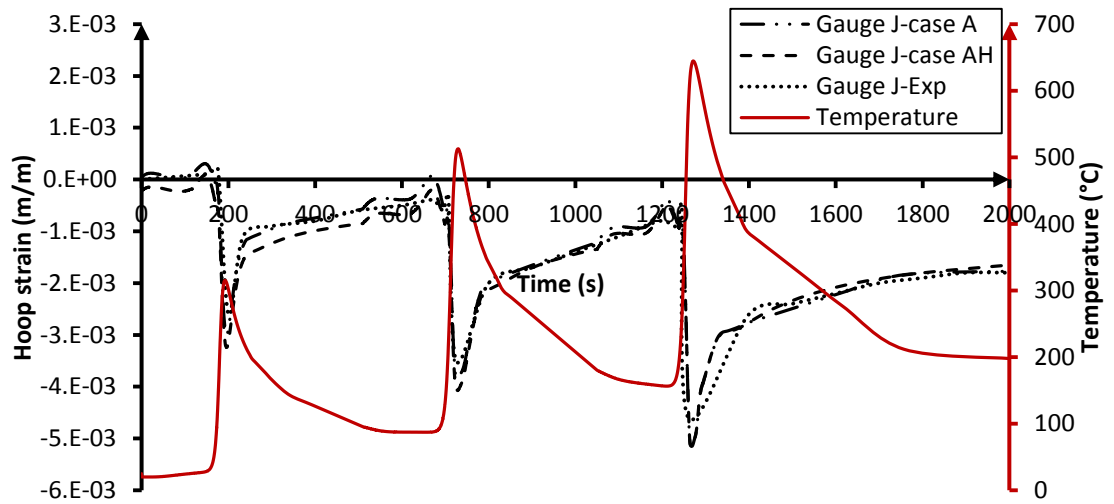
(a)



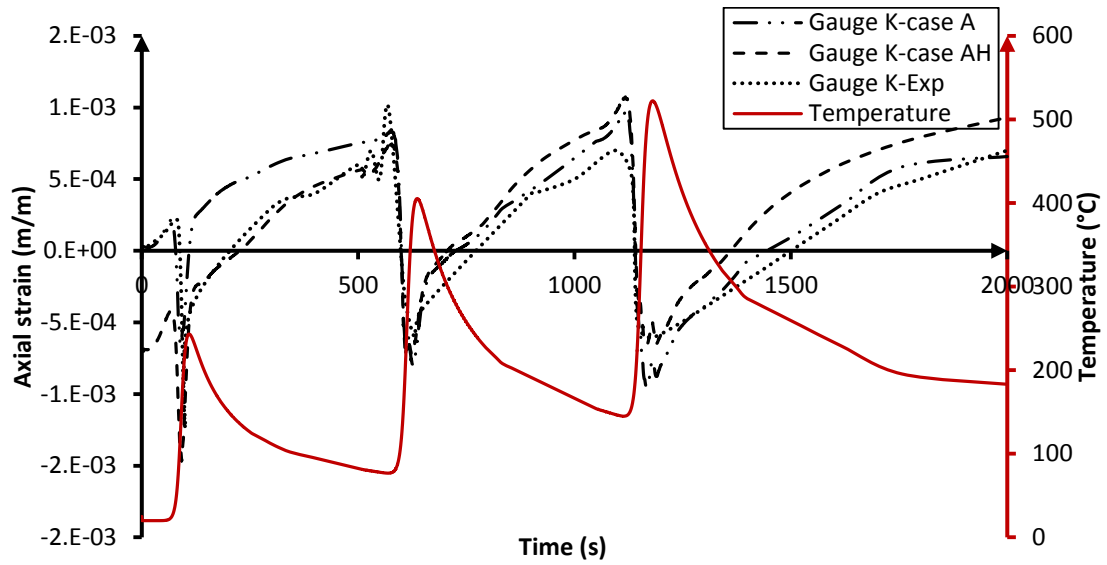
(b)



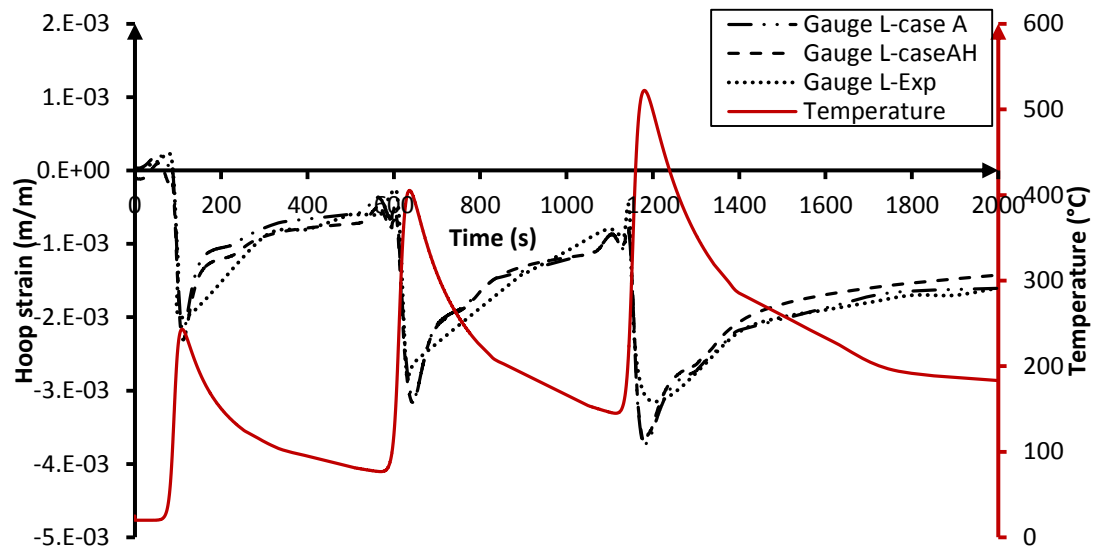
(c)



(d)



(e)



(f)

Figure 6-10 Mechanical strain history during welding associated with thermal history on the inner surface for (a) gauge G (b) gauge H (c) gauge I (d) gauge J (e) gauge K (f) gauge L

6-4-2-2. Residual Plastic Strains

The axial and hoop residual plastic strain distributions on the inner surface (AISI304) for both cases at 180° circumferential angle are depicted in Figure 6-11 and Figure 6-12, respectively. The magnitudes of axial residual plastic strains in case A and AH reach zero and -0.002 with steady state at 24 mm away from WCL,

respectively, as shown in Figure 6-11. Both curves almost have the same distribution along the axial direction. On the hoop direction, the residual plastic strain distributions in case A and AH have a bifurcation at 24 mm and then case A reaches the value of 0 strain at 37 mm axially away from WLC. The magnitudes of residual plastic strain in case AH are uniform and slightly less than zero beyond 37 mm because of the influence of pre-heat treatment as depicted in Figure 6-12. Approximately, it is clear that the axial extent of the influence of the welding process stretches to 24 mm and 37 mm in the axial and hoop direction on the inner surface, respectively.

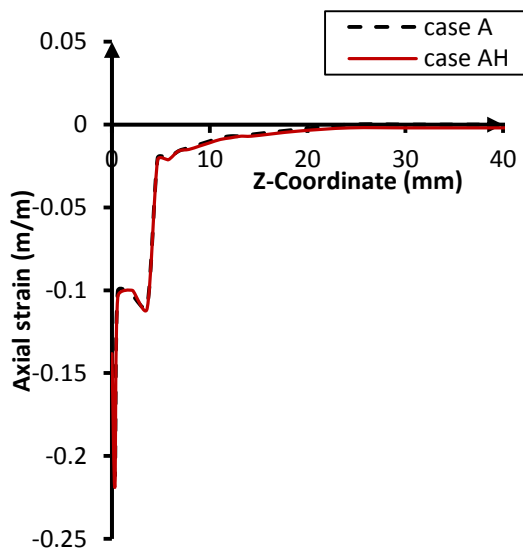


Figure 6-11 Axial residual strain at 180° central angle on the inner surface along the axial direction

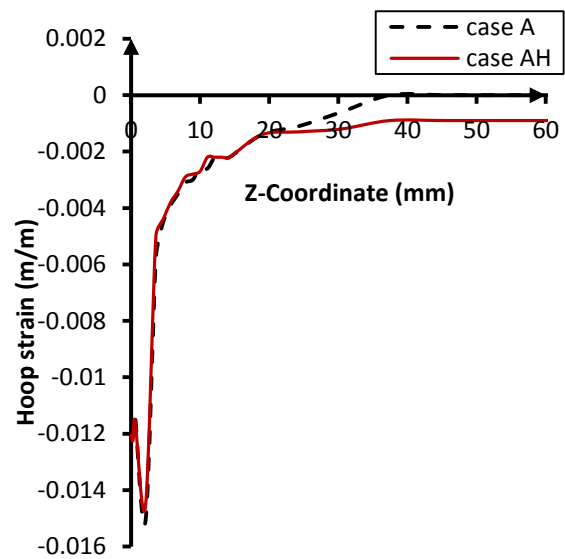


Figure 6-12 Hoop residual strain at 180° central angle on the inner surface along the axial direction

On the outer surface (C-Mn), the axial and hoop residual plastic strain distributions are portrayed in Figure 6-13 and Figure 6-14 for both cases A and AH at 180° circumferential angle, respectively. On the axial direction, it could be observed that, when the distance from the WLC is over 24 mm, the plastic strain goes to zero for both cases in the outer surface as clarified in Figure 6-13. Returning to the hoop direction on the outer surface, the hoop plastic strain curves for case A and AH have somewhat identical shape at circumferential location with 180°. It is clear from Figure 6-14 that case AH slightly has larger magnitudes of plastic strain than those in

case A especially at the FZ. Both cases go down steadily to reach magnitude of zero strain at 37 mm far away from WCL.

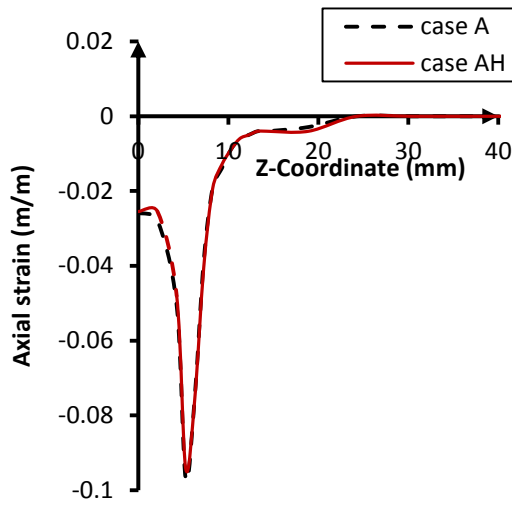


Figure 6-13 Axial residual strain at 180° central angle on the outer surface along the axial direction

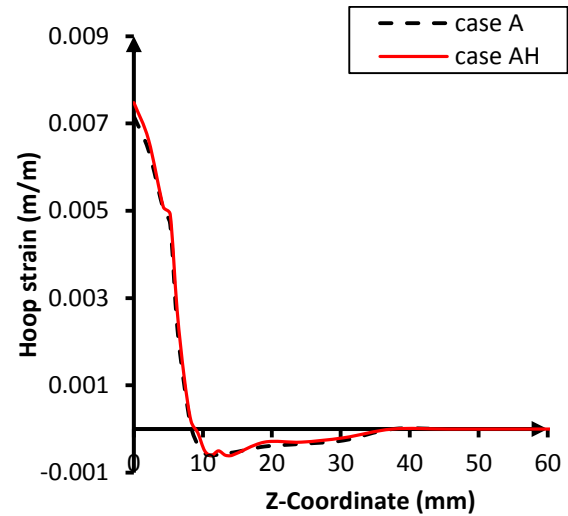


Figure 6-14 Hoop residual strain at 180° central angle on the outer surface along the axial direction

As for the plastic strain on the outer surface, the critical axial and hoop plastic strain limit is also located at axial position with 24 and 37 mm starting from the WLC, respectively.

According to the proceeding comparison, it is noticeable that the absolute magnitudes of the residual axial plastic strain are much greater than those of the residual hoop plastic strain at the FZ and HAZ on the inner and outer surfaces. The intensity of constraint and the peak temperature characterize the effect of residual plastic strain on the material during welding process (Luo, 1997). As a result, the hoop plastic strain extent is larger than the axial plastic strain along the axial direction because of the influence of weld overlay and girth welding temperatures and the intensity of constraint in the circumferential direction (symmetric plane and lateral constraints at pipe ends). In other words, the intensity of constraints on the hoop direction is relatively larger compared to those on the axial direction. On the other hand, the axial plastic strain extent on the inner and outer surface is lower due to less restraints and temperature magnitudes with respect to that of the hoop plastic strain.

6-5. Residual Stress and Plastic Deformation

6-5-1. Residual Stresses on the Inner Surface

The axial residual stress distributions on the inner surface, which is made of AISI304 stainless steel for two cases, are compared against the experimental results obtained from residual strain gauges at 180° central angle from start/stop welding as shown in Figure 6-15. The numerical results for case A are only affected by the welding process, whereas for case AH they take into account the pre-heat treatment to insert the liner inside the backing pipe. Both cases are plotted in the same graph along the axial direction starting from the WCL in order to facilitate the comparison. From the figure, it is observed that the peak residual axial stress at the weld zone of C-Mn, 606 MPa, is higher than the value of yield strength for welding and base materials of C-Mn and AISI304 at room temperature. The values of residual axial stress at the HAZ of weld overlay are lower than the yield stress of the liner base material at room temperature, 265 MPa. From Figure 6-15, we can also find out that the bifurcation between case A and case AH starts at 24 mm far from the WCL. The distributions of two cases diverge away smoothly to reach $Z=77$ mm at which the divergence limit is being the widest and then remains constant. Beyond $Z=77$ mm, the maximum variation between the axial residual stress distributions on the inner surface in case A and case AH is about 164 MPa (absolute value) where case AH reaches 122 MPa.

It is clear that the distributions of two cases are significantly close within the FZ and HAZ, for $Z \leq 24$ mm. Furthermore, the experimental results are consistent with the numerical results of both cases. Within the range $24 < Z < 77$ mm, the axial residual stresses are subjected to the effect of the welding process and the pre-heat treatment, and the experimental results are located between the distributions of two cases.

To shed light on these ranges more, the FZ and HAZ are heated up higher than other areas which make the base material AISI304 soft enough. Consequently, the inherent residual stresses, which existed in the base material because of the heat treatment, are removed completely. Thus, the axial residual stress distribution in case AH goes along with that in case A at the inner surface. Beyond $Z \geq 24$ mm, temperatures during welding are drastically lower and their effect disappears completely at $Z > 77$

mm. In other words, the closer the distance from the WCL, the bigger the convergence between case A and case AH is. Therefore, beyond $Z \geq 77$ mm, the initial axial residual stress on the inner surface is not affected by welding process.

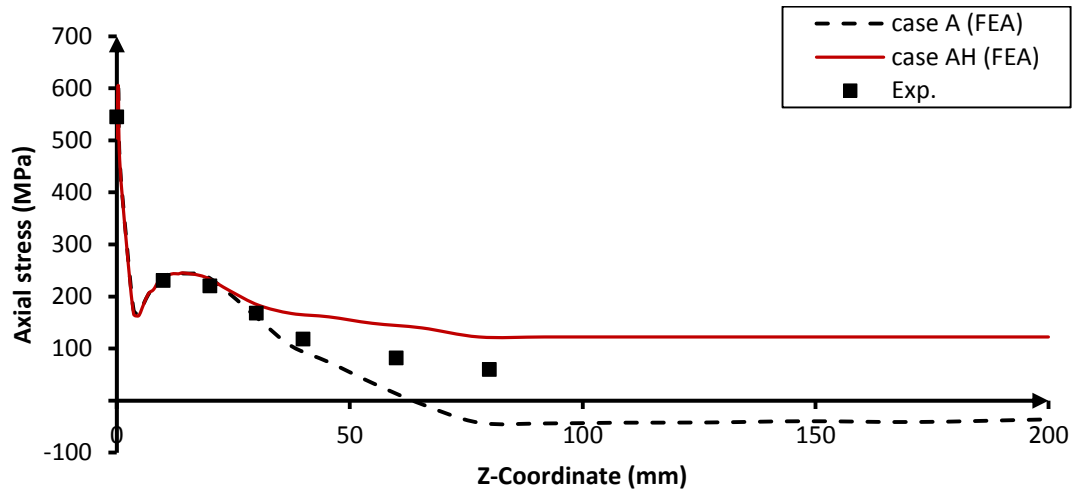


Figure 6-15 Axial residual stress at 180° central angle on the inner surface along the axial direction

Figure 6-16 shows the hoop residual stress distributions on the inner surface for case A and case AH with the experimental points at 180° (central angle). It could be seen that the peak hoop tensile stresses is located at the FZ of the weld overlay, equal to 578 MPa, which is larger than the yield stress of AISI304 welding material. In similar way, two limits characterise the hoop residual stress distribution in case A and AH. Again, it can be observed that, up to a distance of 37 mm away from the WCL, there are no remarkable discrepancies between case A and case AH. Beyond this limit, the divergence between two cases expands to be stable at point ($Z = 91$ mm) where the divergence amplitude reaches 161.7 MPa (absolute value), at which case AH attains 113 MPa. Beyond $Z = 91$ mm, for both cases the residual stress remains constant along the axial direction. It is obvious that within the range $37 \text{ mm} \leq Z \leq 91 \text{ mm}$ the final hoop stresses are affected by both the welding process and the inherent residual stress resulted from the pre-heat treatment. The more influence the welding process has, the closer the distance from the WCL. Therefore, the

experimental points are also located above the distribution of case A and below the distribution of case AH.

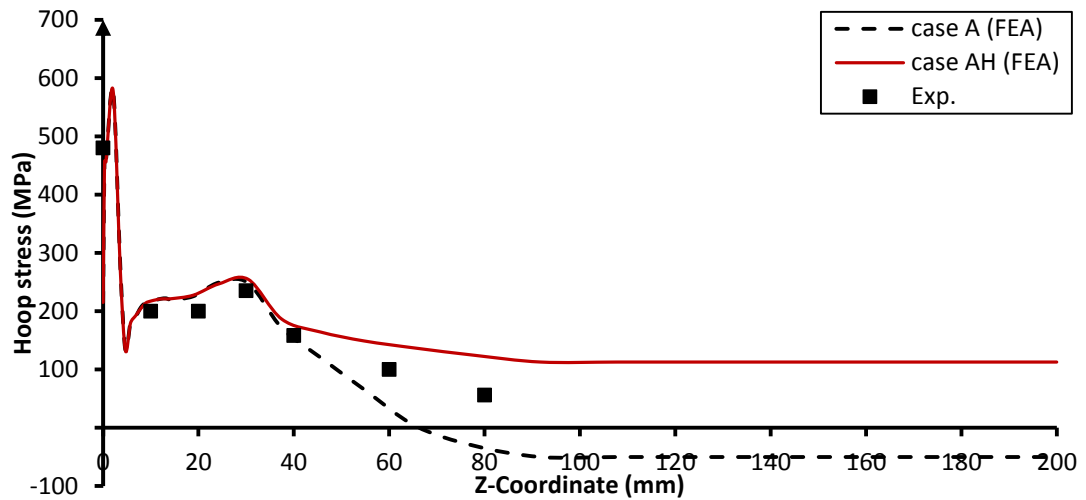


Figure 6-16 Hoop residual stress at 180° central angle on the inner surface along the axial direction

6-5-2. Residual Stresses on the Outer Surface

Figure 6-17 shows the axial residual stress distributions on the outer surface, which is made of C-Mn, along the axial direction of the lined pipe at 180° (central angle) for cases A, AH and the experimental results. Two cases are plotted in the same graph to compare case A with case AH in which the pre-heat treatment is considered. Similarly to what already discussed for the residual stresses on the inner surface, there is a good correlation between the results of case A and case AH at the FZ and HAZ within the range $Z \leq 24$ mm. Beyond this limit, a slight bifurcation occurs between two cases, but then the results intersect again before reaching a constant value. At the zone $Z \geq 77$ mm, the distance between the axial residual stress distributions keeps to a large extent constant for case A and case AH. The experimental results are in good agreement with two cases.

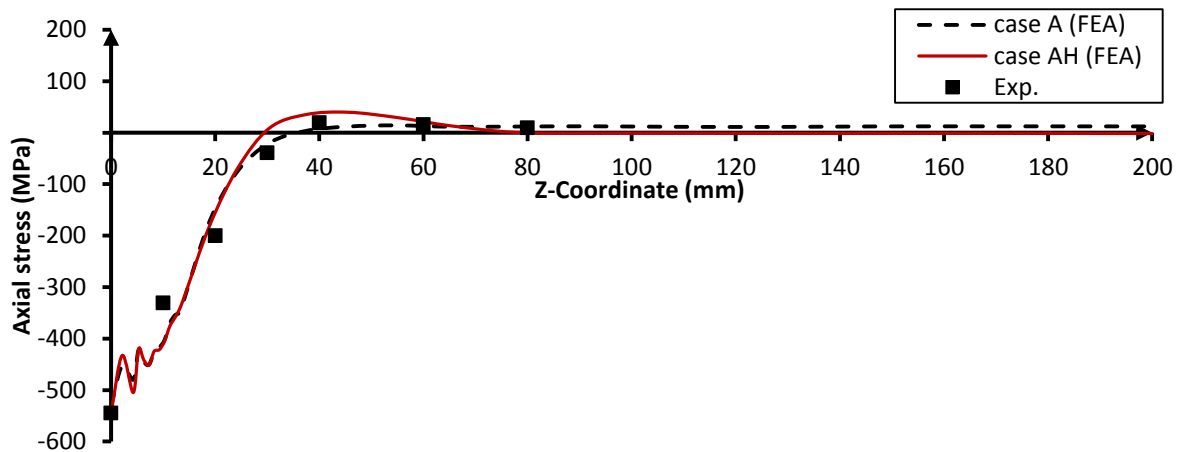


Figure 6-17 Axial residual stress at 180° central angle on the outer surface along the axial direction

In a similar way, the same discussion is applied for the hoop residual stress distributions in case A and AH on the outer surface at 180° from start/stop welding location as depicted in Figure 6-18. The two distributions slightly branch at $Z = 37$ mm. Beyond $Z = 91$ mm, case A distribution is being stable to some extent with zero stress and case AH distribution is stable with slightly positive stress. Within the range $Z < 37$ mm, there is only a slight difference between the distributions of case A and case AH at the FZ. The experimental results are again in good agreement with both distributions.

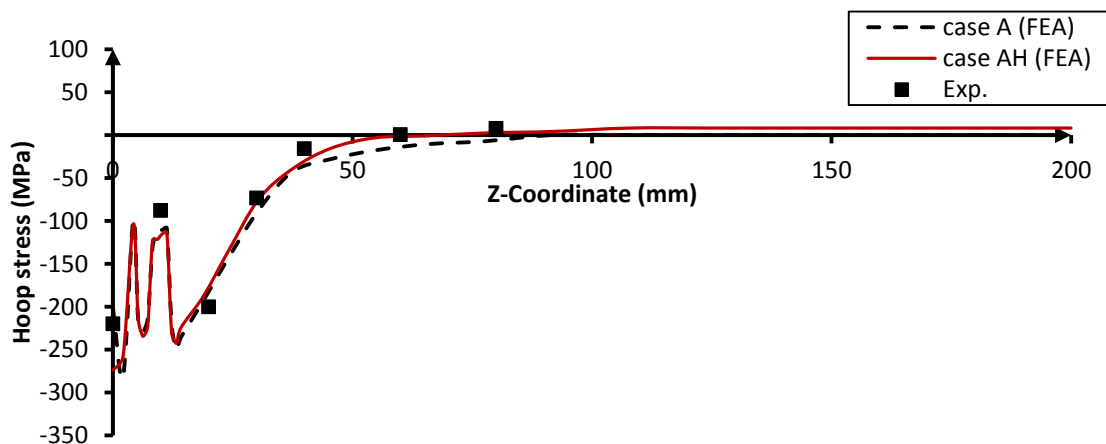


Figure 6-18 Hoop residual stress at 180° central angle on the outer surface along the axial direction

It can be observed that the residual axial stress distributions on the inner surface and outer surface have opposite shape for both cases because of the shrinkage of the lined pipe radius during cooling after completing the welding process. As a result, a bending deformation is produced in the lined pipe resulting in compressive residual stresses on the outer surface and tensile residual stresses on the inner surface. For example, Figure 6-19 shows the magnitude of reduction in the pipe radius on the inner surface along the axial direction at location of 180° from start/stop point for case A and case B. It could be seen from this figure that the maximum shrinkage in case A and AH is located at $Z = 2.1$ mm far away from the WCL with 0.44 mm and 0.53 mm reduction in pipe radius, respectively.

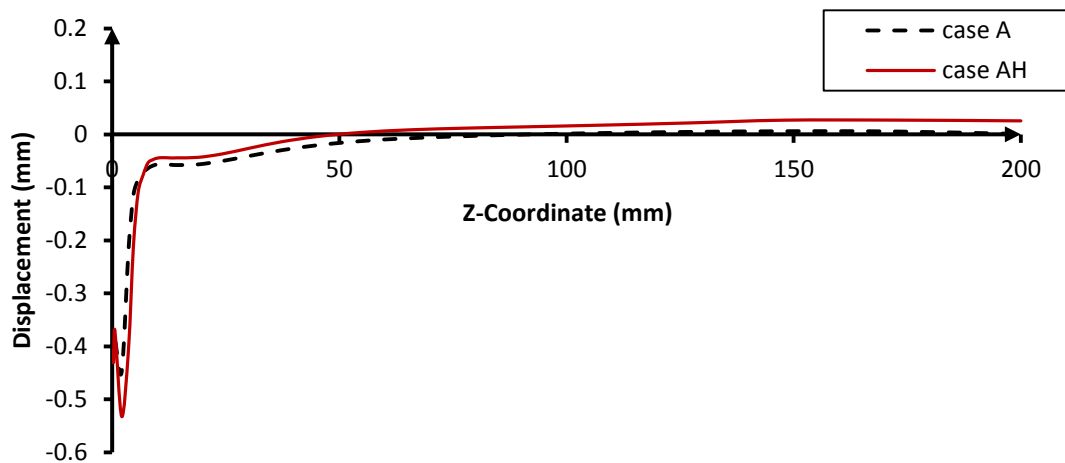


Figure 6-19 Radial shrinkage at 180° central angle on the inner surface along the axial direction

6-6. Verification of the Experimental Results

To check the accuracy of experimental thermal and mechanical results, the welding test was repeated two times for case A, with the same conditions every time. The thermocouples and residual stress gauges using were placed in the same locations for both tests. To double check the reliability of residual stress results, X-ray diffraction XRD has also been used for the first test.

Figure 6-20 compares the thermal history recorded from TC1 and TC4 for two tests at 180° central angle. It can be noticed that the peak temperatures and cooling rate are extremely close.

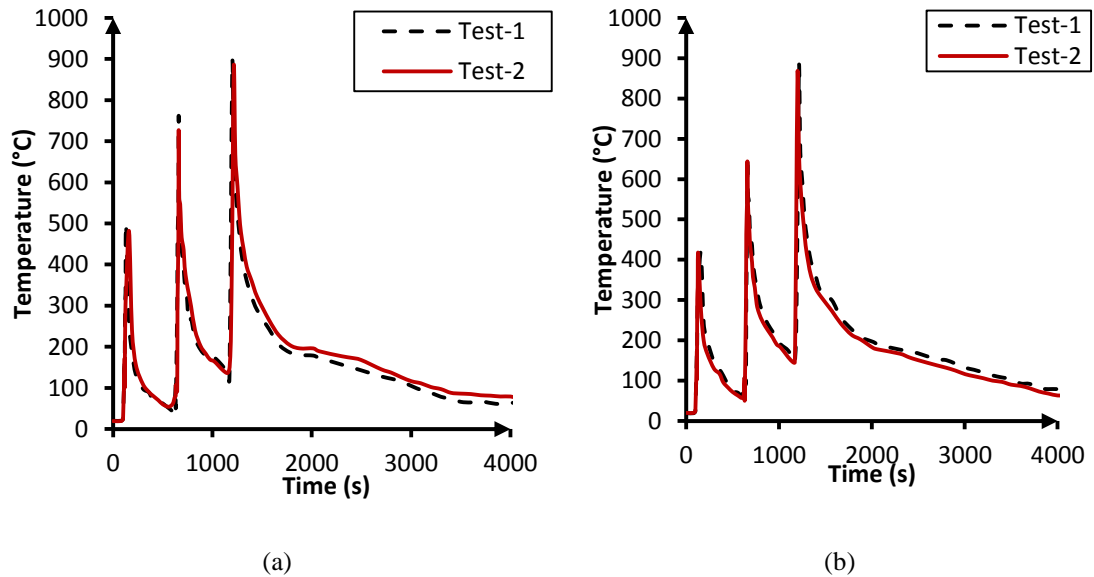


Figure 6-20 Temperature results of repeated tests for case A at (a) TC1 and (b) TC4 at 180° central angle

Figure 6-21 shows the axial residual stresses on the inner and outer surfaces obtained by the hole-drilling technique using residual stress gauges, FRS-2, for two tests. Also, the residual stress results of XRD for the first test are plotted in the same figure. It could be observed that all results in the first test are consistent with their counterparts in the second one and the results of XRD prove the reliability of the experimental residual stress results.

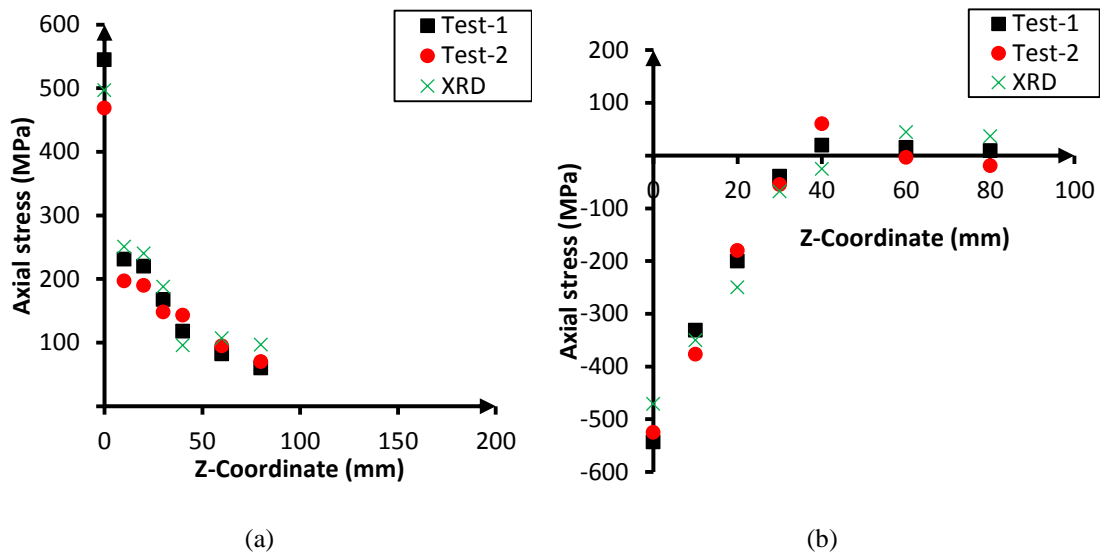


Figure 6-21 Axial residual stress results of repeated tests for case A on (a) the inner surface and (b) the outer surface at 180° central angle

6-7. Conclusions

This chapter has presented the results of 3-D FE thermomechanical simulations of the welding process of a lined pipe, executed using ABAQUS 6.13-1, compared with the experimental results. The study included an investigation of the effect of the pre-heat treatment on the thermal fields and residual stresses. To produce the lined pipe, the TFP is an essential process to insert the liner (AISI304 pipe) inside the backing pipe (C-Mn pipe). Unfortunately, this process could generate initial residual stresses in the lined pipe which in turn may initiate cracks growing during service and cause detrimental damage in case of critical operating conditions. The initial residual stress levels generated by the TFP are based on the temperature levels and the mechanical properties of both base materials. In this chapter, the numerical and experimental results have proven that the initial residual stresses due of TFP are important in AISI304 pipe whereas hardly existed in C-Mn pipe. According to the numerical and experimental results in this work, the following conclusions can be drawn:

- (1) Based on the thermal results, it is clear that the temperatures of all points located on the same circumferential line are quite constant when the welding torch moves to fill the weld overlay and the girth welding. From the outcomes of our investigation, it is possible to conclude that the temperature

fields are not sensitive to the variations of the circumferential angles. Furthermore, the thermal history during welding is not completely affected by the TFP process because that the temperature returns back to room temperature during naturally cooling for 7200 seconds. During TFP, the liner temperature sharply ramp up in 4.30 seconds from -200°C to meet the temperature of C-Mn pipe at 419°C .

- (2) The high temperature strain gauges on the inner surface record a larger drop in the axial and hoop strains just before the welding torch is close enough to the location of the particular gauge than their counterparts on the outer surface during both the weld overlay, and the first and second girth welding. This can be attributed to the increase in pipe radius because of heating nearby the welding torch.
- (3) The lengths of the zones with significant axial and hoop plastic strains along the axial direction are based on the intensity of constraint and the peak temperature. Consequently, the hoop plastic strain zone is wider than that of the axial plastic strain along the axial direction. Furthermore, these are also the lengths of the zones with significant residual stresses induced by the welding process.
- (4) The residual stress distributions are divided into three sections. In the first one closer to the WCL, the residual stresses are solely affected by the welding process. The length of this zone depends on the extent of the axial and hoop plastic strains. The second one stretches from the previous limit to the limit where the residual stress distributions become constant along the length. This section is under the influence of both the welding process and the TFP pre-heat treatment. The last section starts when the residual stress distribution has become quite constant, in which the pipe is just under the influence of the initial residual stresses resulted from the TFP process. The initial residual stresses are relatively small in the AISI304 pipe whilst they are negligible in the C-Mn pipe for case AH.
- (5) Welding tests have been repeated two times thermally and mechanically. Due to importance of residual stresses, X-ray diffraction has been used to double check the residual results obtained by residual strain gauges. All thermal and

mechanical results in the first test are consistent with their counterparts in the second test.

Chapter 7

Parametric Study of Lined Pipe Welding

7-1. Introduction

Welding is a reliable process widely used in industry to join two specimens together with high strength bond. In particular, Oil and Gas applications significantly depend on welding. Although it is a necessary process, the main problems of using welding arise from high temperatures to pour filler materials in welding grooves, which in turn lead to residual stresses concentrated in the FZ and HAZ. Therefore, predicting the locations and magnitudes of residual stresses after completing the welding operation is important to determine the reliability and integrity of welded structures. Welded cylindrical structures such as boilers, pressure vessels and transportation pipes are widely used in Oil and Gas units. Therefore, the precise prediction of the thermal and strain fields due to the circumferential welding is a major concern for estimating the maintenance works and working life of cylinders which contribute to avoid sudden failure during service. The FEM is an effective tool to predict the temperature and residual stress behaviours induced by welding. Validation of the FEM results against small-scale experimental results steers to guarantee the FEM results on large-scale models where there is no need to do more experiments consuming time and money.

A lot of research work has been conducted to study the isothermal and residual stress fields induced by circumferential welding, and the reader is referred to the literature review in Chapter 2 for a detailed review. However, there are no detailed experimental or numerical studies conducted for lined pipes. In particular, no study has investigated the influence of different factors on the quality of welding.

Therefore, further to the experimental and numerical results presented in Chapter 6, in this chapter, six cases have been conducted by changing different factors affecting

the quality and results of welding process. Case A is considered the reference case, where the weld overlay and girth welding have been modelled with different materials of their base metals, accordingly, and is the same case studied in the previous chapter (Chapter 6). In case B, the material of girth welding is the same material used in the weld overlay, which is austenitic stainless steel. Case C considers the effect of neglecting the weld overlay where the two joints of lined pipe have been solely adjoined using girth welding. In this case, the material of girth welding is the same used in case A. The heat input plays a key role in the quality of welding and consuming the rod materials used in TIG welding (Gery et al., 2005). Therefore, in case D, the heat input is lowered to 75% of the heat input in case A for all welds. In a similar way, the heat input in case E is dropped to 50% of that in case A. The last case is case F where the liner with weld overlay is not considered.

To study the effect of each specific parameter, the other parameters are kept constant and equal to the values of the reference case (case A). Furthermore, the mesh topology for all FE models remains the same as in case A. The thermo-mechanical properties used for case A in the previous chapter are the same properties applied in case A herein. In this work, the numerical thermal fields and residual stress distributions are compared against the experimental ones in all cases by means of thermocouples and hole-drilling strain gauges.

7-2. Results and Discussion

7-2-1. Thermal Results

Incorporating the heat source movement within the heat transfer analysis during welding is complicated by mathematical and physical issues, because of the need of considering two different types of welding (weld overlay and girth welding) associated with two different parent materials at the same time. It is important to validate the FE model experimentally to verify the accuracy of the moving heat source and heat transfer equations. The macrograph of cross section at 270° in case A has been taken by means of microscope where the FZ and HAZ boundaries are clearly distinct as shown in Figure 7-1. From this figure, it could also be seen that the predicted FZ and HAZ isotherms correlate well with the numerical one. The

minimum temperature value at the FZ is 1365 °C and 1500 °C for weld overlay and girth welding, respectively. The HAZ extends in the FZ vicinity to attain minimum 800 °C.

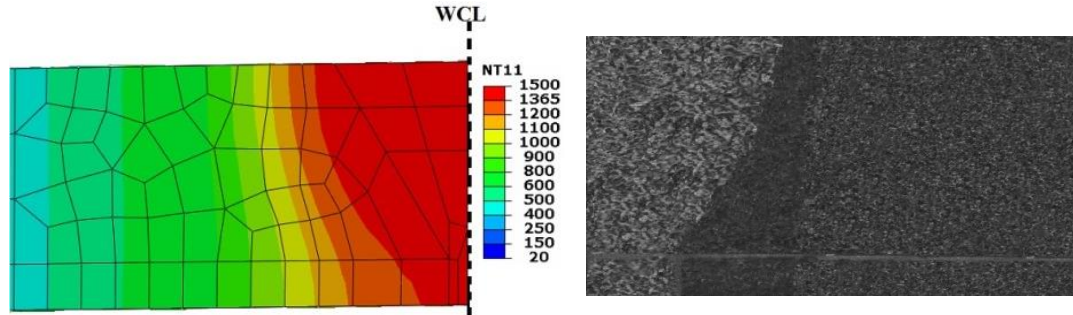


Figure 7-1 Experimental and numerical macrograph at 270° central angle

Consequently, the measured and numerical results of FZ and HAZ isotherms prove that the accuracy is not only in the thermal equations used in this work but also in the parameters applied on these equations such as welding pool geometries and heat input values.

As discussed in Chapters 5 and 6, the movement of the heat source during the one-pass weld overlay and the two-pass girth welding has been simulated by coding the DFLUX subroutine according to Eq. 6.6 using the same variable values given in Table 6-5. Moreover, the heat transfer subroutine FILM utilizes the same equations (6.3-6.5) associated with same variables in Table 6-4.

To record the thermal history, thermocouples, type K, were placed at 6 axial locations with 270° central angle for all cases. Three thermocouples were mounted on the outer surface (C-Mn pipe) and the others on the inner surface (AISI304) to record the thermal history upon these locations during welding and cooling as shown in Figure 7-2.

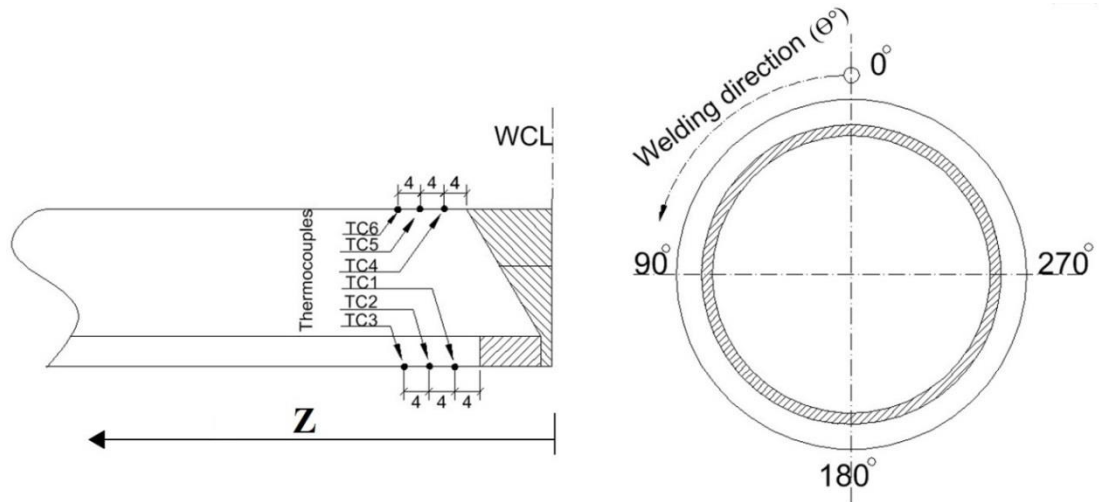


Figure 7-2 Locations of thermocouples and the welding direction for three passes, dimensions in mm

Table 7-1 shows the peak temperatures at the six thermocouples during the weld overlay, the first and second pass of girth welding. The numerical temperature gradients are also compared with the results recorded experimentally.

Table 7-1 Comparison between numerical and experimental results at six location during welding

Case	Pass		Inner surface °C			Outer surface °C		
			TC1	TC2	TC3	TC4	TC5	TC6
A	Overlay	Num.	540	350	271	446	342	271
		Exp.	525	343	265	432	333	263
	1-Girth	Num.	798	565	450	709	554	448
		Exp.	775	550	441	695	540	435
	2-Girth	Num.	929	703	573	918	690	570
		Exp.	913	685	562	910	681	558
B	Overlay	Num.	538	348	271	446	341	271
		Exp.	525	331	260	430	332	264
	1-Girth	Num.	790	564	450	708	554	448
		Exp.	775	552	443	690	539	441
	2-Girth	Num.	928	704	574	911	692	570
		Exp.	911	685	561	895	680	561
C	Overlay	Num.	-	-	-	-	-	-
		Exp.	-	-	-	-	-	-

D	1-Girth	Num.	689	482	374	614	472	374	
		Exp.	670	471	362	605	460	361	
	2-Girth	Num.	894	669	539	878	658	537	
		Exp.	882	650	525	865	645	525	
	Overlay	Num.	408	271	212	345	268	212	
		Exp.	401	265	208	337	262	208	
E	1-Girth	Num.	610	440	352	552	432	353	
		Exp.	600	431	340	540	422	339	
	2-Girth	Num.	716	553	453	701	548	453	
		Exp.	701	542	438	688	535	451	
	Overlay	Num.	276	191	151	240	188	151	
		Exp.	270	185	145	232	179	142	
	1-Girth	Num.	412	306	248	388	302	248	
		Exp.	405	301	245	375	295	235	
	2-Girth	Num.	496	387	320	492	386	320	
		Exp.	485	375	315	485	378	315	
	F	Overlay	Num.	-	-	-	-	-	-
			Exp.	-	-	-	-	-	-
1-Girth		Num.	730	531	417	610	475	374	
		Exp.	721	520	412	600	461	362	
2-Girth		Num.	1010	744	599	875	655	535	
		Exp.	992	732	585	861	645	526	

Comparing thermal results of case A against case B, it could be observed that the peak temperatures of all points are close enough to each other where the difference is less than 10 °C in all points. Consequently, changing the girth welding material to austenitic stainless steel does not have influence on the thermal results during welding. This can be attributed to the thermal properties, namely the specific heat and conductivity, which are close to each other especially at high temperatures.

In case C, the differences in temperatures measured by thermocouples drop drastically down compared with case A during the first pass of girth welding because the inter-pass temperature is neglected in case C. In the second pass of girth welding, the variations in temperatures between two cases are significantly narrower.

Decreasing the heat input which comes from the heat source leads to a strongly decrease in temperatures during all welding passes. In more detail, the maximum temperatures predicted and recorded by thermocouples in cases D and E are significantly lower than their counterparts in case A. Furthermore, temperatures in case D are larger than those in case E because case D has 75% of the heat input of case A, whilst case E just has 50%.

Removing the liner and weld overlay in case F keeps the whole thickness minimized to that of the C-Mn pipe, equal to $t = 6.35$ mm. In this case, it can be seen that the peak temperatures recorded and predicted at each thermocouple during the first girth welding pass are lower than their counterparts in case A because the inter-pass temperature is not there anymore. During the second pass of girth welding, the temperatures in case F are higher than those in case A on the inner surface where the thickness of pipe is 6.35 mm. On the outer surfaces, the temperatures are much closer to their counterparts in case C.

It could be observed that there is a good agreement between the numerical and experimental temperatures which are within the maximum variation of less than 6%. Thus, the developed thermal FE models for all cases can be considered further validated experimentally. Also, the disparity between the results of case A and other cases becomes larger as the distance from the WCL decreases. It is also observed from Table 6.1 that the thermocouple upon either the outer or inner surface located nearer to the WCL experiences a peak temperature higher than that located farther to the WCL (Yaghi et al., 2011).

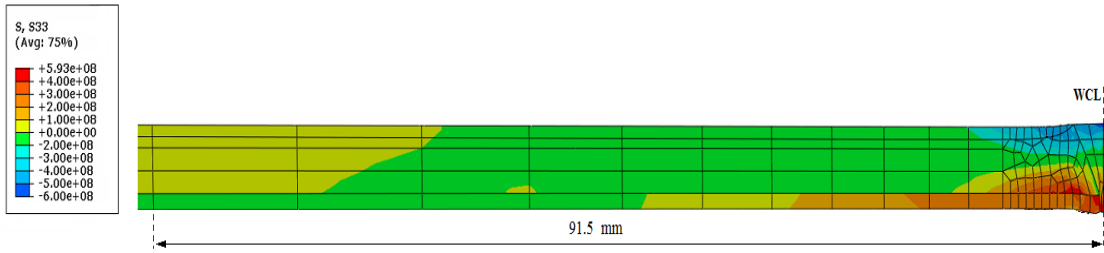
7-2-2. Structural Response

In this section, case A is considered the reference case to be compared with other cases. Only half of the lined pipe is examined due to symmetry. In case A, the axial residual stress distributions at 270° central angle are depicted in Figure 7-3(a) The bottom row of elements is the liner, AISI304 pipe, with the weld overlay, whereas the rest of pipe is the backing steel pipe, C-Mn pipe, with the girth welding. It could be seen that maximum axial residual tensile stresses are located at the toes of the girth welding, weld overlay and HAZ on the inner surface. On outer surface, the tensile stresses on the inner surface are balanced by the compressive stresses on the

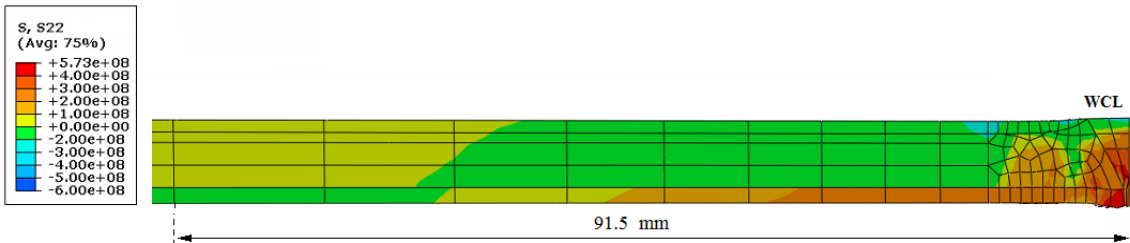
FZ and HAZ of girth welding (Sattari and Farahani, 2009). Therefore, axial bending deformation is produced through the pipe cross section. As a result, the diameter of lined pipe becomes smaller in the FZ and HAZ regions after cooling down to room temperature because of the radial shrinkage (Dar et al., 2009). Also, it could be seen the length needed to reverse the tensile stresses to compressive on the inner surface is narrower than that to reverse the compressive stresses to tensile on the outer surface.

Turning to the hoop residual stress distributions shown in Figure 7-3(b), the absolute values of tensile stresses in the FZ and HAZ on the inner surface are significantly larger than those of the compressive stresses in the girth welding region and its vicinity on the outer surface. The magnitudes of residual axial stresses have a significant influence on the value of residual hoop stresses (Lee and Chang, 2008). The lengths of reversal stresses on the inner and outer surface are somewhat close to each other.

It is evident that the area of C-Mn steel at which the weld overlay is fixed with the C-Mn pipe has axial and hoop tensile residual stresses higher than the yield stress of the C-Mn base material. This region is affected more than others by the thermal cycles of weld overlay, first pass and second pass of girth welding. Consequently, it is more likely that a crack initiates at this point as shown in Figure 7-4. In particular, the crack has not been modelled in lined pipe. Consequently, the welded lined pipe model would not capture cracking initiation and propagation as a cutting trajectory, but used to simulate the regions which could likely contain crack formation and propagation. Furthermore, choose other metals with different properties could lead to completely change the path of crack propagation based on the residual stress levels in the model. As a result, the material properties should be taken into account with other metals.



(a)



(b)

Figure 7-3 (a) Axial and (b) hoop residual stress distributions of case A at 270° central angle

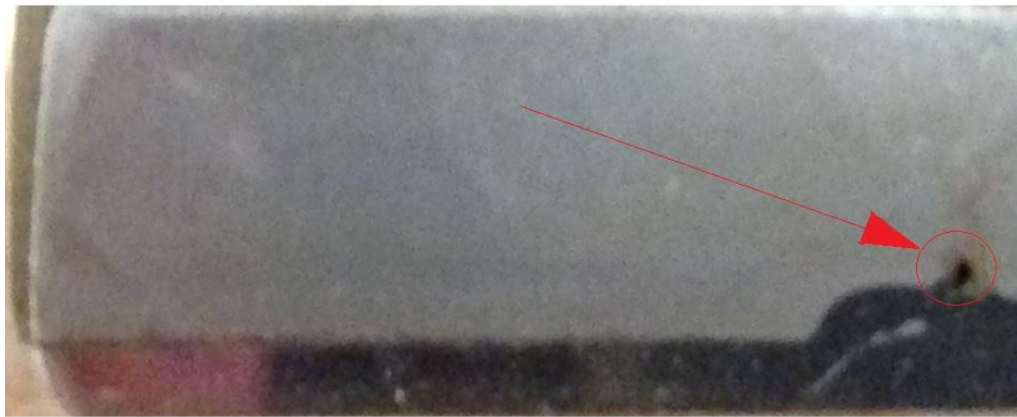


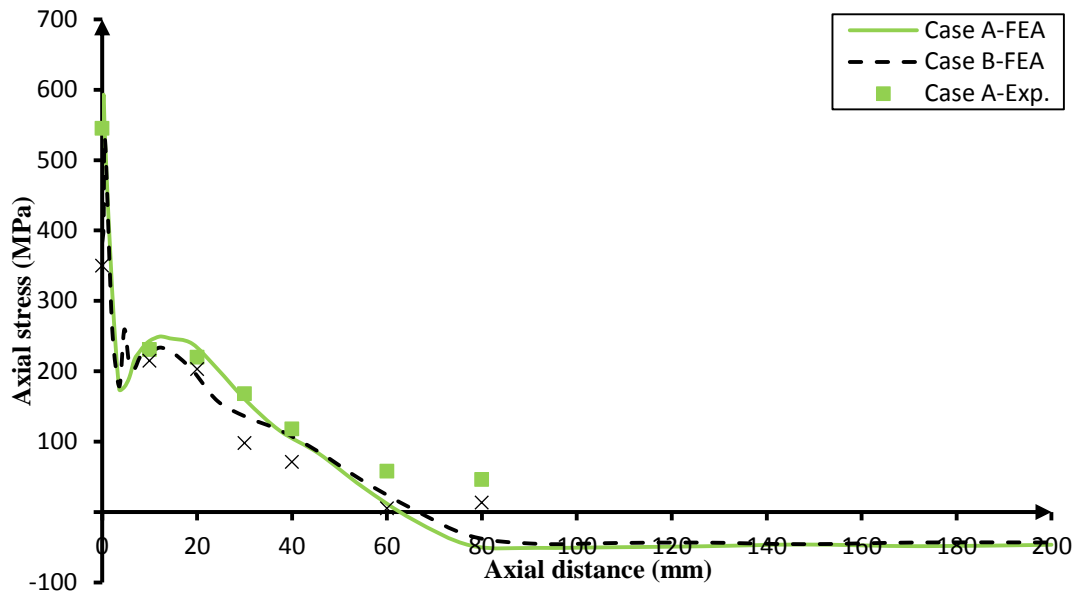
Figure 7-4 Initiation and growth of crack at the area of C-Mn pipe above weld overlay

7-2-2-1. Effect of Welding Materials on Residual Stresses

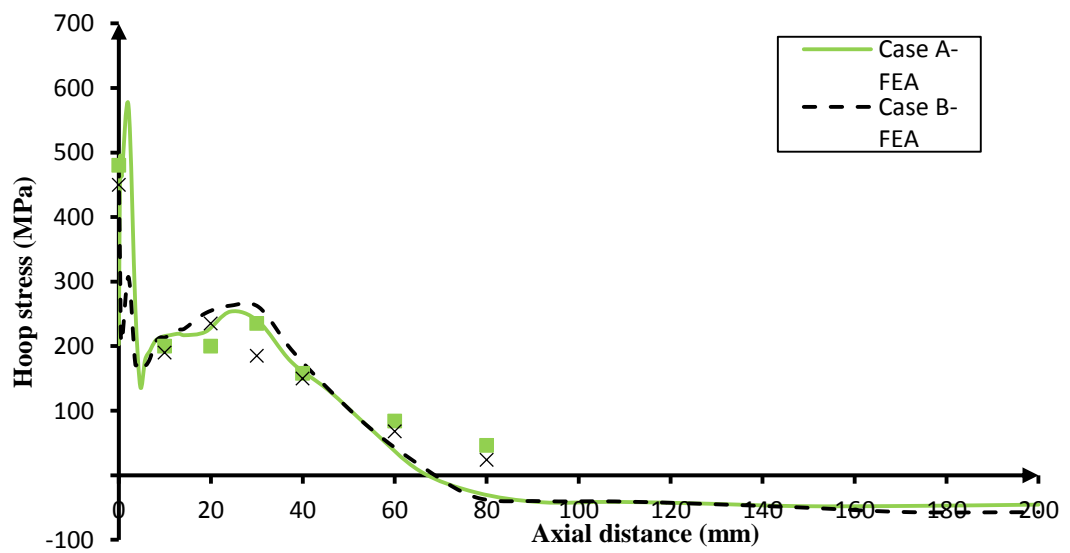
To avoid cracking and corrosion in the FZ, stainless steel is a proper material to join two specimens together. Stainless steel is more capable to expand and contract naturally during welding because of its larger coefficient of thermal expansion (British Stainless Steel Association, 2016). Conversely, carbon steel is a good conductor of heat which in turns will cool more rapidly and shrink faster as the joint cools (Benson, 2014). Moreover, stainless steel has a better corrosion resistance than carbon steel because of its chemical compositions. As a result, stainless steel welding is preferred more in oil and gas industry.

Figure 7-5(a)-(d) shows a comparison between the numerical results for case A and B at 270° central angle from the start/stop welding point along the axial direction starting from the WCL, $Z=0$. The experimental results are also plotted for both cases accordingly using residual stress gauges. The numerical axial and hoop residual stress distributions on the inner surface (liner) for both cases are in a good correlation except at the toes of weld overlay and girth welding ($Z \leq 3.6$ mm). Within this zone, the maximum axial residual stress is 593 MPa at $Z = 0.3$ mm in case A whilst the maximum one in case B is 529 MPa located at $Z = 0.6$ mm as shown in Figure 7-5(a). Similarly on the circumferential direction, the maximum hoop residual stress is 573 MPa at $Z = 2.1$ mm in case A whereas the maximum one in case B is 481 MPa on the WCL. On the outer surface, it can be seen that significant discrepancies exist between the numerical results of case A and B in the FZ and its vicinity, for $Z \leq 45$ mm, as shown in Figure 7-5(c) and (d). Beyond this zone, the results in both cases are almost identical in the axial and hoop residual stress distributions.

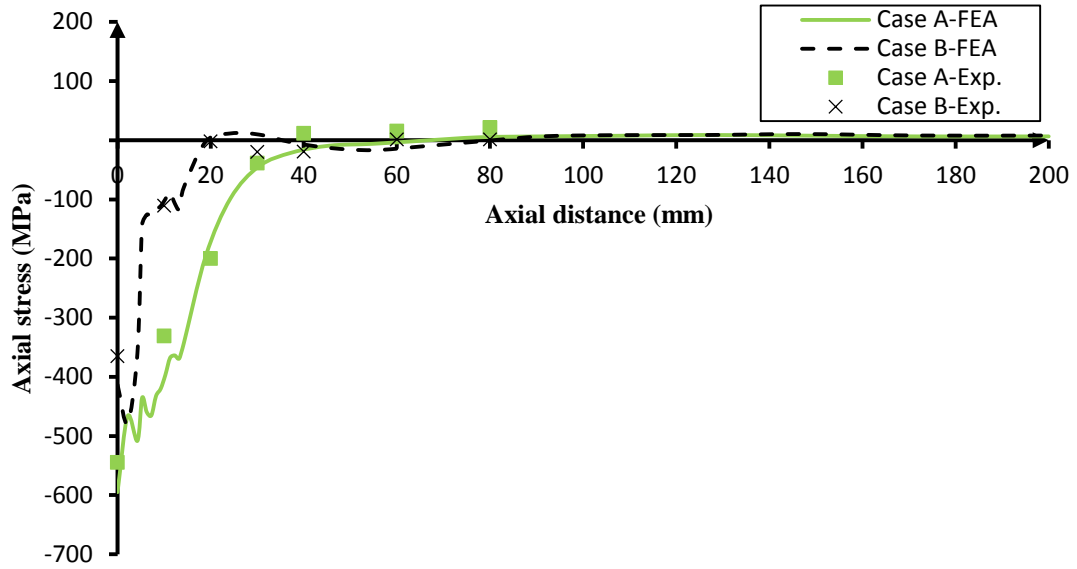
The experimental results recorded on the inner and outer surface with 270° central angle are consistent well with the numerical results in the FZ and HAZ because the initial residual stresses produced by heat treatment are removed by the high temperatures of welding. Beyond this range, temperature magnitudes are significantly lower. As a result, the initial stresses still remain in the pipe and the experimental results are somewhat larger.



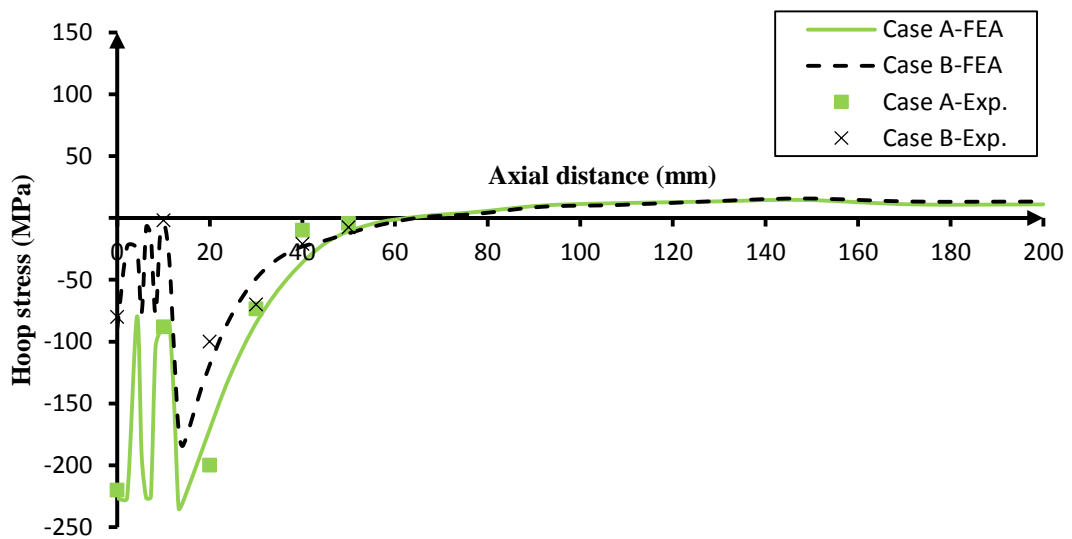
(a)



(b)



(c)



(d)

Figure 7-5 Comparison of residual stresses at 270° central angle between case A and case B: (a) axial stress distributions on the inner surface, (b) hoop stress distributions on the inner surface, (c) axial stress distributions on the outer surface, and (d) hoop stress distributions on the outer surface

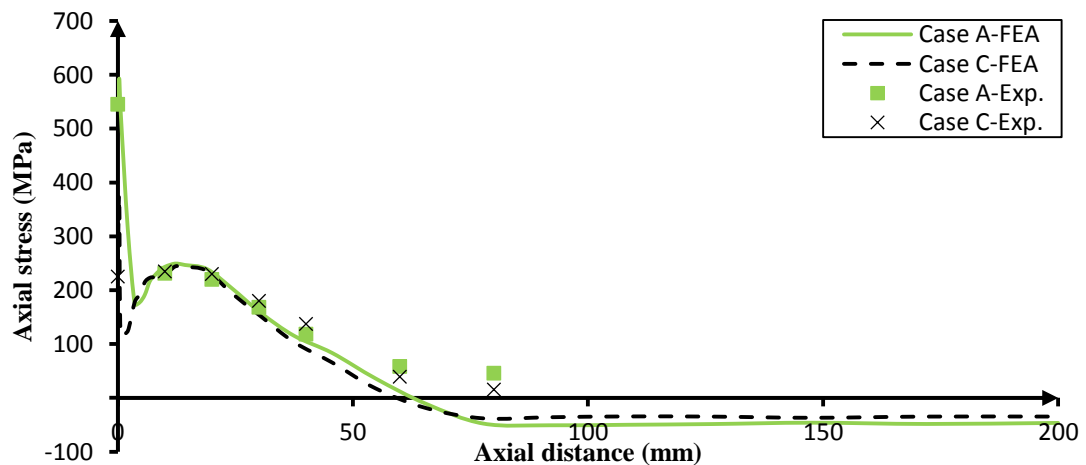
7-2-2-2. Effect of Welding Overlay

Omitting the weld overlay results in allowing dust and grease to go inside the gap between the liner and backing steel pipe. Consequently, these go inside girth welding and deteriorate the quality of girth welding by forming voids and inclusions.

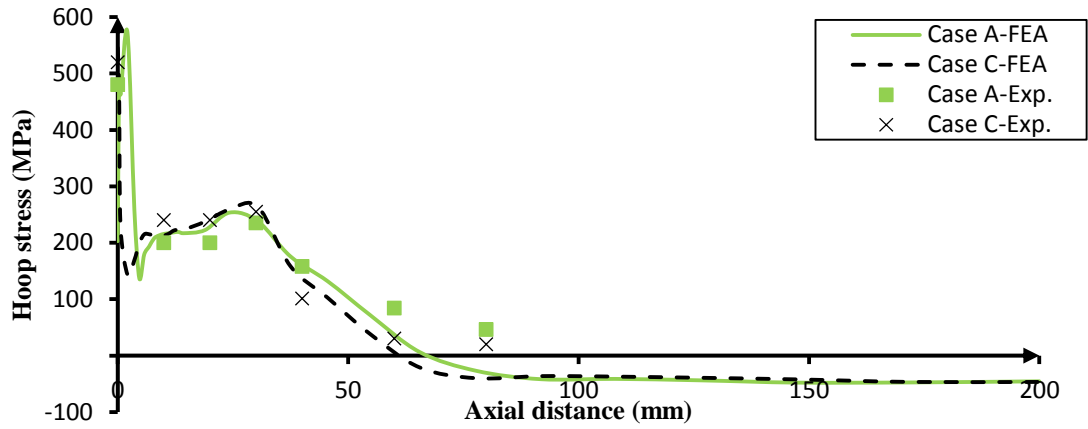
Therefore, in case C welding is conducted without weld overlay to study the influence of this factor on the stress behaviour.

Figure 7-6(a)-(d) shows the hoop and axial residual stress distributions at 270° central angle on the inner and outer surfaces for cases A and C. In this figure, the experimental results are also plotted along the axial distance. It could be observed that there is a significant discrepancy in the axial residual stress at the WCL where it is 540 MPa and 252 MPa in case A and C, respectively. Beyond these weld zones, the axial residual stress distributions in both cases A and C are much closer to each other as shown in Figure 7-6(a). Similarly on the hoop direction, there is a difference in the hoop residual stress at the weld zones. Beyond that, the results are closer to each other in both cases as depicted in Figure 7-6(b).

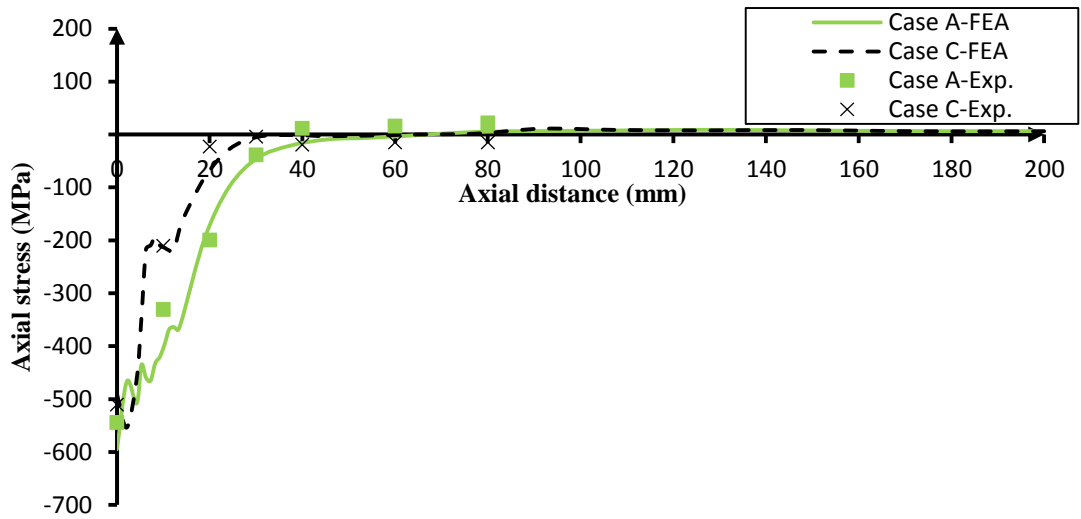
On the outer surface, there are significant discrepancies between the results of axial and hoop residual stress in case A with their counterparts in case C at the weld zone of girth welding and its HAZ as shown in Figure 7-6(c)-(d). The experimental results are in good agreement with the numerical results for both cases at the FZ and HAZ but they are larger beyond that especially at the inner surface due to the effect of initial residual stresses of pre-heat treatment.



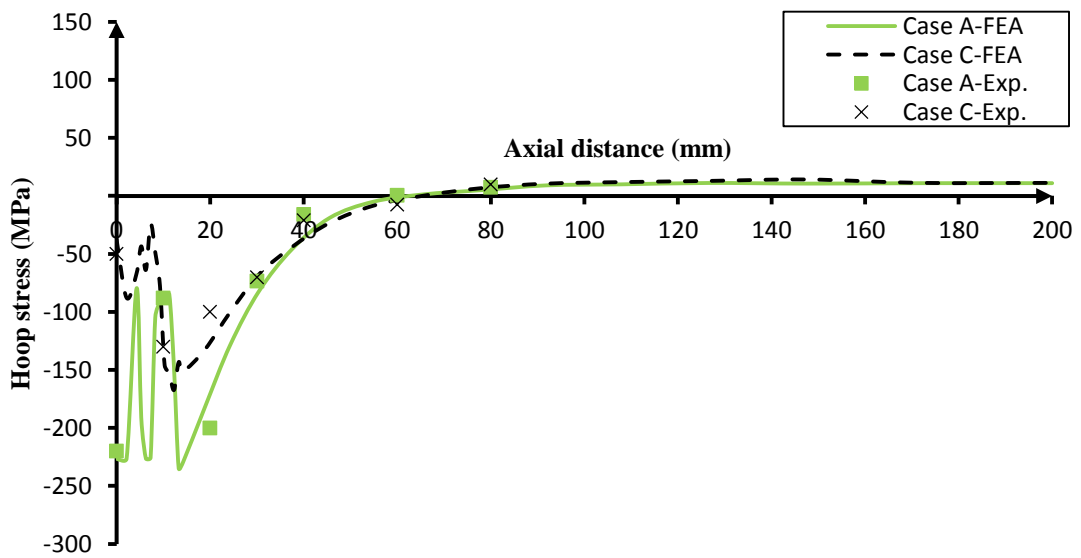
(a)



(b)



(c)



(d)

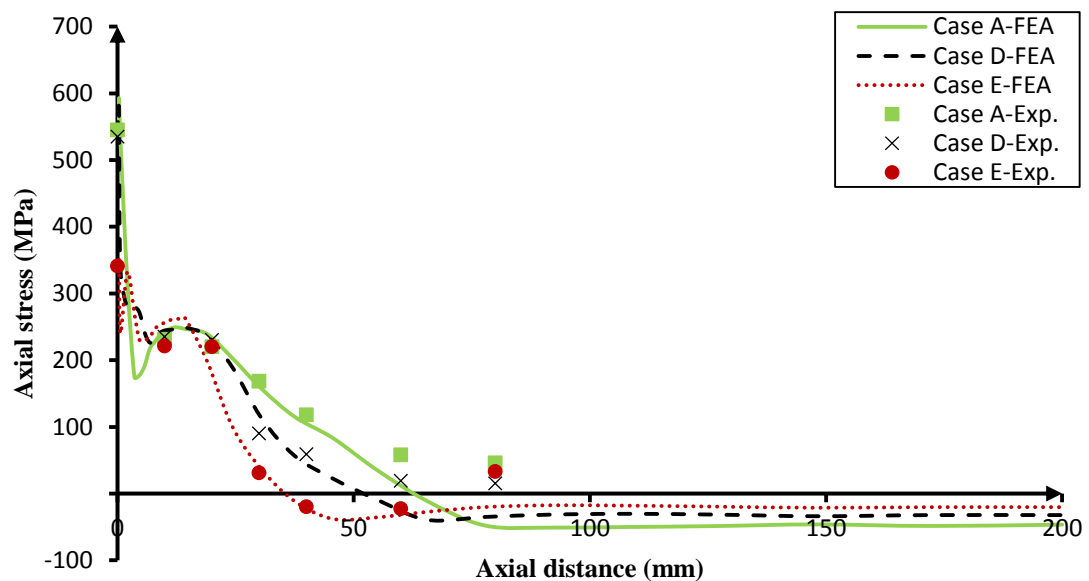
Figure 7-6 Comparison of residual stresses at 270° central angle between case A and case C: (a) axial stress distributions on the inner surface, (b) hoop stress distributions on the inner surface, (c) axial stress distributions on the outer surface, and (d) hoop stress distributions on the outer surface

7-2-2-3. Effect of Heat Input on Welding Residual Stress

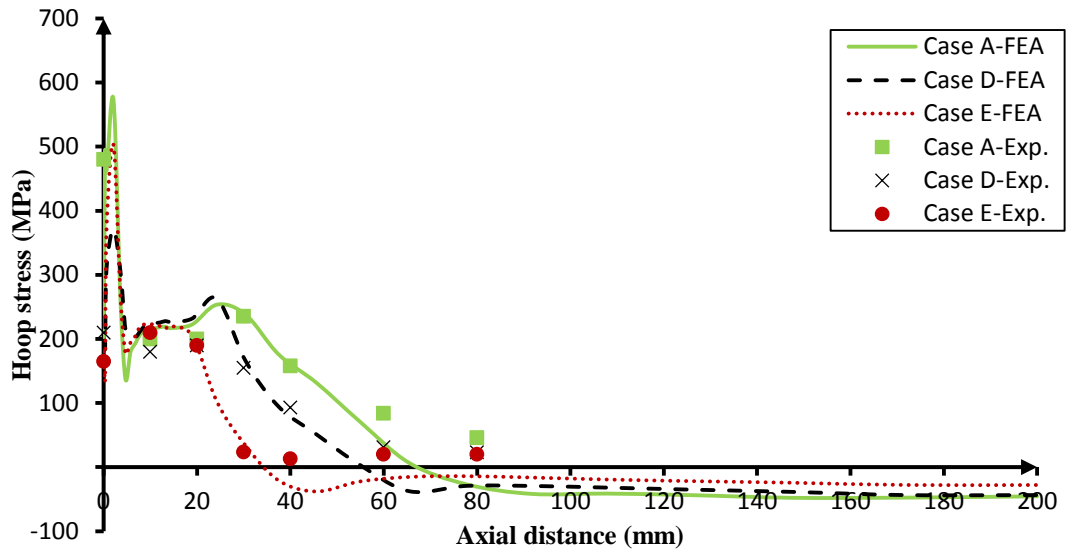
The heat input plays a key role in affecting the temperature distributions, which in turn leads to significant changes in residual stresses. In this section, all welding parameters are kept constant, such as the welding speed and welding pool geometries. The total heat input, Q , is identified as $Q = IV\mu$ (watt) where I is current (amperes), V is voltage (volts) and μ is the weld efficiency. In case A, the total heat inputs are 850, 1700 and 1800 watt for weld overlay, first-pass of girth welding and second-pass of girth welding, respectively. These parameters go along with the American Welding Standard AWS D1 (2010) and API 1104 (2005) to get the required quality for all welding passes. Reducing the heat input has some benefits in reducing consumption of the rod in TIG welding provided the quality of welding is achieved without porosity (bubbles) in the weld because of lack of fusion. In this section, the influence of heat input on residual stresses has been investigated through cases D and E. The total heat input is lowered to 0.75 and 0.5 of the heat input of case A for case D and E, respectively. In more detail, the total heat inputs become 638, 1275 and 1350 watt for weld overlay, first-pass of girth welding and second-pass of girth welding in case D, respectively. In case E, the portions of heat input which have been provided to the weld overlay, first-pass of girth welding and second-pass of girth welding are 425, 850 and 900 watt, respectively.

Figure 7-7(a)-(d) portrays the axial and hoop residual stresses along the longitudinal distance starting from the WCL at 270° from the start/stop welding location in case A, D and E with measured results. On the inner surface (AISI304 pipe), the maximum axial residual stresses in three cases are located at $Z = 0.3$ mm at the toe of girth welding with 590, 577 and 352 MPa in case A, D and E, respectively, as shown in Figure 7-7(a). Turning to the hoop direction, it could be seen that the maximum tensile hoop residual stresses in cases A, D and E take place at the centre of the weld overlay region, $Z = 2.1$ mm, with 573, 371 and 502 MPa as given in Figure 7-7(b),

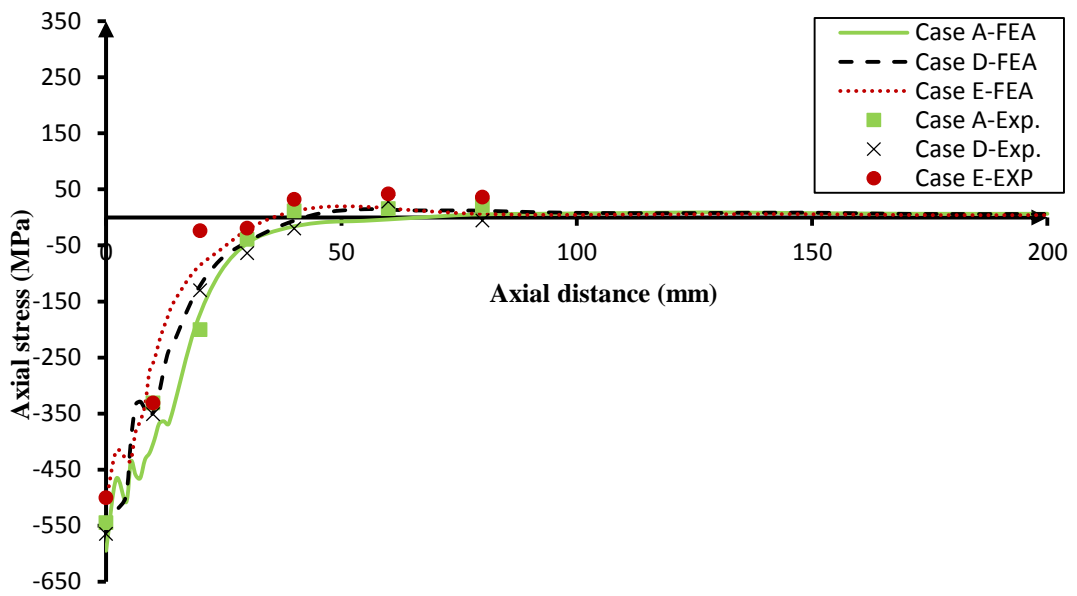
respectively. From Figure 7-7(a) and (b), it is observed that the length of the zone with tensile residual stress becomes narrower by reducing the heat input magnitude. Figure 7-7(c) and (d) depicts the axial and hoop residual stress distributions on the outer surface (C-Mn pipe) for cases A, D and E at 270° central angle with respect to the axial distance. The maximum axial compressive stresses on the outer surface are located at the WCL with -595, -561 and -508 MPa for three cases A, D and E, respectively. The lengths of the zones with compressive residual stress are slightly close to each other where the zone for case E is still narrower than others as clarified in Figure 7-7(c). It is observed that the magnitude of hoop residual stress on the outer surface is affected by its axial residual stresses. The larger the compressive axial residual stress is, the larger the compressive hoop residual stress is. In similar way, case E has the narrowest compressive range of other cases, as clarified in Figure 7-7(d). Likewise, experimental results are in a good correlation with their counterparts in the FZ and HAZ for all cases.



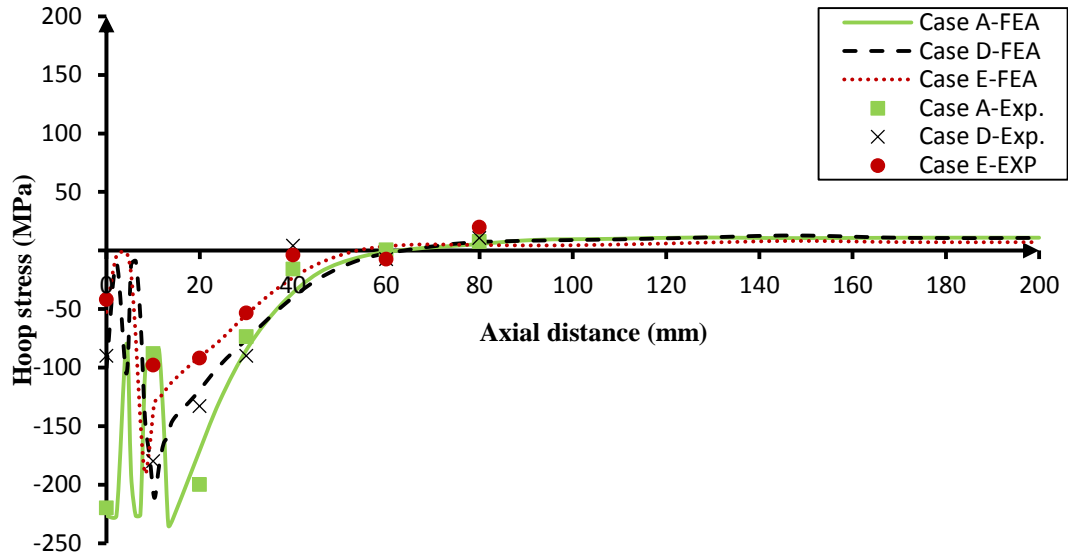
(a)



(b)



(c)



(d)

Figure 7-7 Comparison of residual stresses at 270° central angle among case A, case D and case E: (a) axial stress distributions on the inner surface, (b) hoop stress distributions on the inner surface, (c) axial stress distributions on the outer surface, and (d) hoop stress distributions on the outer surface

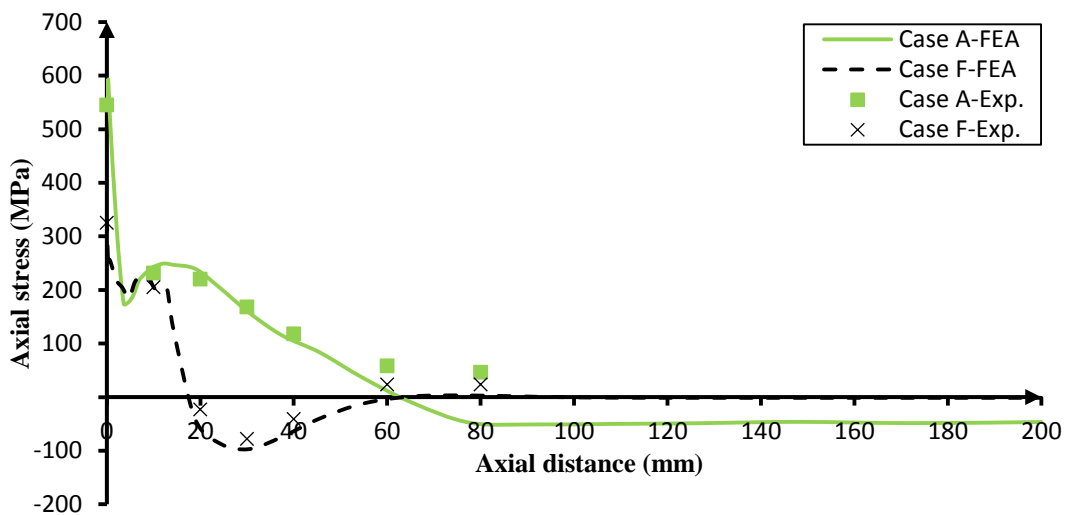
7-2-2-4. Effect of the Liner on the Welding Residual Stresses

The function of the liner is to protect the inner surface of the carbon steel pipe from corrosion. With this function, it is made of corrosion resistant alloy CRA, austenitic stainless steel. Consequently, removing the liner will not only lead to corrosion of the pipe in oil and gas applications but it will also affect the residual stress behaviour especially at welding regions.

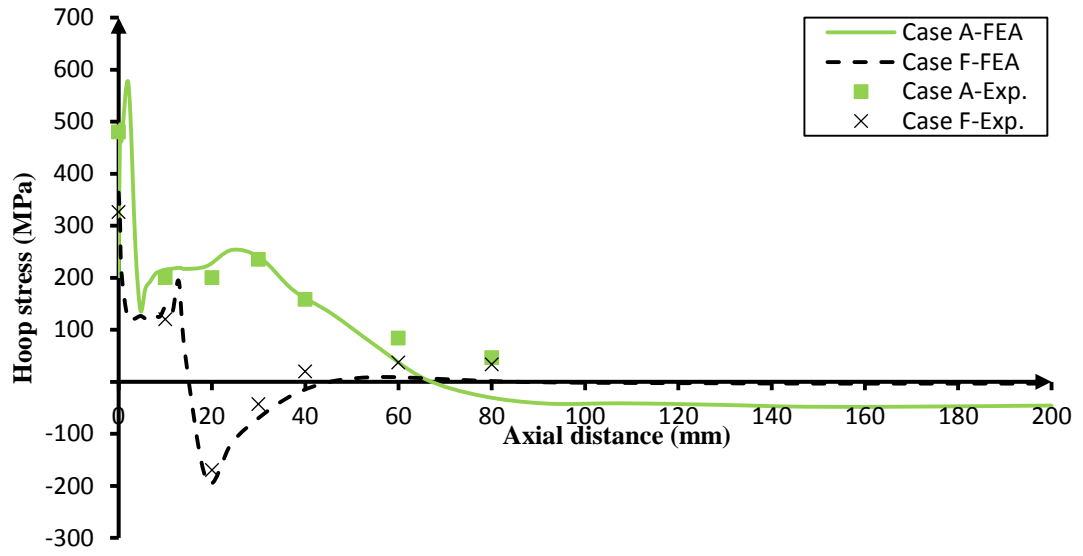
Figure 7-8(a)-(d) compares the axial and hoop residual stress distributions on the inner and outer surface numerically and experimentally for case A and case F in which the liner with weld overlay is removed. On the inner surface, the axial residual stress at the WCL in case F, 333 MPa, is lower than that in case A, 540 MPa, as depicted in Figure 7-8(a). On the hoop direction, the magnitude of hoop residual stress at the WCL in case F, 364 MPa, is larger than its counterpart in case A, 203 MPa. Afterwards, the hoop residual stress distribution drops rapidly down in case F whereas the distribution in case A goes sharply up within the weld overlay region as shown in Figure 7-8(b). Furthermore, the extent of the axial tensile stress in case F is

relatively narrower, $Z = 18.9$ mm, than that of case A, $Z = 65.5$ mm, on the inner surface as clarified in Figure 7-8 (b). This can be attributed to the absence of the liner and of the weld overlay at the inner surface which in turn slows down the heat transfer of the exposed surface to environment.

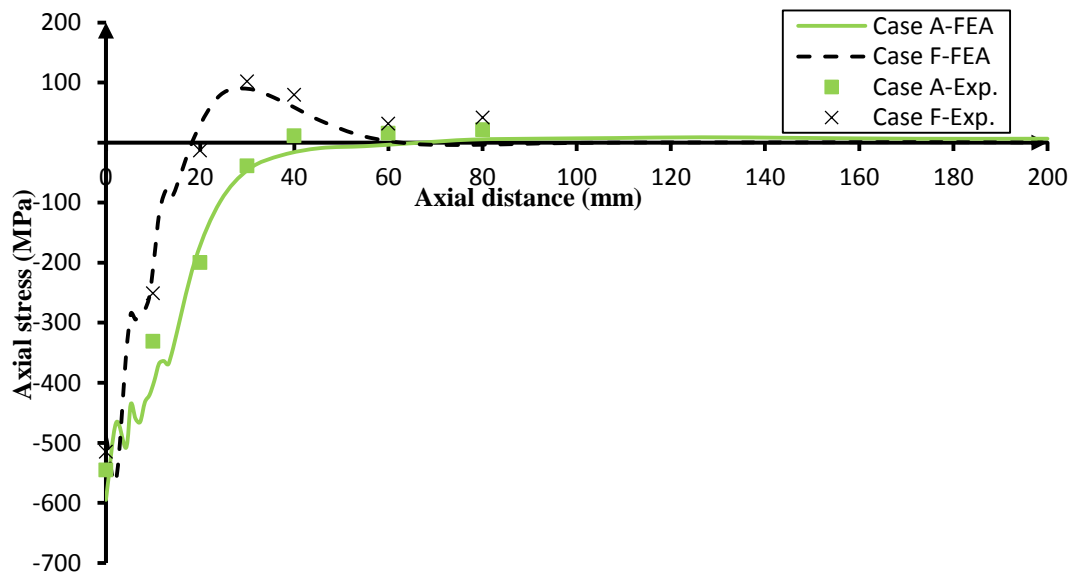
On the outer surface, the maximum compressive axial stress in case F, -562 MPa, is located within the FZ, at $Z = 2.1$ mm, whilst the maximum compressive axial stress in case A is located at the WCL, -595 MPa, as clarified in Figure 7-8(c). In both cases, the hoop residual stress distributions have a wave shape as shown in Figure 7-8(d). In a similar way, the compressive extent in case F is relatively narrower than that of case A. the numerical residual stress results agree reasonably well with the experimental results obtained by using the hole-drilling strain gauge method.



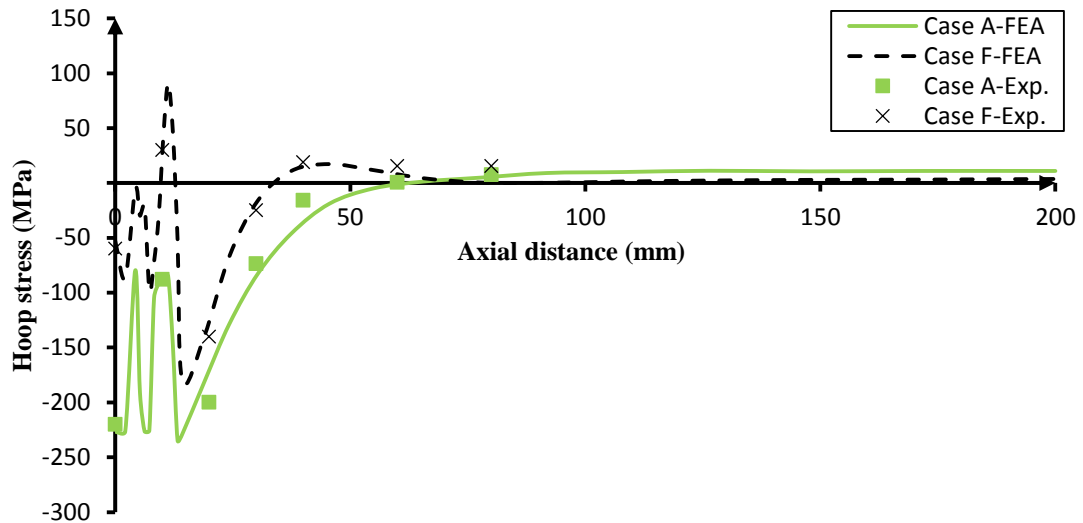
(a)



(b)



(c)



(d)

Figure 7-8 Comparison of residual stresses at 270° central angle between case A and case F: (a) axial stress distributions on the inner surface, (b) hoop stress distributions on the inner surface, (c) axial stress distributions on the outer surface, and (d) hoop stress distributions on the outer surface

7-3. Mesh Convergence Analysis

The FE mesh density plays a key role in determining the accuracy of thermal and mechanical numerical results. To assess such accuracy, a coarse mesh analysis has been used for both the thermal and the mechanical analyses for case A. The coarse mesh model consists of 14000 nodes associated with 2880 elements. The element type is DC3D20 and C3D20 in the thermal and mechanical analyses, respectively. Also, the element birth technique is adopted in the FEM coarse model to simulate depositing the filler materials in the weld overlay and girth welding during moving the heat source. The coarse mesh size is equal or larger than 1.5 times of the normal mesh size utilized in this study for case A (see Figure 6-3 in the previous chapter) where the coarse mesh model is composed of 40 circumferential elements instead of 60 elements as shown in Figure 7-9.

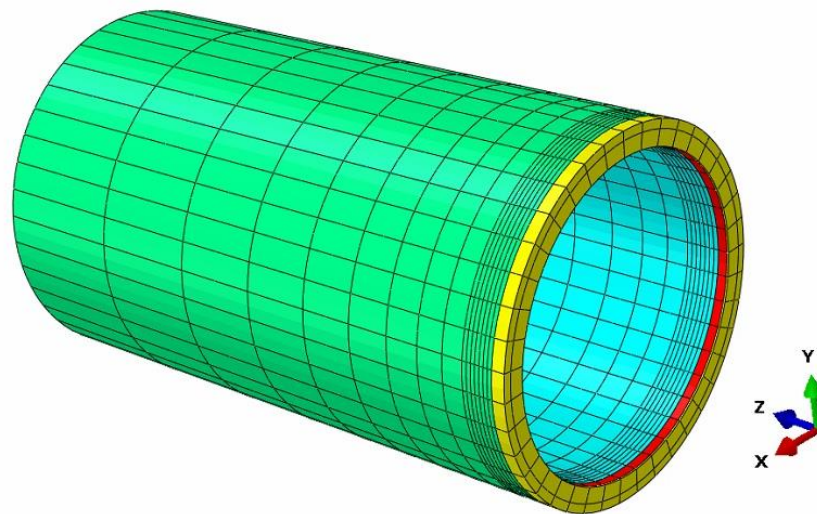


Figure 7-9 Coarse 3-D FE model

In the thermal analysis, Figure 7-10 compares the temperature distributions during weld overlay for the coarse mesh model, denoted as 1.5h, against the normal mesh model, denoted as 1h, at 90°, 180° and 270° central angle. The maximum temperature is achieved at the welding pool centre of weld overlay which is 1650°C in the coarse mesh model and 1634°C in the normal mesh model of case A.

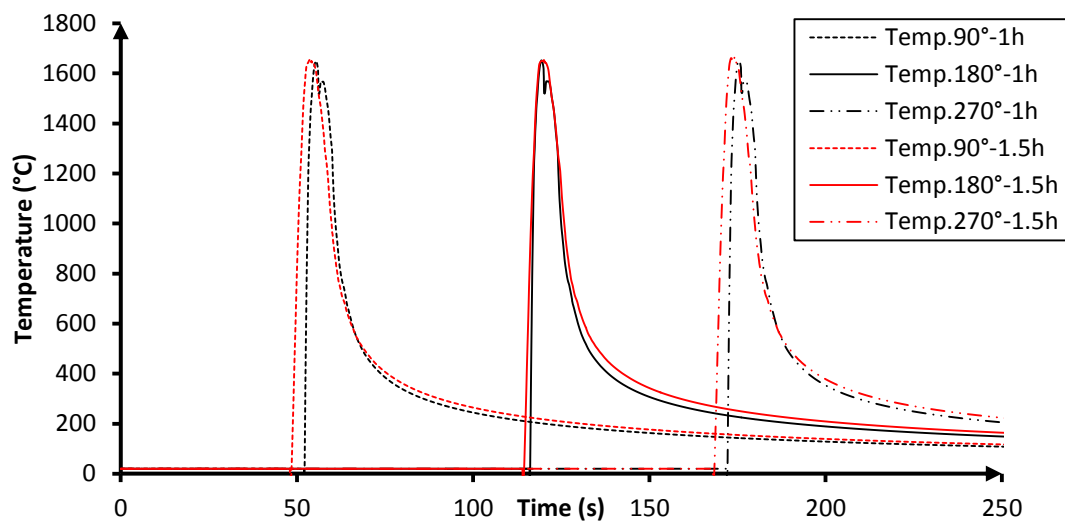


Figure 7-10 The thermal history of weld overlay centre at 90°, 180° and 270° central angle for coarse and normal mesh

Likewise, the temperature fields of the second pass of girth welding have also extremely close distributions around symmetric line at three locations, 90°, 180° and

270° central angle for the coarse and the normal mesh model. The peak temperature of the coarse mesh is 2085°C whereas the peak one of the normal mesh is 2076°C, as shown in Figure 7-11.

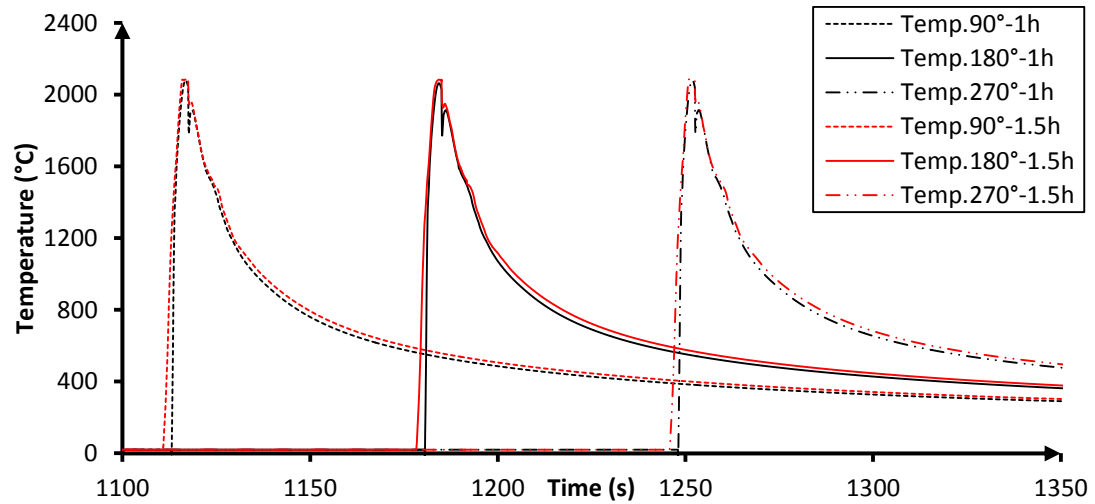
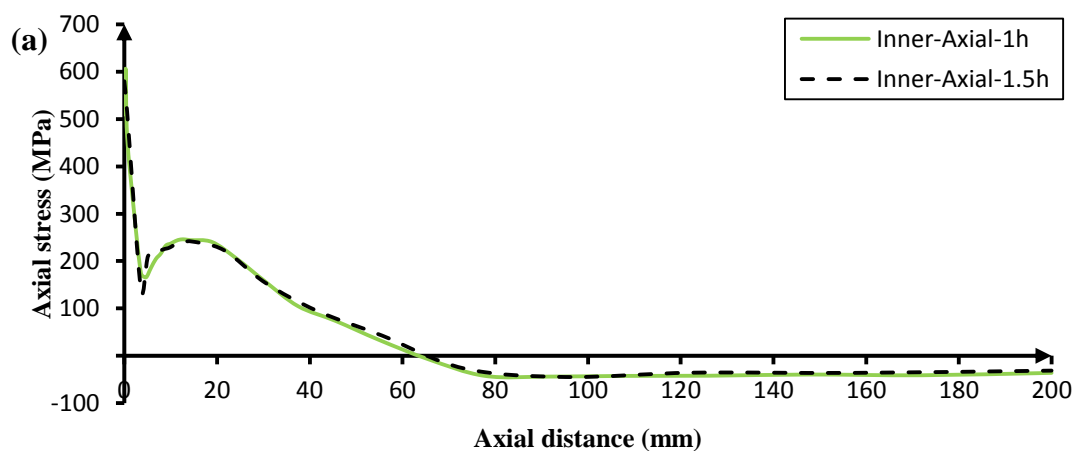


Figure 7-11 The thermal history of second pass centre of girth welding at 90°, 180° and 270° central angle for coarse and normal mesh

One may note that there is a very good correlation in the thermal fields between the coarse mesh and the normal mesh models. As a result, the residual stress distributions on the inner and outer surfaces for the coarse mesh model should also be consistent with the results of the normal mesh model of case A. Figure 7-12(a)-(d) plots the residual stress comparisons between the coarse mesh model and the normal mesh model at 270° central angle.



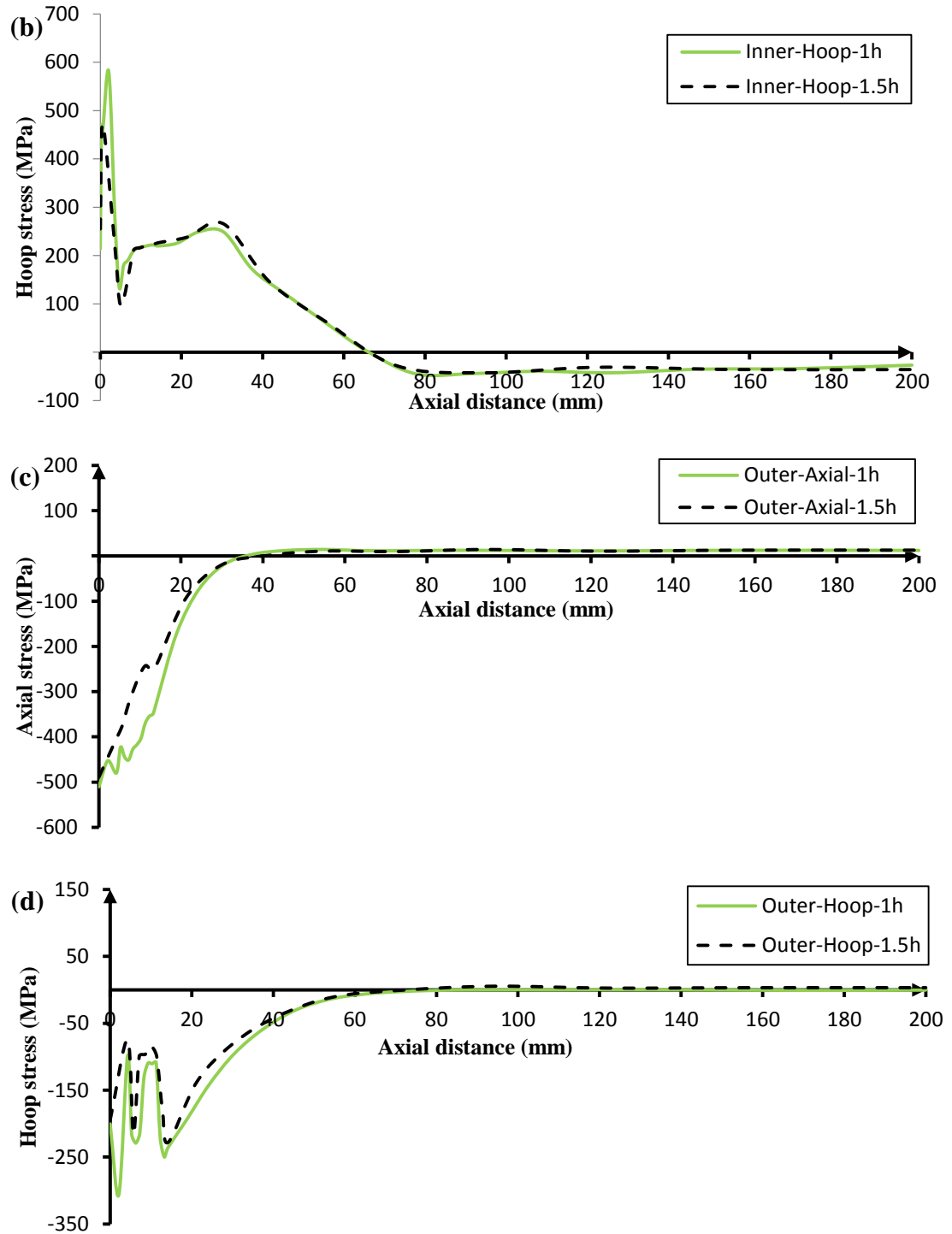


Figure 7-12 Residual stress distributions for coarse and normal mesh models at 270° central angle: (a) axial stress distributions on the inner surface, (b) hoop stress distributions on the inner surface, (c) axial stress distributions on the outer surface, and (d) hoop stress distributions on the outer surface

Consequently, the normal mesh used in cases A, B, C, D, E and F can be considered appropriate to obtain accurate numerical results thermally and mechanically.

7-4. Radial Shrinkage

Moving the heat source circumferentially to deposit the filler materials is mainly responsible for the radial shrinkage during lined pipe welding. In fact, the magnitudes of heat input provided during three welding passes are quite enough for the filler materials to flow through welding regions. Thus, a series of radial expansions is produced due to uniform high temperatures through the pipe thickness. After completing the welding process, subsequent radial contractions take place during solidification and cooling down to room temperature. As a result, a local inward deformation in the weld zones results in a simple linear bending in conjunction with compressive stresses over the outer surface balanced by tensile stresses on the inner surface. Moreover, the magnitude of radial shrinkage is significantly affected by the magnitude of axial stresses. Radial deformations on the inner surface of the lined pipe for six cases at 270° central angle with respect to the longitudinal direction starting from the WCL are plotted in Figure 7-13. It is noticeable that the case with larger axial tensile at the WCL has larger radial shrinkage. In other words, larger axial tensile residual stress on the inner surface leads to larger bending moment at the WCL which is in conjunction with radial shrinkage.

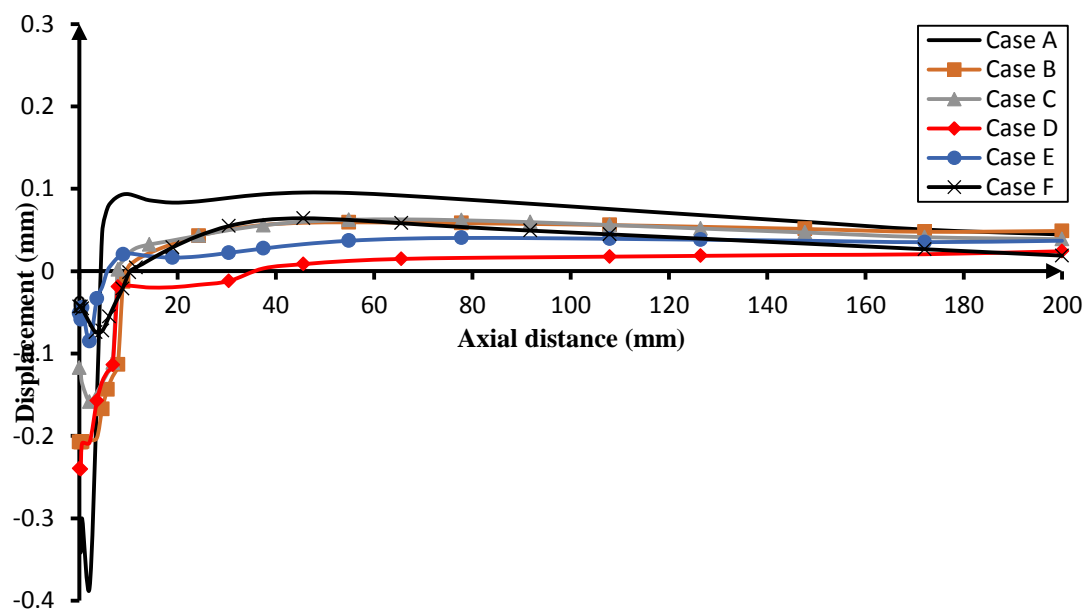


Figure 7-13 Radial shrinkage for six cases on the inner surface at 270° from the WCL

7-5. Conclusions

In this chapter, 3-D FE models have been developed and experimental tests have been conducted to study the influence of a number of factors on the thermal and structural response in lined pipe welding. These factors include welding properties (weld overlay and girth welding materials), geometric parameters (using weld overlay and liner) and welding process parameters (heat input). In detail, the thermal history and residual stress distributions have been studied for particular locations on the inner and outer surfaces in comparison with their experimental counterparts, measured using thermocouples and residual stress gauges. Based on the results, the following main conclusions can be drawn:

- (1) The numerical thermal results are consistent with the experimental results with variation less than 6%. Furthermore, the discrepancies between the thermal results of reference case A and other parametric cases decrease by heading far away from the WCL along the axial direction.
- (2) The tensile stresses on the inner surface are balanced by the compressive stresses on the outer surface at the FZ and HAZ to produce local inward deformation through the pipe cross section. The area of C-Mn pipe at which the weld overlay is fixed with the C-Mn pipe is affected by high thermal cycles, which in turn lead to higher hoop and axial tensile residual stresses and possible cracks forming.
- (3) Changing steel type of girth welding material from carbon steel to stainless steel leads to enhanced corrosion resistance and reduction in the axial and hoop residual stresses on the inner and outer surfaces at the FZ.
- (4) Omitting the weld overlay leads to a significant reduction in the axial and hoop residual stresses at the FZ on the inner and outer surface but the detrimental effect of leaving a gap between liner and C-Mn pipe should be taken into account.
- (5) Reducing heat input produces lower residual stresses at the FZ and its vicinity on the inner and outer surface.
- (6) The extents of tensile and compressive stresses on the inner and outer surfaces become significantly narrower by removing the liner.

- (7) Increasing the residual axial tensile stress leads to an increase in the radial shrinkage at the WCL.
- (8) Increasing the element size to 1.5 times of the normal one used in this work does not result in a significant change on the thermal and residual stresses results.

Chapter 8

Experimental and FE Models of Lined Pipe Impact

8-1. Introduction

Oil & Gas pipelines face indeed cyclic loading generated by fluid pressure changes, especially in the case of offshore pipelines which have high internal pressure, or as a result of waves and currents, the latter possibly leading to vortex-induced vibrations (Hilberink, 2011). Furthermore, corrosive production fluids make the use of C-Mn steel pipe for flow line impossible, whereby lined pipes are used as an alternative, as widely discussed in the previous chapters. Due to the high cost of lined pipe manufacturing, the thickness of C-Mn pipe is reduced, likely up to a half. In this case, the lined pipe is more affected by either the construction damage or the external interference (third party). In general, a dent can form as a result of construction damage or as a result of third party, but both of them can be responsible of catastrophic failure in pipelines.

Pipeline and Hazard Materials Safety Administration PHMSA (2007) reported that the external interference was responsible for 27% of failures in liquid transmission pipelines and for 31% of failures on natural gas pipelines in the USA. Furthermore, the failure resulted from third party damage could be either immediate or not immediate. In the latter case, generated cracks can grow and cause pipe failure in service after short time of the first impact. Thus, dented pipes require more monitoring and the high localized stresses in the dented zone need to be evaluated.

In Chapter 2, analytical and numerical methods proposed in the literature to conduct a stress analysis in dented pipes have been reviewed. However, one of the most critical problems in lined pipes is the stress/strain behaviour under dynamic impact

and it was observed that, to the best of the author's knowledge, very few articles in the literature have addressed the effect of dynamic impact on the lined pipes (compound pipes) using a non-linear numerical approach.

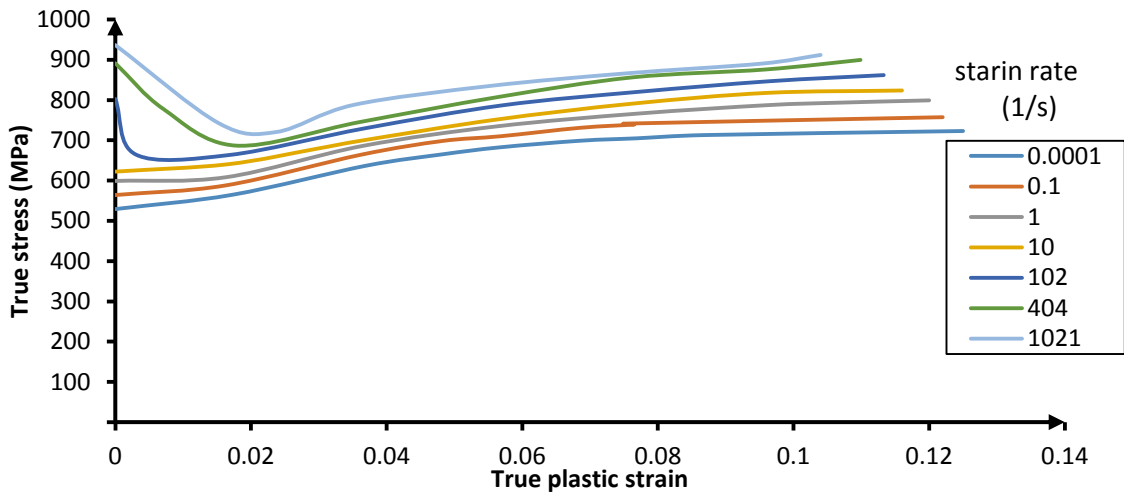
Therefore, main objective of this chapter is to study the stress and strain behaviour of small-scale lined pipe specimens, with and without liner, subjected to a radial collision from different heights, numerically and experimentally. To achieve this objective, a weight of 200 kg equipped with a semi-spherical indenter with diameter of 51.75 mm is dropped freely from 1, 1.5 and 2 m on specimens of C-Mn pipe without liner (case A) and with liner (case B). Additionally, some tests are repeated to assess the reliability and validity of the experimental results. Strain results are obtained by mounting different type of strain gauges to record the strain history during the whole impact process. In more detail, four strain rosettes (GR1, GR2, GR3 and GR4) are placed symmetrically around the expected dent centre which is located at the pipe middle section. The strain history is transferred from strain gauges to a data logger via LabVIEW code.

8-2. Numerical Model

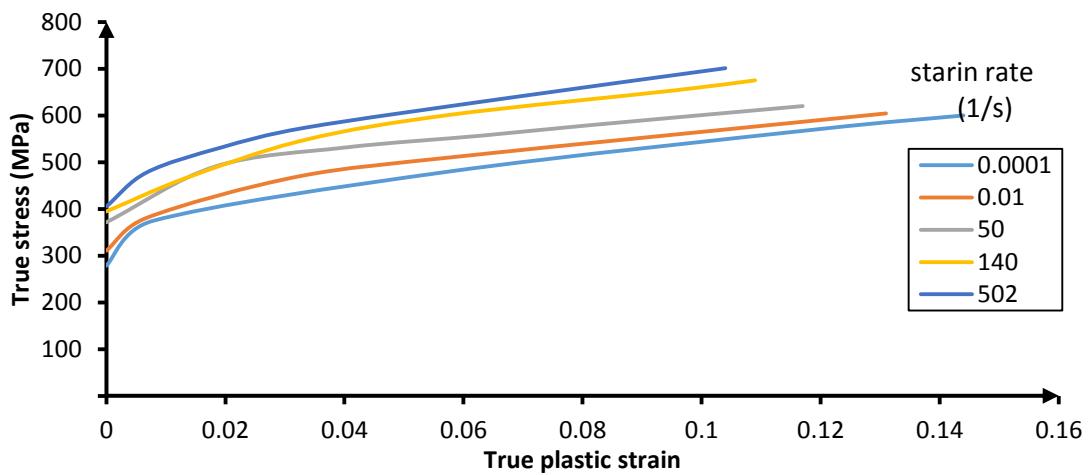
3D FE models have been developed to simulate the vertical free drop of a weight from different altitudes resulting in damage of the pipe. Models were executed using a three-dimensional dynamic explicit non-linear finite element code, ABAQUS/EXPLICIT 6.13. In order to precisely simulate the response of the collided pipe to subsequent impacts and spring back, an elastic-plastic constitutive behaviour is adopted using the isotropic Hooke's law whereas the plastic behaviour is accounted for by means of the Von Mises yield criterion. The work hardening is based on isotropic hardening rule associated with the equivalent plastic strain rate. Strain-rate dependent properties are specified for both materials, C-Mn and AISI304.

Impact is a dynamic test where the equivalent plastic strain rate plays a key role in determining the mechanical properties of punched material (Nicholas, 1980). Typically, the maximum velocity during impact occurs with the initial contact between the indenter and external surface of the pipe, and becomes gradually lower afterwards during the indentation process. As a result, the pipe material undergoes

different strain rates during indentation. Increasing strain rates result in higher stress/strain curves. Furthermore, increasing strain rates lead to higher ultimate strength and lower ductility whereby AISI304 material tends to be more sensitive to change in strain rates than C-Mn material. Figure 8-1 shows the dynamic stress-strain curves for C-Mn and AISI304 steels (Handbook, 1973; Wiesner, 1999).



(a)



(b)

Figure 8-1 Plastic strain rate for (a) C-Mn pipe (Wiesner, 1999) and (b) AISI304 pipe (Handbook, 1973)

8-2-1. FE Mesh of Impact Components

The FE model is composed of the outer pipe (C-Mn pipe), the inner pipe (AISI304 pipe), indenter (denting tool), rigid bottom plate and rigid side plate. A lined pipe with 200 mm length lies down on a bottom plate and trapped between two plates on sides with 3 mm gap on each side. The outer pipe, C-Mn, has an outer diameter (D_{carbon}) of 114.3 mm with a variance of ± 1.45 mm whereas the wall thickness (t_{carbon}) is 6.35 mm with a variance of ± 0.35 mm. The AISI304 pipe, the liner, has an external diameter ($D_{\text{stainless}}$) and thickness ($t_{\text{stainless}}$) of 101.6 mm and 1.5 mm with variance of ± 1.1 and ± 0.15 mm, respectively as shown in Figure 8-2. The tip of indenter is numerically in direct contact with the centre of dent located at the pipe middle section having the velocity and mass of dropping weight accordingly.

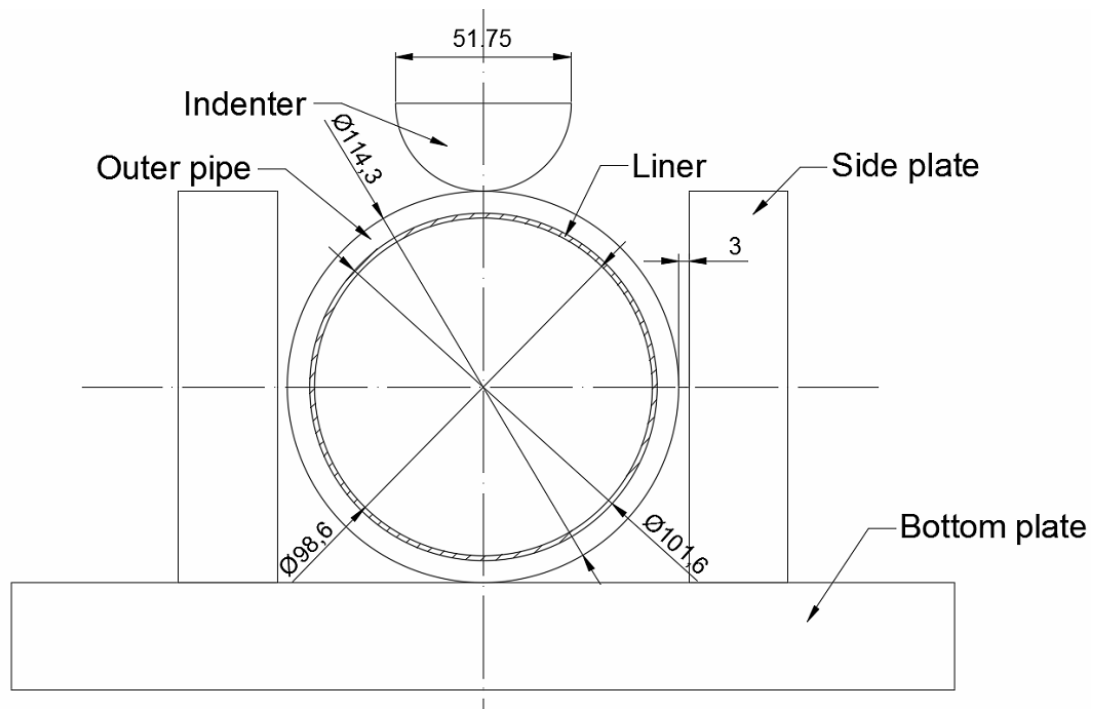


Figure 8-2 Schematic of dented lined pipe dimensions in mm.

The pipes in both cases A and B are idealized with solid 8-node continuum brick elements, with full integration (C3D8). Three translation degrees of freedom are active at each node. The mesh is refined more in the dented region in both cases to get more precise results. The indenter is modelled using C3D4, 4-node linear tetrahedron elements, with a density of 7860 kg/m^3 . The bottom and two side plates

are modelled using element type of C3D8, 8-node linear brick elements, with density of 7860 kg/m³.

8-2-2. Contact Regions, Velocity and Loads

Since the impact process includes hitting bodies with each other, surfaces in the lined pipe are exposed to be in contact internally and externally. In more detail, four contact regions are defined in the model. First contact is modelled between the surface of the semi-sphere (denting tool) and the whole surfaces of the C-M pipe and the AISI304 pipe located in the expected dented region. A second region of contact is located between the inner surface of the C-Mn pipe and the outer surface of AISI304. A third contact region is specified between the external surface of C-Mn pipe and the side plate because of the increasing width of pipe cross section during impact. The last contact occurs between the external surface of the C-Mn pipe and the bottom plate, where striking makes lined pipe bounce up and down as a reaction of every collision. In case A, the second contact area is neglected because AISI304 pipe is not considered.

The weight drops down freely vertically on the pipe from different heights of 1, 1.5 and 2 m. Consequently, the velocity of free drop increases linearly with time to reach its ultimate value as the tip of indenter touches the external surface of the C-Mn pipe. In this moment, neglecting friction and air resistance, the velocity of free drop (v) would be given according to the conservation of energy law as $v = \sqrt{2gh}$, where g and h are the acceleration of gravity and height, respectively. However, the resistance of air and friction between square block (weight) and internal walls of impact apparatus chamber are taken into account. The loss in speed value is calculated using video frames recorded for the whole impact operation by a high speed camera. It was found out that the ultimate speed loses 9.7% of its value as the tip of indenter touches the pipe. The corrected values of maximum drop speed are 4, 4.9 and 5.657 m/s when the weight drops vertically from different height (h) 1, 1.5 and 2 m, respectively.

In the explicit impact analysis, self-weights of C-Mn pipe, AISI pipe, indenter and block mass, 200 kg, are considered in the FE model to return the bodies back after every jump because of collision. It is clear that FE model consumes much time

because of contact regions and subsequent collisions. Thus, an appropriate mesh refinement is implemented in the numerical analysis, where the size of elements increases outwards the dented region. Furthermore, a quarter model is simulated, because of symmetry with respect to the axial and transverse planes, planes X-Y and Y-Z, respectively. In case A model (without liner), the AISI304 pipe is not considered in the FE model. Thus, contact between the C-Mn pipe and AISI304 pipe and also self-weight of liner are not needed. Figure 8-3 shows the FE mesh for the main parts of lined pipe impact process, for case B.

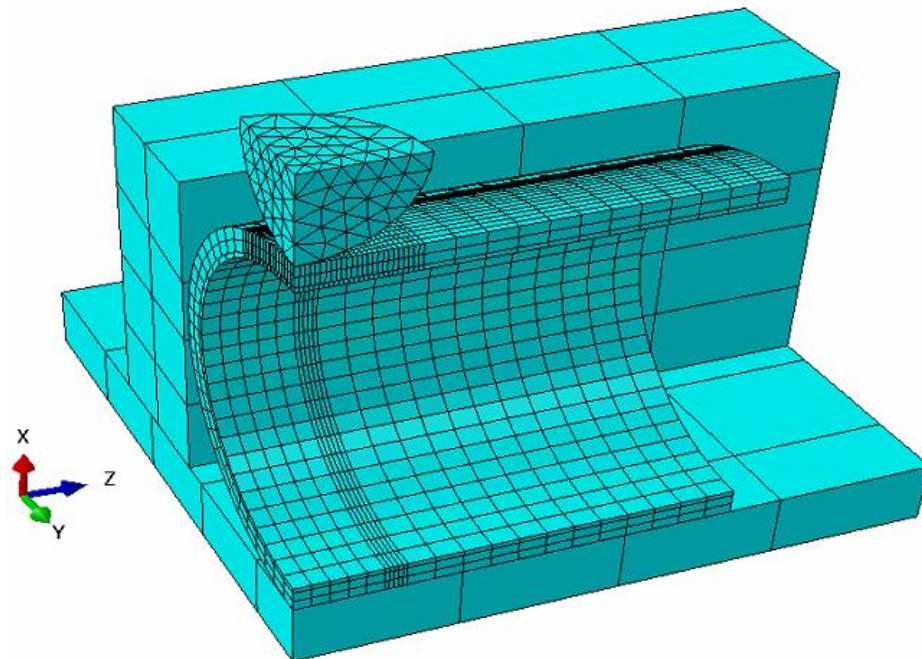


Figure 8-3 FE mesh of the quarter lined pipe model, case B

8-3. Parametric Study

8-3-1. Finite Element Analysis

The steps of the FE analysis reflect the procedure employed in the experimental tests. Initially, the indenter freely drops down from a specific height to punch the external surface of C-Mn pipe with a specified velocity. The kinematic energy has been consumed completely to produce indentation in the lined pipe before the indenter and

pipe retreat vertically as a reaction of collision. The hitting tool and pipe fall down afterward because of their self-weight. The weights include those of block, spherical indenter, liner and C-Mn pipe. The indenter hits the lined pipe frequently, reducing the maximum distance of collision every time because of the kinetic energy being consumed. Consequently, the collision leaves permanent deformation in the lined pipe, which in turn produces residual stresses in the base materials, AISI304 and C-Mn. Figure 8-4 shows the position of the indenter with respect to the lined pipe, for case B, at different stages of the analysis. When the indenter (with the mass and weight of the block added to it) is pushed up, elastic stresses in the pipe wall are released, which in turn results in rebound the dent depth slightly. Nevertheless, the residual stresses remain in the base materials with different levels of plasticity, where the highest level is located in the dented region.

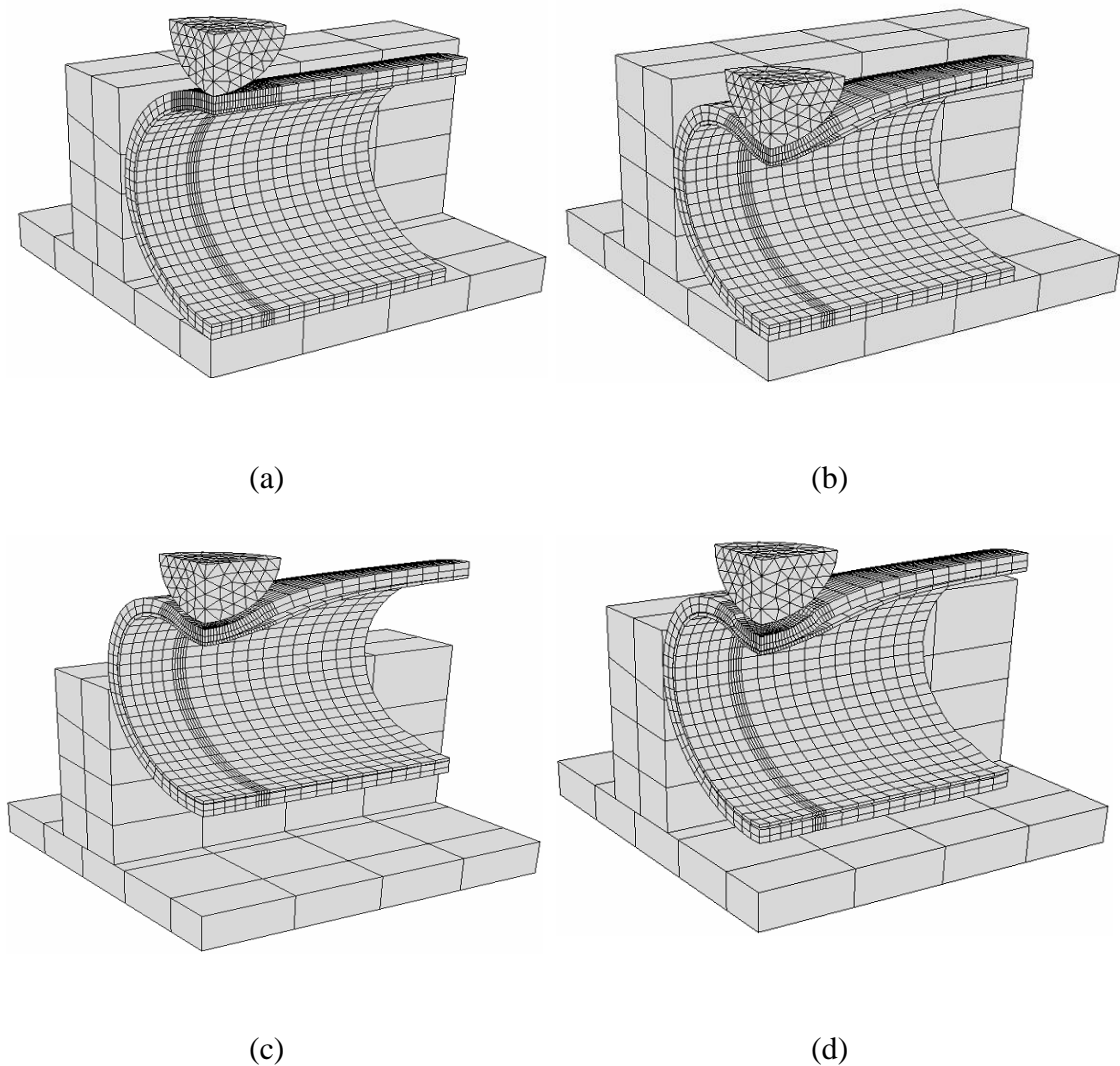


Figure 8-4 The stages of collision at (a) original position of indenter and lined pipe (undeformed mesh), (b) deformed shape at 7.5 ms, (c) deformed shape at 75 ms and (d) deformed shape at 250 ms

8-3-2. Dented Pipe Geometries

The deformed geometries of the pipe were experimentally obtained with the aid of conventional callipers and a displacement transducer just after completing the strikes and removing the indenter equipped with mass of 200 kg. The deformed geometries resulting from the FE simulations, including the dent depth, are then compared with their counterparts taken experimentally for case A (without liner) and case B (with liner) as reported in Table 8-1, where Figure 8-5 clarifies the tabulated deformed geometries of dented pipe.

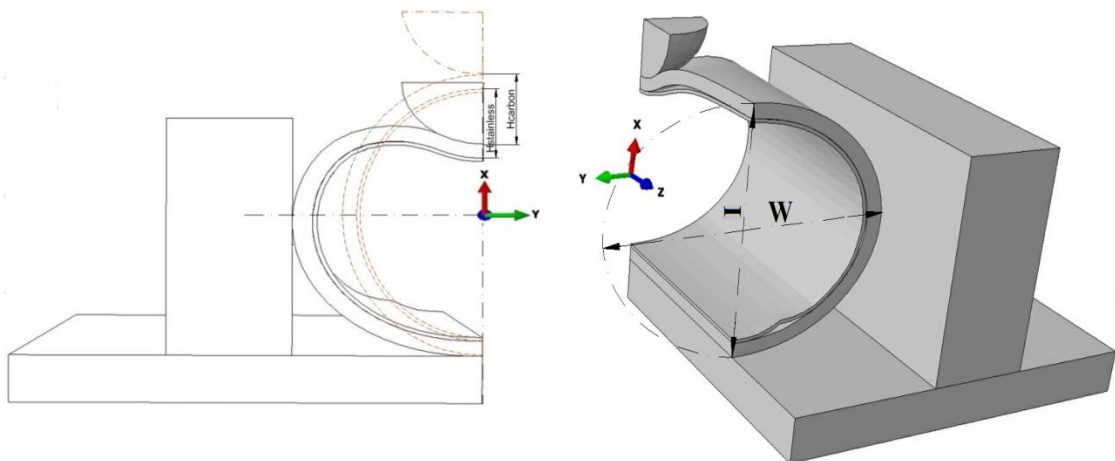


Figure 8-5 Deformed geometries of dented pipe

Table 8-1 Numerical and experimental results of pipe geometries including dent depth.

Specimen	Pipe case	Height (m)		I (mm)	W (mm)	H _{carbon} (mm)	H _{stainless} (mm)	H/D %	
								C-Mn	AISI304
								H _{carbon} /D _{carbon}	H _{stainless} /D _{stainless}
H1A	A	1	Exp.	109.0	118.2	13.4	-	11.7	-
			Num.	109.1	118.8	14.21	-	12.43	-
H2A	A	1.5	Exp.	109.0	118.5	20.20	-	17.67	-
			Num.	109.0	118.84	20.25	-	17.71	-
H3A	A	2	Exp.	108.9	119	24.5	-	21.43	-
			Num.	108.84	118.88	24.67	-	21.58	-
H1B	B	1	Exp.	109.5	117.74	13.1	13.1	11.46	12.89

			Num.	109.92	118.26	13.35	13.4	11.67	13.18
H2B	B	1.5	Exp.	109.2	118.44	18.65	18.65	16.31	18.36
			Num.	109.6	118.54	18.97	18.7	16.6	18.41
H3B	B	2	Exp.	109.1	119	22.3	22.3	19.51	21.95
			Num.	109.5	118.5	23.47	23.33	20.53	22.96

The European Pipeline Research Group (EPRG) (Roovers et al., 2000) has found out that the pipe with a smooth dent (plain dent) in the non-pressurized condition does not fail in two cases. The first condition is that the internal pressure is less than the maximum operating pressure (MOP) which is calculated as that corresponding to the stress given by 72% of the specified minimum yield stress (SMYS). The second one is that the dent depth is equal or less than 10% of the pipe outside diameter. In our study, in all cases, pipes are dented under non-pressurized condition.

In case that the pipe is dented in the pressurised condition, the dent is pushed outwards by the internal pressure. As a result, the dent depth in a pressurised pipe is less than that in a non-pressurised pipe. According to EPRG, the correlated ratio between dent depth in non-pressurised pipe to that in pressurised pipe is 1.43. Therefore, the minimum ratio of dent depth-to-pipe outer diameter to get failure in pressurised pipe is 7% (Roovers et al., 2000; Keith Escoe, 2006).

8-3-3. Strain Behaviour in the Dented Region

In this chapter, the main aim is to study the strain and stress behaviour in the dented region by comparing the numerical predictions with the experimental strain results recorded during the impact test. With this aim, four groups of strain gauges were mounted on the external surface of C-Mn. First and second group, GR1 and GR2, were located on the longitudinal plane with positions given by $\phi = 0^\circ$ and $Z = \pm 23$ mm. The last two groups of strain gauges, GR3 and GR4, were placed on the transverse plane with locations of $\phi = \pm 23.7^\circ$ and $Z = 0$ mm as shown in Figure 8-6.

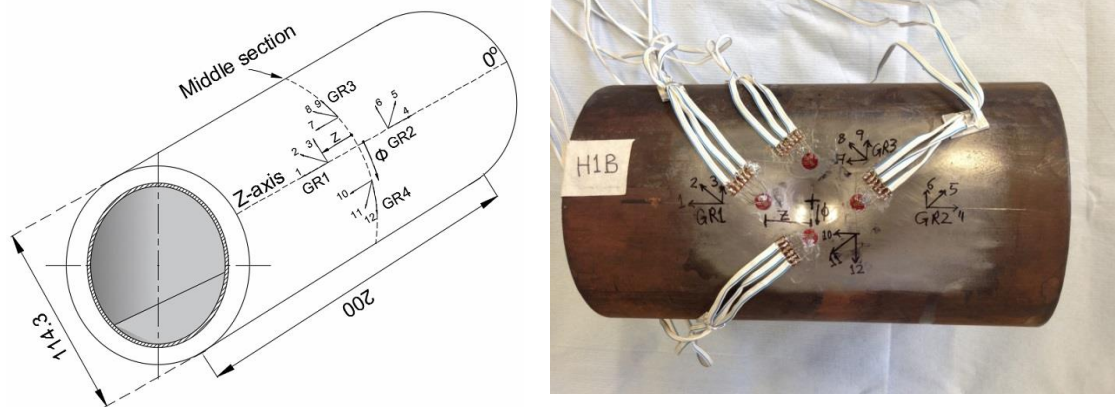


Figure 8-6 positions of the strain gauges, dimensions in mm

Those locations kept the strain gauges safe from damage by punching from indenter. Moreover, the levels of strain in these positions are suitable to the maximum limit of strain in the gauges. The closer the distance from the dent centre is, the larger the strain level of the gauge records and the choice of a proper position was based on numerical models for all cases. During the impact test, the signals from the strain gauges were recorded by a computer based data acquisition system run via LabVIEW code. Each group contained at least two strain gauges (biaxial strain gauges) where one gauge (element) measured the axial strain and the other one measured the hoop strain. Some gauges were tri-axial, known as 3-axis rosette gauge, but the diagonal strain with 45° in XY-plane was found to record significantly lower strain values compared to the axial and hoop strain values. However, the experimental results of longitudinal strain gauge groups, GR1 and GR2, were almost identical and also the transversal strain gauge groups had very close results. The symmetric-plane strain groups were used to double check the reliability of experimental results and also to record strains from at least one gauge in case one of the gauges had been lost by damage or detachment by dropping the weight from high altitudes. To sum up, the experimental results recorded from GR1, located on the longitudinal plane, and from GR4 have been compared with the numerical results located at the same positions on the quarter pipe FE model. Figure 8-7(a)-(k) shows these comparisons in case A and case B. As mentioned earlier, the indenter and the pipe collided many times during one impact process before the indenter settled over the pipe in all cases (with and without liner). The most severe collision was the first

one in the impact process, when significant plastic deformation occurred in the dented region.

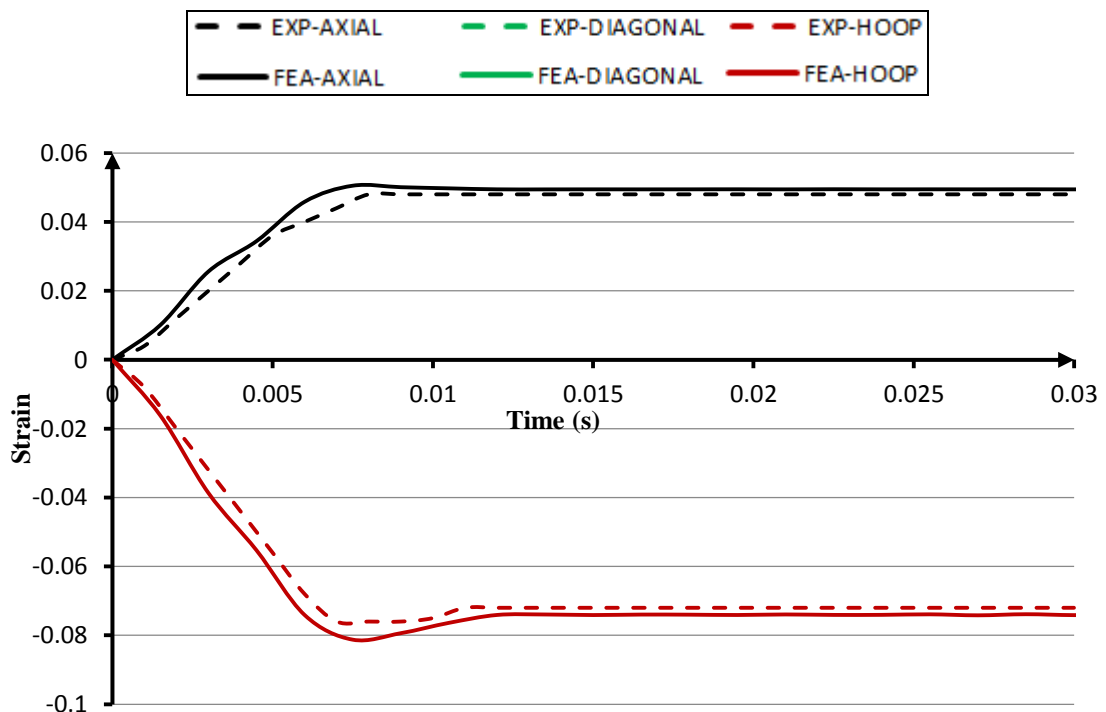
Figure 8-7(a) shows the axial and hoop strains generated by GR1 rosette on the C-Mn pipe without liner (H1A specimen), where the free drop height is 1 m. The FEA results in the same location of GR1 are also plotted in the same figure. GR1 rosette is positioned on the longitudinal plane at $Z = 23$ mm far from the dent centre. GR1 rosette is a biaxial strain gauge recording the strain history in the axial and hoop (circumferential) direction. The numerical time is synchronised with the experimental time, assuming time to be zero when the tip of indenter touches the external surface of pipe. The hoop strain gauge records compressive mechanical strains reaching a maximum of -8.12% after 7.5 ms of striking. After that, the strains reduce in the pipe due to the so-called 'spring back', because the indenter with weight block rebounds vertically away from the pipe. After that, the strain reaches a steady-state with -7.4% as residual plastic strain. Consequently, 0.72% of the initially compressive strain was elastic strain. On the axial direction, the gauge records a tensile strain history in which the peak tensile strain reaches a steady-state value of 5% after 7.5 ms.

Upon free drop of the weight from 1 m over H1A specimen, GR4 rosette records strain history on the transverse plane. It is positioned with clockwise circumferential angle $\phi = 23.7^\circ$ far from the dent centre. Like the GR1 rosette, GR4 rosette measures the strain history at axial and hoop direction. In contrast to GR1, axial strain gauge records compressive strain whereas hoop one records tensile strain. It is clear from Figure 8-7(b), there is also a convex kink in the compressive strain curve at 7.5 ms from the onset of strike where the dent reaches its maximum depth. After that, the spring back phenomenon is dominated in the dent region when the hitting tool rebounds away from the C-Mn pipe to keep the compressive strain steady-state curve. It is also observed that there is no protruding kink in the positive hoop strain curve. One may note from Figure 8-7(a) and (b) that the absolute values of compressive strains are larger than those of tensile strains. Furthermore, the absolute values of compressive and tensile strains on the longitudinal plane, Fig. 8.6(a), are larger than their counterparts on the transverse plane, Figure 8-7(b). It is also noticeable in specimen H1A that the tangent strains to the periphery of the dent are

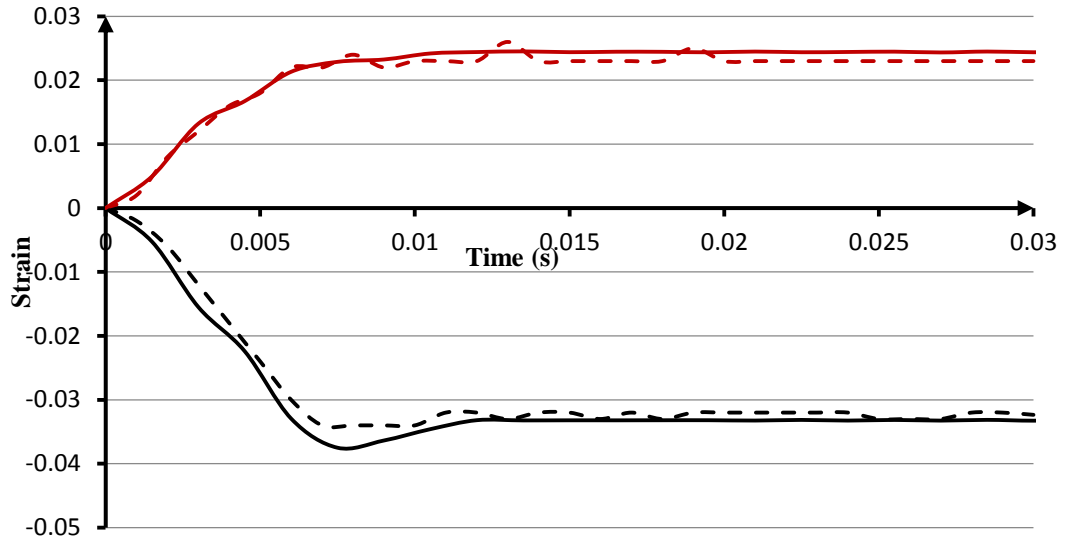
compressive whereas their perpendicular counterparts are always positive (Cunha et al., 2009). In more detail, the gauge on the longitudinal plane, GR1 records a tensile strain in the axial direction whilst the gauge on the transverse plane, GR4, records a compressive strain in the axial direction.

In case of dropping 200 kg freely from 1.5 m over H2A specimen, the absolute values of strains in GR1 and GR4 rosettes are larger than their counterparts in the H1A specimen. Figure 8-7(c) shows that the steady state of axial strain in GR1 after the first strike is 7.4% whereas its counterpart in H1A specimen is 5%. Moreover, Figure 8-7(d) clarifies that the maximum tensile hoop strain reaches 3% strain while its counterpart in H1A specimen reaches just 2.45% strain.

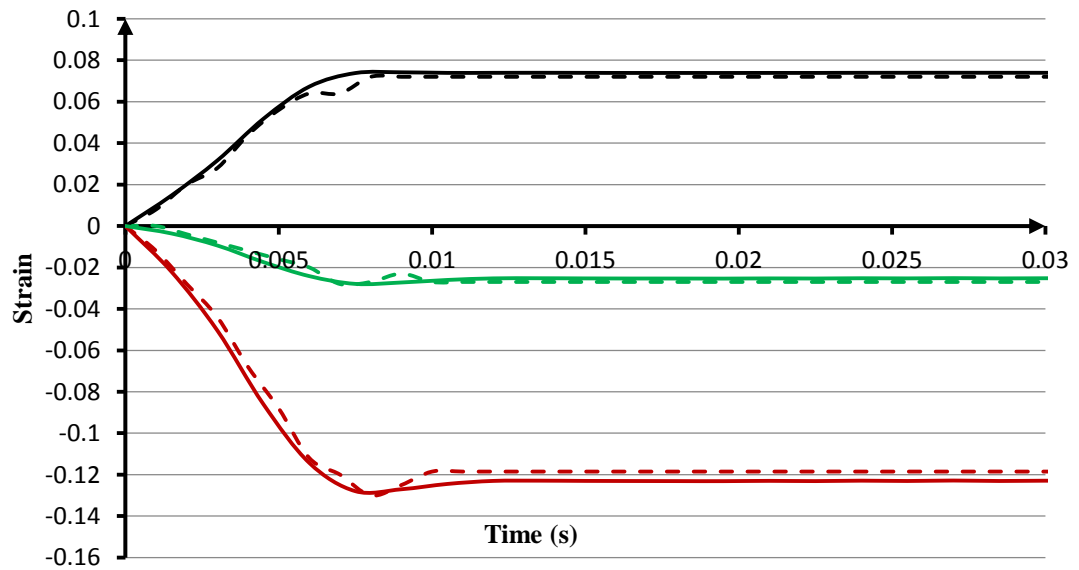
The same foregoing discussion applies to the other figures with respect to the pipe of cases A and B. It is also observed that the absolute values of the strains in case A are larger than their counterparts in case B. It can be observed that strains which are tangent to the dent periphery (hoop and axial strains in GR1 and GR4, respectively) are always compressive whereas their orthogonal counterparts (axial and hoop strains in GR1 and GR4, respectively) are always tensile.



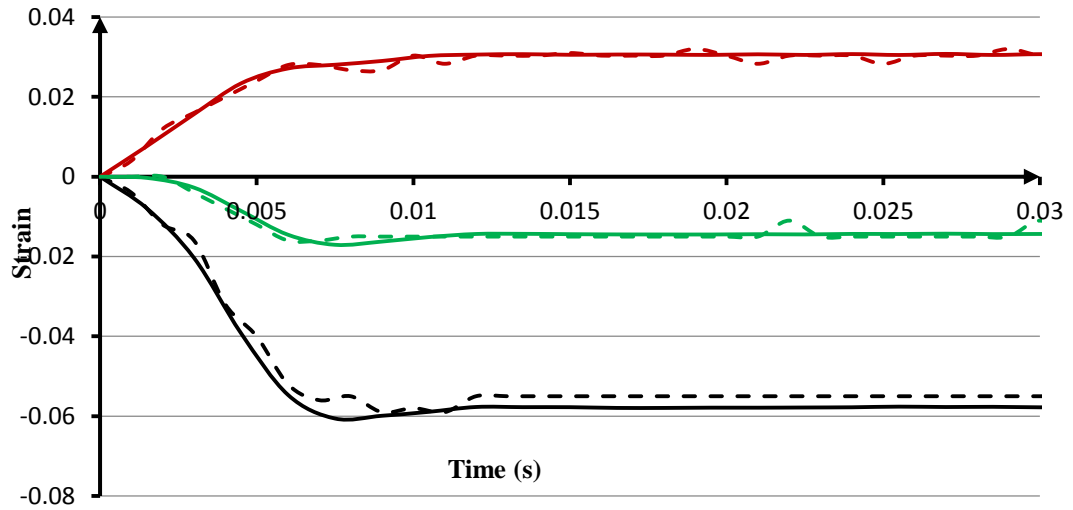
(a)



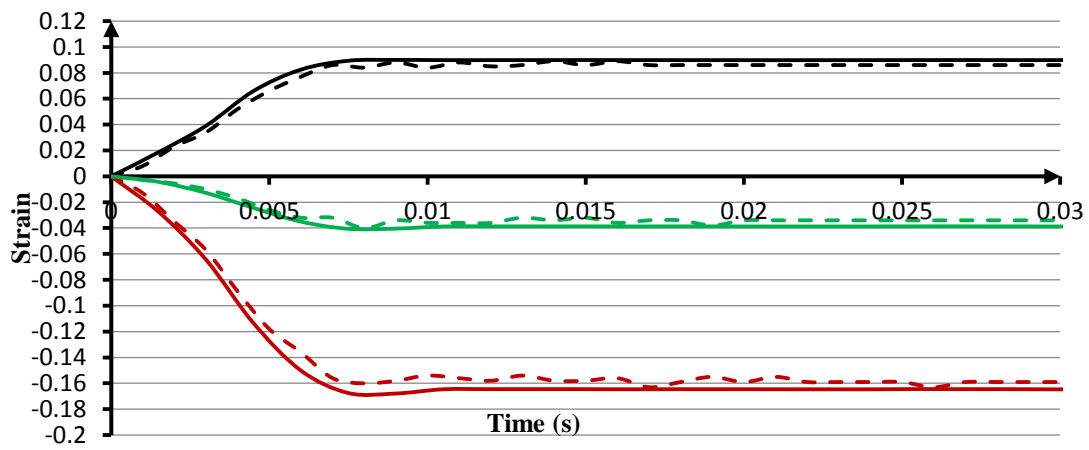
(b)



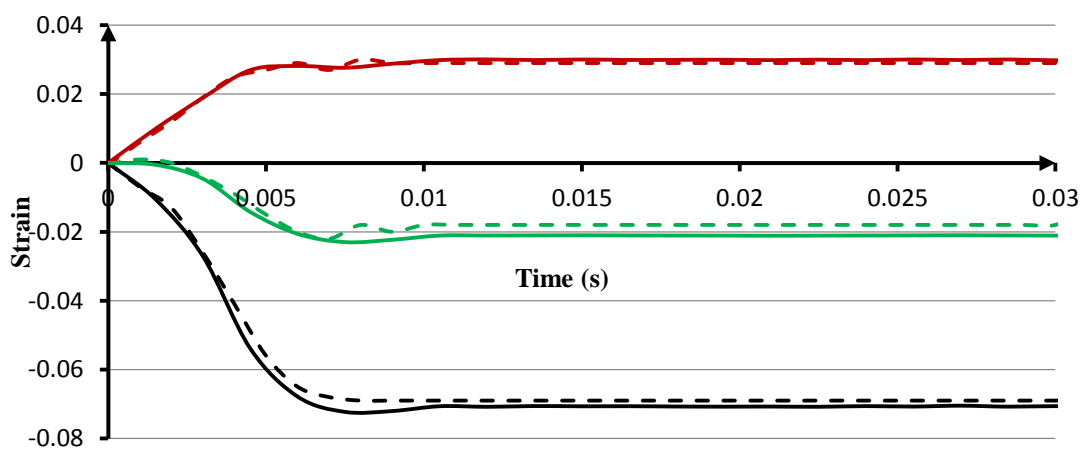
(c)



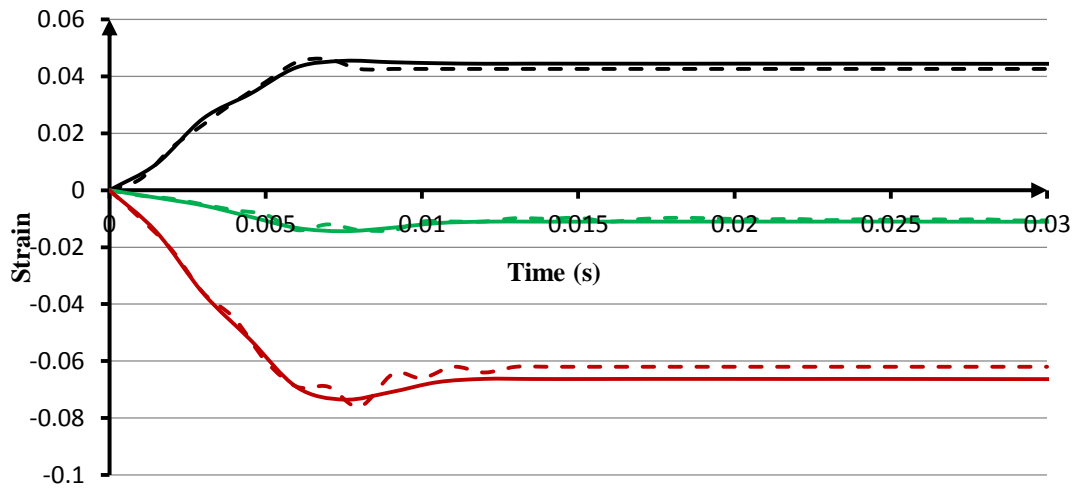
(d)



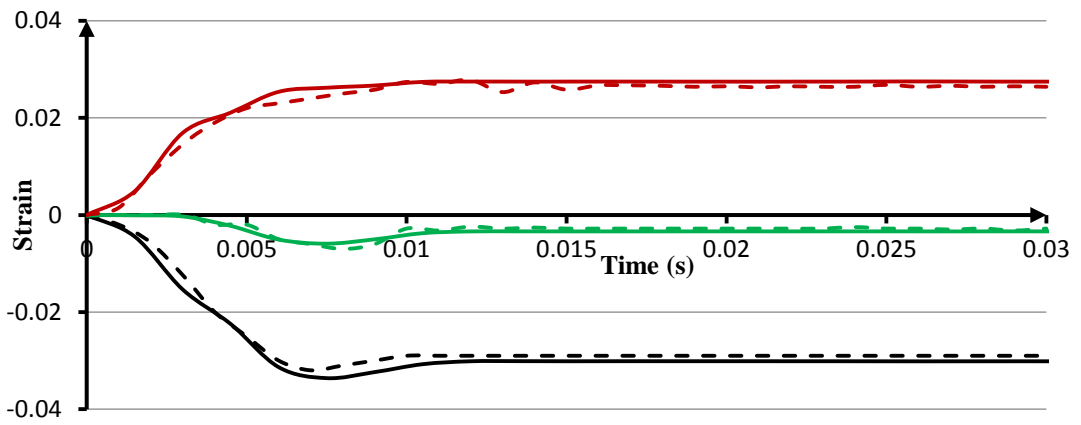
(e)



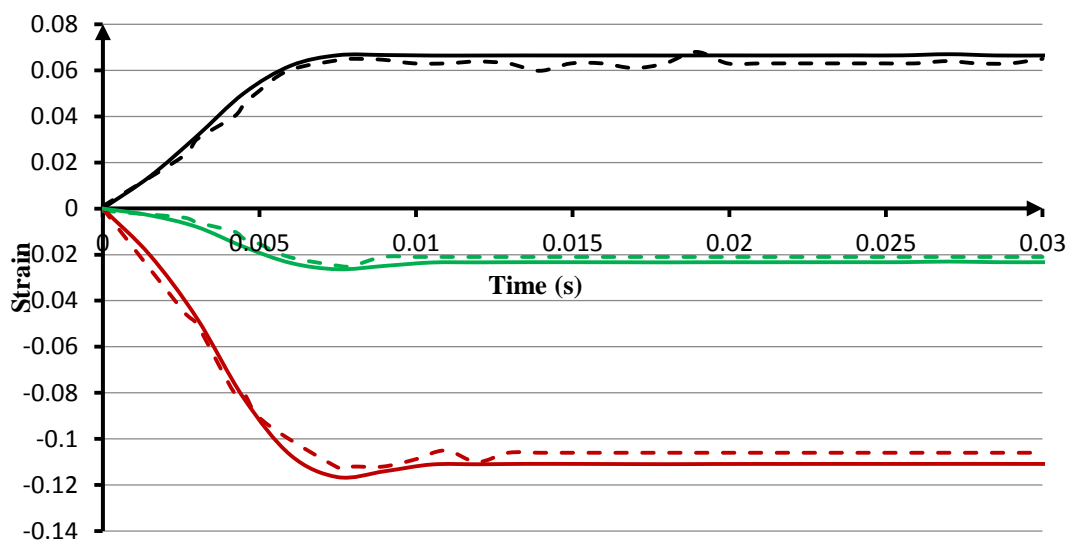
(f)



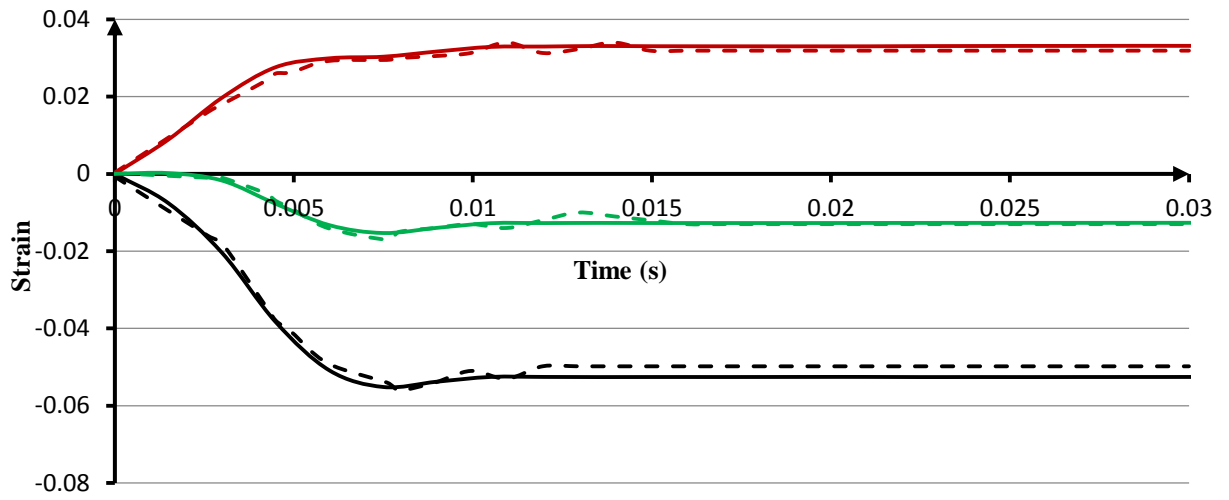
(g)



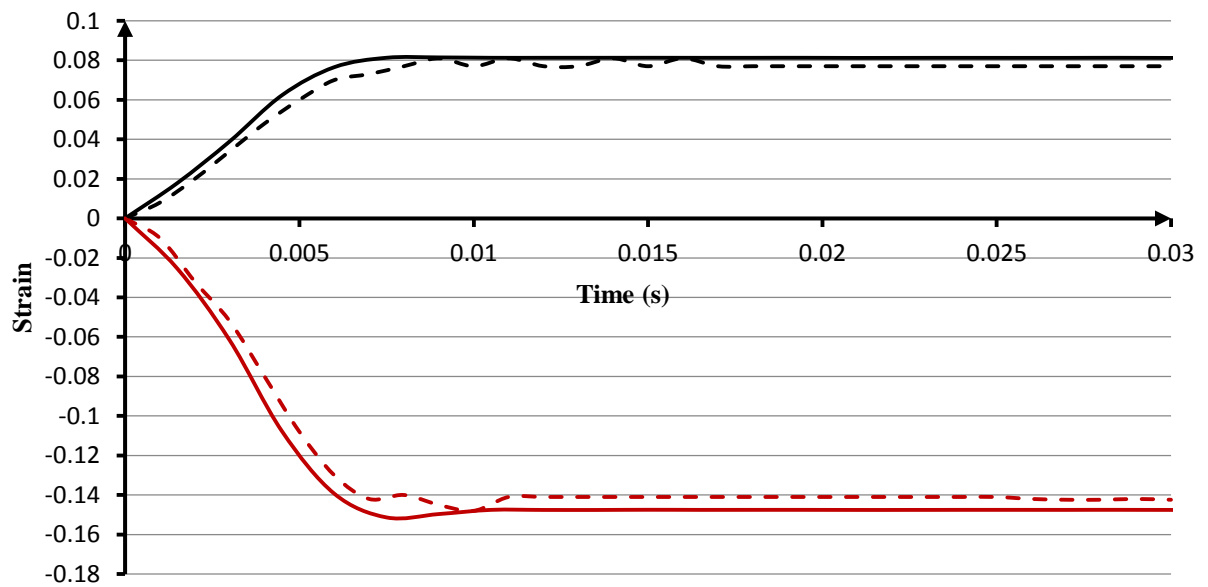
(h)



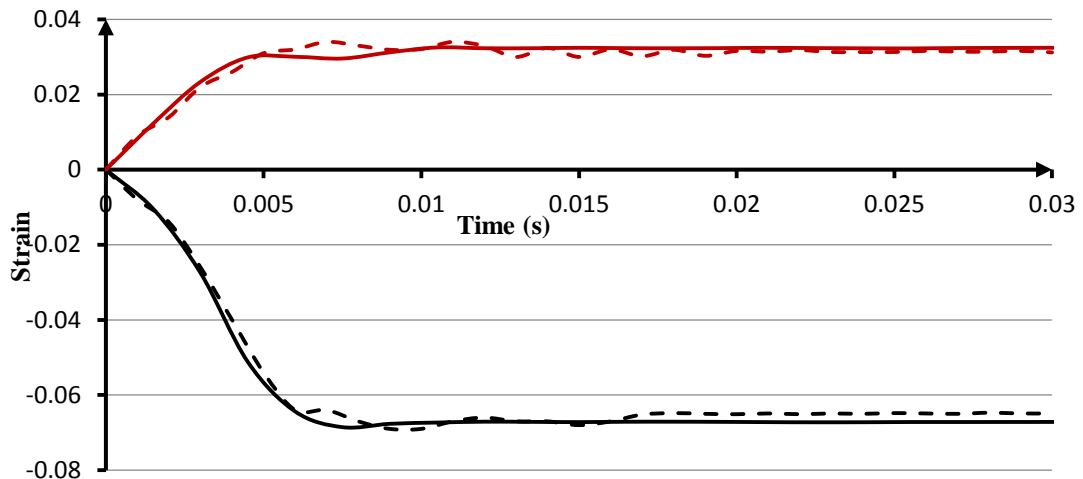
(i)



(j)



(k)



(l)

Figure 8-7 Strain histories in Rosette (a) GR1 (H1A), (b) GR4 (H1A), (c) GR1 (H2A), (d) GR4 (H2A), (e) GR1 (H3A), (f) GR4 (H3A), (g) GR1 (H1B), (h) GR4 (H1B), (i) GR1 (H2B), (j) GR4 (H2B), (k) GR1 (H3B) and (l) GR4 (H3B)

8-3-4. Residual Stresses

Good correlation between experimental results and numerical results in terms of deformed geometries and strains led us to study the residual stresses numerically with sufficient confidence. In general, all cases consumed 2 seconds to implement a series of explicit sequential strikes for each case and 1 second to static spring back step where the dent takes the last shape with permanent deformation.

According to ASME B31.4 (2012), a smooth dent in liquid pipelines with a dent depth-to-pipe diameter ratio (H/D) exceeding 6% should be repaired when the hoop stress levels are over 20% of the SMYS. In a similar way, for gas pipelines, ASME B31.8 (2010) states that repair is required when the ratio (H/D) exceeds 2% and hoop stress levels exceed 40% of the SMYS. In this work, all cases with liner or without liner have a ratio of H/D over 10% as reported in Table 8-1. As a result, hoop stress levels in the dented pipe play a significant role in making a decision regarding maintenance work (Rinehart, 2004). To shed light more on the stress behaviour, specimen H1B is chosen to analyse the Von Mises stress distributions in the dented region on different surfaces after the impact process (spring back) as depicted in Figure 8-8. It is observed that the maximum stress concentration is located at the dent

periphery on the outer surface, not in the dent centre (Keating and Hoffmann, 1997). Consequently, the outer surface of C-Mn pipe in all cases is more vulnerable to the nucleation of crack propagation.

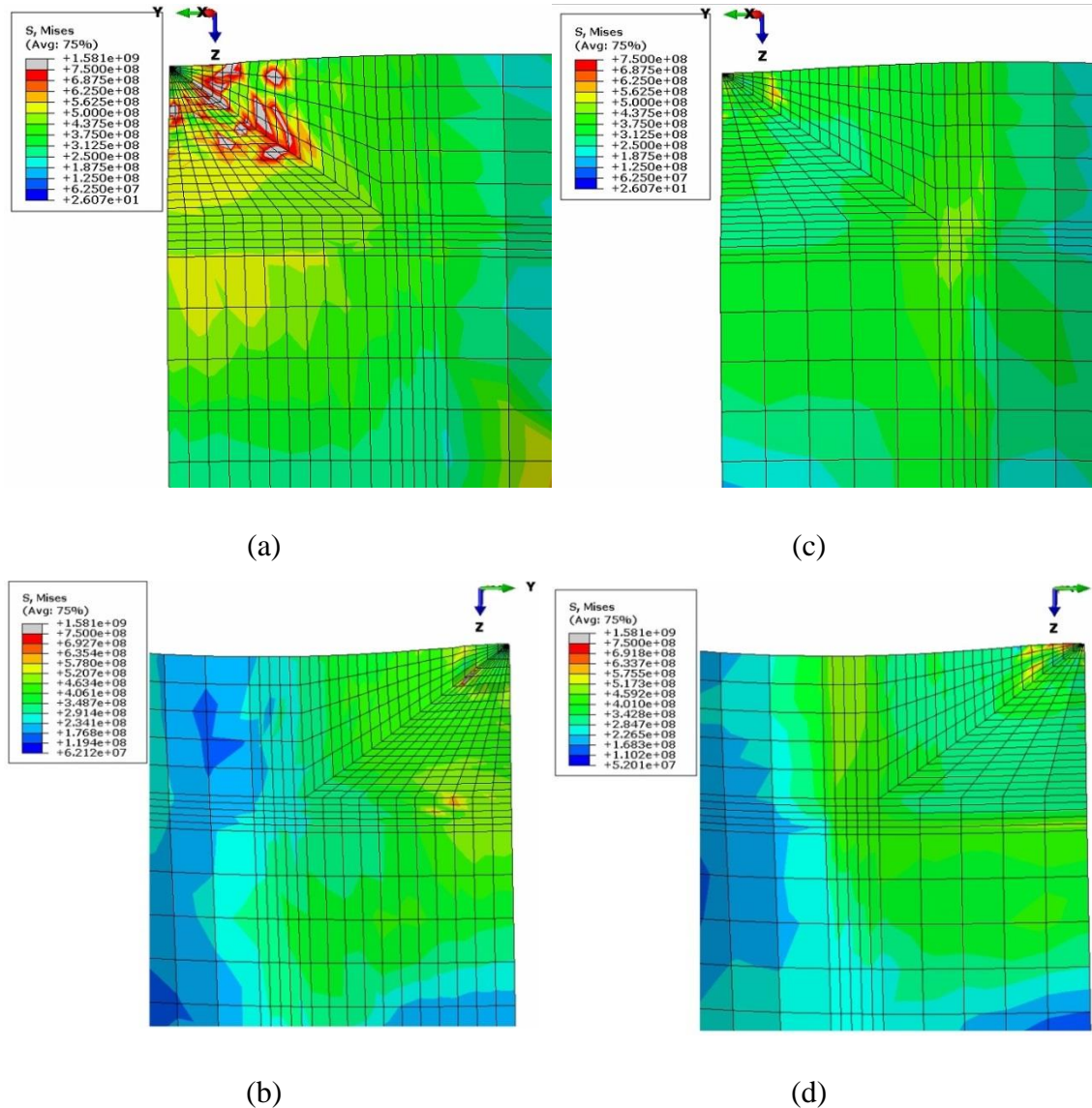


Figure 8-8 Residual Von Mises stresses in the dented region of H1B specimen on the (a) top surface of C-Mn pipe (b) bottom surface of C-Mn pipe (c) top surface of AISI304 pipe (d) bottom surface of AISI304 pipe

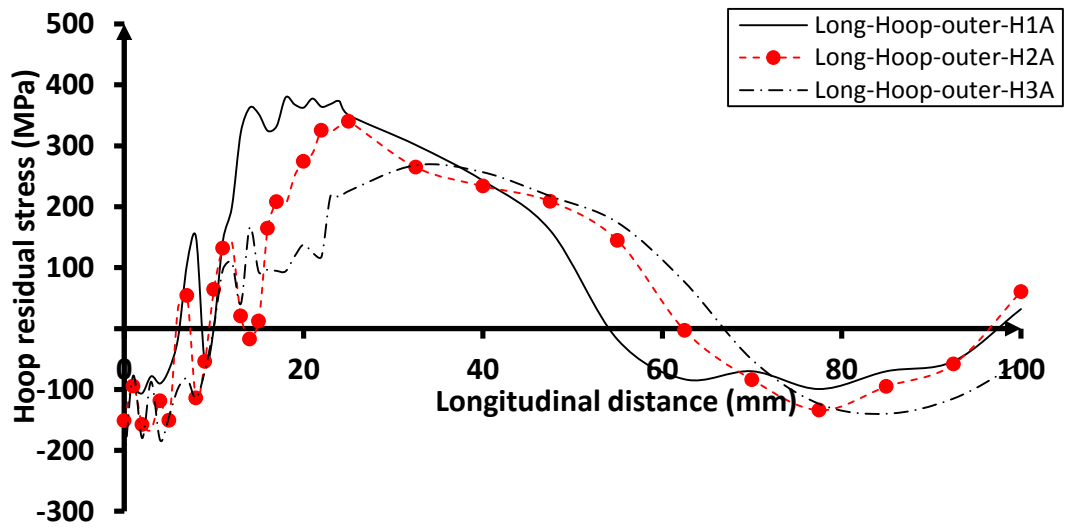
As for the residual stress distributions on the outer surface, the hoop stresses have larger magnitudes of tensile stresses than axial stresses. As a matter of fact, the hoop stress is twice the axial stress in the pressurized pipe in service. Therefore, the hoop residual stresses should be considered more important when studying the stress behaviour in the dented region as per ASME B31.4 (2012) and ASME B31.8 (2010).

In this section, the hoop residual stress distributions in the longitudinal and transverse planes starting from the dent centre have been investigated. Figure 8-9 shows the hoop residual stresses at the longitudinal and transverse planes on the outer surface for case A (without liner) and case B (with liner).

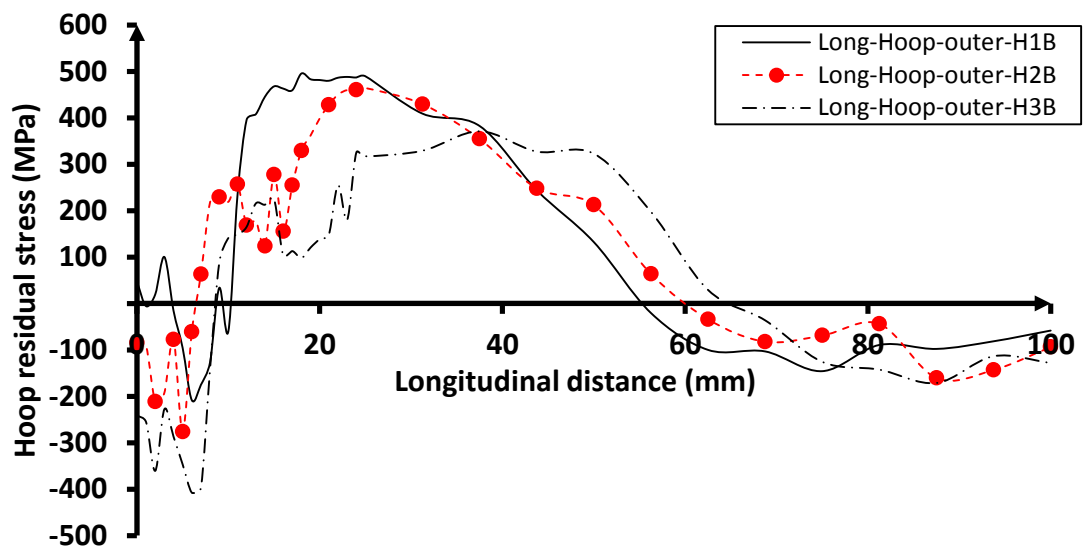
It is observed from Figure 8-9(a)-(d) that increasing the drop height leads to reduce the maximum tensile residual stresses, probably because the equivalent plastic strain rate plays a vital role. Increasing the equivalent plastic strain rate pushes highly the yield stress of material (Lee and Liu, 2006). Furthermore, the maximum tensile residual stresses are located on the periphery of the dent. Increasing the drop height leads also to expand the dent diameter which in turns pushes the maximum tensile stresses farther away from the dent centre.

On the longitudinal direction, it could be seen from the comparison between Figure 8-9(a) and (b) that the maximum tensile stresses in case A (without liner) are lower than their counterparts in case B (with liner). In more detail, the maximum tensile stresses in cases H1A and H1B associated with the free dropping weight from 1 m are 380 and 496 MPa, respectively. This can be attributed to the accumulation of residual stresses because of the sequential strikes in each impact process where the indenter hits the pipe with different velocity in each strike. For example, the velocity in the second sequential strike in case H1B is lower than its counterpart in case H1A because of the dissipation of internal energy which is, for example, increased by 3% in case H1B compared to its counterpart in case H1A when forming the maximum dent depth in the first strike. Dissipation of energy and impact velocity are discussed later in next sections.

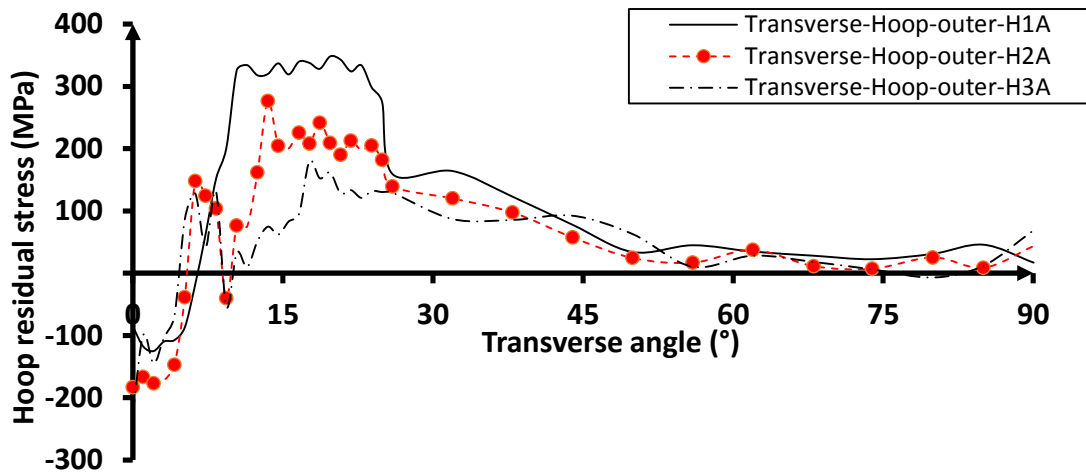
On the transverse direction, it is noticeable from Figure 8-9(c) and (d) that the maximum tensile stresses in cases A and B are lower than their counterparts on the longitudinal direction. In detail, the maximum tensile residual stress along the longitudinal direction of case H1B is 496 MPa whereas the maximum one around the transverse direction of case H1B is 352 MPa. In a similar way, the maximum tensile stresses in case A are somewhat lower than their counterparts in case B.



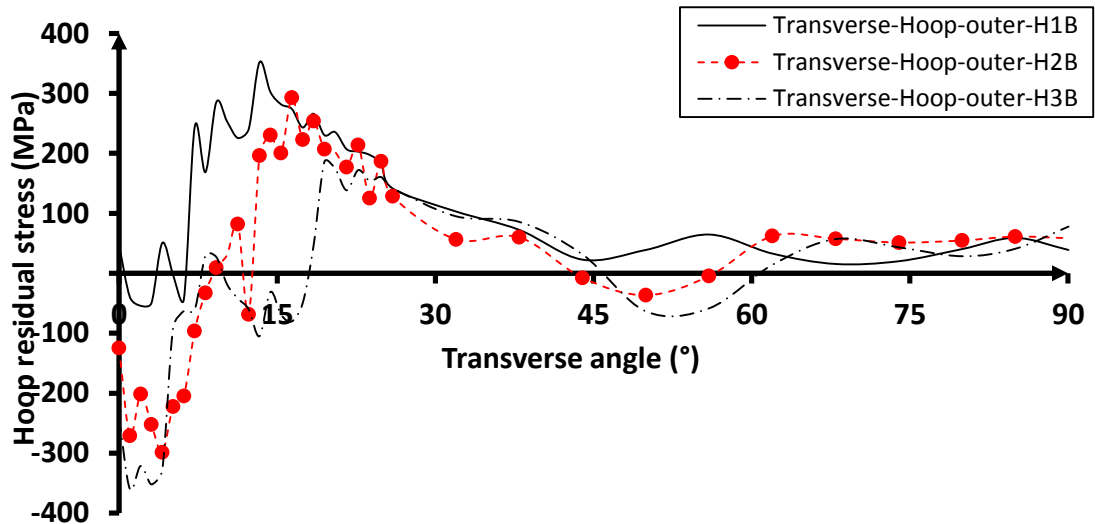
(a)



(b)



(c)



(d)

Figure 8-9 Hoop residual stress distribution starting from the dent centre on the outer surface (C-Mn pipe) at (a) the longitudinal planes in case A (b) the longitudinal planes in case B (c) the transverse planes in case A (d) the transverse planes in case B

A concise summary of the forgoing discussion is that the onset of the cracks is most likely to be at the dent periphery and to propagate predominantly along the longitudinal direction on the outer surface, where the tensile residual hoop stresses are higher than their counterparts around the transverse direction.

In this study, crack initiation and propagation have not been modelled. In particular, the impact model is executed to specify the regions which could probably contain crack formation and propagation.

8-3-5. Energy Consumed in the Whole Model

The principle of conservation of energy states that energy cannot be eliminated or generated from nothing but transmitted from one type to another one. In our work, the total energy, E_{TOT} , for the whole model during the impact is composed of different types given as follows:

$$E_{TOT} = E_I + E_{VD} + E_{KE} + E_{FD} - E_W = constant \quad (8.1)$$

$$E_I = E_{SE} + E_{PD} \quad (8.2)$$

where E_I , E_{VD} , E_{KE} , E_{FD} , E_W , E_{SE} and E_{PD} are the internal energy, viscous dissipation energy, kinetic energy, frictional dissipation energy, work energy, recoverable (elastic) strain energy and plastic dissipation energy, respectively. Other types of energy have not been discussed in this section or considered in the FE model because their changes are either zero or close to zero.

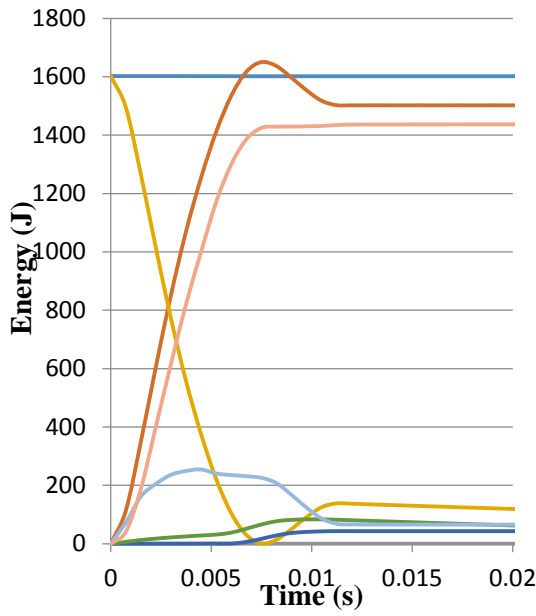
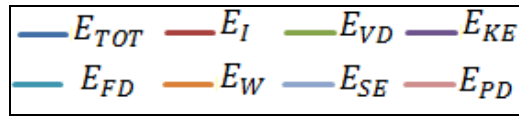
Figure 8-10(a)-(d) represents the evolution of all the energy terms during the first strike in the impact test. It is clear that the kinetic energy is equal to the total energy at the beginning of contact between the indenter and pipe. Moreover, the kinetic energy after 7.5 ms, time required to form the dent at the end of the first strike, is completely consumed and changed into other types.

Figure 8-10(a) may help to shed light on the types of energy during the first strike in case H1A. As discussed, the kinetic energy starts with 1600 J to drop rapidly to zero after 7.5 ms. Meanwhile, the energy internally stored or dissipated rises rapidly up from zero to reach the maximum value, 1650 J, at 7.5 ms. The majority of this internal energy is consumed as plastic dissipation energy, around 86% at 7.5 ms. This energy is used to form the dent and other permanent deformations in the pipe, such as expanding the width of the pipe. The elastic strain energy is responsible for the rebound the dent depth after the strike. The work energy is composed of the work

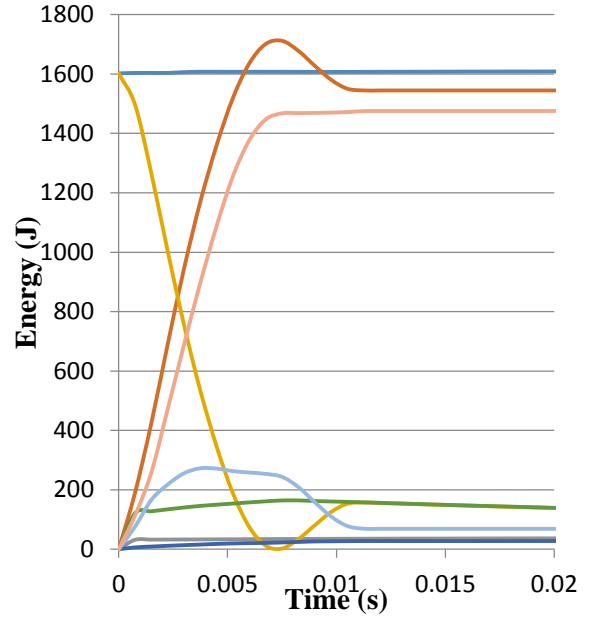
of the penalty contact forces and the external work done by the indenter, whose maximum is attained at 9 ms.

In order to examine the effect of using the liner, it could be seen that the internal energy is increased by 3% in case H1B corresponding to its counterpart in case H1A, when forming the maximum dent depth, after 7.5 ms, as shown in Figure 8-10(d). This increase is attributed to the increase in plastic energy which is applied to deform two pipes. Furthermore, the penalty contact between the AISI304 pipe and C-Mn pipe on the entire length has a significant effect on the work energy and the viscous dissipation energy in case H1B. The frictional energy increases slightly with increasing friction between the C-Mn pipe and the indenter. It could be seen that the frictional energy is doubled in case H1A with respect to that of H1B where the dent depth is larger.

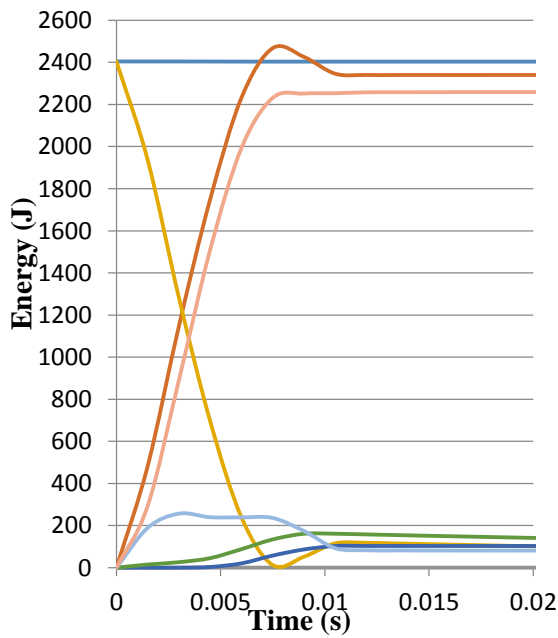
In all tests, increasing the height of the free load drop leads to an increase in the kinetic energy, which in turns raises the value of the plastic dissipation energy. The other types of energy have almost the same values in all cases. On other side, the properties of material should be taken into account in modelling the dynamic impact especially with spherical projectiles associated with higher kinetic energy and smaller geometry such as bullets. Consequently, the spherical projectiles in this case could most likely penetrate the pipe where elements located in this punched region should be deleted from the model. In our model, there is no penetration for the pipe and the deletion of elements is not modelled.



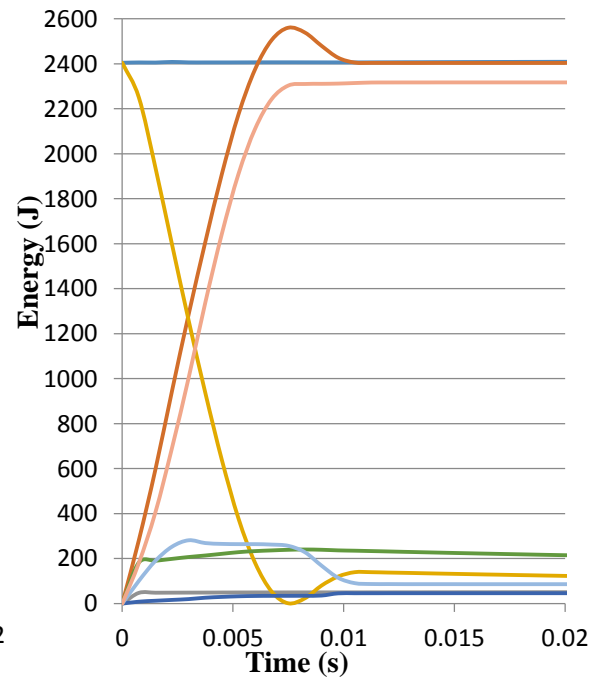
(a)



(d)



(b)



(e)

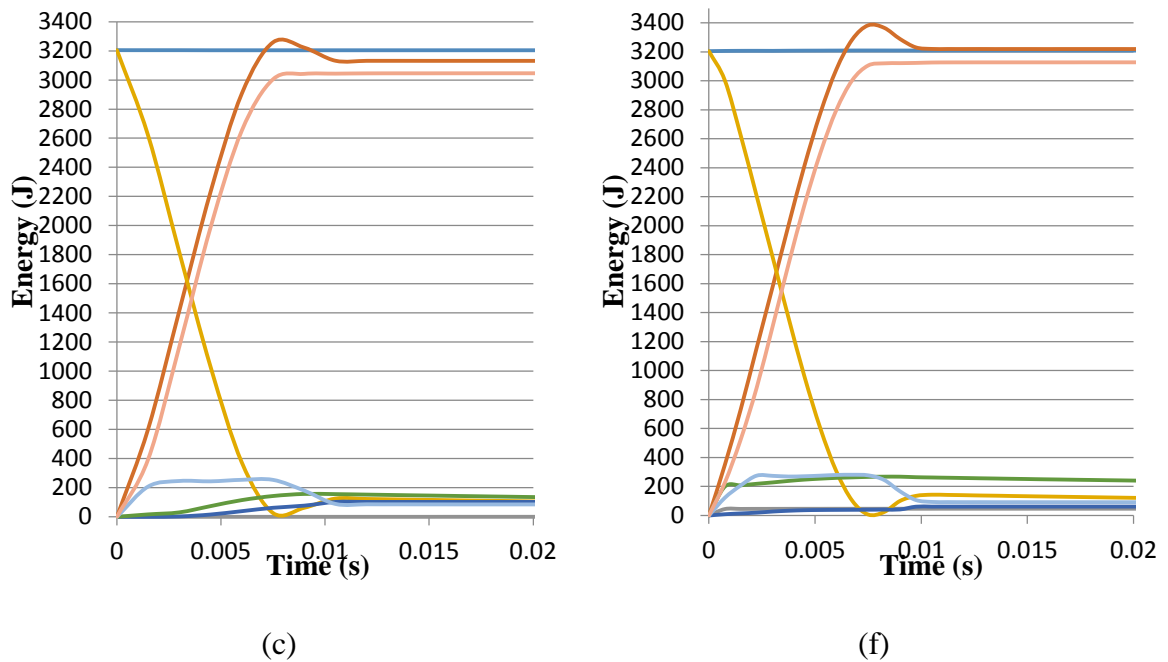


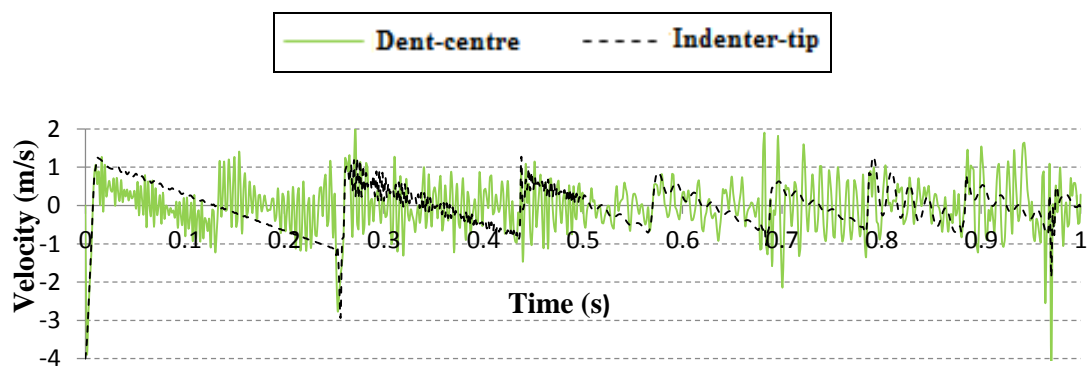
Figure 8-10 Consuming energy in the whole model in test (a) H1A, (b) H2A, (c) H3A, (d) H1B, (e) H2B, (f) H3B

8-3-6. Collision Velocity

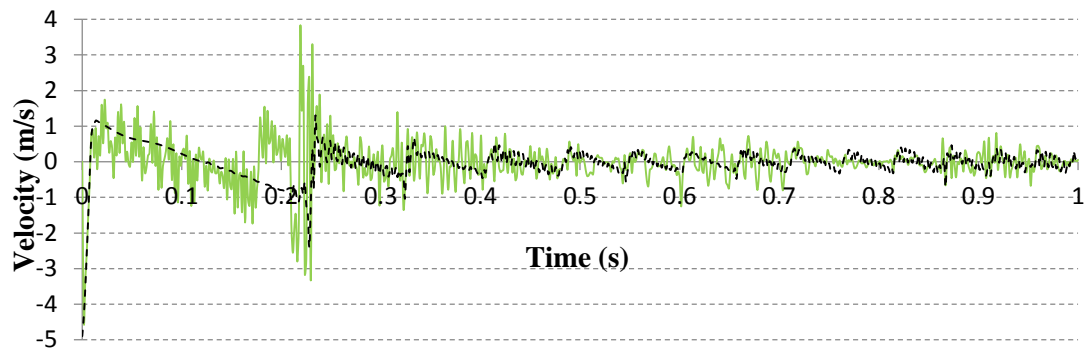
The dynamic impact test is characterized by a series of sequential strikes between the pipe and indenter. As a result of successive strikes in one impact test, the indenter hits the pipe with different velocity at every strike. Also, the pipe possesses a velocity after the strike because of bouncing over the bottom plate. Changes in velocity of the indenter and pipe during impact play a key role on consuming the energy and changing it to other types. Figure 8-11(a)-(f) shows the changes in the indenter velocity during the first minute of impact test starting from the moment when the indenter hits the pipe. It is clear from Figure 8-11(a)-(f) that the dent centre in the pipe without liner (case A) has more intensive oscillations in velocity than that in the lined pipe (case B). This can be attributed to the absence of the self-weight of the liner, AISI304 pipe, in case A which in turns enables the C-Mn pipe to bounce after the first strike with larger velocities comparing to their counterparts in case B. Moreover, the strikes in case A cause a deeper depth of dent, which in turns increases the width of pipe and urge the pipe to hit and contact the side plates through the entire impact process.

It can be seen from Figure 8-11(a) that the indenter hits the pipe with velocity of -4 m/s (negative because downward) and forces the dent centre to deform downwards with the same velocity of the indenter for 7.5 ms from the beginning of first strike. After that, both pipe and indenter go gradually up, with the velocity of pipe relatively lower because of the effect of collision between the pipe and side plate. After 133 ms, the indenter starts drop freely down (negative velocity) whilst the pipe in this moment bounces up, then down at 185 ms and then again up at 236 ms to meet the indenter at 252 ms over the ground. Collision over the ground results in dropping the pipe rapidly down to the ground with the same speed of indenter, -2.7 m/s. The actual second strike occurs on the ground at 258 ms. Ratcheting of the velocity of indenter tip slightly up and down is attributed to the resistance of the pipe to follow the direction of indenter especially when both the pipe and the indenter are in contact over the ground. The same observations can be repeated for the successive collisions with decreasing velocity of the indenter every time.

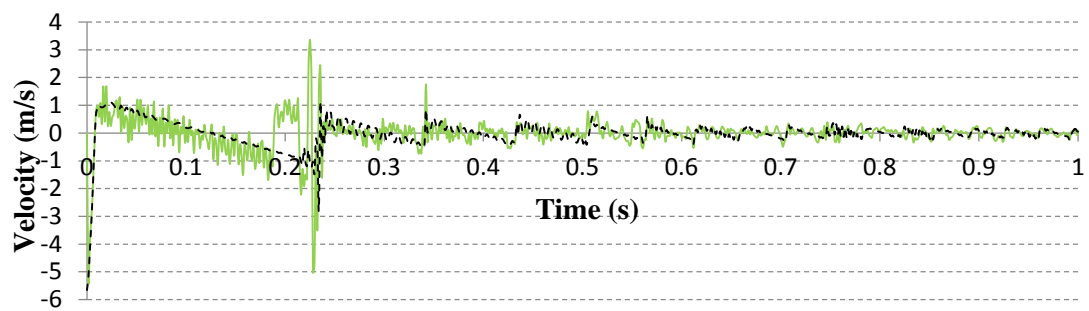
The preceding discussion applies to other pipes in cases A and B. It can be observed in all cases that increasing the height of free drop leads to an increase in the number of successive collisions. The times between the successive strikes in case B are longer than their counterparts in case A. It can also be seen that the velocity of the indenter does not oscillate in case B because there is no significant resistance to change its direction by the lined pipe.



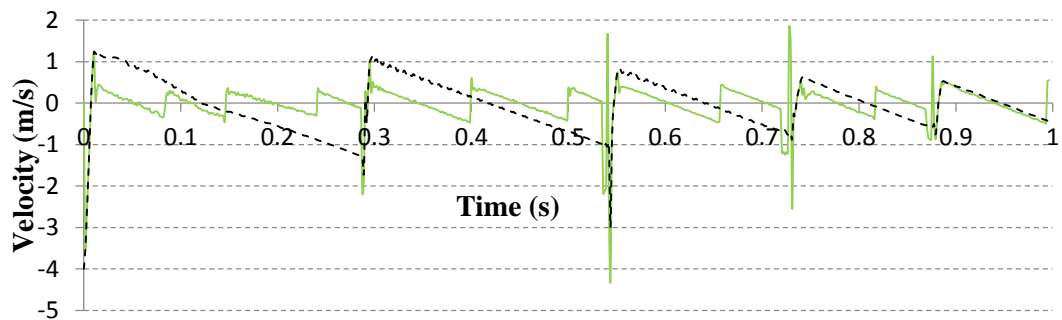
(a)



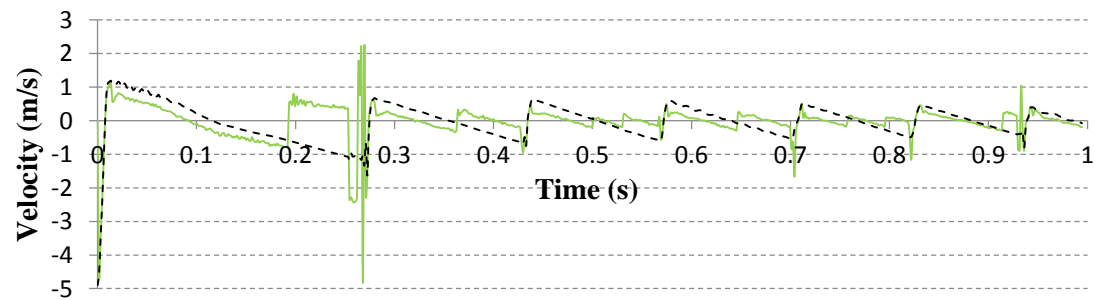
(b)



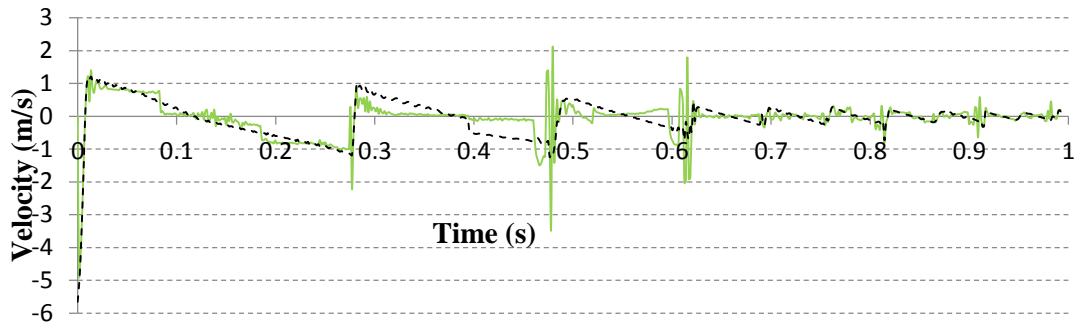
(c)



(d)



(e)



(f)

Figure 8-11 Velocity of dent centre and indenter-tip during the first minute of impact in test (a) H1A, (b) H2A, (c) H3A, (d) H1B, (e) H2B, (f) H3B

8-4. Mesh Convergence Analysis

The mesh density plays a decisive role in determining the accuracy of the FE results. As long as a proper mesh is used to simulate the dynamic impact, the element size should not affect the results of interest. To verify this is the case, two coarse mesh analyses have been conducted for case H1A to examine the stability of impact results. The C-Mn pipe in the normal mesh, first coarse mesh, and second coarse mesh is discretised with 7488, 2700 and 1064 nodes associated with 5355, 1680 and 486 elements, respectively, as shown in Figure 8-12. The first coarse mesh size, 1.5h, is equal or larger than 1.5 times of the normal mesh size, 1h, utilized in this study for case H1A whereas the second one is equal or larger than 2 times, 2h, of the normal one. However, the material properties and the element type, C3D8, in all meshes are kept the same.

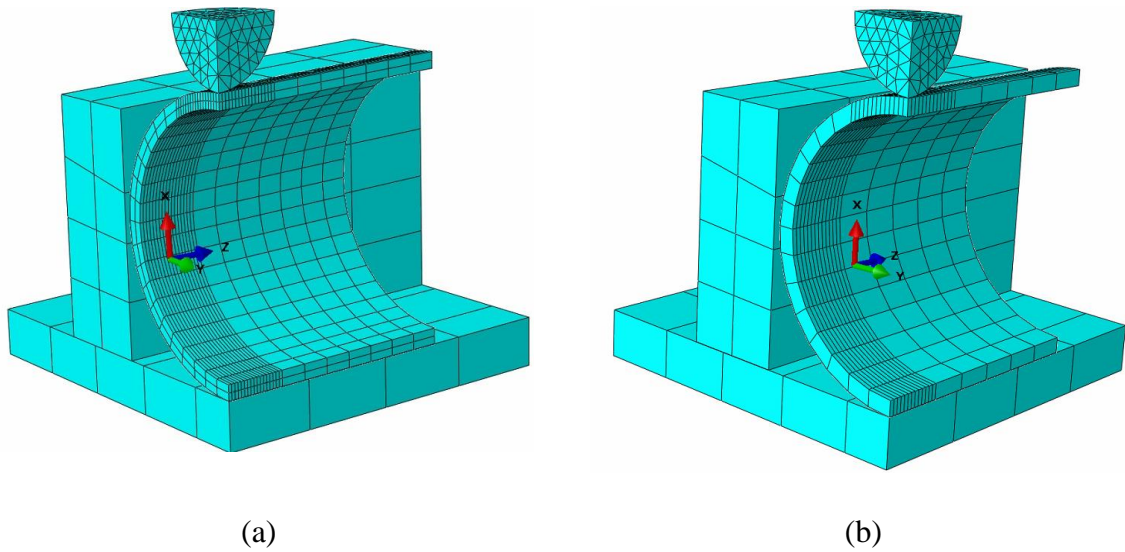


Figure 8-12 Coarse mesh of the quarter lined pipe model of case H1A with (a) 1.5h size and (b) 2h size

Comparing the strain results among the three mesh sizes at the GR1 location, it could be observed that the axial and hoop strain results of the 1.5h mesh model is firmly consistent with the results of the normal one, 1h mesh. It could also be seen there is a remarkable variation in the results between the 2h mesh model and the normal mesh model, with an absolute increase of 43% and 11% in the axial and hoop strain results, respectively, as shown in Figure 8-13.

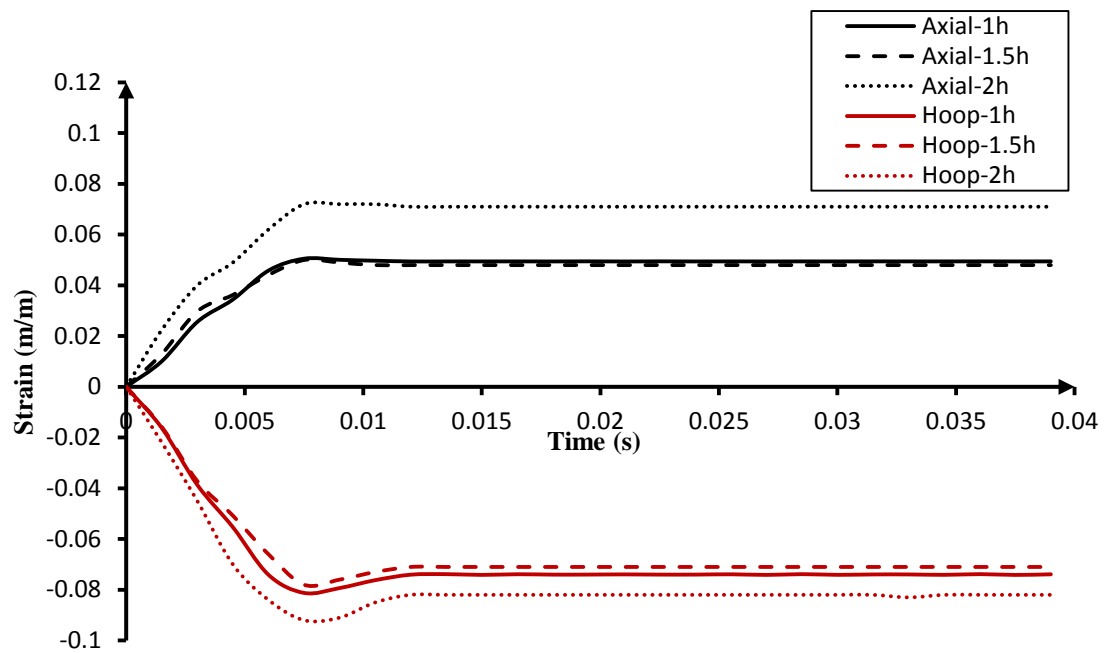


Figure 8-13 Axial and hoop strain histories of case H1A at Rosette GR1 location for three mesh sizes

Consequently, the normal mesh used in all cases in impact models can be considered appropriate to obtain sufficiently accurate numerical results, which present very little variation by increasing the mesh size to 1.5 times of the normal one.

8-5. Verification of the Experimental Results

In order to validate the accuracy of experimental results obtained in this study, the impact tests were repeated three times for cases H1A and H1B under the same conditions every time. Figure 8-14 and Figure 8-15 depict the axial and hoop strain distributions at rosette GR1 in cases H1A and H1B for three tests, respectively.

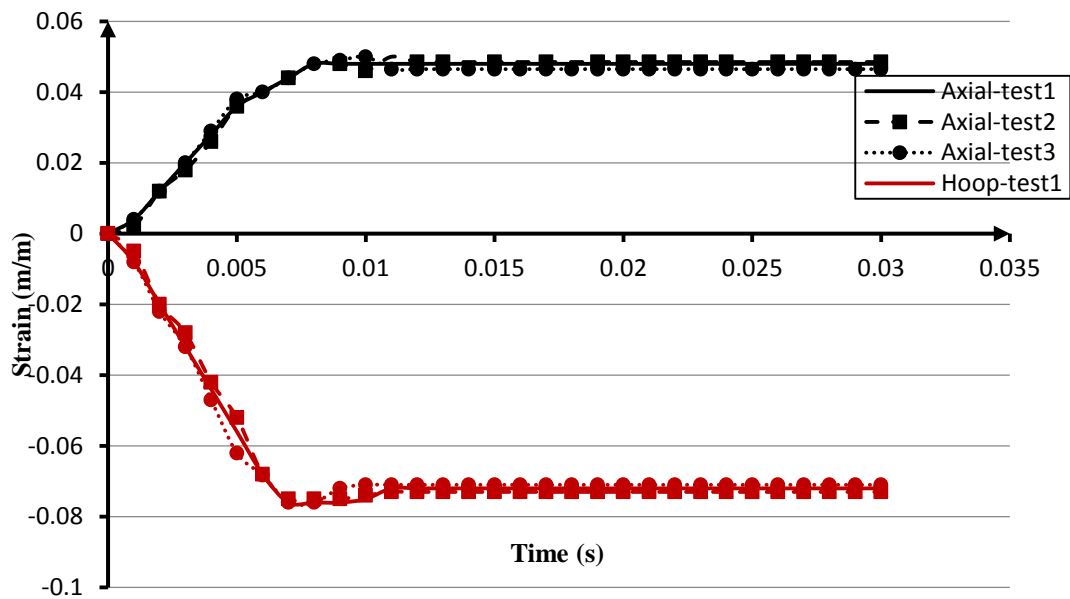


Figure 8-14 Strain results of repeated test for case H1A at rosette GR1

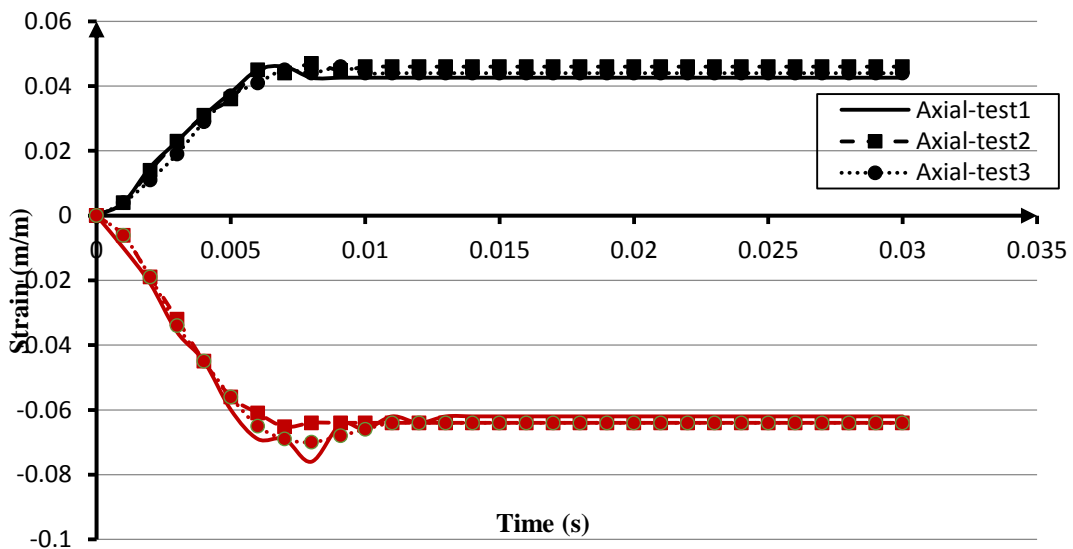


Figure 8-15 Strain results of repeated test for case H1B at rosette GR1

From Figure 8-14 and 8-15, it could be seen that there is a very good correlation among all repeated tests, which in turn confirm the reliability of the experimental procedure used and, therefore, of the other experimental results.

8-6. Conclusions

In this chapter, the results of an experimental and numerical study of the impact of a 200 kg weight freely dropped from different heights over lined pipe specimens has been reported, including in particular the evaluation of the stress/strain behaviour in the dented region. The effect of the liner on the dynamic impact process has also been investigated. The numerical strain results have been compared with the experimental ones recorded by four strain gauge rosettes positioned symmetrically around the dent centre. The various types of energy dissipation and the velocity of impact process have been also evaluated and discussed. In general, the reliability of our numerical and experimental findings in this work is confirmed by the mesh convergence analysis and by the repeated dynamic impact tests respectively.

The following main conclusions can be drawn:

- (1) There is a very good correlation between the numerically predicted deformed geometries and the experimental ones in all cases. Increasing the dropping altitude leads to an increase in the ratio of dent depth-to-pipe outside diameter which is over 10% in all case. With this ratio, all cases have a high susceptibility to burst in service according to EPRG (Roovers et al., 2000).
 - (2) During the first strike of the impact process, it is evident that the pipe detrimentally deforms from the first collision to form a dent characterized by tangential compressive strains to the dent periphery and perpendicular tensile strains to it. Also, increasing the dropping height leads to increase in the strain value. Due to the effect of the liner, the absolute values of strain in case A are larger than their counterparts in case B associated with the same altitude.
 - (3) Removing the indenter leads to a higher concentration of residual stresses at the dent perimeter on the top surface of pipe. At the dent periphery, the longitudinal plane has significant higher tensile hoop residual stresses than the transverse plane which in turn contribute to initiate and grow crack along this direction.
 - (4) Due to deformation of the two pipes together, the plastic energy consumed in case B (with liner) is higher by 3% than that in case A whilst the elastic strain
-

energy to a large extent remains the same in all cases. Furthermore, penalty contact between the liner and C-Mn pipe plays an important role in increasing the work energy during impact.

- (5) Removing the liner enables the C-Mn pipe to bounce higher and hits the indenter again over the ground. Furthermore, the time elapsed between the actual successive strikes is significantly shorter in case A than that in case B (with liner).
- (6) The credibility of predicted and measured strain results have been examined numerically and experimentally through three mesh convergence analyses and three repeated tests, respectively. Consequently, results in this study have a high reliability numerically and experimentally.

Chapter 9

Summary, Conclusions and Future Work Recommendations

Based on the major and minor research questions stated in Chapter 1, it is possible to confirm that this research work answered these questions successfully.

9-1. Major conclusions

By referring specifically to the main questions, the following major conclusions can be broken down as follows:

- *What procedures should be applied to develop, execute and validate a FE model capable of simulating the welding process of lined pipe with high accuracy?*

Uncoupled FE thermo-mechanical analyses have been conducted to simulate the weld overlay and girth welding using ABAQUS (Dassault Systèmes, 2014). Therefore, the thermal analysis is simulated first to acquire the thermal history at each node through the lined pipe. This thermal history is then transferred as thermal load for the mechanical analysis, which is conducted the same mesh associated with the same arrangement of nodes and elements used in the thermal analysis.

A moving heat source combined with the element-birth technique is used to simulate the deposition of the elements of weld bead incrementally. This technique involves deactivating all beads first and then depositing the weld beads sequentially, once the heat source reaches the targeted bead. Moreover, two user-subroutines have been coded using FORTRAN codes to model a distributed power density of the moving welding torch and to use a non-linear heat transfer coefficient accounting for both radiation and convection.

In Chapter 5, the welding procedure has been validated first against experimental results in the literature related to two separated cases involving the welding of a C-Mn pipe (Karlsson and Josefson, 1990) and a stainless steel pipe (Deng and Murakawa, 2006). A good correlation between the numerical thermal and mechanical results and their counterparts obtained from (Karlsson and Josefson, 1990) and (Deng and Murakawa, 2006) was the motivation to develop a 3-D model of the welded lined-pipe joints, in which two segments of lined pipe are joined together with a one-pass weld overlay and a one-pass girth welding. Only one-half of the lined pipe specimen, one segment, was modelled due to the symmetry around the weld centreline (WCL). Furthermore, a sensitivity analysis to determine the influence of the cooling time between weld overlay and girth welding, i.e. the inter-pass time, and of the welding speed has been conducted thermally and mechanically. From the outcome of our investigation it is possible to conclude that the temperature history is not sensitive to the variations of the circumferential angles. As expected, the less interval time is applied, the higher temperature is obtained during the girth welding. Doubling or halving the weld overlay and girth welding speeds leads to significantly decrease or increase the width of the FZ, respectively. Furthermore, the largest tensile and compressive axial residual stresses occur at the FZ and its vicinity on the inner and outer surfaces, respectively. Minimizing the inter-pass time to 1 second leads to a reasonable increase in the absolute magnitudes of axial residual stresses at the WCL about 21% on the inner surface and 10% on the outer surface. Halving the weld overlay and girth welding speeds has more influence in increasing the absolute values of hoop and axial residual stresses at the WCL whereas doubling speed does not have that effect on the results at the FZ according to the basic case, case A.

- *Is it possible to develop an effective procedure to manufacture small-scale lined pipe specimens in a lab environment at a reasonable cost, maintaining the levels of initial residual stresses acceptable?*

The TFP procedure has been successfully implemented, as reported in detail in Chapter 3, by heating up the outer pipe in a furnace to about 500°C, moving it away from the furnace into a portable jacket heater, inserting the liner into liquid Nitrogen until it cools down at -200°C, inserting the liner vertically inside the C-Mn pipe,

while the latter is still hot inside the jacket, and finally letting the lined pipe cool naturally, exposed to ambient air temperature.

The TFP method is responsible to generate initial residual stresses in the lined pipe although required conditions have been taken into account to reduce these initial residual stresses, such as the temperatures of contraction, expansion and cooling the produced lined pipe naturally. Two techniques have been used to measure the initial residual stresses induced by TFP, namely hole-drilling and X-ray diffraction.

In Chapter 6, a 3-D model has been executed in ABAQUS 6.13 (Dassault Systèmes, 2014) corresponding to the configuration of the welded line pipe experimentally tested. The aim in this chapter was to study the effect of the TFP pre-heat treatment on the thermal fields and residual stresses in the welded lined pipe. The findings point out that the thermal history during welding is not completely affected by the TFP process. In particular, the residual stress distributions are divided into three sections. In the first one closer to the WCL, the residual stresses are solely affected by the welding process. The length of this zone relies on the extent of the axial and hoop plastic strains. The second one stretches from the previous limit to the limit where the residual stress distributions become constant along the length. This section is under the influence of both the welding process and the TFP pre-heat treatment. In the last section, which starts when the residual stress distribution is practically constant, the pipe is just under the influence of initial residual stresses caused by the TFP process. The initial residual stresses occur with small levels in the AISI304 pipe whilst it is practically negligible in the C-Mn pipe.

A small level of initial residual stresses in the AISI304 pipe was found whilst residual stresses in the C-Mn pipe were found to be negligible. The maximum numerically computed axial and hoop initial residual stresses on the inner surface, AISI304 pipe, are 122 and 113 MPa whilst their experimental counterparts are lowered by 50%, respectively. The initial residual stress on the inner surface is attributed to TFP process where the liner temperature jump higher in 4.3 seconds from -200°C to $+419^{\circ}\text{C}$ to be in balance with outer pipe temperature.

- *What are the main factors which can affect the quality and results of the welding process of a lined pipe?*

Six cases were experimentally and numerically studied in Chapter 7, by considering different factors affecting the quality and results of the welding process. The first case was considered the reference case where the weld overlay and girth welding have been executed with different materials of their base metals, accordingly. In the second case, the material of girth welding was the same as the weld overlay material. In the third case, the effect of neglecting the weld overlay has been discussed. In this case, the two parts of the lined pipe have been solely joined using girth welding. The material of girth welding in this case is the same used in first case. In the fourth case, the heat input was lowered to 75% of the heat input in first case for all welds. In a similar way, the heat input in the fifth case was dropped to 50% of that in first case. The liner with weld overlay is not considered in the last case.

The thermal history and residual stress distributions have been investigated for particular locations on the inner and outer surfaces in comparison with their experimental counterparts using thermocouples and residual stress gauges. The main findings point out that the numerical thermal results are consistent with the experimental results with variation less than 6% for all cases. Furthermore, the discrepancies between the thermal results of the reference case and other parametric cases decrease by heading far away from the WCL along the axial direction. From the outcome of mechanical investigation it is possible to conclude that change in steel type of girth welding material from carbon steel to stainless steel leads to a reduction in the axial and hoop residual stresses on the inner and outer surfaces at the FZ. Moreover, removing the weld overlay leads to a significantly reduction in the axial and hoop residual stresses at the FZ on the inner and outer surface. Also, reducing the heat input produces lower residual stresses at the FZ and its vicinity on the inner and outer surface. Finally, the extents of tensile and compressive stresses on the inner and outer surfaces become significantly narrower by omitting the liner.

- *What procedures should be applied to develop, execute and validate a FE model capable of simulating a lined pipe subject to a dynamic impact comparable with the ones which might occur during installation?*

3D FE models were developed to simulate the mechanism of vertical free drop of a weight from different heights resulting in damage in the pipe. Simulations were executed using the non-linear explicit dynamics FE code, ABAQUS/EXPLICIT 6.13

(Dassault Systèmes, 2014), and the FE results were compared with the experimental results. The steps of the analysis reflect typically the procedure employed in experimental tests. Initially, the indenter freely drops down from a specific height to punch the external surface of C-Mn pipe with a specified actual velocity. The kinematic energy is dissipated completely to produce indentation in the lined pipe before the indenter and pipe retreat vertically as a reaction of collision. The hitting tool and the pipe fall down afterward because of their self-weight. The weights include those of block, spherical indenter, liner and C-Mn pipe. The indenter hits the lined pipe frequently, the maximum distance of collision reducing every time because of the dissipation of the kinetic energy. Consequently, the collision leaves permanent deformation in the lined pipe which in turn produces residual stresses in the base materials, AISI304 and C-Mn. Removing the indenter and the block releases somewhat elastic stresses in the pipe wall, which in turn result in a slight rebound of the dent depth. Nevertheless, the residual stresses remain in the base materials with different levels of plasticity, the highest level being located in the dented region.

The experiments include two groups of pipes. The first one, case A, is implemented just on a C-Mn pipe without liner. The second group, case B, is conducted on a lined pipe composed of a C-Mn pipe clad with AISI304 pipe internally. To conduct the impact test, a weight of 200 kg equipped with a semi-spherical indenter with diameter of 51.75 mm was dropped freely from 1, 1.5 and 2 m on the specimens. During the impact process, a digital high speed camera was utilized to measure the actual impact velocity and also to capture the sequential strikes after the first collision between the indenter and pipe. After the impact process, the geometries of pipe were measured with the aid of conventional callipers and a displacement transducer sliding on a greased flat plate, while the pipe was mounted on V-groove blocks. It is possible to conclude that there is a very good correlation between the numerically computed deformed geometries and the experimental ones in all cases of dynamic impact. Furthermore, increasing the dropping height leads to an increase in the ratio of dent depth-to-pipe outside diameter which is over 10% in all cases. With this ratio, all cases have a high susceptibility to burst in service according to EPRG (Roovers et al., 2000). The strain results obtained during impact show that the pipe detrimentally deforms from the first collision to form the dent, which is characterized by tangential compressive strains at the dent periphery and tensile strains

perpendicular to it. Also, increasing the dropping height leads to an increase in the strain value.

- *To what extent the response of a lined pipe subject to dynamic impact differs from the response of a similar pipe without liner in terms of the residual stresses and strains?*

The maximum tensile hoop stresses on the longitudinal direction in cases with liner are larger than their counterparts without liner about 30%. Due to the effect of the liner, the absolute values of strain in cases without liner are larger than their counterparts in cases with the liner corresponding to the same drop height.

- *What is the effect of the energy and the velocity of the impact on the damage within a lined pipe?*

In all tests, increasing the height of the free drop contributes to an increase in the kinetic energy which in turn raises the value of the plastic dissipation energy. The maximum plastic energy consumed in cases with liner is higher by 3% than that in cases without liner. On the other side, the elastic strain energy and other types of energy have almost the same values in all cases.

Increasing the height of free drop leads also to increase the collision velocity and the number of successive collisions. The cases with liner have longer times between the successive strikes than their counterparts without liner. There is no oscillation in the velocity of indenter in cases with liner because there is no significant resistance to change its direction by the lined pipe.

On the other hand, strain rate plays a key role in determining the residual stresses, where increasing the strain rate leads to push highly the yield stress of material. As a result, increasing the drop height contributes to reduce the residual stresses on the dented regions where the maximum ones are located at the dent periphery. At this region, the longitudinal plane has significant higher tensile hoop residual stresses by 40% than that on the transverse plane, which in turn contribute to initiate and grow crack along this direction.

9-2. Limitations

Our work still has some limitations which require further discussion outside the scope of this work and to be taken up in a separate work. The main caveats can be listed as follows:

1. The thermal isotherms are not measured perfectly at the centre of FZ with temperatures are over 2000°C where the maximum temperature range calibration for the infrared camera used, FLIR T, is up to 2000°C.
2. During welding, the strain history at the FZ is not measured due to the high temperature.
3. The strain history during dynamic impact is not recorded on the inner surface at the dented region where it is difficult to mount strain gauges on the liner.
4. The strain history is also not measured at the centre of the dented region on the outer surface where the indenter hits the outer pipe.

In FE model, the crack initiation and propagation have not been modelled for both cases in lined pipe, impact and welding. Consequently, the welded and dented lined pipe models are used to simulate the regions which could likely contain crack formation and propagation but not used to simulate a cutting trajectory through elements. Moreover, other metals could contribute to change the mechanical behaviour of lined pipe under impact and welding including the residual stress levels in impact and welding models. In the impact models, the deletion of elements because of the pipe penetration by spherical projectiles, bullets, associated with higher kinetic energy and smaller geometry are not simulated.

9-3. Recommendations for Future Work

In the previous comprehensive conclusions were drawn on the work conducted in this PhD project, which can be considered the first phase in evaluating the welding and dynamic impact in lined pipe numerically and experimentally. The major area of concern in lined pipe welding domain is simulating two different welding materials associated with two different base materials. Also, modelling the dynamic impact with respect to moving bodies and the subsequent strikes is a considerable achievement. Furthermore, finding a proper procedure to insert the liner inside the C-

Mn pipe according to the materials and resources available in a University lab is an important achievement in this study. Therefore, this thesis has provided significant contribution in addressing the above critical issues successfully.

It is recommended that the following points are addressed in future work.

- (1) The computational methodology and techniques used to develop 3-D FEA to simulate the lined pipe welding can also be utilized with different materials other than carbon steel and stainless. Also, the materials used in the impact FE analysis can easily be changed to different ones.
- (2) The welding FE model has been applied in this work for TIG welding. Other types of welding such as MIG and laser can also be modelled according to the welding technique applied in this work but the nature and requirement of this process, especially the welding efficiency, should be adjusted and considered.
- (3) The developed welding FE model can be applied to a compound pipe with more than two layers with different welding locations, in conjunction with different base and welding materials. Furthermore, the FE welding model is suited to a pipe fitted with various buttering and cladding layers. Also, the FE impact model can be easily applied on a compound pipe.
- (4) The movement of the heat source in the FE welding model can easily change its direction and path sequence to different ones either in the same pass or in other passes. For example, instead of a continuous 360-degree revolution, regular angles can be skipped in order to complete the entire circular welding pass but not in one continuous revolution, in order to reduce the residual stresses. The developed FE models can easily be used to investigate these techniques and optimise the welding process without the need of expensive experimental testing.
- (5) Fatigue tests can be conducted with the application of cyclic internal pressure in welded and dented lined pipe specimens. The stress concentrations localised in the dented and welded regions should be considered as the initiation of cracks and leaking.
- (6) The most complicated case in FE modelling includes simulating the circumferential welding process first, then applying the impact process and finally studying the fatigue loading. This case can be done using the impact

and welding FE modelling procedures presented in this work, by a proper sequence of thermal, structural, dynamic and static analyses.

References

- Abid, M. and Siddique, M. (2005) 'Numerical simulation to study the effect of tack welds and root gap on welding deformations and residual stresses of a pipe-flange joint', *International Journal of Pressure Vessels and Piping*, 82(11), pp. 860-871.
- Abid, M., Siddique, M. and Mufti, R.A., 2005. Prediction of welding distortions and residual stresses in a pipe-flange joint using the finite element technique. *Modelling and Simulation in Materials Science and Engineering*, 13(3), p.455.
- Akbari, D. and Sattari-Far, I. (2009) 'Effect of the welding heat input on residual stresses in butt-welds of dissimilar pipe joints', *International Journal of Pressure Vessels and Piping*, 86(11), pp. 769-776.
- Alexander, C. and Brownlee, K. (2007) 'Methodology for assessing the effects of plain dents, wrinkle bends and mechanical damage on pipeline integrity', *NACE2007-07139. NACE International Corrosion 2007 Conference & Expo. Nashville, Tennessee.*
- Alexander, C.R. and Kiefner, J. (1997) 'Effects of smooth and rock dents on liquid petroleum pipelines', *1999 API Pipeline Conference, Dallas, Texas.*
- Allouti, M., Schmitt, C., Pluvinage, G., Gilgert, J. and Hariri, S. (2012) 'Study of the influence of dent depth on the critical pressure of pipeline', *Engineering Failure Analysis*, 21, pp. 40-51.
- Aloraier, A., Almazrouee, A., Shehata, T. and Price, J.W. (2012) 'Role of welding parameters using the flux cored arc welding process of low alloy steels on bead geometry and mechanical properties', *Journal of materials engineering and performance*, 21(4), pp. 540-547.
- American National Standards Institute (1995) *Gas transmission and distribution piping systems*. American Society of Mechanical Engineers.
- American National Standards Institute. Committee B31, Code for Pressure Piping (2012) *Pipeline Transportation Systems for Liquids and Slurries: ASME Code for Pressure Piping, B31*. American Society of Mechanical Engineers.
- ASTM, E. (2008) '837 Standard method for determining residual stresses by the hole-drilling strain gage method', *Annual book of ASTM standards*.
- Attarha, M. and Sattari-Far, I. (2011) 'Study on welding temperature distribution in thin welded plates through experimental measurements and finite element simulation', *Journal of Materials Processing Technology*, 211(4), pp. 688-694.
- Benson, D. (2014) 'Tips for Successfully Welding Stainless Steel to Carbon Steel', *Welding journal*, 93(5), pp. 54-56.

- Brickstad, B. and Josefson, B. (1998) 'A parametric study of residual stresses in multi-pass butt-welded stainless steel pipes', *International Journal of Pressure Vessels and Piping*, 75(1), pp. 11-25.
- British Stainless Steel Association, 2016. BRITISH STAINLESS STEEL ASSOCIATION Making the Most of Stainless Steel.
- Corder, I. and Chatain, P. (1995) 'EPRG Recommendations for the Assessment of the Resistance of Pipelines to External Damage', *Proceedings of the EPRG/PRC 10th Biennial Joint Technical Meeting On Line Pipe Research, Cambridge, UK*.
- Cosham, A. and Hopkins, P. (2004) 'The effect of dents in pipelines—guidance in the pipeline defect assessment manual', *International Journal of Pressure Vessels and Piping*, 81(2), pp. 127-139.
- Cunha, S., Pasqualino, I. and Pinheiro, B. (2009) 'Stress-life fatigue assessment of pipelines with plain dents', *Fatigue & Fracture of Engineering Materials & Structures*, 32(12), pp. 961-974.
- Cunha, S.B., Pinheiro, B.C. and Pasqualino, I.P. (2007) 'High Cycle Fatigue of Pipelines With Plain Dents: Simulations, Experiments and Assessment', *ASME 2007 26th International Conference on Offshore Mechanics and Arctic Engineering*. American Society of Mechanical Engineers, 123-132.
- Dar, N.U., Qureshi, E.M. and Hammouda, M. (2009) 'Analysis of weld-induced residual stresses and distortions in thin-walled cylinders', *Journal of Mechanical Science and Technology*, 23(4), pp. 1118-1131.
- Dassault Systèmes (2014) *ABAQUS 6.14 Analysis User's Guide, Volume III: Materials*. USA.
- Davis, P., Dubois, J., Gambardella, F., Sanchez-Garcia, E. and Uhlig, F. (2011) *Performance of European cross-country oil pipelines. Statistical summary of reported spillages in 2009 and since 1971*.
- De Deus, A.M. (2004) 'A thermal and mechanical model of laser cladding', *Dissertation Abstracts International*, 65(04)
- De Koning, A., Nakasugi, H. and Li, P. (2004) 'TFP and TFT back in town (Tight fit CRA lined pipe and tubing)', *Stainless Steel World*, , pp. 53-61.
- Deng, D. and Kiyoshima, S., 2010. Numerical simulation of residual stresses induced by laser beam welding in a SUS316 stainless steel pipe with considering initial residual stress influences. *Nuclear Engineering and Design*, 240(4), pp.688-696.
- Deng, D., Kiyoshima, S., Ogawa, K., Yanagida, N. and Saito, K. (2011) 'Predicting welding residual stresses in a dissimilar metal girth welded pipe using 3D finite element model with a simplified heat source', *Nuclear Engineering and Design*, 241(1), pp. 46-54.
- Deng, D. and Murakawa, H. (2006) 'Numerical simulation of temperature field and residual stress in multi-pass welds in stainless steel pipe and comparison with experimental measurements', *Computational materials science*, 37(3), pp. 269-277.

- Deng, D., Murakawa, H. and Liang, W. (2008) 'Numerical and experimental investigations on welding residual stress in multi-pass butt-welded austenitic stainless steel pipe', *Computational Materials Science*, 42(2), pp. 234-244.
- Deus, A. and Vilar, R. (1996) 'One-dimensional thermal model including the dependence of absorptivity on temperature using Hagen-Rubens equation', in *Laser Processing: Surface Treatment and Film Deposition*. Springer, pp. 195-201.
- Durkin, S. (1987) 'An analytical method for predicting the ultimate capacity of a dented tubular member', *International Journal of Mechanical Sciences*, 29(7), pp. 449-467.
- Eiber, R.J. (1981) *The Effects of Dents on Failure Characteristics of Line Pipe*. American Gas Assn.
- Escoe, K. (2006) *Piping and pipelines assessment guide*. Gulf Professional Publishing.
- Fachinotti, V.D., Anca, A.A. and Cardona, A. (2011) 'Analytical solutions of the thermal field induced by moving double-ellipsoidal and double-elliptical heat sources in a semi-infinite body', *International Journal for Numerical Methods in Biomedical Engineering*, 27(4), pp. 595-607. Focke, E.S. (2007) *Reeling of tight fit pipe*. TU Delft, Delft University of Technology.
- Focke, E., Gresnigt, A., Meek, J. and Nakasugi, H. (2006) 'The influence of heating of the liner pipe during the manufacturing process of tight fit pipe', *The Sixteenth International Offshore and Polar Engineering Conference*. International Society of Offshore and Polar Engineers.
- Focke, E., Gresnigt, A., Meek, J. and Nakasugi, H. (2005) 'Experimental research on local buckling behaviour of tight fit pipe', *The Fifteenth International Offshore and Polar Engineering Conference*. International Society of Offshore and Polar Engineers.
- Focke, E., Van Oosten, J., Meek, J., Romeijn, A. and Nakasugi, H. (2005) 'The Influence of the Reeling Installation Method on the Integrity of Circumferential Welds in Tight Fit Pipe', *The Fifteenth International Offshore and Polar Engineering Conference*. International Society of Offshore and Polar Engineers.
- Fowler, J. (1993) 'Criteria for dent acceptability in offshore pipeline', *Offshore Technology Conference*. Offshore Technology Conference.
- Fowler, J., Alexander, C., Kovach, P. and Connelly, L. (1995) *Fatigue life of pipelines with dents and gouges subjected to cyclic internal pressure*, .
- Fowler, J., Alexander, C., Kovach, P. and Connelly, L. (1994) *Cyclic Pressure Fatigue Life of Pipelines with Plain Dents, Dents With Gouges, and Dents With Welds*.
- Gery, D., Long, H. and Maropoulos, P. (2005) 'Effects of welding speed, energy input and heat source distribution on temperature variations in butt joint welding', *Journal of Materials Processing Technology*, 167(2), pp. 393-401.
- Goldak, J., McDill, M., Oddy, A., House, R., Chi, X. and Bibby, M. (1986) 'Computational heat transfer for weld mechanics', *Proceeding of International Conference on Trends in Welding Research*, 15-20.

- Goldak, J.A. and Akhlaghi, M. (2006) *Computational welding mechanics*. Springer Science & Business Media.
- Goldak, J., Chakravarti, A. and Bibby, M. (1984) 'A new finite element model for welding heat sources', *Metallurgical transactions B*, 15(2), pp. 299-305.
- Gorman, D.G., Reese, J.M. and Zhang, Y.L., 2000. Vibration of a flexible pipe conveying viscous pulsating fluid flow. *Journal of Sound and Vibration*, 230(2), pp.379-392.
- Guidebook, E.R. (2006) *Pipeline and Hazardous Materials Safety Administration, US Department of Transportation*.
- Hamdan, F. (2001) *Design guide for steels at elevated temperatures and high strain rates*.
- Handbook, M. (1973) 'Vol. 8', *ASM, Metals Park, OH*, 263.
- Hilberink, A. (2011) *Mechanical behaviour of lined pipe*. PhD Thesis. TU Delft.
- Hui, Z.H.A.O., 2011. The Quality Management of Pipe Welding in Standard of API1104. *Journal of Xinjiang Vocational University*, 6, p.024.
- International Nickel Limited (1974) *Materials for Cryogenic Service-Engineering, Properties of Austenitic Stainless Steels: Publication No. 4368*. Nickel Development Institute, courtesy of Inco Limited.
- Johnston, D.C. and Hrnecir, T.G. (2002) 'Using in-line inspection to address deformations containing near-neutral pH stress corrosion cracking', *2002 4th International Pipeline Conference*. American Society of Mechanical Engineers, 1549-1553.
- Jonsson, M. and Josefson, B. (1988) 'Experimentally determined transient and residual stresses in a butt-welded pipe', *The Journal of Strain Analysis for Engineering Design*, 23(1), pp. 25-31.
- Josefson, L., Jonsson, M., Karlsson, L., Karlsson, R., Karlsson, T. and Lindgren, L. (1989) 'Transient and residual stresses in a single-pass butt welded pipe', *International Conference on Residual Stresses*. Springer, 497-503.
- Karlsson, C. (1989) 'Finite element analysis of temperatures and stresses in a single-pass butt-welded pipe-influence of mesh density and material modelling', *Engineering Computations*, 6(2), pp. 133-141.
- Karlsson, R. and Josefson, B. (1990) 'Three-dimensional finite element analysis of temperatures and stresses in a single-pass butt-welded pipe', *Journal of pressure vessel technology*, 112(1), pp. 76-84.
- Keating, P. and Hoffmann, R. (1997) 'Fatigue behavior of dented petroleum pipelines', *Texas A&M University Final Report to US Department of Transportation*, .
- Lee, C. and Chang, K. (2008) 'Three-dimensional finite element simulation of residual stresses in circumferential welds of steel pipe including pipe diameter effects', *Materials Science and Engineering: A*, 487(1), pp. 210-218.
- Lee, C., Chang, K. and Park, J. (2013) 'Three-dimensional finite element analysis of residual stresses in dissimilar steel pipe welds', *Nuclear Engineering and Design*, 256, pp. 160-168.

- Lee, W. and Liu, C. (2006) 'The effects of temperature and strain rate on the dynamic flow behaviour of different steels', *Materials Science and Engineering: A*, 426(1), pp. 101-113.
- Leggatt, R. (1982) 'Residual stresses at circumferential welds in pipes', *Welding Institute Research Bulletin*, 23(6), pp. 181-188.
- Lindgren, L. (2014) *Computational welding mechanics*. Elsevier.
- Luo, Y. (1997) *Description of inherent strain and its application to prediction of welding deformation and residual stress under multi-pass welding*, .
- Malik, A.M., Qureshi, E.M., Dar, N.U. and Khan, I. (2008) 'Analysis of circumferentially arc welded thin-walled cylinders to investigate the residual stress fields', *Thin-Walled Structures*, 46(12), pp. 1391-1401.
- Measurements, V.M. (2007) *Measurement of residual stresses by the hole drilling strain gage method*.
- Michaleris, P. and DeBiccari, A. (1997) 'Prediction of welding distortion', *Welding Journal-Including Welding Research Supplement*, 76(4), pp. 172s.
- Netto, T., Ferraz, U. and Estefen, S. (2005) 'The effect of corrosion defects on the burst pressure of pipelines', *Journal of constructional steel research*, 61(8), pp. 1185-1204.
- Nicholas, T. (1980) *Dynamic tensile testing of structural materials using a split Hopkinson bar apparatus*, .
- Noyan, I., Huang, T. and York, B. (1995) 'Residual stress/strain analysis in thin films by X-ray diffraction', *Critical Reviews in Solid State and Material Sciences*, 20(2), pp. 125-177.
- Pavelic, V., Tanbakuchi, R., Uyehara, O. and Myers, P. (1969) 'Experimental and computed temperature histories in gas tungsten-arc welding of thin plates', *WELD J*, 48(7), pp. 295.
- Pinheiro, B.d.C. and Pasqualino, I.P. (2009) 'Fatigue analysis of damaged steel pipelines under cyclic internal pressure', *International Journal of Fatigue*, 31(5), pp. 962-973.
- Pipeline transportation systems for liquids and slurries. (2012). New York: American Society of Mechanical Engineers.
- Qureshi, M.E., 2008. *Analysis of Residual Stresses and Distortions in Circumferentially Welded Thin-Walled Cylinders* (Doctoral dissertation, National University of Sciences and Technology).
- Race, J. (2008) 'REPORT PREPARED FOR UKOPA'.
- Race, J.M., Haswell, J.V., Owen, R. and Dalus, B. (2010) 'UKOPA dent assessment algorithms: a strategy for prioritising pipeline dents', *2010 8th International Pipeline Conference*. American Society of Mechanical Engineers, 923-933.
- Rinehart, A.J. and Keating, P.B. (2002) 'Length effects on fatigue behavior of longitudinal pipeline dents', *2002 4th International Pipeline Conference*. American Society of Mechanical Engineers, 1849-1858.
- Rinehart, A.J. (2004) *Effects of localized geometric imperfections on the stress behavior of pressurized cylindrical shells*.

- Roovers, P., Bood, R., Galli, M., Marewski, U., Steiner, M. and Zaréa, M. (2000) 'EPRG methods for assessing the tolerance and resistance of pipelines to external damage', *Pipeline technology*, 2, pp. 405-425.
- Sattari-Far, I. and Farahani, M. (2009) 'Effect of the weld groove shape and pass number on residual stresses in butt-welded pipes', *International Journal of Pressure Vessels and Piping*, 86(11), pp. 723-731.
- Seng, O.L., Wing, C.Y. and Seet, G. (1989) 'The elastic analysis of a dent on pressurised pipe', *International Journal of Pressure Vessels and Piping*, 38(5), pp. 369-383.
- Shan, X., Davies, C.M., Wangsdan, T., O'Dowd, N.P. and Nikbin, K.M., 2009. Thermo-mechanical modelling of a single-bead-on-plate weld using the finite element method. *International Journal of Pressure Vessels and Piping*, 86(1), pp.110-121.
- Spina, R., Tricarico, L., Basile, G. and Sibillano, T. (2007) 'Thermo-mechanical modeling of laser welding of AA5083 sheets', *Journal of Materials Processing Technology*, 191(1), pp. 215-219.
- Standard, A. '1104, 2005,'', *Welding of Pipelines and Related Facilities*, " American Petroleum Institute, Washington, USA, .
- Teng, T. and Chang, P. (1998) 'Three-dimensional thermomechanical analysis of circumferentially welded thin-walled pipes', *International Journal of Pressure Vessels and Piping*, 75(3), pp. 237-247.
- Vaidyanathan, S., Todaro, A. and Finnie, I. (1973) 'Residual Stresses due to Circumferential Welds, J1. of Eng', *Materials and Technology*, 23.
- Vedeld, K., Osnes, H. and Fyrileiv, O., 2012. New interpretations of gripping force tests for lined pipes. *Marine Structures*, 29(1), pp.152-168.
- Welding, A. (2010) 'Qualify procedures and personnel according to AWS D1. 1/D1. 1M,'', *Structural Welding Code-Steel*, 60.
- Wiesner, C. and MacGillivray, H. (1999) 'Loading rate effects on tensile properties and fracture toughness of steel', *7 th Symposium on Fracture, Plastic Flow and Structural Integrity*. , 149-173.
- Woghiren, C.O. and Brennan, F.P., 2009. Weld toe stress concentrations in multi-planar stiffened tubular KK joints. *International Journal of Fatigue*, 31(1), pp.164-172.
- Yaghi, A., Hyde, T., Becker, A., Sun, W., Hilson, G., Simandjuntak, S., Flewitt, P., Pavier, M. and Smith, D. (2010) 'A comparison between measured and modeled residual stresses in a circumferentially butt-welded P91 steel pipe', *Journal of Pressure Vessel Technology*, 132(1), pp. 011206.
- Yaghi, A., Tanner, D., Hyde, T., Becker, A. and Sun, W. (2011) 'Abaqus Thermal Analysis of the Fusion Welding of a P92 Steel Pipe', *SIMULIA Customer Conference*. , 622-638.
- Yuan, L. and Kyriakides, S., 2014. Liner wrinkling and collapse of bi-material pipe under bending. *International Journal of Solids and Structures*, 51(3), pp.599-611.
- Zhang, Z., Holloway, G. and Marshall, A. (2008) 'Properties of T/P92 steel weld metals for ultra super critical (USC) power plant', *Weld.World*, 52, pp. 455.

- Zhang, Y.L., Gorman, D.G. and Reese, J.M., 2003. Vibration of prestressed thin cylindrical shells conveying fluid. *Thin-Walled Structures*, 41(12), pp.1103-1127.

Appendix A

In this appendix, a number of tools used in welding and impact tests are presented corresponding to their arrangement in Chapter 3 and Chapter 4.

A-1. Tools utilized in Welding tests

To record the thermal history during welding, 16-Channel thermocouple module, NI-9213, was used as shown in Figure A-1. The NI 9213 is a high-density thermocouple module for NI series where thermocouples can be added to mixed-signal test systems without taking up too many slots.



Figure A-1 Thermal module used to convert analogue signal to digital signal (ADC)

To record the strain history during welding, 8-Channel strain input module, NI-9235, was utilized as depicted in Figure A-2. The NI-9235 measures dynamic strain on all channels simultaneously, allowing for synchronized, high-speed measurements. This capability is important for applications, such as impact tests, that require comparison across many channels at a particular instant in time.

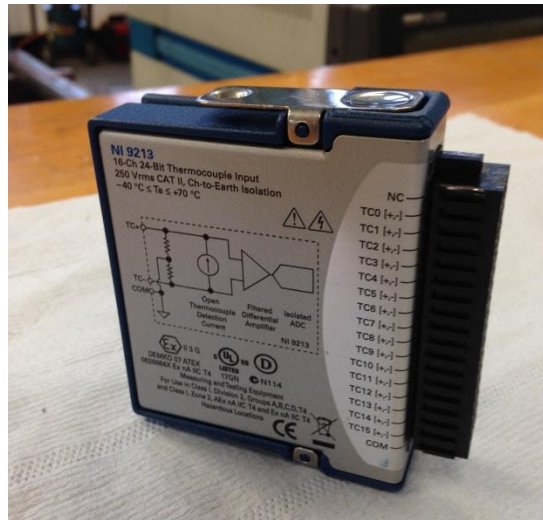


Figure A-2 Strain module used to convert analogue signal to digital signal (ADC)

To execute the TIG welding, a welding power source, GENESIS 150 AC-DC, was used to deposit the filler materials in their corresponding grooves as shown in Figure A-3 in Appendix A-1.



Figure A-3 Welding power source, GENESIS 150

A-2. Tools utilized in impact tests

To specify the precise height of free drop from the tip of indenter to the middle section of lined pipe, a laser distance measuring tool is used as shown in Figure A-4.

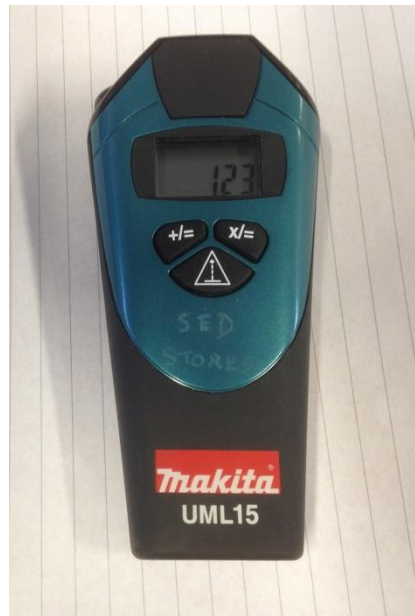


Figure A-4 Laser distance measuring tool to specify the heights.

To measure the actual impact velocity, a digital high speed camera, MEMRECAM HX-7, is used as shown in Figure A-5.

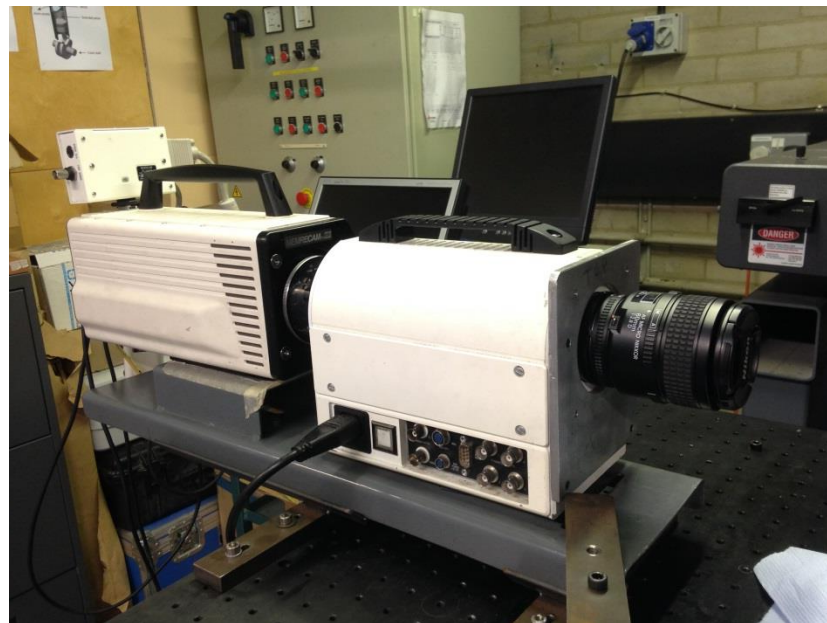


Figure A-5 High digital speed camera

